RESPONSE OF CO_2 SINK AND BIOGEOCHEMISTRY TO SEA-ICE LOSS IN THE WESTERN ARCTIC OCEAN

by

Zhangxian Ouyang

A dissertation submitted to the Faculty of the University of Delaware in partial fulfillment of the requirements for the degree of Doctor of Philosophy in Oceanography

Spring 2021

RESPONSE OF CO_2 SINK AND BIOGEOCHEMISTRY TO SEA-ICE LOSS IN THE WESTERN ARCTIC OCEAN

by

Zhangxian Ouyang

Approved: ____

Mark A. Moline, Ph.D.
Director of the School of Marine Science and Policy

Approved: ____

Estella Atekwana, Ph.D.
Dean of the College of Earth, Ocean, and Environment

Approved: ____

Louis F. Rossi, Ph.D.
Dean of the Graduate College and Vice Provost for Graduate and Professional Education

I certify that I have read this dissertation and that in my opinion it meets the academic and professional standard required by the University as a dissertation for the degree of Doctor of Philosophy.

Signed: ____

Wei-Jun Cai, Ph.D.
Advisor, Professor in charge of dissertation

I certify that I have read this dissertation and that in my opinion it meets the academic and professional standard required by the University as a dissertation for the degree of Doctor of Philosophy.

Signed: ____

George W. Luther III, Ph.D.
Member of dissertation committee

I certify that I have read this dissertation and that in my opinion it meets the academic and professional standard required by the University as a dissertation for the degree of Doctor of Philosophy.

Signed: ____

David L. Kirchman, Ph.D.
Member of dissertation committee

I certify that I have read this dissertation and that in my opinion it meets the academic and professional standard required by the University as a dissertation for the degree of Doctor of Philosophy.

Signed: ____

Andreas Muenchow, Ph.D.
Member of dissertation committee

I certify that I have read this dissertation and that in my opinion it meets the academic and professional standard required by the University as a dissertation for the degree of Doctor of Philosophy.

Signed: ____

Meibing Jin, Ph.D.
Member of dissertation committee

ACKNOWLEDGMENTS

For the past five years, I have been very fortunate to pursue my Ph.D. at University of Delaware, School of Marine Science and Policy. This is the best time and most exciting adventure I have ever had. I will treasure it for the rest of my life.

First, I would like to express my deepest gratitude to my advisor, Dr. Wei-Jun Cai, for his dedicated mentorship and tremendous support. Without his mentoring in research, I would not be where I am today. His outstanding guidance and generous encouragement always help me to confront the challenges and overcome difficulties on the road of scientific research. During this journey, I am always deeply inspired by his passion and dedication in scientific research, which greatly drives me to think harder, try harder and seek my goal of life bravely – as a scientist to discover the world, pass knowledge and make an impact.

I would also like to extend my gratitude to my dissertation committee: Dr. David Kirchman, Dr. George Luther, Dr. Andreas Muenchow and Dr. Meibing Jin for their generous guidance. They represent the role models of integrity, brilliance and excellence in scientific research I always look up to and work towards.

I am very grateful to my lab mates in Cai's Lab: Drs. Yonghui Gao, Hongjie Wang, Qian Li, Baoshan Chen. Their work and expertise greatly shaped my PhD training. Special thanks to our lab manager, Dr. Najid Hussain, for his generous help for both my cruise and lab works. I am also grateful to my friends and colleagues: Dr. Yuanyuan Xu, Dr. Jianzhong Su, Xinyu Li, Michael Scaboo, Xue Deng, who made my time at UD colorful and wonderful.

My sincere gratitude goes to our collaborators: Drs. Taro Takahashi, Liqi Chen, Di Qi, Wenli Zhong, Yun Li, Akihiko Murata, Shigeto Nishino, Zhongyong Gao, Heng Sun, Yingxu Wu, Qiang Li, Deb Jaisi, for their help with sample collecting and analysis, data contributions and fruitful discussions. Without such a great collaboration, I doubt that I could complete my dissertation work today.

Finally, I would like to express my very profound gratitude to my family for providing me with unfailing love and support. I owe many thanks to my wife, Lingjue, for her unconditional love and sacrifice. After a few years of separation, we finally joined together. I can't imagine a better gift than our marriage during my Ph.D. study. Thank you for always standing by me and being my only love and best friend.

I dedicate this accomplishment to you, Lingjue.

TABLE OF CONTENTS

LIST OF TABLES

LIST OF FIGURES

ABSTRACT

The oceanic uptake of atmospheric CO_2 is of global importance as it affects the pace of climate change. The Arctic Ocean acts as a carbon sink for atmospheric CO_2, benefiting from high solubility of CO_2 in cold seawater and high summer biological production. It has been known that amplified warming and accelerated sea ice loss in the Arctic Ocean since 1980s have profoundly altered the Arctic Ocean environment and related biogeochemical processes. However, less is known about how oceanic CO_2 uptake and biological production changes in different biogeochemical provinces in respond to warming and sea ice loss and how fast are these changes. Based on results from two cruises conducted in the western Arctic Ocean in 2016 and 2018, we examined seasonal and regional variabilities in metabolic status and the coupling of biological production and oceanic CO_2 uptake, which provided a mechanistic view of the summer evolution of net community production and CO_2 flux in the various stages of ice-melt and nutrient status. By compiling historical datasets of underway measurements of sea surface partial pressure of CO_2 (pCO_2), we found that despite the western Arctic Ocean as a whole continuing to act as an oceanic carbon sink, regional carbon flux dynamics differ greatly; the Chukchi Sea continues to absorb CO_2 at pace with the atmospheric CO_2 increase, whereas Beaufort Sea and Canada Basin become a weakened or diminishing CO_2 sink as the sea surface CO_2 increased at more than twice the rate of CO_2 in the atmosphere. In addition to examination of the long-term trend of sea surface CO_2, we further assessed seasonal and interannual variations in CO_2 uptake between 1994 and 2019. Two complementary approaches (observation-based and model-based) were conducted. Our results suggest that CO_2 uptake in the Chukchi Sea significantly increased at a rate of 1.4 $\pm$0.4 Tg C decade^{-1}, which was primarily due to a longer ice-free period with a larger open area and increased primary production and partially due to enhanced wind. However, no significant change in CO_2 uptake was found in the Canada Basin and Beaufort Sea. Our model results further revealed that the greatly decreased sea ice extent in summer indeed promoted CO_2 uptake and resulted in a weak increased CO_2 sink by 0.6$\pm$0.3 Tg C decade^{-1} in the Canada Basin, but this increasing sink was counteracted by a rapidly decreasing air-sea CO_2 gradient.

Chapter 1

INTRODUCTION

1.1 Warming and sea ice loss in the Arctic Ocean

In the past two hundred years and in particular recent decades, global climate has changed as a consequence of human activities and resultant emissions of greenhouse gases (e.g., CO_2). The Arctic Ocean is widely viewed as one of the most sensitive regions on the Earth responding to undergoing global climate change (AMAP, 2018). Across a variety of disciplines and perspectives, it is unambiguous that the Arctic Ocean is actively transforming to a warmer, less ice, fresher, more acidic and greener region (AMAP, 2018; Meredith et al., 2019; Thoman et al., 2020). The climate change in the Arctic has been amplified through snow, ice and permafrost feedbacks and is expected to be unavoidable and irreversible on timescales relevant to human societies and ecosystems (Meredith et al., 2019).

The rapid increased air temperature and accompanying substantial decline in sea ice extent are two of the most iconic indicators of climate change across the Arctic environment. As natural variability is larger in the Arctic region than in lower latitudes, the air temperature record proves that warming in the Arctic over the past century has amplified at a rate that is roughly double that of the global mean, which is due to a phenomenon known as Arctic Amplification (Figure 1.1; Ballinger et al., 2020). From 1971 to 2017, the average Arctic surface air temperature rose by 3.1℃ in winter and 1.8℃ in summer (Box et al., 2019).

The amplified warming greatly accelerates thawing of permafrost and glaciers on the land as well as snow and sea ice in the ocean. Since 1979, sea ice extent (area with sea ice concentration > 15%) has declined by nearly 40% (–13.1% per decade ± 2.3% relative to 1981–2010 mean; Onarheim et al., 2018; Perovich et al., 2020), with the strongest trend in September and lowest trend in March (Figure 1.2). Sea ice loss in the summer Arctic Ocean is unprecedented in the past 150 years based on historical reconstructions (Walsh et al., 2017). It has been predicted that the Arctic Ocean will become ice-free in summer in the 2030s-2040s (Overland and Wang, 2013; Overland et al., 2019). Besides the decline of sea ice extent, the Arctic sea ice has become younger and thinner. Between 1985 and 2020, the proportion of multi-year ice (>4 years old) in the Arctic Ocean decreased from 33% to 4.4% (Figure 1.3; Tschudi et al., 2019). Over the same period, first-year sea ice increased from 40% to 60-70% (Figure 1.3; Stroeve and Nots, 2018). Data from in-situ observations and satellite altimeter missions show ice thickness reduced by 65% from 3.59 m to 1.25 m between 1975 to 2012 (Lindsay and Schweiger, 2015).

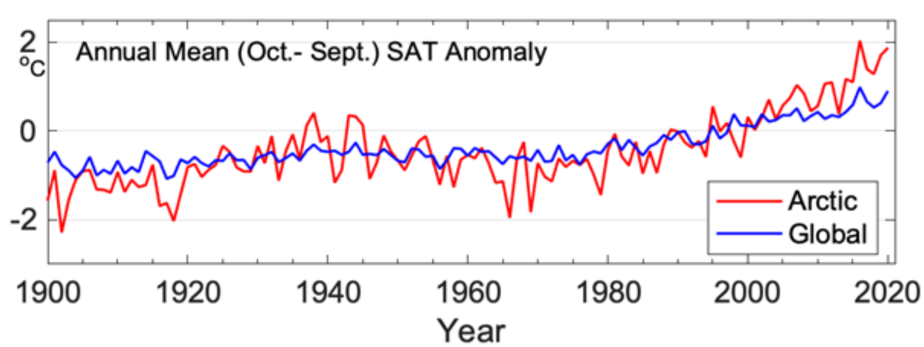

Figure 1.1: Mean annual surface atmospheric temperature anomalies in the Arctic (60ºN-90ºN; red line) and globally (blue line) for the 1900-2020 period, relative to the 1981-2010 means. Source: CRUTEM4 data (Jones et al., 2012). Taken from Ballinger et al. (2020).

Sea surface temperature (SST) in the Arctic Ocean is strongly linked to sea ice presence as well as ocean currents and atmospheric parameters. The reduced albedo for solar radiation greatly stimulates sea surface warming (Perovich, 2016). The latest assessment shows that the Arctic SST is increasing over much of the Arctic Ocean. The trend of August SST reveals that the mixed layer temperature increased by 0.5-0.7 ℃ per decade from 1982 to 2017 (Timmermans et al., 2017).

Warming and sea ice loss as two fundamental drivers have substantially altered the characteristics of Arctic physical processes, biogeochemical cycles, and ecosystems, with relevant influences far beyond the region for people who live in the Arctic and rely on this unique ecosystem (Meredith et al., 2019). Thus, how the amplified warming and accelerated sea ice loss affects the Arctic biogeochemistry and ecosystem is of great interest to scientific and societal communities.

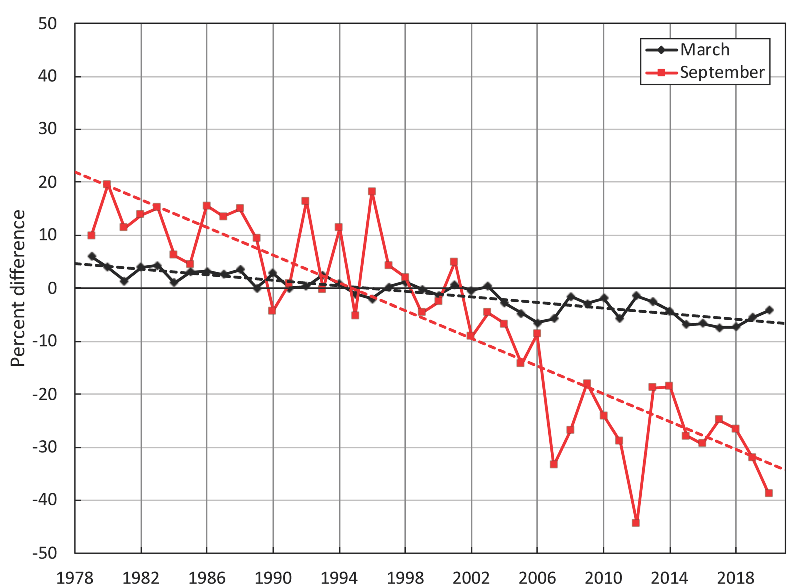

Figure 1.2: Percentage change in monthly sea ice extent relative to the 1981-2010 average climatology and linear trend (dashed lines) for March (black) and September (red) from 1979 to 2020. Taken from Perovich et al. (2020).

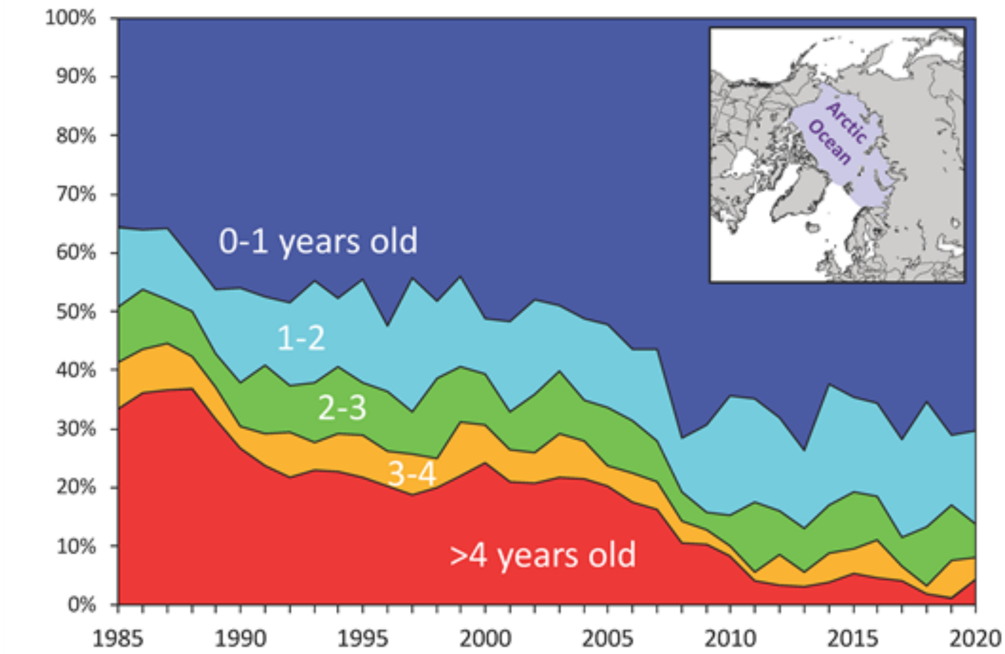

Figure 1.3: Sea ice age percentage within the Arctic Ocean for the week of 11-18 March 1985-2020. Data are from NSIDC (Tschudi et al., 2020). Taken from Perovich et al. (2020).

1.2 The role of sea ice in Arctic Ocean biogeochemistry

Sea ice plays a critical role on regulating the biogeochemical processes in the Arctic Ocean as it provides a thermal isolation between the surface ocean and the atmosphere, mechanic barrier to air-sea gas exchange, and habitat for ice-associated species. The seasonal cycle of sea ice melting-formation directly affects ice-albedo feedback, thermohaline circulation, surface freshening and stratification, and light and nutrient availability (Meredith et al., 2019).

The accelerated loss of sea ice over the past few decades has triggered shifts in the timing and intensity of primary production (Kahru et al., 2010; Ardyna et al., 2014; Kahru et al., 2016). Increased ice-free area and longer growing season result in a long-term increase in annual net primary production (NPP) in open water by 30%

between 1998 and 2012 (Arrigo and van Dijken, 2015). A more recent satellite-based study (Lewis et al., 2020) revealed that NPP continued to increase between 2012 and 2018 at twice the rate (13.5 Tg C yr^{-1}) than that between 1998 and 2012 (6.4 Tg C yr^{-1}), which is associated with higher surface chlorophyll a (Chl a) concentrations, likely sustained by an influx of new nutrients (Figure 1.4). Such changes in NPP have great impacts throughout the food web in the Arctic ecosystems, suggesting that the future Arctic Ocean may support higher trophic-level production and larger carbon export (Lewis et al., 2020).

Although sea ice loss has increased light penetration, photosynthesis, and primary production over the entire Arctic Ocean, the responses of primary production to seasonal sea ice retreat and advance could vary greatly among different regions. In the inflow shelves (e.g., the Chukchi Sea and Barents Sea), Atlantic and Pacific waters move northward bringing heat and nutrients into the Arctic Ocean, resulting in the largest increases in Chl a and NPP (Lewis et al., 2020). The shelfbreak regions have been considered as the harbor for massive phytoplankton blooms (Arrigo et al., 2014; Arrigo et al., 2012) as the removal of sea ice will enhance wind-driven upwelling (Mathis et al., 2012). The resulting water mixing and nutrient flux from the subsurface water stimulate high primary production in these regions. Another hotspot for enhanced primary production is the sea ice edge. Arrigo et al. (2012) reported massive phytoplankton blooms occurred beneath the ice at the ice-marginal zone, which they attributed to a thinning sea ice cover with more numerous melt ponds, with enhanced light penetration through the ice into the upper water column. Mundy et al. (2009) reported an ice-edge bloom associated with an upwelling event and suggested under-ice blooms are a widespread but under-documented phenomenon in the polar areas.

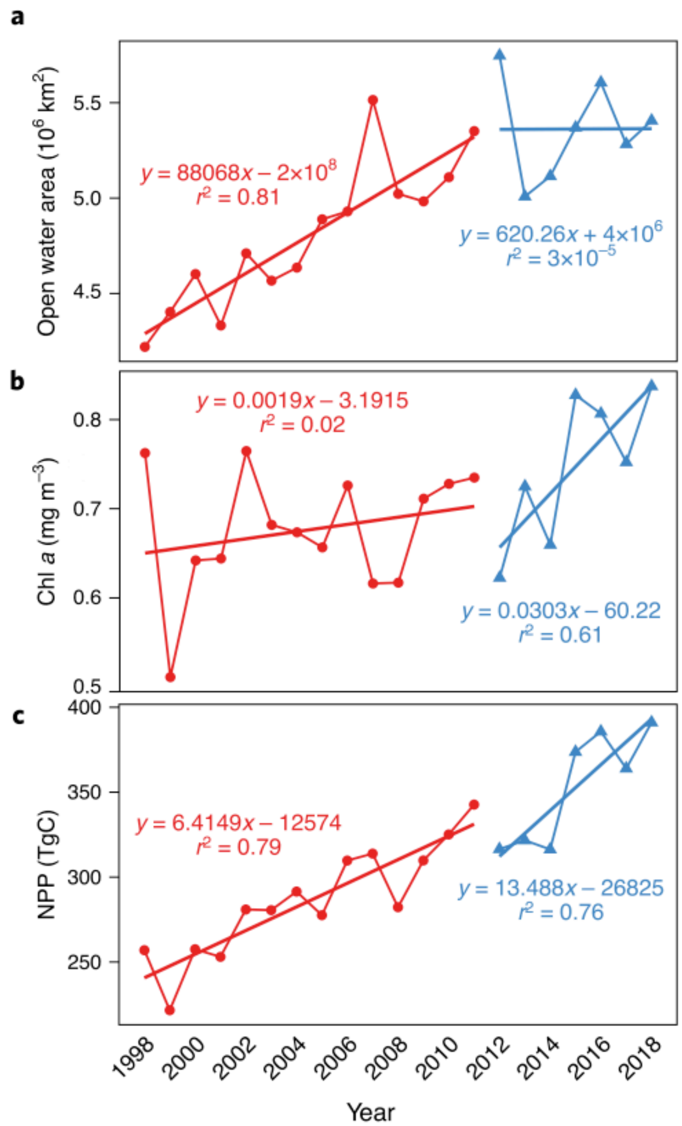

Figure 1.4: Trends in Arctic primary production over the two last decades. Annual time series of Arctic Ocean mean open-water area (a), mean Chl a (b) and NPP (c). The time series is separated into two time periods because from 1998–2012, loss of sea ice was responsible for the increase in NPP for the Arctic Ocean. After that time, the loss of sea ice slowed considerably but NPP continued to increase. This increase from 2012–2018 was due primarily to an increase in phytoplankton biomass, likely because of increased nutrient supplies into Arctic surface water. Source: Lewis et al., (2020). Taken from Ardyna and Arrigo, (2020).

Contrary to these hotspots of primary production, the current view of the upper layer in the Arctic Ocean basins is an oligotrophic ocean, characterized by nutrient limitation (Tremblay et al., 2011; Ji et al., 2019). A typical example is the Canada Basin which is greatly influenced by the Beaufort Gyre. McLaughlin and Carmack (2010) suggested that the efficiency of the biological pump within the Beaufort Gyre is low because freshwater accumulation within the gyre strengthens surface stratification and limits nutrient supply from subsurface water. Nishino et al., (2011) also found that the biological pump decreased within the Beaufort Gyre whereas it increased outside the Beaufort Gyre. A physical-biologically coupled model showed that in the central Arctic Ocean new production will not increase proportionately with increasing light availability due to nutrient limitation (Slagstad et al., 2011).

More and more studies of under-ice blooms suggest that the under-ice phytoplankton communities appear to be well-adapted to low-light condition (Arrigo et al., 2012; Mundy et al., 2009; Lewis et al., 2019) so that at least the first-year sea ice may not limit primary production at the ice bottom. As more and more multi-year ice (4-5 m) is replaced by first-year ice (0.8-1.8 m) in a few decades, the under-ice algal blooms are likely to spread beneath the ice over the central Arctic Ocean.

Therefore, it is of great interest and importance to investigate the distribution and evolution of Arctic Ocean primary production. We hypothesize that surface primary production in the oligotrophic basin is intimately associated with the presence of sea ice, and that rate it changes with the ice melting process. Unlike Arctic shelf ecosystems where oceanic inflow and terrestrial river runoff contribute most of the nutrients, brine stored in the ice may be a dominate nutrient source for algal communities inside and beneath the sea ice that can support weak but ubiquitous under-ice primary production. Whether the ice-algal primary production will vanish quickly once ice completely melts remains to be investigated as ice-algae lose their habitats and nutrient source. If that is the case, surface biological CO_2 removal in the central Arctic Ocean also depends on the presence of sea ice. Although the under-ice primary production is not as high as that in the shelf, it is enough to maintain the water with undersaturated $p$$CO_2$ and a high buffer capacity to resist surface acidification.

To explore these issues, we conducted underway measurements of net community production via the O_2/Ar approach in summers of 2016 and 2018 to improve our understanding of the different mechanisms controlling primary production in the shelf and the basin, and the role of sea ice in controlling the under-ice primary production and biological drawdown of CO_2 (Chapter 2).

1.3 The western Arctic Ocean

The western Arctic Ocean is of great interest to the interdisciplinary research community, as it has experienced dramatic climate-driven sea ice loss (Onarheim et al., 2018) and substantial alterations in the seasonal biogeochemical dynamics in recent decades. Additional scientific interest arises from its unique geographic setting. The western Arctic Ocean consists of the inflow shelf (the Chukchi Sea), which is impacted by nutrient-rich Pacific Ocean Water, the interior shelf (Beaufort Sea), which is narrow and influenced by the Mackenzie River and coastal upwelling, and the Canada Basin, which is greatly regulated by the nutrient-poor Beaufort gyre and sea ice meltwater (Figure 1.5).

One particularly notable change in the western Arctic Ocean is that the annual Bering Strait throughflow increased by 50% from 2001 to 2011(Woodgate et al., 2012; Woodgate 2018), as a primary physical driver for other relative ecological and geochemical changes. The increased Pacific Water has resulted in one of the largest increases in net primary production on this inflow shelf—Chukchi Sea (Arrigo and van Dijken, 2015; Lewis et al., 2020).

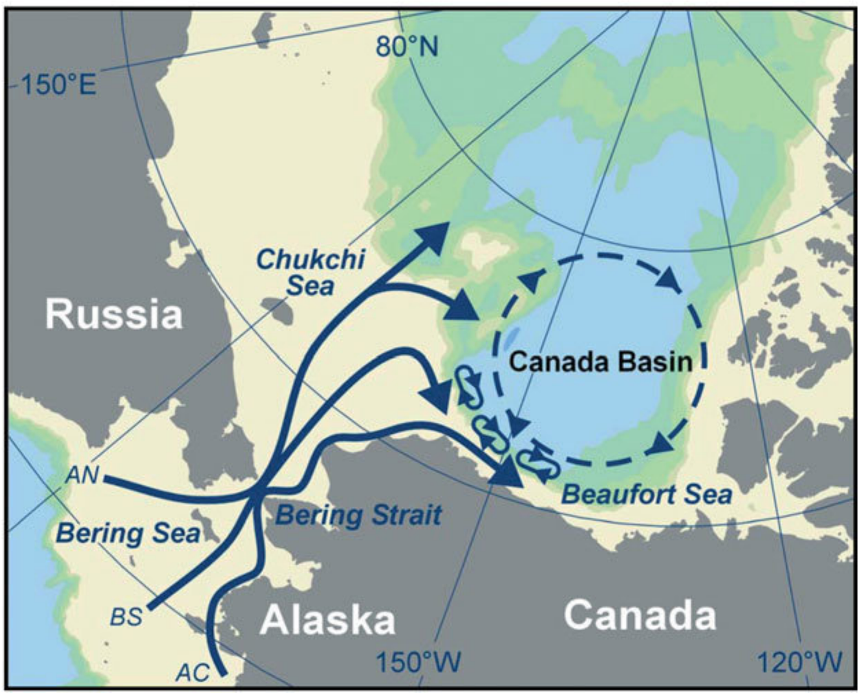

Figure 1.5: Pathways of currents and oceanographic features of the western Arctic Ocean. Heavy lines indicate general pathways taken by currents flowing from the Bering Sea into the western Arctic Ocean: Anadyr (AN), Bering Shelf (BS), and Alaskan Coastal (AC). The Beaufort Gyre (dashed line) centered over the Canada Basin and the area of formation of eddies along the shelf break of the Chukchi and Beaufort Seas. Taken from Nelson et al. (2009).

In addition, the Beaufort Gyre region has become the largest freshwater reservoir in the Arctic Ocean, having increased by 40% between 2003 and 2017 mainly due to massive sea ice melt and the Beaufort Gyre's strengthening (Krishfield et al., 2014; Proshutinsky et al., 2015). Increased river outflow also intensified the freshwater accumulation (Fichot et al., 2013). Consequently, stratification is expected to increase in the Canada Basin (Toole et al., 2010; Carmack et al., 2016), which may inhibit nutrient flux from the subsurface and hence primary production (Ji et al., 2019; Lewis et al., 2020).

Although such shelf–basin spatial heterogeneity has attracted many researchers' attention, from a biogeochemical cycle perspective, it has not been extensively studied. In addition, the pronounced loss of summer sea ice in the western Arctic Ocean over recent decades provides an ideal experimental field and observational window for examining the impacts of sea ice loss on biogeochemical processes. Thus, in this dissertation research, the study area is focused on the western Arctic Ocean.

1.4 Debate of the future carbon sink of Arctic Ocean

As carbon cycle in the Arctic Ocean is intimately linked to sea ice, the accelerated sea ice loss inevitably induces great complexity and uncertainty in how the carbonate system is changing accordingly. The Arctic Ocean was predicted to be an important sink for anthropogenic CO_2 as the sea surface pCO_2 under the sea ice cover was found to be much lower than atmospheric pCO_2 (Bates et al., 2006; Bates and Mathis, 2009). This large air-sea gradient of pCO_2 (ΔpCO_2) indicates a large CO_2 sink potential as sea ice melts. Ocean uptake of CO_2 from the atmosphere is expected to be larger because more area becomes ice-free and exposed to the atmosphere in the future. Meanwhile, the improved light availability also promotes primary production, which further enlarges the air-sea gradient of pCO_2 and thus biological drawdown of CO_2 and CO_2 sink. This rational has been supported by early observations of a strong capacity of CO_2 uptake and a large CO_2 sink on the high-productive Chukchi shelves and shelfbreak regions (Murata and Takizawa, 2003; Bates et al., 2006; Jutterström and Anderson, 2010;). By synthesizing studies prior to 2006 in the entire Arctic Ocean, Bates and Mathis (2009) estimated that the entire Arctic Ocean takes up atmospheric CO_2 on the order of -66 to -199 Tg C yr^{-1}, which contributes up to 5-14% of the global carbon sink.

However, the Arctic CO_2 uptake potential has been questioned by observations of high pCO_2 in the ice-free southern Canada Basin in 2008-2009 (Cai et al., 2010; Else et al., 2013). They attributed the high pCO_2 in the ice-free basin to rapid air-sea equilibration and a warming effect. This newly emerged high pCO_2 has been repeatedly observed in later years (2010-2018), suggesting that ice-free Arctic basins may not be a significant carbon sink as expected.

These contrasting conclusions and projections of the Arctic carbon sink remind us that different physical and biogeochemical conditions between shelves and basins may shape different mechanisms controlling the carbon cycle and relevant processes. Therefore, it is of significant interest to better understand how sea surface pCO_2 on the productive shelves and in the oligotrophic basin behaves differently in response to Arctic environmental changes. Here we report new sea surface pCO_2 data together with historical data from multiple international databases to examine the seasonal and decadal variations, and quantify the contributions of multiple drivers (Chapter 3).

While sea ice loss may initially promote CO_2 uptake as undersaturated pCO_2 water is exposed to the atmosphere and increased light improves productivity, it is poorly known about whether such a CO_2 uptake potential will last for the entire summer or just a short period and whether biological CO_2 removal could enlarge the CO_2 sink over the whole Arctic Ocean or only be locally important. To resolve the spatial and temporal variability in air-sea CO_2 flux and determine how carbon sink and source changes in response to multiple changes driven by sea ice loss, we analyzed long-term changes in sea surface pCO_2 (Chapter 3) and employed a box-model simulation to further quantify the seasonal and interannual variations in air-sea CO_2 fluxes and CO_2 sink for the western Arctic Ocean over the period of 1994 to 2019 (Chapter 4). These studies improved the understanding of processes regulating seasonal and interannual variabilities of the Arctic Ocean sea surface pCO_2 and CO_2 uptake, which is essential for forecasting responses of the oceanic carbon cycle to climate change. A summary chapter is at the end.

REFERENCES

AMAP, 2018. AMAP Assessment 2018: Arctic Ocean Acidification. Arctic Monitoring and Assessment Programme (AMAP), Tromsø, Norway.

Ardyna, M. et al. Recent Arctic Ocean sea-ice loss triggers novel fall phytoplankton blooms. Geophys. Res. Lett. 41, 6207–6212 (2014).

Arrigo, K. R. et al. Phytoplankton blooms beneath the sea ice in the Chukchi Sea. Deep Sea Res. Pt. 2 105, 1–16 (2014).

Arrigo, K. R. et al. Massive phytoplankton blooms under Arctic sea ice. Science 336, 1408 (2012).

Arrigo, K.R. and G.L. van Dijken, 2015: Continued increases in Arctic Ocean primary production. Progress in Oceanography, 136, 60–70, doi:10.1016/j. pocean.2015.05.002.

Ballinger, T. J., J. E. Overland, M. Wang, U. S. Bhatt, E. Hanna, I. Hanssen-Bauer, S-J. Kim, R. L. Thoman, and J. E. Walsh. Arctic Report Card 2020: Surface Air Temperature. (2020).

Bates, N.R., Moran, S.B., Hansell, D.A., Mathis, J.T., 2006. An increasing CO2 sink in the Arctic Ocean due to sea-ice loss. Geophys. Res. Lett. 33, L23609. http://dx.doi.org/10.1029/2006GL027028.

Bates, N. R., &Mathis, J. T. (2009). The Arctic Oceanmarine carbon cycle: Evaluation ofair-sea CO2 exchanges, ocean acidification impacts and potential feedbacks. Biogeosciences, 6(11), 2433–2459. https://doi.org/10.5194/bg-6-2433-2009

Box, Jason E., William T. Colgan, Torben Røjle Christensen, Niels Martin Schmidt, Magnus Lund, Frans-Jan W. Parmentier, Ross Brown et al. Key indicators of Arctic climate change: 1971–2017. Environmental Research Letters 14, no. 4 (2019): 045010.

Cai, W. J., Chen, L., Chen, B., Gao, Z., Lee, S. H., Chen, J., ... & Zhang, H. (2010). Decrease in the CO2 uptake capacity in an ice-free Arctic Ocean basin. Science, 329(5991), 556-559.

Carmack, E. C. et al. Freshwater and its role in the Arctic marine system: sources, disposition, storage, export, and physical and biogeochemical consequences in the Arctic and global oceans. J. Geophys. Res. Biogeosci. 121, 675–717 (2016).

Fichot, C. G. et al. Pan-Arctic distributions of continental runoff in the Arctic Ocean. Sci. Rep. 3, 1053 (2013).

Else, B. G. T., Papakyriakou, T. N., Galley, R. J., Mucci, A., Gosselin, M., Miller, L. A., ... & Thomas, H. (2012). Annual cycles of pCO2sw in the southeastern Beaufort Sea: New understandings of air-sea CO2 exchange in arctic polynya regions. Journal of Geophysical Research: Oceans, 117(C9).

Ji, Brenda Y., Zoe O. Sandwith, William J. Williams, Oana Diaconescu, Rubao Ji, Yun Li, Emma Van Scoy, Michiyo Yamamoto-Kawai, Sarah Zimmermann, and Rachel HR Stanley. Variations in rates of biological production in the Beaufort Gyre as the Arctic changes: Rates from 2011 to 2016. *Journal of Geophysical Research: Oceans* 124, no. 6 (2019): 3628-3644.

Jones, P. D., D. H. Lister, T. J. Osborn, C. Harpham, M. Salmon, and C. P. Morice, 2012: Hemispheric and large-scale land-surface air temperature variations: An extensive revision and an update to 2010. J. Geophys. Res., 117, D05127, https://doi.org/10.1029/2011JD017139.

Jutterström, Sara, and Leif G. Anderson. Uptake of CO2 by the Arctic Ocean in a changing climate. *Marine Chemistry*122, no. 1-4 (2010): 96-104.

Kahru, M., Lee, Z.-P., Mitchell, B. G. & Nevison, C. D. Effects of sea ice cover on satellite-detected primary production in the Arctic ocean. Biol. Lett. 12, 20160223 (2016).

Kahru, M., Brotas, V., Manzano-Sarabio, M. & Mitchell, B. G. Are phytoplankton blooms occurring earlier in the Arctic? Glob. Change Biol. 17, 1733–1739 (2010).

Krishfield, R.A. et al., 2014: Deterioration of perennial sea ice in the Beaufort Gyre from 2003 to 2012 and its impact on the oceanic freshwater cycle. Journal of Geophysical Research: Oceans, 119 (2), 1271–1305, doi:10.1002/2013JC008999.

Lewis, K. M. et al. Photoacclimation of Arctic Ocean phytoplankton to shifting light and nutrient limitation. Limnol. Oceanogr. 64, 284–301 (2019).

Lewis, K. M., van Dijken, G. & Arrigo, K. R. Changes in phytoplankton concentration, not sea ice, now drive increased Arctic Ocean primary production. Science 369, 198–202 (2020).

Lindsay, R. and A. Schweiger, 2015: Arctic sea ice thickness loss determined using subsurface, aircraft, and satellite observations. The Cryosphere, 9 (1), 269–283, doi:10.5194/tc-9-269-2015.

Mathis, Jeremy T., Robert S. Pickart, Robert H. Byrne, Craig L. McNeil, G. W. K. Moore, Laurie W. Juranek, Xuewu Liu et al. Storm-induced upwelling of high pCO2 waters onto the continental shelf of the western Arctic Ocean and implications for carbonate mineral saturation states. Geophysical Research Letters 39, no. 7 (2012).

McLaughlin, Fiona A., and Eddy C. Carmack. Deepening of the nutricline and chlorophyll maximum in the Canada Basin interior, 2003–2009. *Geophysical Research Letters* 37, no. 24 (2010).

Meredith, M., M. Sommerkorn, S. Cassotta, C. Derksen, A. Ekaykin, A. Hollowed, G. Kofinas, A. Mackintosh, J. Melbourne-Thomas, M.M.C. Muelbert, G. Ottersen, H. Pritchard, and E.A.G. Schuur, 2019: Polar Regions. In: IPCC Special Report on the Ocean and Cryosphere in a Changing Climate [H.-O. Pörtner, D.C. Roberts, V. Masson-Delmotte, P. Zhai, M. Tignor, E. Poloczanska, K. Mintenbeck, A. Alegría, M. Nicolai, A. Okem, J. Petzold, B. Rama, N.M. Weyer (eds.)].

Mundy, C. J., Michel Gosselin, Jens Ehn, Yves Gratton, Andrea Rossnagel, David G. Barber, Johannie Martin et al. Contribution of under-ice primary production to an ice-edge upwelling phytoplankton bloom in the Canadian Beaufort Sea. *Geophysical Research Letters* 36, no. 17 (2009).

Murata, A., &Takizawa, T. (2003). SummertimeCO2 sink in shelf and slope waters of the western Arctic Ocean. Continental Shelf Research, 23, 753–776.

Nelson, R. J., Carmack, E. C., McLaughlin, F. A., & Cooper, G. A. (2009). Penetration of Pacific zooplankton into the western Arctic Ocean tracked with molecular population genetics. *Marine Ecology Progress Series*, *381*, 129-138.

Nishino, Shigeto, Takashi Kikuchi, Michiyo Yamamoto-Kawai, Yusuke Kawaguchi, Toru Hirawake, and Motoyo Itoh. Enhancement/reduction of biological pump depends on ocean circulation in the sea-ice reduction regions of the Arctic Ocean. *Journal of oceanography* 67, no. 3 (2011): 305-314.

Onarheim, I.H., T. Eldevik, L.H. Smedsrud and J.C. Stroeve, 2018: Seasonal and regional manifestation of Arctic sea ice loss. Journal of Climate, 31 (12), 4917–4932, doi:10.1175/jcli-d-17-0427.1.

Overland, James, Edward Dunlea, Jason E. Box, Robert Corell, Martin Forsius, Vladimir Kattsov, Morten Skovgård Olsen, Janet Pawlak, Lars-Otto Reiersen, and Muyin Wang. The urgency of Arctic change. *Polar Science* 21 (2019): 6-13.

Overland, J.E. and M.Y. Wang, 2013: When will the summer Arctic be nearly sea ice free? Geophysical Research Letters, 40 (10), 2097–2101, doi:10.1002/grl.50316.

Perovich, D.K., 2016: Sea ice and sunlight. In: Sea Ice [Thomas, D.N. (ed.)]. Wiley Online Library, 110–137.

Perovich, Donald, W. Meier, M. Tschudi, S. Hendricks, A. A. Petty, D. Divine, S. Farrell et al. Arctic Report Card 2020: Sea Ice. (2020).

Proshutinsky, A. et al., 2015: Arctic circulation regimes. Phil. Trans. R. Soc. A, 373 (2052), 20140160, doi:10.1098/rsta.2014.0160.

Slagstad, D., I. H. Ellingsen, and P. Wassmann. Evaluating primary and secondary production in an Arctic Ocean void of summer sea ice: an experimental simulation approach. *Progress in Oceanography* 90, no. 1-4 (2011): 117-131.

Stroeve, J., and D. Notz, 2018: Changing state of Arctic sea ice across all seasons. Environ. Res. Lett., 13, 103001, https://doi.org/10.1088/1748-9326/aade56.

Thoman, R. L., J. Richter-Menge, and M. L. Druckenmiller, Eds., 2020: Arctic Report Card 2020, https://doi.org/10.25923/mn5p-t549.

Timmermans, M.-L., C. Ladd and K. Wood, 2017: Sea surface temperature [NOAA (ed.)].Arctic Report Card, NOAA, https://arctic.noaa.gov/Report-Card/Report-Card-2017/ArtMID/7798/ArticleID/698/Sea-Surface- Temperature).

Toole, J. M. et al. Influences of the ocean surface mixed layer and thermohaline stratification on Arctic Sea ice in the central Canada Basin. J. Geophys. Res. Oceans 115, C10018 (2010).

Tremblay, J-É., S. Bélanger, D. G. Barber, M. Asplin, J. Martin, G. Darnis, L. Fortier et al. Climate forcing multiplies biological productivity in the coastal Arctic Ocean. *Geophysical Research Letters* 38, no. 18 (2011).

Tschudi, M., W. N. Meier, J. S. Stewart, C. Fowler, and J. Maslanik, 2019: EASE-Grid Sea Ice Age, Version 4. NASA National Snow and Ice Data Center Distributed Active Archive Center, Boulder, CO, USA, https://doi.org/10.5067/UTAV7490FEPB.

Tschudi, M. A., W. N. Meier, and J. S. Stewart, 2020: An enhancement to sea ice motion and age products at the National Snow and Ice Data Center (NSIDC). Cryosphere, 14, 1519-1536, https://doi.org/10.5194/tc-14-1519-2020.

Walsh, J.E., F. Fetterer, J. Scott Stewart and W.L. Chapman, 2017: A database for depicting Arctic sea ice variations back to 1850. Geographical Review, 107 (1), 89–107, doi:10.1111/j.1931-0846.2016.12195.x.

Woodgate, Rebecca A. Increases in the Pacific inflow to the Arctic from 1990 to 2015, and insights into seasonal trends and driving mechanisms from year-round Bering Strait mooring data. *Progress in Oceanography* 160 (2018): 124-154.

Woodgate, Rebecca A., Thomas J. Weingartner, and Ron Lindsay. Observed increases in Bering Strait oceanic fluxes from the Pacific to the Arctic from 2001 to 2011 and their impacts on the Arctic Ocean water column. *Geophysical Research Letters* 39, no. 24 (2012).

Chapter 2

SUMMERTIME EVOLUTION OF NET COMMUNITY PRODUCTION AND CO_2 FLUX IN THE WESTERN ARCTIC OCEAN

2.1 Abstract

To examine seasonal and regional variabilities in metabolic status and the coupling of net community production (NCP) and air–sea CO_2 fluxes in the western Arctic Ocean, we collected underway measurements of surface O_2/Ar and partial pressure of CO_2 (pCO_2) in the summers of 2016 and 2018. With a box-model, we demonstrate that accounting for local sea ice history (in addition to wind history) is important in estimating NCP from biological oxygen saturation ($\Delta(O_2/Ar)$) in polar regions. Incorporating this sea ice history correction, we found that most of the western Arctic exhibited positive $\Delta(O_2/Ar)$ and negative pCO_2 saturation, $\Delta(pCO_2)$, indicative of net autotrophy but with the relationship between the two parameters varying regionally. In the heavy ice-covered areas, where air-sea gas exchange was suppressed, even minor NCP resulted in relatively high $\Delta(O_2/Ar)$ and low pCO_2 in water due to limited gas exchange. Within the marginal ice zone, NCP and CO_2 flux magnitudes were strongly inversely correlated, suggesting an air to sea CO_2 flux induced primarily by biological CO_2 removal from surface waters. Within ice-free

---

Ouyang, Z., Qi, D., Zhong, W., Chen, L., Gao, Z., Lin, H., Sun, H., Li, T., Cai, W-J. (2021). Summertime evolution of net community production and CO_2 flux in the western Arctic Ocean. *Global Biogeochemical Cycles.* https://doi.org/10.1029/2020GB006651

waters, the coupling of NCP and CO_2 flux varied according to nutrient supply. In the oligotrophic Canada Basin, NCP and CO_2 flux were both small, controlled mainly by air-sea gas exchange. On the nutrient-rich Chukchi Shelf, NCP was strong, resulting in great O_2 release and CO_2 uptake. This regional overview of NCP and CO_2 flux in the western Arctic Ocean, in its various stages of ice-melt and nutrient status, provides useful insight into the possible biogeochemical evolution of rapidly changing polar oceans.

2.2 Introduction

The Arctic Ocean is currently experiencing rapid environmental and ecological changes in response to climate change. In recent decades, sea ice extent has drastically declined, resulting in earlier seasonal ice retreat and thinning (Onarheim et al. 2018; Stroeve et al., 2018). This change has profound and potentially cascading effects, as sea-ice state is a crucial factor to regulate light availability, water column stability and nutrient availability (Taylor et al., 2013). In addition, sea ice provides habitat for numerous autotrophs in polar regions (Selz et al .2018; Fernández-Méndez et al., 2018). Thus, these important factors intimately associated with ice can greatly affect the timing, location, and intensity of Arctic Ocean primary production.

Still, the role of sea ice distribution and melt history on the seasonal evolution of net community production (NCP) in the Arctic Ocean is under-documented, and the alteration of biological production by climate warming and sea-ice retreat is poorly understood. Net community production is quantified from the difference between the oxygen produced by plankton during photosynthesis and the oxygen consumed by the entire marine community during respiration. The rapidly changing sea ice brings great variability and uncertainty regarding timing and magnitudes of NCP. In addition, a better understanding of how changing NCP might affect sea surface carbon dioxide (CO_2) distributions and sea-air CO_2 fluxes is crucially required for reliably modeling current and future Arctic Ocean carbon budgets. Several studies have assessed regional variations of Arctic Ocean sea-air CO_2 fluxes (Bates et al., 2006; Cai et al., 2010; Evans et al., 2015; Yasunaka et al., 2018), but few have directly examined the coupling of NCP and CO_2 uptake and variabilities associated with sea ice change (Islam et al. 2016; Eveleth et al. 2017).

Predicting how NCP will change in the future is complex, for both ice-covered and ice-free areas. One hypothesis is under-ice NCP is expected to increase, with continuing ice thinning and the replacement of multi-year ice by first-year ice (Maslanik et al., 2011; Arrigo et al., 2012). Some studies, however, suggest that ice-algae primary production is not always positively related to sea ice recession. Some specialized ice-algae communities are well adapted to low light (Lewis et al., 2019) and their growth depends on the presence of ice habitat (Fernández-Méndez et al., 2018). Thus, some areas with sea ice melt in early summer could cause under-ice NCP to decrease. For example, one model study estimated that annual ice-algae net primary production on the Chukchi Shelf decreased by 22% between 1980 and 2015 due to earlier onset of ice melt and retreat, which in turn led to an earlier termination of the algal growing season and an overall shorter growing season (Selz et al., 2018). Similarly, NCP in the ice-free central Arctic Ocean would not necessarily be expected to increase in proportion to increasing light availability as sea ice decreased, because the countervailing effects of increased stratification and nutrient limitation may also play a role (Slagstad et al., 2011; McLaughlin and Carmack, 2010; Ulfsbo et al., 2014; Ji et al., 2019).

The marginal ice zone (the transition between the ice-free ocean and heavy ice-covered region) is of particular interest with respect to NCP and CO_2 flux. In this unique, dynamic, and transient habitat, both physical and biological processes can significantly influence gas exchange. As the sea ice begins its annual melt, a shallow mixed layer establishes and light availability increases, providing conditions favorable for phytoplankton growth, which in turns leads to positive NCP and CO_2 drawdown. In summer 2008, for example, an ice-edge bloom was observed in the Canadian Beaufort Sea in association with an upwelling event that brought nutrient-rich water to the sea surface (Mundy et al., 2009). A pan-Arctic analysis of satellite ocean-color and sea-ice data found that ice-edge blooms sometimes form long (>100 km) belts along ice edges and are important features of Arctic primary production (Perrette et al., 2011). Because ice-edge blooms are short-lived and highly variable, responsive to seasonal sea ice deformation and rapid recession, field assessments of NCP and CO_2 uptake in the marginal ice zone are difficult to achieve.

At present, we lack adequate knowledge of how the seasonal progression of sea ice alters the timing and magnitude of Arctic NCP and CO_2 flux and of how NCP couples with CO_2 uptake in the different physical and biogeochemical regimes (e.g., nutrient-rich shelf versus oligotrophic basin, or ice-covered versus ice-free regions). Bridging the occasional snapshot views provided by field observations is important to achieving a coherent overview of summer-to-fall seasonal NCP evolution in the Arctic Ocean. Here we report underway observations of $\Delta(O_2/Ar)$ (from which NCP can be derived) and the partial pressure of carbon dioxide (pCO$_2$, from which CO_2 flux can be derived) in the western Arctic Ocean during the summers of 2016 and 2018. Our data cover a range of ecological regimes, including the ice-covered central Arctic, the highly dynamic marginal ice zone (the Mendeleev Ridge and Chukchi Plateau), the nutrient-rich Chukchi Shelf, and the oligotrophic ice-free Canada Basin. The result is an unprecedented view of the spatial variability of western Arctic Ocean biological production and CO_2 flux. The wide coverage of the observations also enables us to examine relationships between $\Delta(O_2/Ar)$ and pCO_2 and the coupling of NCP and CO_2 uptake under rapidly changing ice conditions, thus better elucidating important control mechanisms.

2.3 Methods and modeling

2.3.1 Study area

The biogeochemical properties of Arctic surface waters are fundamentally determined by physical setting but then modified by biological processes over time. Additional complexity arises from rapidly changing sea ice conditions and the accompanying changes in light and nutrients, factors that dominantly control seasonal biological productivity. The study area covers most of the western Arctic Ocean between 65°N to 85°N and 137°W to 180°W. All samples were collected on the RV *Xuelong* during two Chinese National Arctic Research Expedition (CHINARE) cruises conducted from July 24 to September 4 in 2016 and from July 29 to September 8 in 2018. The cruise tracks of 2016 and 2018 covered generally the same areas within a similar time window (Figure 1a and b), which provides an opportunity to examine seasonal and interannual variations in $\Delta(O_2/Ar)$ and pCO_2, as well as NCP and CO_2 flux. Based on topography, circulation, and ice condition, we divided the western Arctic Ocean into four subregions: (1) the nutrient-rich Chukchi Shelf (CS), sometimes further divided into the southern Chukchi Shelf (sCS, 65°N–69°N) and the northern Chukchi Shelf (nCS, 69°N–72°N); (2) the oligotrophic Canada Basin (CB), separated from the Chukchi Shelf mainly along the 200–250 m isobaths; (3) the Mendeleev Ridge (MR) and Chukchi Plateau (CP), site of the marginal ice zone during our field visits, separated from the Canada Basin along 167°W; and (4) the high-latitude area of perennial ice cover (IC), separated from the more southerly regions along 77°N–79°N.

2.3.2 Underway measurements

Underway temperature and salinity were measured by an underway water monitoring system in an intake port near the bow of the ship (~7 m below waterline). We removed any measurements that reflected interference from ice rubble when the ship was breaking ice, but we retained measurements collected when the ship was on station or tethered to ice (with less interference from ice rubble), especially for the high-latitude regions (>77°N) where observations are especially scarce.

To quantify oxygen status as influenced by both physical and biological processes in the mixed layer, oxygen saturation percentage (O_2%) was measured every 30 s underway using an Aanderaa optode (model 4531A). The optode was calibrated before each cruise with 0% and 100% O_2-saturated water according to manufacturer's instructions. Discrete water samples collected from both the underway water pipeline and CTD Niskin bottles (surface samples) were used to check and validate the optode measurements. Excluding measurements that were possibly compromised by air injection or ice rubble during ice-breaking operations, the average deviation between the optode and titration O_2% measurements was less than 1.5% (N=50). The relatively larger deviation was found in the heavy ice-covered region, which is possibly due to

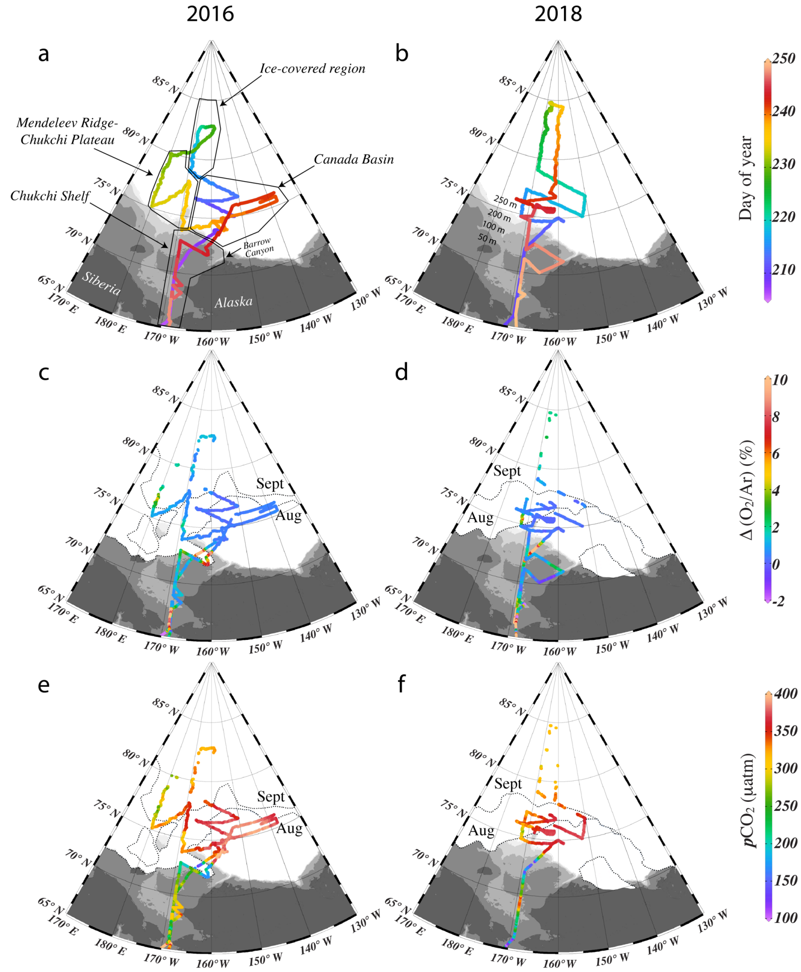

Figure 2.1 Cruise tracks of the 2016 and 2018 CHINARE cruises (a and b), with sea surface biological oxygen saturation ($\Delta(O_2/Ar)$; c and d) and partial pressure of CO_2 (pCO_2; e and f) shown in color. The direction of ship and timing of measurements are indicated by color scale (a and b). We divided the western Arctic Ocean into four subregions (a): (1) Chukchi Shelf (CS); (2) Canada Basin (CB), separated from the Chukchi Shelf mainly along the 200–250 m isobaths; (3) the Mendeleev Ridge (MR) and Chukchi Plateau (CP), separated from the Canada Basin along 167°W; and (4) the high-latitude area of perennial ice cover (IC), separated from the more southerly regions along 77°N–79°N. The light gray shading indicates ocean bathymetry (see depth contour labels on panel b). The white areas with dotted black lines on panel c-f indicate monthly sea ice extent (ice concentration >15%) in August and September (National Snow and Ice Data Center, http://nsidc.org/data/seaice_index/). Plots were produced by Ocean Data View (Schlitzer, 2018).

the effect of ice rubble in the underway water pipe. Note that O_2% results are only used to demonstrate the total O_2 state in the mixed layer, not for NCP calculation.

Sea surface underway pCO_2 was measured using an underway CO_2 system with a nondispersive infrared analyzer (General Oceanic, USA) that quantified CO_2 in the gas of an equilibrated headspace. This system was monitored and calibrated with four certified gas standards every 3 hours, which provided an overall precision of ± 2 μatm in the pCO_2 measurements. The underway CO_2 system and data reduction procedure are further described in Pierrot et al. (2009).

The ratio of oxygen and argon concentrations (O_2/Ar) was continuously measured underway by equilibrator inlet mass spectrometry (EIMS; Cassar et al., 2009). Surface water was pumped through the underway system at a flow rate of 100 mL min^{-1}, through two filters to remove particulates, then to a gas-permeable membrane contactor cartridge (MicroModule 0.75×1). The equilibrated gas in the headspace was sent to a quadrupole mass spectrometer (Pfeiffer Prisma model QMG 220) for measurement. The O_2/Ar ratio was recorded every 2 s, then averaged into 2 min intervals. This measurement was calibrated with ambient air every 3 hours. The precision of the EIMS system is better than ±0.3% (Cassar et al., 2009).

2.3.3 Estimation of NCP from measured $\Delta(O_2/Ar)$

The major atmospheric gases O_2 and Ar have similar physical properties (i.e., similar Henry's law constants and diffusion coefficients) but different responses to biological processes, with Ar being biologically inert. Changes in O_2 in seawater may arise from physical and biological processes, then, but changes in Ar arise from physical processes alone (Craig and Hayward, 1987; Emerson et al., 1991). The ratio of oxygen to argon (O_2/Ar) in seawater has been developed as a proxy for net community production (Emerson et al., 1991). The sea-to-air flux of biological oxygen, which is equivalent to NCP under certain conditions (described below), can be estimated from dissolved O_2/Ar (Reuer et al., 2007; Jönsson et al., 2013; Teeter et al., 2018). This ratio is insensitive to bubble injection and temperature change (Craig and Hayward, 1987; Eveleth et al., 2014).

Measurements of the ratio of oxygen and argon concentrations relative to their saturated state allow for the effects of physical forcing to be removed from the effects of biological and physical forcings combined. Here, the biological oxygen saturation, $\Delta(O_2/Ar)$, is defined as

$$\Delta(O_2/Ar) = \frac{(O_2/Ar)_{meas}}{(O_2/Ar)_{sat}} - 1 \tag{2.1}$$

where $(O_2/Ar)_{meas}$ is the ratio of dissolved gases measured in the water and $(O_2/Ar)_{sat}$ is the ratio of the equilibrium saturated concentrations based on underway sea surface temperature (SST) and salinity (SSS) (Garcia and Gordon 1992; Hamme and Emerson 2004).

Under several assumptions: constant NCP and mixed layer depth (MLD), and no lateral or vertical exchange of O_2, bioflux, the sea-to-air flux of biological oxygen (Jönsson et al., 2013), can be calculated as

$$O_2 \text{ bioflux } (\text{mmol } O_2 \text{ m}^{-2} \text{ d}^{-1}) = \Delta(O_2/Ar) \cdot k_{O2} \cdot [O_2]_{sat} \cdot \rho \tag{2.2}$$

where k_{O2} is the gas transfer velocity of oxygen; $[O_2]_{sat}$ is the saturated concentration of O_2, calculated from sea surface temperature and salinity (Garcia and Gordon, 1992), ρ is the density of the water parcel. $[O_2]_{sat}$ is also corrected for atmospheric pressure by multiplying the ratio of sea level pressure (ship-based measurement) to standard pressure. The value of k_{O2} is estimated from the second moment of wind speed at 10 m height above the sea surface, $<U_{10}^2>$ (Wanninkhof 2014):

$$k_{O2} = 0.251 \cdot <U_{10}^2> \cdot (Sc/660)^{-0.5} \tag{2.3}$$

To calculate $<U_{10}^2>$, we used the wind product from the NCEP-DOE Reanalysis 2 data set (https://www.esrl.noaa.gov/psd/data/gridded/data.ncep.reanalysis2.html). For each day, the 6-hour wind speed squared was calculated and then averaged into a daily mean. Bioflux can be converted from units of oxygen to equivalent units of carbon via the quotient O_2 bioflux/PQ (mmol C m^{-2} d^{-1}), where PQ indicates the photosynthetic quotient (1.4; Laws, 1991).

Teeter et al. (2018), in revisiting the weighting scheme of Reuer et al. (2007) for estimating NCP from $\Delta(O_2/Ar)$, show that bioflux is equivalent to exponentially weighted NCP ($NCP_{exp\text{-}w}$) over several O_2 residence times.

$$NCP_{exp-w} = \frac{\sum_{i=1}^{n} NCP_i \omega_i}{\sum_{i=1}^{n} \omega_i} \tag{2.4}$$

$$\omega_i = e^{-\frac{n-1}{\tau/\Delta t}} \tag{2.5}$$

where n is the index of the most recent NCP to the calculated time step and is equal to the weighting period divided by the time resolution of the wind data (Δt, 1 day in our case), and τ is the residence time of O_2 in the mixed layer (MLD divided by the gas transfer velocity).

Here, we used the weighting scheme of gas transfer velocity ($k_{weighted}$) with 60-day weighting time of Teeter et al. (2018), which is a modification to the approach of Reuer et al., (2007),

$$k_{weighted} = \frac{\sum_{i=1}^{n} k_i w_i}{\sum_{i=1}^{n} w_i} \qquad (2.6)$$

$$w_n = 1,\ w_i = w_{i+1}\,(1 - f_{i+1}) \qquad (2.7)$$

$$f_i = \frac{k_i \cdot \Delta t}{MLD},\ k_i \cdot \Delta t < MLD \qquad (2.8)$$

where k_i, w_i, and f_i are the gas transfer velocity, weighting coefficient, and fraction of the mixed layer that is ventilated, respectively, at the time of (60-i) days prior to the most recent day (Reuer et al., 2007; Teeter et al., 2018). The parameter *n* is the index of the most recent gas transfer velocity to the calculated time step, so its value is equal to the weighting period divided by the time resolution of the wind data (Δt, 1 day in our case). Finally, MLD is estimated with CTD profile data by using a threshold criterion of $\Delta\sigma$=0.1 kg m^{-3}, where $\Delta\sigma = \sigma(Z) - \sigma(Z_{min})$; $\sigma(Z)$ is the potential density at depth Z, and Z_{min} is the shallowest measured depth (Peralta-Ferriz and Wooddgate, 2015). For locations between CTD stations along the cruise tracks, linear interpolation is used to determine MLD.

2.3.4 Estimation of sea-air CO_2 flux

Sea-air CO_2 flux, FCO_2, is calculated as:

$$\mathrm{FCO_2} = \mathrm{K_s} \cdot \mathrm{k_{CO2}} \cdot \Delta p\mathrm{CO_2} \tag{2.9}$$

where K_s is the solubility of CO_2, and k_{CO2} is the CO_2 gas transfer velocity. The K_s was calculated using underway SST and SSS (Weiss, 1974). The value of k_{CO2}, similar to the O_2 gas exchange velocity (equation (3)), was calculated following the equation of Wannikhof (2014). Note that a negative value of FCO_2 indicates a flux of CO_2 gas from the atmosphere to the ocean.

The difference between sea surface (water) pCO2 and atmospheric (air) pCO2 is calculated as

$$\Delta p\mathrm{CO_2} = p\mathrm{CO}_2^{\mathrm{water}} - p\mathrm{CO}_2^{\mathrm{air}} \tag{2.10}$$

The parameter $p\mathrm{CO}_2^{\mathrm{water}}$ was measured as described in section 2.2. The term $p\mathrm{CO}_2^{\mathrm{air}}$ was based on monthly average atmospheric CO_2 concentrations in dry air (xCO_2) measured at Point Barrow, Alaska. These data were downloaded from the website of the NOAA Earth System Research Laboratory (https://www.esrl.noaa.gov/gmd/dv/data/index.php?parameter_name=Carbon%2BDioxide&frequency=Monthly%2BAverages&site=BRW), then corrected to pCO_2 for water vapor pressure:

$$pCO_2^{air}{}_{(monthly)} = xCO_{2(monthly)} \cdot (Psl_{(monthly)} - Pw_{(monthly)}) \qquad (2.11)$$

where Psl is sea level pressure and Pw is water vapor pressure. Monthly Psl along the cruise tracks was obtained from a satellite reanalysis product (NCEP-DOE Reanalysis 2, https://www.esrl.noaa.gov/psd/data/gridded/data.ncep.reanalysis2.html) with a resolution of 2.5° × 2.5°. Monthly Pw was calculated from Psl and SST (Buck, 1981).

2.3.5 Gas transfer velocity correction in presence of sea ice

The effect of wind history on NCP estimation has been extensively discussed in recent publications (Reuer et al., 2007; Jönsson et al., 2013; Teeter et al., 2018), and the weighting scheme for describing gas exchange velocity has been explored and modified (Reuer et al., 2007; Teeter et al., 2018). Sea ice is also important because ice acts as an imperfect barrier to gas exchange, thus influencing the gas transfer velocities for O_2 and CO_2 (Long et al., 2011; Loose et al., 2009 & 2014; Butterworth and Miller, 2016; Prytherch et al., 2017). However, impact of ice history on gas exchange velocity and estimations of NCP and CO_2 flux are less well studied.

Although whether the effect is linear (Butterworth and Miller, 2016; Prytherch et al., 2017) or non-linear (Loose et al., 2009 & 2014) is still under debate, for simplicity, only a linear ice correction is used in this work. Note that the differences between linear and non-linear ice corrections for k_{O2} and k_{CO2} is negligible in the nearly ice-free area, but the non-linear corrected k becomes relatively larger (~up to 4 times) than linear corrected one as ice% increases (Loose et al., 2009).

We incorporate local sea ice history (in addition to wind history) in the weighting scheme of gas exchange velocity (equations (2.3)) as follows:

$$k_{O_2 i} \text{ or } k_{CO_2 i} = k_{i(\text{uncorrected})} \cdot (100 - \text{ice}\%_i) \quad (2.12)$$

and then applied the same weighting scheme described earlier for wind speeds in equations (2.6–2.8). The term ice%$_i$ indicates sea ice concentration at time (60−i) days prior to sampling day. We obtained daily sea ice% data from the Scanning Multichannel Microwave Radiometer (SMMR) on the Nimbus-7 satellite and the Special Sensor Microwave/Imager (SSM/I) sensors on the Defense Meteorological Satellite Program's (DMSP)-F8, -F11, and -F13 satellites; the resolution was 25 km ×25 km (Comiso, 2015).

2.4 Box model

We explore the impact of ice history on estimations of NCP and CO_2 flux by using a simple box model to calculate the time evolution of $\Delta(O_2/Ar)$ and pCO_2 in the presence of ice. For simplicity, we assume that there is no contribution from mixing or advection to O_2 and CO_2 change in the box and that surface concentration of Ar equals to saturated state ($[Ar] = [Ar]_{sat}$), so that any changes of O_2 or CO_2 are attributable to some combinations of net community production and air-sea gas exchange. Temperature is set to −1 °C, and salinity is set to 28. MLD is set to 20 m, and the time step is 1 day.

In the box model, both initial $\Delta(O_2/Ar)$ is equal to 0 and pCO_2 is in equilibrium with the atmosphere. We derive $\Delta(O_2/Ar)$ at each time step based on the value of NCP and gas exchange rate at that time step, governed by following equation,

$$\frac{\Delta O_2}{\Delta t} = (\text{NCP} - k_{O_2}\ ([O_2] - [O_2]_{sat}))/\text{MLD} \quad (2.13).$$

Accordingly, we simulate the time evolution of pCO_2 using total alkalinity (TA) and dissolved inorganic carbon (DIC) at each time step. TA was set to a constant as 2013 μmol kg $^{-1}$ throughout the simulation and initial DIC was set to 1946 μmol kg $^{-1}$, based on the assumption that sea surface pCO_2 was initially at equilibrium with the atmosphere (400 μatm in this case). For each simulation step, NCP decreases DIC while gas exchange increases DIC, thus, a new DIC at the time step t is calculated as follows:

$$\Delta DIC_t = (FCO_{2t} + NCP_t \,/\, PQ) \,/\, MLD \tag{2.14}$$

$$DIC_{t+1} = DIC_t + \Delta DIC_t \tag{2.15}$$

where FCO_{2t} is CO_2 flux at the time step t, calculated using equation (2.9) with ΔpCO_2 at that time step. Different gas exchange velocity (k_{CO2} in equation (2.9)) is considered based on different weighting schemes (See below).

Four simulation runs are shown here, to illustrate the effects of (a) different methods of accounting for sea ice history and (b) constant versus variable winds. We preset a typical melt-formation seasonal cycle of ice% for simulation, with a 45-day ice melting period, 50-day ice-free period, and 20-day ice formation period (Figure 2.2 a). In Run-1 (Figure 2.2 a-c), wind is held constant at 7.5 m s^{-1} (Figure 2.2 a) and NCP reproduces the setting used in Jönsson et al. (2013) and Teeter et al. (2018). A box-car function is imposed for days 60 to160 (NCP = 20 mmol O_2 m^{-1} d^{-1} during that time window; otherwise, NCP = 0 mmol O_2 m^{-1} d^{-1}; Figure 2.2 b). With derived $\Delta(O_2/Ar)$ (Figure 2.2 c) based on the value of NCP and gas exchange, we calculate the bioflux in two different ways (Figure 2.2 b): (a) taking into account the ice% observed on the day of sampling and (b) taking into account the history of ice% observed over the 60 days prior to the day of sampling. Finally, we compare bioflux with $NCP_{exp\text{-}w}$ (Teeter et al. 2018) to examine the impact of different approaches for ice corrections.

We notice that ice cover suppresses O_2 outgassing by reducing gas exchange velocity, which leads to higher $\Delta(O_2/Ar)$ during periods of ice melt and formation than during the intervening ice-free period (Figure 2.2 c). For the calculation of bioflux, taking into account only the ice% observed on sampling day can lead to an overestimate of O_2 bioflux (black line vs red dashed line in Figure 2.2 b) during ice melt and an underestimate during ice formation. Taking into account the ice history of the 60 days prior to sampling day yields a O_2 bioflux (orange line in Figure 2.2 b) that is closer to the $NCP_{exp\text{-}w}$ — i.e., yields a better bioflux estimate.

For Run-2 (Figure 2.2 d-e), conditions are identical to those of Run-1 except that the imposed NCP is held constant. Now, when only day-of-sampling ice% is considered, the errors of overestimation (during ice melt) and underestimation (during ice formation) become more pronounced (Figure 2.2 d). These model runs illustrate that bioflux calculations based on the ice% present on sampling day only may have more sampling bias and computational error induced by recent ice changes. Thus, we recommend that when $\Delta(O_2/Ar)$ approach is used to estimate NCP in sea ice–influenced regions, investigators should consider not only wind history but also sea ice history in their calculations.

Run-3 and Run-4 are the same as Run-1 and Run-2, respectively, except for the specification of time-varying winds (Figure 2.3). These model results are similar to

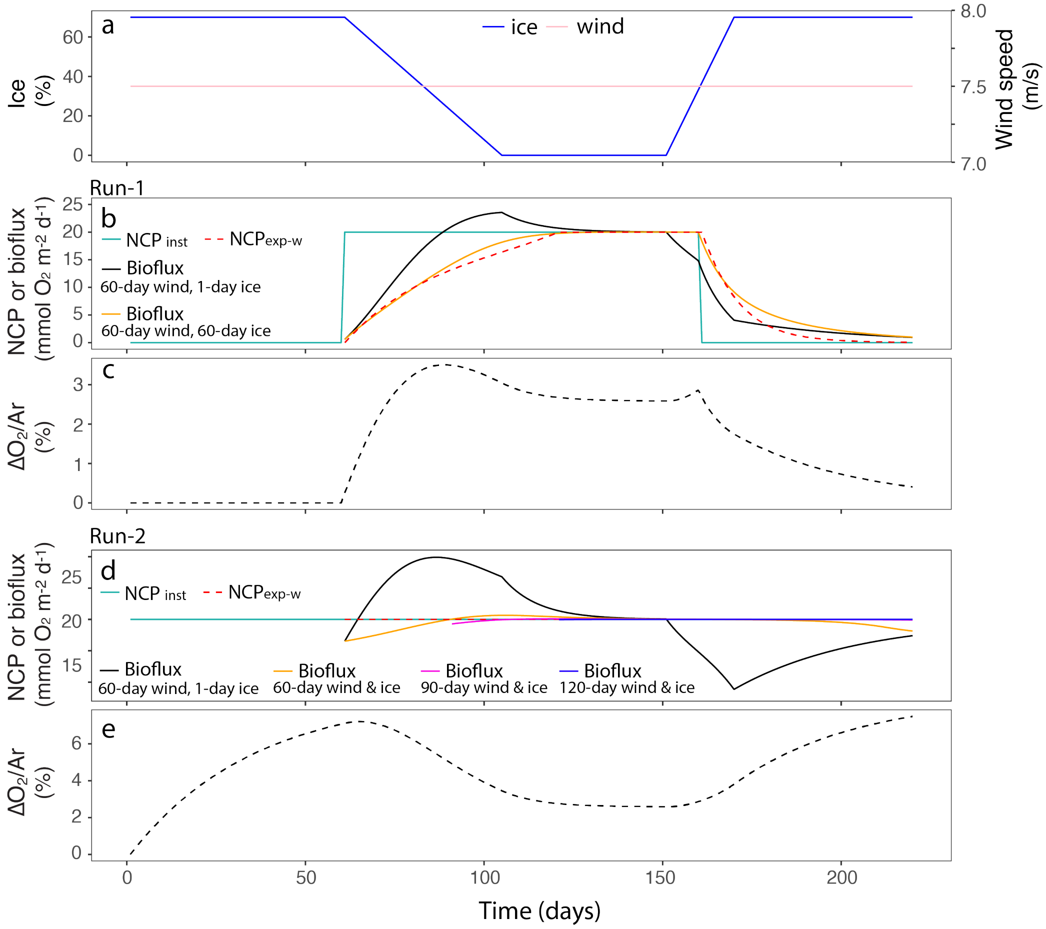

Figure 2.2: Simulated bioflux and $\Delta(O_2/Ar)$ under a constant wind. In all model runs, preset net community production (NCP, green), exponentially weighted NCP ($NCP_{exp\text{-}w}$, red dashed line), and calculated biofluxes are show together. (a) Specified inputs of ice concentration (ice%) and wind speed. (b–c) Run-1: NCP is set as a box-car function, with NCP = 20 mmol O_2 m^{-1} d^{-1} on days 61–160 and 0 on the preceding and following days. Biofluxes (b) are computed from the supersaturation of O_2 (c), which is analogous to $\Delta(O_2/Ar)$ because no lateral and vertical mixing are included. The results of two different approaches to accounting for sea ice in the calculation of bioflux are compared with $NCP_{exp\text{-}w}$ in panel b: considering ice% on sampling day only (black line) and considering ice% over the prior 60 days (orange line). Because the exponentially weighted NCP and biofluxes are calculated using rates from the first 60 days, they are undefined for the first 60 days of the model run. (d–e) Run-2: Same as Run-1 but with NCP specified constant over the entire model run. Biofluxes weighted over longer periods: 90 days (pink) and 120 days (purple) are also examined in Run-2 (d).

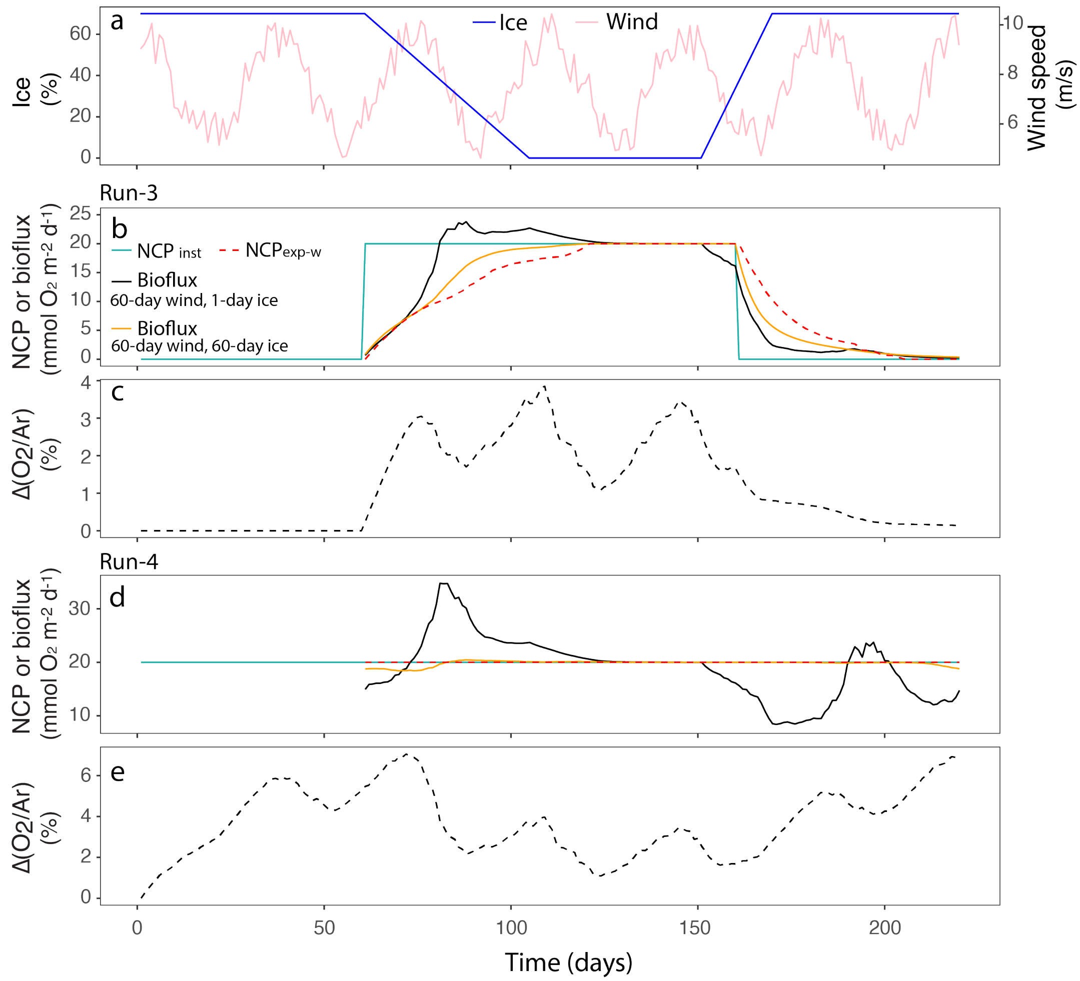

Figure 2.3: Box model simulations for bioflux and $\Delta(O_2/Ar)$ under variable wind speed. In all model runs, preset net community production (NCP, green), exponentially weighted NCP ($NCP_{exp\text{-}w}$, red dashed line), and calculated biofluxes are show together. (a) Specified input conditions of ice concentration (ice%) and wind speed. (b-c) Run-3: NCP is set as a box-car function, with NCP = 20 mmol O_2 m^{-1} d^{-1} on days 61–160 and 0 on the preceding and following days. Biofluxes (b) are computed from the supersaturation of O_2 (c), which is analogous to $\Delta(O_2/Ar)$ because no lateral and vertical mixing are included. The results of two different approaches to accounting for sea ice in the calculation of bioflux are compared with $NCP_{exp\text{-}w}$ in panel b: considering ice% on sampling day only (black line) and considering ice% over the prior 60 days (orange line). Because the exponentially weighted NCP and biofluxes are calculated using rates from the first 60 days, they are undefined for the first 60 days of the model run. (d–e) Run-4: Same as Run-3 but with NCP specified constant over the entire model run.

those of the constant-wind runs (Figure 2.2). The implication is that including ice history with the NCP weighting technique is appropriate for estimating biofluxes from measured $\Delta(O_2/Ar)$ in not only the simple case of constant winds but also the more realistic case of variable winds.

Meanwhile, we notice that there is still some deviation between 60-day weighted bioflux and $NCP_{exp\text{-}w}$, especially in the period with heavy ice% (Figure 2.2 d). In fact, presence of sea ice not only affects the gas exchange velocity, but also changes the estimated O_2 residence time in the mixed layer (τ = MLD/k). The typical O_2 residence time in the Arctic Ocean is ~1-2 weeks in the ice-free area, whereas it may prolong to ~100 days in the areas with 90% ice cover. Obviously, for those areas with heavy sea ice, the weighting time of 60 days are not long enough. Therefore, we compared the bioflux weighted over 60 days with biofluxes weighted over longer time of 90 days and 120 days (Figure 2.2 d). These results indicate that increasing weighting time will make bioflux estimate more equivalent to $NCP_{exp\text{-}w}$ as the residual unventilated portion of mixed layer becomes smaller. However, we also realized that a longer weighting time, to some degree, increases the risk of assumption of constant MLD and physical isolated mixed layer. It may become very difficult to interpret the observed bioflux results over a time scale of 3-4 months. Thus, as a compromise, we applied a 60-day weighting time to interpret the data in this study.

Bearing this in mind, we further evaluate the performance of the 60-day ice history parameterization that is incorporated into our bioflux estimates. We use the same box model setting in Run-1 to examine the effects of different ice concentrations by varying ice levels from 0 to 90% (Figure 2.4). As expected, a higher ice% results in higher $\Delta(O_2/Ar)$ (Figure 2.4 b) under the same preset NCP; however, the latter does not necessarily translate to a higher calculated bioflux (Figure 2.4 a). For ice% in excess of ~65%, the estimated bioflux is substantially lower than the corresponding NCP_{exp-w}. This pattern holds regardless of whether winds are constant (Figure 2.4) or variable (Figure 2.5). This underestimation of NCP implies that, with 60-day weighting time, the use of $\Delta(O_2/Ar)$ to represent NCP_{exp-w} in heavily ice-covered regions (i.e., ice% > ~65% coverage) may not be appropriate because 60 days may not be long enough to ventilate the entire mixed layer beneath heavy ice than in the absence of lateral and vertical mixing. Thus, we should interpret NCP values from $\Delta(O_2/Ar)$ measurements with caution, aware that there may be a methodological tendency toward underestimation in the area with heavy ice.

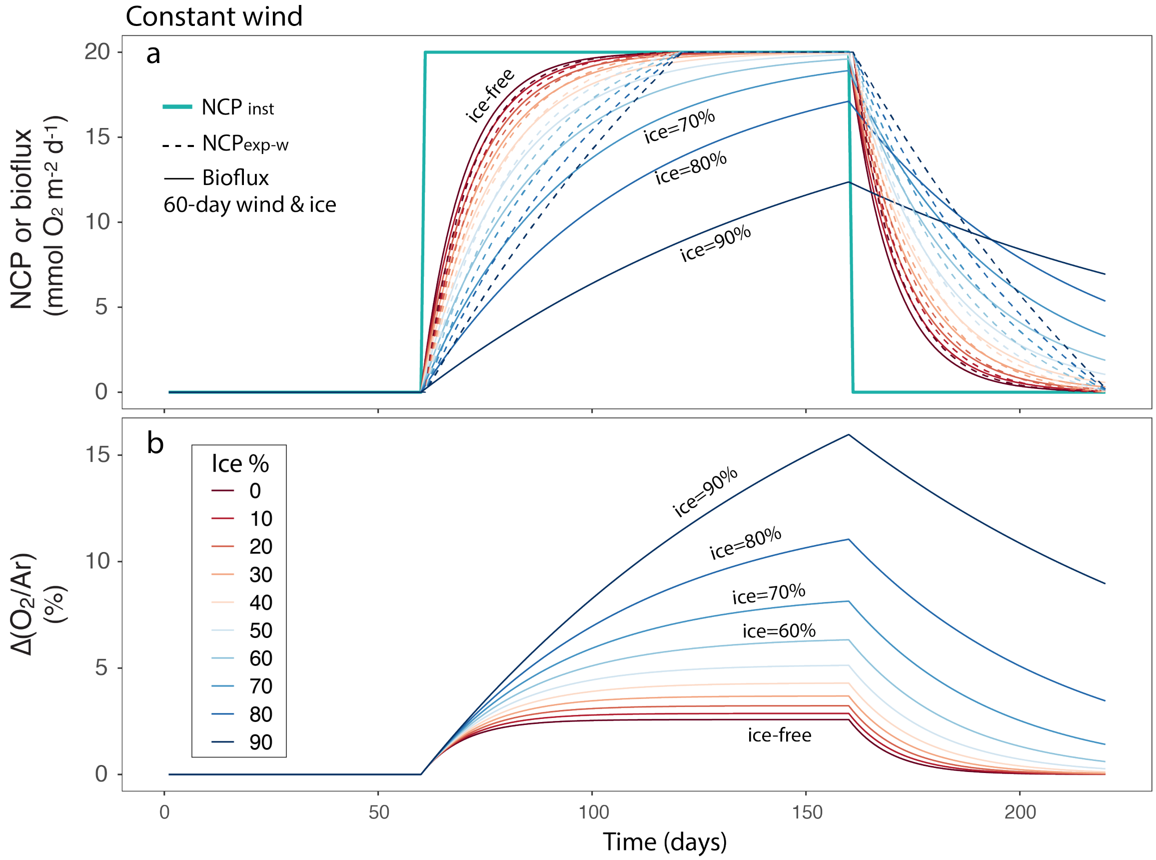

Figure 2.4: Simulated effect of ice concentration (0 to 90%) on $\Delta(O_2/Ar)$ and bioflux, for the case of constant winds. (a) Net community production (input, green line), exponentially weighted NCP ($NCP_{exp\text{-}w}$, dashed lines) and bioflux (output, solid lines). The basic model settings and calculations were the same as those for Run-1 (Figure 2.2 b-c): NCP box-car function (days 61–160), with constant wind at 7.5 m s^{-1}. Within each run, ice concentration is held constant for the entire 220-day simulation period. Biofluxes are computed from the $\Delta(O_2/Ar)$ values shown in panel b. (b) Simulated $\Delta(O_2/Ar)$. All biofluxes values are calculated by considering the histories of both wind speed and ice concentration over the 60 days prior to sampling day.

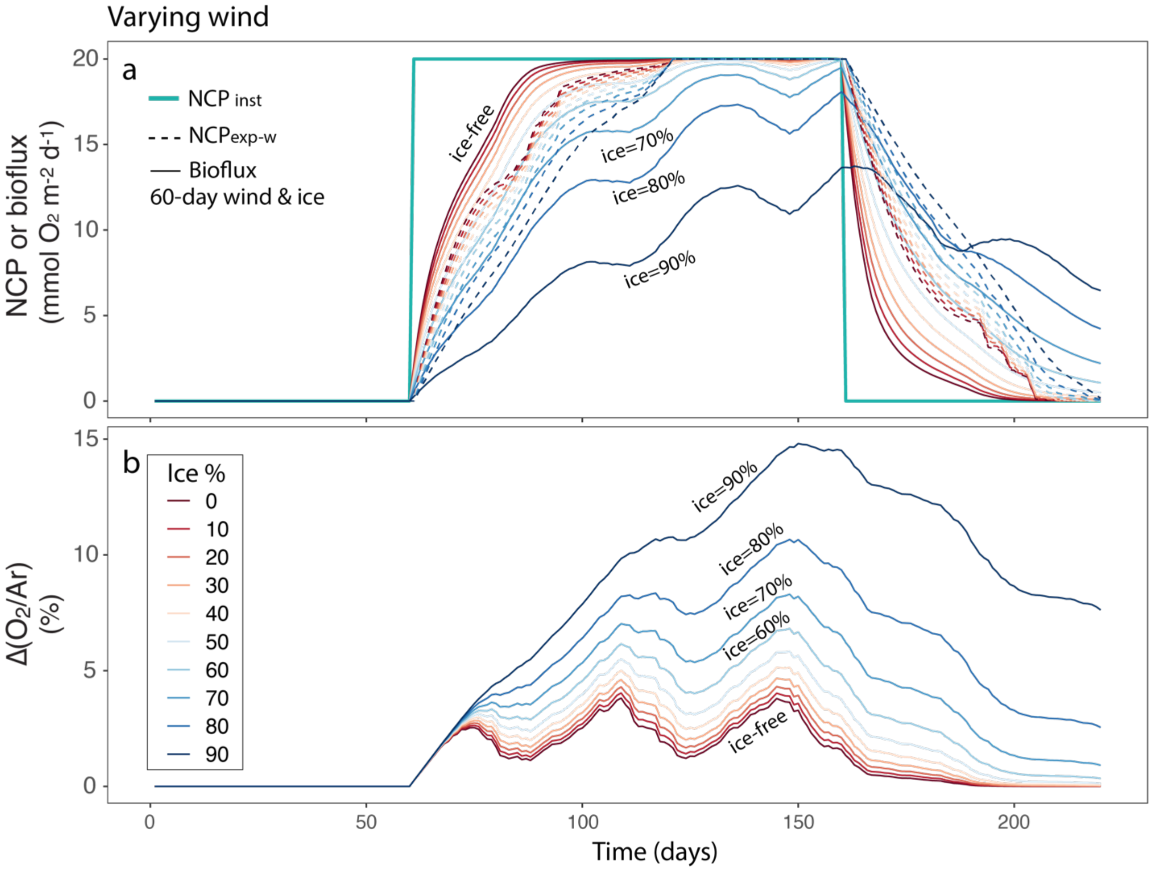

Figure 2.5: Simulated effect of ice concentration, 0 to 90%, on $\Delta(O_2/Ar)$ and bioflux, for the case of varying winds. (a) Net community production (input, green line), exponentially weighted NCP ($NCP_{exp\text{-}w}$, dashed lines) and bioflux (output, solid lines). The basic model settings and calculations were the same as those for Run-3 (Figure 2.3 a-c): NCP box-car function (days 61–160), with varying wind. Within each run, ice concentration is held constant for the entire 220-day simulation period. Biofluxes are computed from the $\Delta(O_2/Ar)$ values shown in panel b. (b) Simulated $\Delta(O_2/Ar)$. All biofluxes values are calculated by considering the histories of both wind speed and ice concentration over the 60 days prior to sampling day.

In the same simulation runs (Run 1-4), we also examined the effect of ice history on simulated pCO_2 and CO_2 fluxes (Figures 2.6 and 2.7). In these cases, the differences between the results obtained from the two different ice-correction methods (black and orange lines in Figure 2.6 b&d and 2.7) and the instant pCO_2 (red dashed line in Figure 2.6 and 2.7) are small, not as pronounced as bioflux estimates, because any pCO_2 change must be buffered by a much larger DIC reservoir. However, the CO_2 fluxes are more dominated by gas exchange velocity, which is determined by weighted scheme of wind and ice history. For example, CO_2 flux calculated using instant gas exchange velocity responds rapidly to the short-term changes in wind and ice (red dashed line in Figure 2.7 c&e), while CO_2 flux weighted by wind and ice history show smooth evolutions (black and orange lines in Figure 2.7 c&e).

In addition, we compared these results with results obtained using a widely accepted method that incorporates monthly-averaged wind speed and ice% (Bates et al., 2006; Ulfsbo et al., 2014; Evans et al., 2015). In this model exercise, we use the average of wind and ice over 30 days before sampling day to represent the respective monthly means. Although the monthly-average quantities yield even more smooth seasonal variations in pCO_2 and CO_2 flux (blue lines in Figure 2.7 c&e), the magnitudes are similar to the results accounting for 60-day wind and ice histories. Therefore, for the sake of consistency between the two biogenic gases, here, we report results of NCP and CO_2 flux based on the same time-weighting scheme of wind and ice history over 60 days to examine the relationship between NCP and CO_2 flux in the Arctic Ocean. CO_2 fluxes calculated using monthly means of wind speed and ice concentration are also reported for comparing with other CO_2 flux studies.

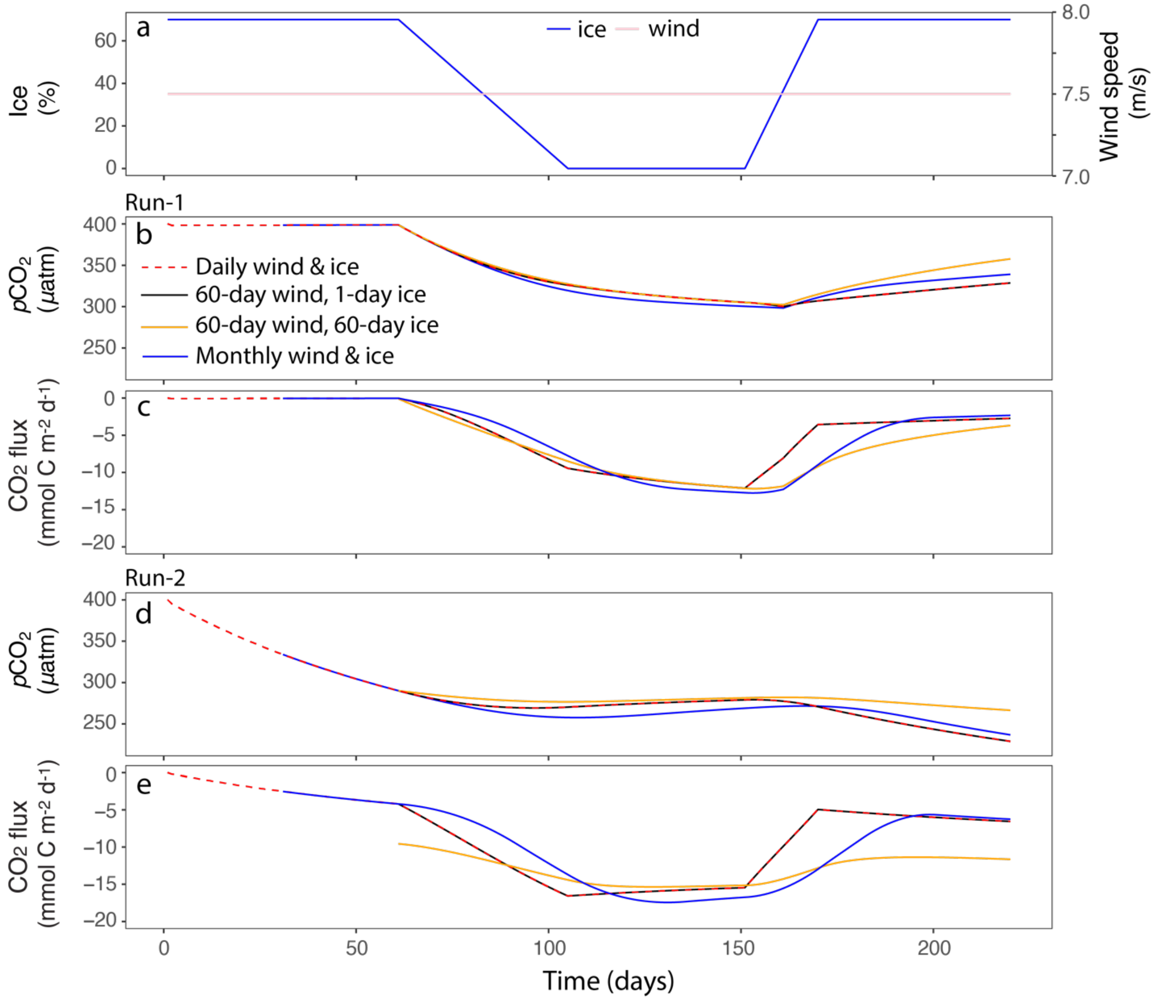

Figure 2.6: Box model simulations for pCO_2 and CO_2 flux under constant wind speed. (b–c) Simulation settings are the same as for Run-1 shown in Figure 2.2 (i.e., box-car NCP function). (d–e) Simulation settings are the same as for Run-2 shown in Figure 2.2 (i.e., constant NCP). Results are shown for four methods of accounting for wind speed and ice% history: (1) daily wind and ice corresponding to instantaneous NCP (red dashed line), (2) 60-day wind history and sampling day ice only (black line), (3) 60-day wind history and 60-day ice history (orange line), and (4) monthly mean wind speed and ice concentration (for the one month before sampling day, blue line). Because the CO_2 flux of (2) and (3) are calculated using rates from the first 60 days, they are undefined for the first 60 days of the model run. Similarly, CO_2 flux of (4) are undefined for the first 30 days. A negative CO_2 flux indicates CO_2 flux from the atmosphere to the ocean.

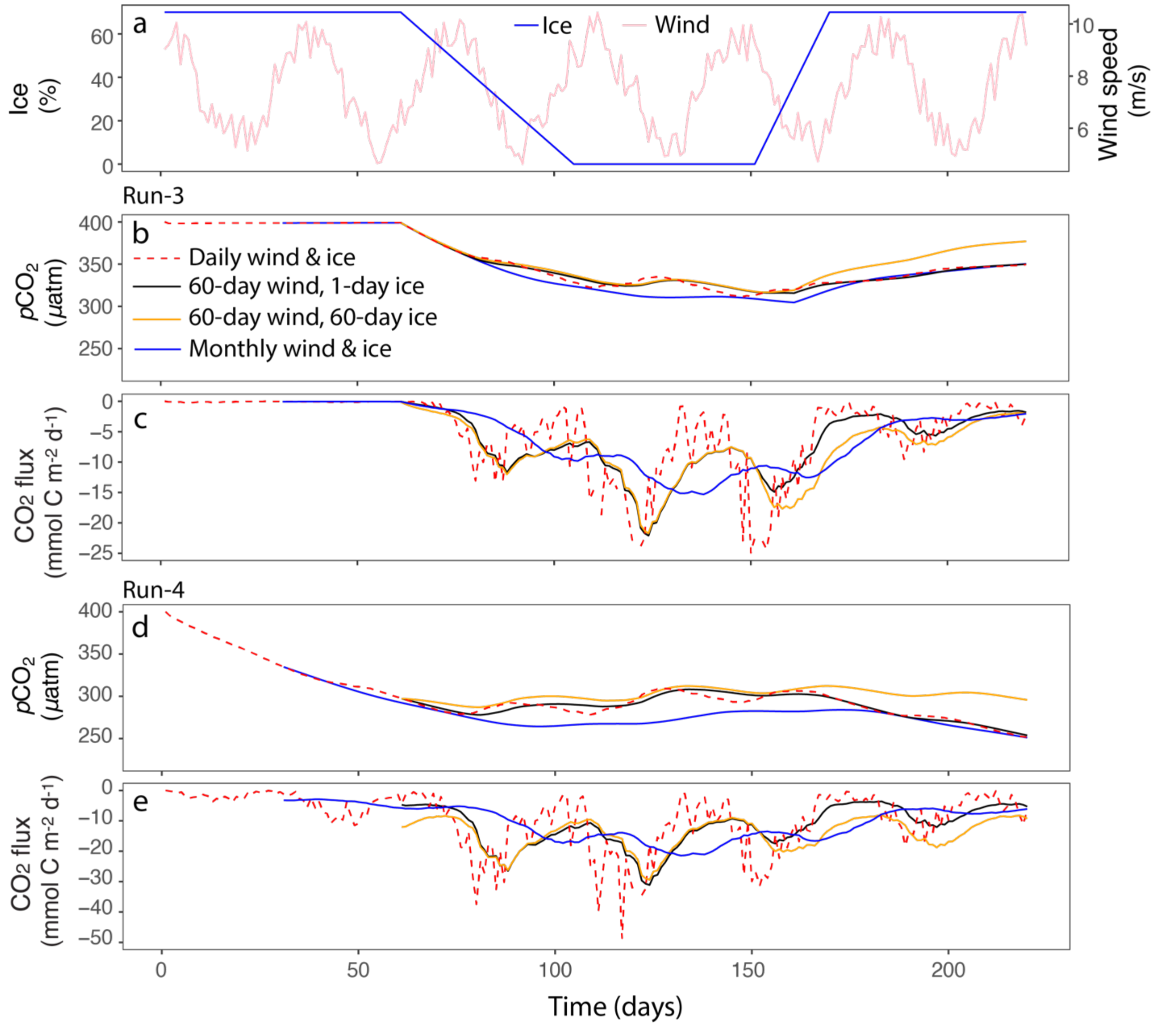

Figure 2.7: Box model simulations for pCO_2 and CO_2 flux under varying wind speed. Simulation settings are the same as those used for the model runs shown in Figure 2.3. (b–c) Same settings as Run-3. (d–e) Same settings as Run-4. For additional details, see Figure 2.3 and 2.6 captions.

2.5 Results

2.5.1 Spatial distribution of $\Delta(O_2/Ar)$ and pCO_2

The spatial distributions of $\Delta(O_2/Ar)$ in 2016 (Figure 2.1 c) and 2018 (Figure 2.1 d) were generally similar, with relatively high $\Delta(O_2/Ar)$ on the inflow shelf, and lower $\Delta(O_2/Ar)$ in the central basins. Patterns of sea surface pCO_2 were opposite to those of $\Delta(O_2/Ar)$, with relatively high values in the central basins, and lower values on the shelf (Figure 2.1 e & f).

On the Chukchi Shelf, the 2016 average $\Delta(O_2/Ar)$ was 4.1% and the 2018 average was 3.3% (Table 2.1). Positive extrema of $\Delta(O_2/Ar)$, as high as 27% to 37%, were found at two locations: in the southern Chukchi Sea in the vicinity of the Bering Strait and in the northern Chukchi Sea in the vicinity of the shelfbreak (CS section in Figure 2.8 e & 2.9 e). Both of these locations have been previously identified as biological hotspots (Grebmeier et al., 2015). A few negative extrema, as low as -5.8% to -3.8%, were also encountered, mostly in the vicinity of the Bering Strait (CS section in Figure 2.8 e & 2.9 e) in association with high SSS, undersaturated O_2%, and supersaturated pCO_2 (Figure 2.8 c-f & 2.9 c-f). In early September 2018, an additional area of weak $\Delta(O_2/Ar)$ undersaturation (~ -1 to -2%) was observed at the upper end of Barrow Canyon (160°W –165°W and 70°N –71.5°N, Figure 2.1 d; Figure 2.9 e). These occurrences were likely due to strong vertical mixing of surface waters with low-O_2 bottom water. The sea surface pCO_2 on the Chukchi Shelf was generally low (220 to 280 μatm) and the spatial patterns were opposite to those of $\Delta(O_2/Ar)$ (Figure 2.1 e-f; Figure 2.9 f). The patchy and widely variable primary production (Grebmeier et al., 2015) resulted in high variabilities in pCO_2 (Figure 2.1 c-f). The lowest pCO_2 values were found at the shelf break and in the vicinity of the Bering Strait (Figure 2.1

e-f). These occurrences were attributable to locally active biological production (Grebmeier et al., 2015).

Table **2.1: Means and the range of first to third quartiles (in brackets) of parameters measured in summer 2016 and 2018.**

Parameter	Chukchi shelf				Mendeleev Ridge and Chukchi Plateau		Canada Basin		Ice-covered region	
	Southern (65°N–69°N)		Northern (69°N–72°N)							
	2016	2018	2016	2018	2016	2018	2016	2018	2016	2018
Ice (%)	0	0	4	1	27	24	17	11	68	79
					(10–44)	(12–47)	(0–31)	(0–18)	(62–75)	(73–87)
$\langle U_{10}^2 \rangle$	97	19	49	24	107	30	64	33	98	54
(m^2/s^2)	(65–119)	(9–28)	(30–51)	(4–39)	(54-174)	(13–41)	(14–113)	(22–40)	(72–138)	(27–68)
$\Delta(O_2/Ar)$	3.9	5.9	4.2	1.9	1.4	0.9	0.3	0.2	1.3	1.8
(%)	(0.8–6.9)	(1.1–9.1)	(1.3–5.5)	(0.5–2)	(0.7–1.8)	(0.3–0.8)	(0.1–0.4)	(0.1–0.3)	(1.2–1.4)	(1.8–2.2)
NCP	41	26	19	9.4	4.5	1.6	1.3	0.7	1.6	1.0
(mmol C m^{-2} d^{-1}) [a]	(8.2–80)	(5.3–43)	(9.8–25)	(2.7–9.7)	(2.5–6.0)	(0.8–2.2)	(0.2–2.3)	(0.4–1.0)	(1.3–1.8)	(0.8–1.0)
$p$$CO_2$	281	219	235	230	319	335	371	367	319	319
(μatm)	(239–309)	(164–255)	(191–282)	(179–275)	(293–345)	(324–349)	(364–384)	(363–372)	(317–320)	(314–322)
CO_2 flux	-20	-12	-21	-19	-5.3	-2.6	-1.6	-2.2	-1.9	-1.1
(mmol C m^{-2} d^{-1}) [a]	(-13– -25)	(-7.4– -16) [c]	(-15– -26)	(-12– -28) [c]	(-4.0– -6.0)	(-1.6– -3.4)	(-0.5– -2.6)	(-1.7– -2.6)	(-1.3– -2.1)	(-0.6– -1.6)
CO_2 flux	-17	-18	-16	-13	-3.2	-1.8	-1.1	-1.4	-1.7	-0.9
(mmol C m^{-2} d^{-1}) [b]	(-12 – -22)	(-8.6– -24)	(-10– -18)	(-7.0– -17)	(-2.1– -4.2)	(-1.4– -2.1)	(-0.4– -1.7)	(-1.1– -1.6)	(-1.5– -1.9)	(-0.5– -1.2)

[a] Values for NCP and sea-air CO_2 flux are calculated applying a linear ice correction for gas exchange velocities, weighted over 60 days. Negative value of CO_2 flux indicates a flux of CO_2 gas from the atmosphere to the ocean.
[b] Values for sea-air CO_2 flux are calculated using monthly wind and ice.
[c] Values represent CO_2 measurements made during the northbound Chukchi Shelf transect only; the instrument was out of commission during the southbound transect (No $p$$CO_2$ data were collected after September 2, 2018).

In the Canada Basin, $\Delta(O_2/Ar)$ was nearly invariant, in contrast to the highly variable shelf values, and close to equilibrium with the atmosphere (Figures 2.1 c-d). Average $\Delta(O_2/Ar)$ was 0.3% in 2016 and was nearly the same in 2018 (Table 2.1), suggesting that surface water in the ice-free southern Canada Basin has the lowest summertime primary productivity of the western Arctic Ocean. Consistently, O_2%

saturation values were near 100% (CB section in Figures 2.8 d & 2.9 d), indicating the surface waters was nearly at equilibrium with respect to the atmosphere. Sea surface pCO_2 values across the southern Canada Basin were high, generally 370 to 380 μatm, approaching equilibrium the atmospheric value (Figure 2.1 e-f). These observations were consistent with the oligotrophic character of the Canada Basin (McLaughlin and Carmack, 2010; Ulfsbo et al., 2014; Ji et al., 2019).

In the marginal ice zone (MR-CP region in Figure 2.1), $\Delta(O_2/Ar)$ exhibited a distinctive pattern, which was closely associated with ice% changes (MR and CP sections in Figures 2.8 a & 2.9 a). The highest $\Delta(O_2/Ar)$ (~3% – 7%) was observed at the dynamic melting zone when ice% was approximately 30% to 50% (Figures 2.8 a & 2.9 a). $\Delta(O_2/Ar)$ decreased towards atmospheric equilibrium when lower (<30%) or higher (>50%) ice% was encountered. However, the average $\Delta(O_2/Ar)$ in this region was still 1.4% in 2016 and 0.9% in 2018 (Table 2.1), which were more than four times higher than those observed in the nearly ice-free southern Canada Basin (Table 2.1). Sea surface pCO_2 in the marginal ice zone was also affected by change of ice%. The lowest pCO_2 values (~260 μatm) were encountered at the ice% range of 30% to 50%, while higher pCO_2 values (300 – 340 μatm) were observed at the areas with higher or less ice coverage.

In the high-latitude ice-covered area (>78°N), average $\Delta(O_2/Ar)$ under the ice was 1.3% in 2016 and 1.8% in 2018 (Table 2.1). These observed values were higher than that of the nearly ice-free southern Canada Basin and close to that of the marginal ice zone (Figure 2.1 c-d; Table 2.1). The under-ice pCO_2 in the high latitudes was found nearly invariant over a latitudinal gradient (78°N to 85°N) in both years with an average of 319 μatm (Table 2.1).

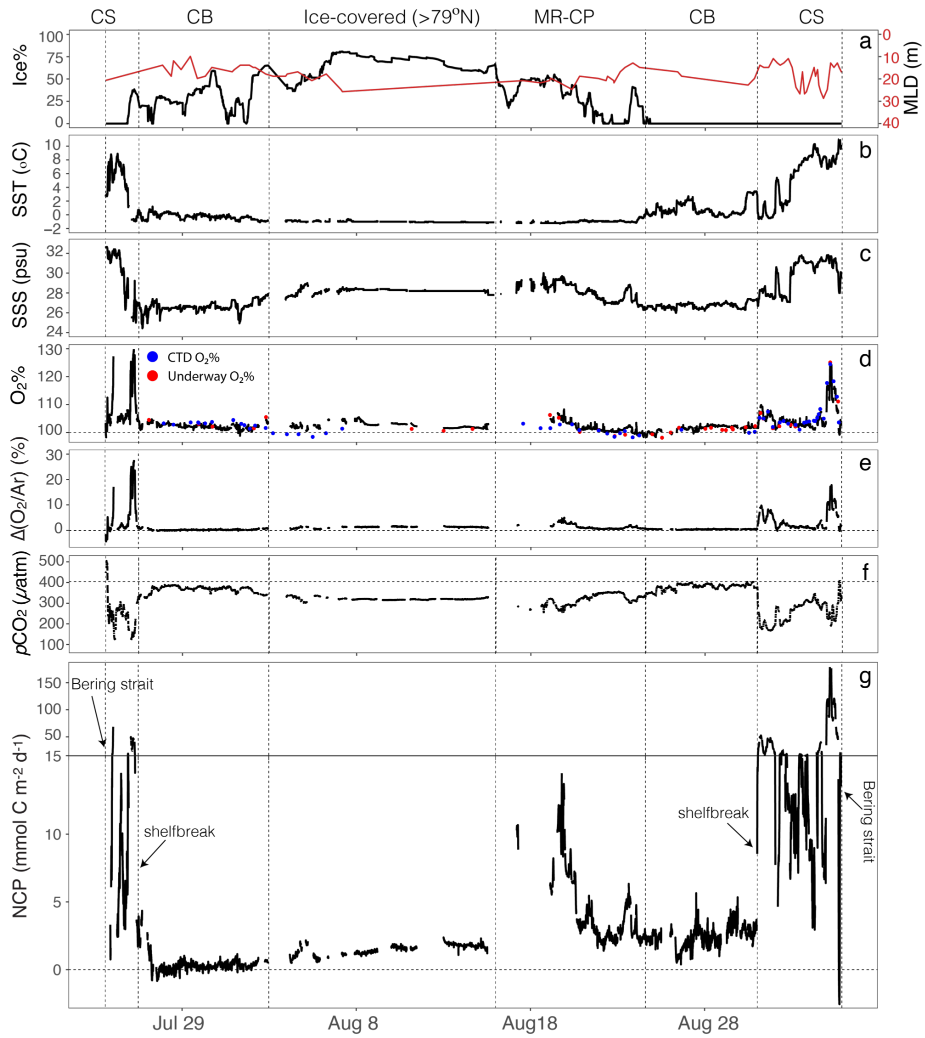

Figure 2.8: Surface ocean observations during the 2016 cruise. (a) Ice concentration (obtained from satellite data) and mixed layer depth (interpolated from CTD profiles). The remaining panels show underway measurements or parameters derived from the underway measurements. (b) Sea surface temperature. (c) Sea surface salinity. (d) Optode O_2 saturation percentage. The colored dots show DO Winkler titration results for samples collected from the underway pipeline (red) and the CTD Niskin bottles (blue). These O_2% values have been corrected to underway water temperatures for comparison. (e) Biological oxygen saturation, $\Delta(O_2/Ar)$. (f) Sea surface pCO_2. (g) Calculated NCP. The vertical dashed lines indicate notable features along the cruise track: Chukchi Shelf, CS; Canada Basin, CB; Mendeleev Ridge–Chukchi Plateau, MR-CP, and ice-covered high-latitude region (>79°N, IC). See Figure 1a for a map view of the cruise track.

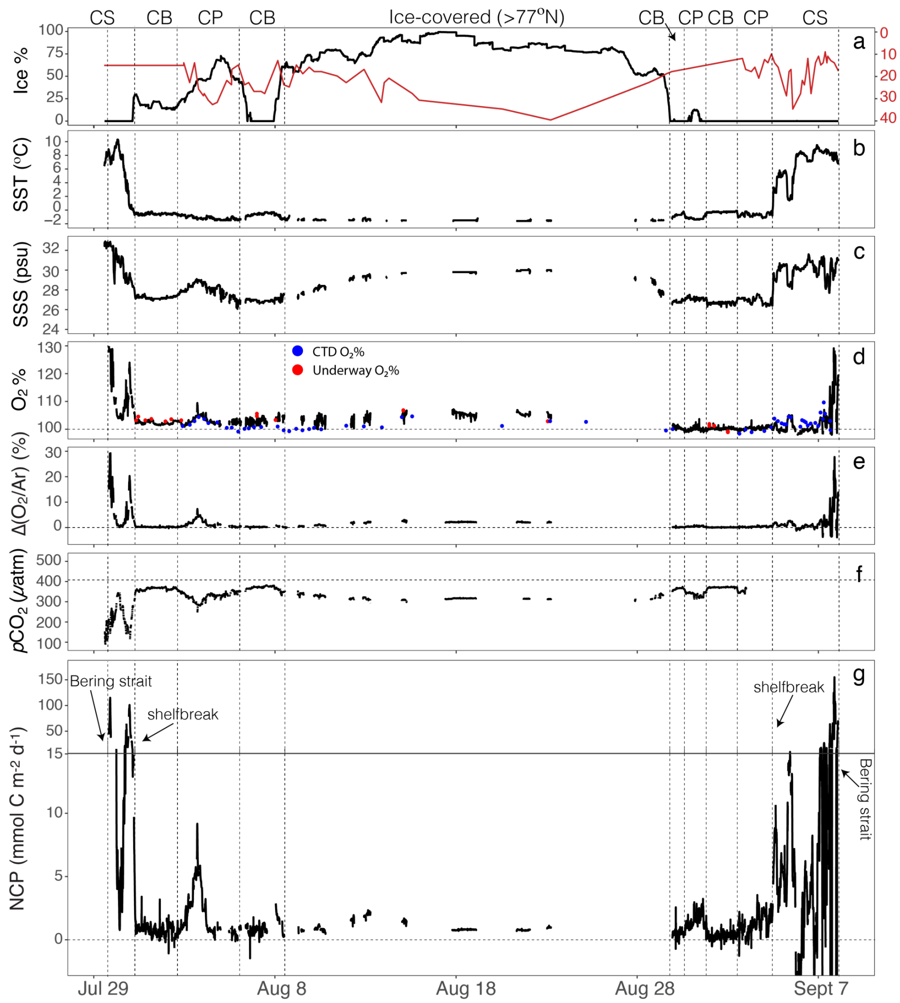

Figure 2.9: Sea surface observations during the 2018 cruise: (a) Ice concentration (obtained from satellite data) and mixed layer depth (interpolated from CTD profiles). The remaining panels show underway measurements or parameters derived from the underway measurements. (b) Sea surface temperature. (c) Sea surface salinity. (d) Optode O_2 saturation percentage. The colored dots show DO Winkler titration results for samples collected from the underway pipeline (red) and CTD Niskin bottles (blue). These O_2% values have been corrected to the underway water temperature for direct comparison. (e) Biological oxygen saturation, $\Delta(O_2/Ar)$. (f) Sea surface pCO_2. No pCO_2 data were collected after September 2, 2018 due to instrument failure. (g) Calculated NCP. The vertical dashed lines indicate notable features along the cruise track: Chukchi Shelf, CS; Canada Basin, CB; Chukchi Plateau, CP; and ice-covered high-latitude region (>79°N, IC). See Figure 1b for a map view of the cruise track.

2.5.2 Temporal evolution of Δ(O_2/Ar) and $p$$CO_2$ in the marginal ice zone

The Chukchi Plateau and Mendeleev Ridge areas, unlike the southern Canada Basin area, experiences minimal influence from coastal currents, river discharge, and the Beaufort Gyre. As a result, ice retreat here comes later and more slowly (see ice extent changes in Figure 2.1), which provided a possible observational window to examine the progression of summertime ice melt and the accompanying temporal evolution of NCP.

In 2018, we sampled the marginal ice zone on the Chukchi Plateau twice (about a month apart), providing an opportunity to track the temporal evolution of ice melt and the accompanying biological changes. During the first visit on August 3-5, ice% was approximately 30% to 50% (northbound cruise track), with an average Δ(O_2/Ar) of 1.6% and an average $p$$CO_2$ of 318 μatm (CP sections in Figure 2.9). The tight positive correlations of Δ(O_2/Ar) with SSS, ice%, and O_2% and the tight negative correlation with $p$$CO_2$ (Table 2.2) strongly suggest that sea-ice melting and the consequent relief from light limitation stimulated local biological activity, which greatly modified surface O_2 and CO_2 dynamics. By the time of the ship's return on August 30-31 (southbound), the area has become completely ice-free (Figure 2.9). The average Δ(O_2/Ar) decreased to ~0.4%, which was comparable to that in the ice-free Canada Basin, suggesting that the dominant melt-induced primary production gradually gave way to air-sea gas exchange. However, the average $p$$CO_2$ just slightly increased to ~335 μatm, which was much lower than the values in the Canada Basin, due to a longer gas exchange timescale for CO_2.

Table **2.2:** **Correlation coefficients (r) between Δ(O_2/Ar) and surface-ocean physical and biogeochemical parameters. All correlation coefficients given here are statistically significant; a hyphen (-) indicates non-significant correlation. The 2018 coefficients shown in parentheses for the Mendeleev Ridge and Chukchi Plateau are for the northbound transect only.**

Parameter*	Chukchi shelf		Mendeleev Ridge and Chukchi Plateau		Canada Basin		Ice-covered region	
	2016	2018	2016	2018	2016	2018	2016	2018
SST	-0.36	-0.13	-0.51	-0.37 (-0.29)	-	-0.46	-0.49	-0.41
SSS	-0.32	0.20	0.83	0.79 (0.79)	0.46	0.41	0.46	0.91
MLD	-0.25	-0.26	0.49	0.41 (0.16)	0.31	0.16	0.63	0.64
$\langle U_{10}^2 \rangle$ **	-0.16	-0.19	-	- (0.29)	0.49	-0.15	-0.32	0.24
Ice% **	0.54	-	0.70	0.53 (0.10)	-	0.45	0.51	0.71
O_2%	0.94	0.96	0.88	0.80 (0.84)	-0.15	0.54	0.11	0.66
pCO$_2$	-0.63	-0.56	-0.94	-0.91 (-0.97)	-0.50	-0.45	−0.81	-0.91

* All parameters, whether measured underway or derived from satellite products, were paired point by point in time.
** Data on the sampling day was used.

2.5.3 Net community production and CO_2 flux

The overall spatial distribution of the calculated NCP (Figure 2.10 a) was similar to that of Δ(O_2/Ar) (Figure 2.1 c-d). On the Chukchi Shelf, NCP was much higher than that in other regions. Exceptions to this pattern of generally high production are seen in the negative values clustered near the Bering Strait and Barrow Canyon (due to vertical mixing). The mean NCP in the southern Chukchi Sea was 41 mmol C m^{-2} d^{-1} in 2016 and 19 mmol C m^{-2} d^{-1} in 2018, almost twice as high as in the northern Chukchi Sea in the respective year (Table 2.1 and Figure 2.10 b). The highest NCP was observed in the vicinity of the Bering Strait and over the shelf break at ~73°N. These Bering Strait observations are consistent with “hotspot” observations

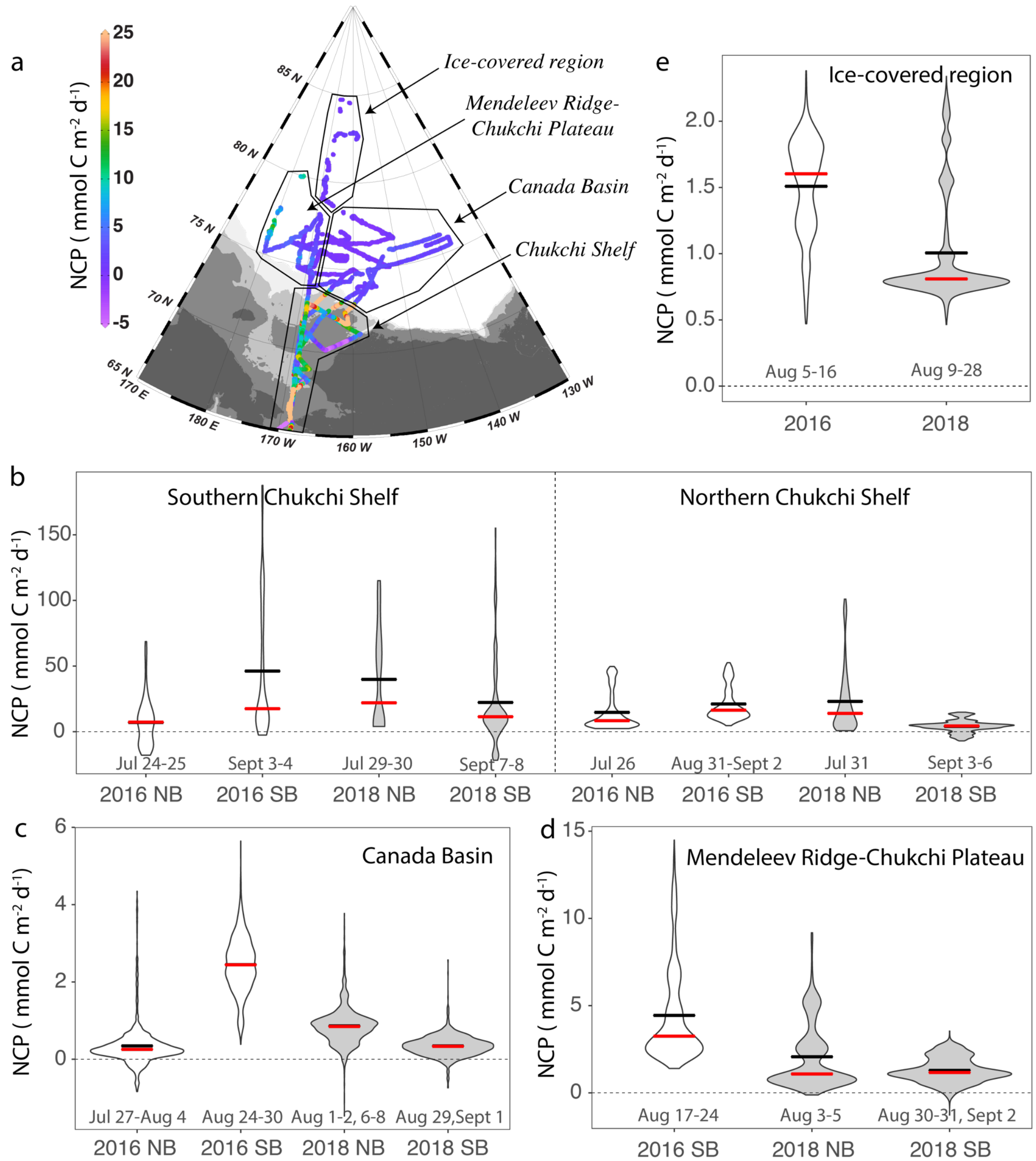

Figure 2.10: NCP in the western Arctic Ocean, as estimated from measured $\Delta(O_2/Ar)$, in 2016 (empty violins) and 2018 (grey shaded violins). (a) Map of NCP during both cruises. The remaining panels are violin plots that show NCP by cruise transect. (b) Chukchi Shelf. (c) Canada Basin. (d) Mendeleev Ridge–Chukchi Plateau. (e) Ice-covered high latitudes. The width of each "violin" indicates the frequency distribution of NCP values. The black and red bars represent the mean and median values, respectively. NB and SB denote the northbound and southbound transects, respectively. The approximate visiting dates are listed.

in this area in October 2011 and 2012 (Juranek et al., 2019). Our early-September results, however, showed a higher peak than their October observations (Juranek et al., 2019), with NCP values of ~150 to 180 mmol C m^{-2} d^{-1} (Figure 2.10 b). For the CO_2 flux estimate, the averages on the Chukchi Shelf were 21 mmol C m^{-2} d^{-1} and 17 mmol C m^{-2} d^{-1} in 2016 and 2018, respectively (Table 2.1). These values were 40-70% larger than the climatological estimates in Evans et al., (2015), while the CO_2 flux calculated from monthly wind and ice was closer to that.

The ice-free southern Canada Basin (Figure 2.10 c) was the site of the lowest mean NCP we encountered in both 2016 and 2018. When the ship crossed over the shelf break from the Chukchi Shelf into the basin, NCP decreased dramatically, by one to two orders of magnitudes to 0 to 2.5 mmol C m^{-2} d^{-1}. Our estimates of NCP in the basin agree well with observations (0.9 to 2.1 mmol C m^{-2} d^{-1}) from discrete O_2/Ar samples collected in this region in 2011–2016 (Ji et al., 2019) and with modeled NCP (0 to 3.5 mmol C m^{-2} d^{-1}) (Islam et al., 2016). Similarly, the CO_2 flux results (-1.6 to -2.2 mmol C m^{-2} d^{-1}) are consistent with other observations in the Canada Basin (Evans et al., 2015; Islam et al., 2016).

At the Mendeleev Ridge–Chukchi Plateau marginal ice zone (Figure 2.10 d), average NCP was relatively high: 4.5 mmol C m^{-2} d^{-1} in 2016 and 1.6 mmol C m^{-2} d^{-1} in 2018 (Table 2.1). Even higher positive peaks of 9.2 to 14.5 mmol C m^{-2} d^{-1} were observed during northbound tracks in early August at the ice edges, where the ice concentration was 30% to 50%. By the time the ship revisited these areas (southbound track) in early September 2018, when this area was ice-free, NCP decreased to just 0.9 to 2.4 mmol C m^{-2} d^{-1}, which was comparable to values in the ice-free Canada Basin (Figure 2.10 c). Although CO_2 exchange was affected by partially ice-covered condition, the CO_2 flux in this dynamic region was still 2-3 times higher than that in the Canada Basin due to the longer timescale and legacy effect of the earlier high biological production there.

In the high-latitude region, with ice concentrations higher than 60%, NCP was slightly lower than that in the marginal ice zone but higher than that in the ice-free southern Canada Basin. Average NCP was 1.6 mmol C m^{-2} d^{-1} in 2016 and 1.0 mmol C m^{-2} d^{-1} in 2018 (Table 2.1). The range of NCP values was from 0.5 to 2.4 mmol C m^{-2} d^{-1} (Figure 2.10 e), which was much smaller than in other regions. Our estimates of CO_2 fluxes were low in both years (-1.1 to -1.9 mmol C m^{-2} d^{-1}) due to the suppression of heavy ice, which agrees well with that estimated from in situ sensor (-2.5 $\pm$ 2.6 mmol C m^{-2} d^{-1}) in the area with heavy ice cover (Islam et al., 2016). Our NCP estimates for this ice-covered region are also in good agreement with earlier observations (0 to 1.8 mmol C m^{-2} d^{-1}) in the ice-covered northern Canada Basin in 2011-2016 (Ji et al., 2019). In the central Arctic Ocean (around 90ºN) during August/September 2011, Ulfsbo et al. (2014) found negative NCP values under multi-year ice, indicative of temporary heterotrophy. Our cruises stayed south of 85°N, in areas dominated by first-year ice, and we encountered no occurrences of negative NCP (Figure 2.10 e).

2.6 Discussion

2.6.1 Assessment of NCP and CO_2 flux estimation

During our two cruises in 2016 and 2018, ice concentrations were always <70% except for the areas poleward of 78°N (Figures 2.8 a & 2.9 a). Thus, as discussed in section 2.4, our field conditions were appropriate for application of the 60-day ice-history accounting for NCP.

When ice history is considered, $\Delta(O_2/Ar)$ and NCP for a given regional transect are strongly linearly correlated (Figure 2.11). These strong correlations can be seen for the Chukchi Shelf (Figure 2.11 a), the ice marginal zone (Figure 2.11 c), and even for the heavily ice-covered region (Figure 2.11 d), where ice melting and formation may violate the assumption of $\Delta Ar \sim 0$ (Eveleth et al., 2014; Ulfsbo et al., 2014). Because of small $\Delta(O_2/Ar)$ and weak NCP, this correlation in the Canada Basin is not strong as in other regions (Figure 2.11 b). When ice history is not taken into account, more data points fall outside the bounds of the 0% and 90% ice-cover end-member cases (Figure 2.12). This comparison suggests that taking both wind and ice histories into account does indeed reduce the bias and uncertainty induced by short-term sea ice change and constrains the NCP estimates in a reasonable and useful way.

Uncertainties in NCP estimate in ice-free water primarily arise from uncertainties in the gas exchange velocity parameterization (~20%, Wanninkhof, 2014). Applying an ice correction for gas exchange velocity could further enlarge the uncertainty up to ~40% (Loose et al., 2014; Lovely et al. 2015). Other uncertainties in regional NCP estimation is likely due to violation of the assumptions, which are difficult to quantify (Jönsson et al. 2013). For example, vertical mixing does impact observed surface $\Delta(O_2/Ar)$ in vicinity of the Bering Strait where negative $\Delta(O_2/Ar)$ co-occurs with positive ΔpCO_2. NCP estimates, including the area with some negative $\Delta(O_2/Ar)$, represents a lower bound on the true NCP (Cassar et al., 2014). In this study, if we remove $\Delta(O_2/Ar) < -2\%$, it will increase the regional means of NCP on the south Chukchi Shelf by 6% to 10%, and has no impact in the other regions.

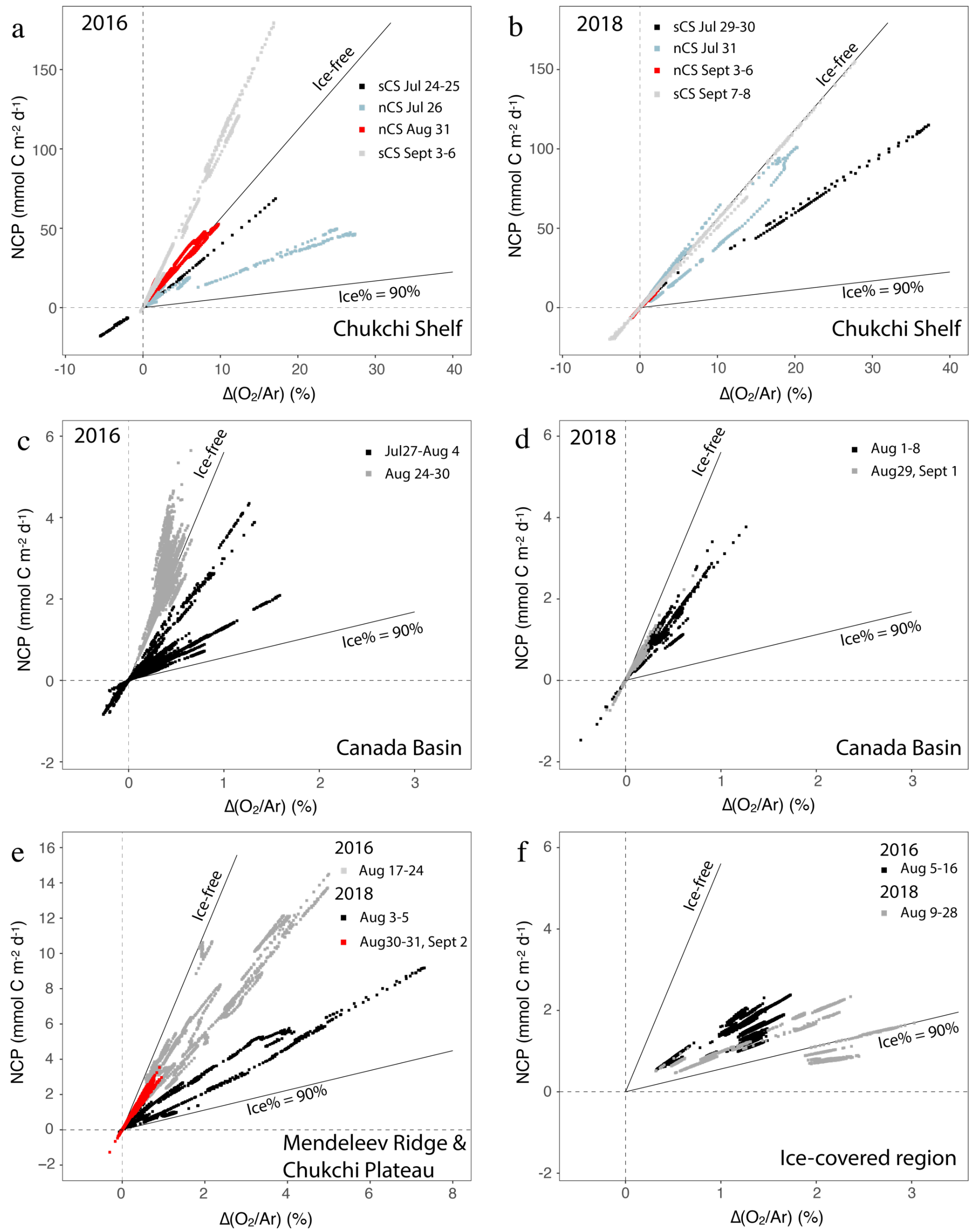

Figure 2.11: Estimated NCP (calculated by considering 60-day wind and ice histories) plotted as a function of the observed $\Delta(O_2/Ar)$. (a-b) Chukchi shelf, with the northern Chukchi Sea (nCS) and southern Chukchi Sea (sCS) data shown separately. (c-d) Canada Basin. (c) Mendeleev Ridge (MR) and Chukchi Plateau (CP). (d) Ice-covered region. Colored symbols indicate the cruise transects with travel date. The black lines show two end-member cases, ice% = 0% and ice% = 90%, both calculated with a wind speed of 7.5 m s^{-1}.

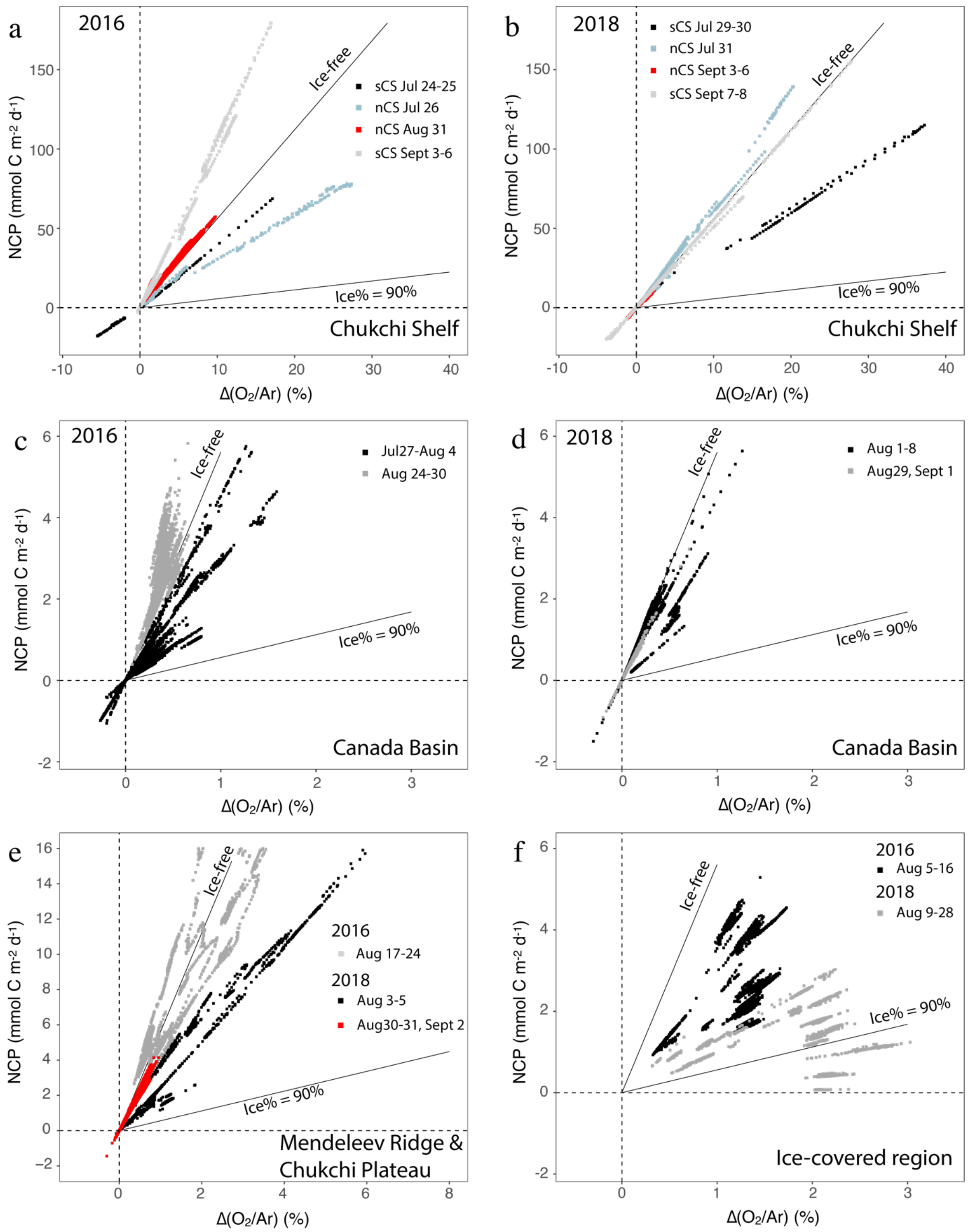

Figure 2.12: Estimated NCP (calculated by considering 60-day wind history and one-day ice%) plotted as a function of $\Delta(O_2/Ar)$. (a-b) Chukchi shelf, with the northern Chukchi Sea (nCS) and southern Chukchi Sea (sCS) data shown separately. (c-d) Canada Basin. (c) Mendeleev Ridge (MR) and Chukchi Plateau (CP). (d) Ice-covered region. The black lines show two end-member cases, ice% = 0% and ice% = 90%, both calculated with a wind speed of 7.5 m s^{-1}.

Uncertainties of gas exchange velocity parameterization similarly exists in CO_2 flux estimation. Interestingly, the regional average of CO_2 flux calculated from monthly wind and ice is likely to be lower by 20% to 30% (Wanninkhof et al., 2002; Wanninkhof et al., 2009) than the CO_2 flux weighted over past 60 days in the nearly ice-free areas, the difference actually becomes much smaller in the heavy ice-covered region (Table 2.1). With the box-model frame of Run-1 (Figure 2.6), we further assessed the differences among different calculation of CO_2 flux by comparing the temporal integrated amount of CO_2 taken up from the atmosphere over the period from day 60 to day 220 (Figure 2.6 c). The difference among the amount of CO_2 been taken up in all cases is less than ~7%, except the one calculated from 60-day weighted approach (orange line in Figure 2.6 c), which is larger by 10% to 20% than others depending on the wind, ice and NCP settings.

The secondary source of uncertainties for NCP and CO_2 flux estimation come from analytical uncertainties. The total uncertainties for air and sea surface pCO_2 measurements are less than 1% ($\pm$0.5 μatm for air pCO_2 and $\pm$2 μatm for underway pCO_2). The uncertainty of $\Delta(O_2/Ar)$ measurement is in the same order of magnitude ($\pm$0.3%, Cassar et al., 2009). Thus, combined with an uncertainty of 5% for sea ice concentration (Peng et al., 2013) and 20% to 40% for gas exchange velocity parametrization, we estimated the overall uncertainty of the NCP and CO_2 fluxes to be ~21% to 42% following the error propagation equation (i.e. $[0.2^2(\text{or } 0.4^2) + 0.05^2 + 0.01^2]^{0.5}$).

2.6.2 Coupling between $\Delta(O_2/Ar)$ and pCO_2 supersaturation ($\Delta(pCO_2)$) and between NCP and CO_2 flux

The dynamics of dissolved O_2 and CO_2 in the surface mixed layer are simultaneously controlled by biological processes (photosynthesis and respiration), physical processes (mixing and meltwater dilution), and gas exchange. Simply speaking, net autotrophy results in net biological O_2 production (evident as an increase in $\Delta(O_2/Ar)$) and net removal of CO_2 (decrease in pCO_2). Net heterotrophy has the opposite effect (decreasing $\Delta(O_2/Ar)$ and increasing pCO_2). At the same time, air-sea exchange of O_2 and CO_2 erases such biological and physical signals and drives the system toward equilibrium.

Studies from many different environments have reported that observed $\Delta(O_2/Ar)$ and pCO_2 are not always correlated, as might be expected from these simple relationships (Eveleth et al. 2017; Teeter et al., 2018; Juranek et al., 2019; Jiang et al., 2019). In dynamic coastal regions, upwelling could perhaps weaken the correlation between O_2 and CO_2 (Teeter et al., 2018). In the Gulf of Mexico, a mismatch of O_2 and CO_2 dynamics was attributed to different equilibrium times for the two gases and also riverine influences (Huang, 2015; Jiang et al., 2019). For the Arctic Ocean, additional complexity arises from melt and formation of sea ice and its associated physical and biological processes.

To improve our understanding of this issue, we use the model described in section 2.4 (see Figures 2.4 & 2.5) to explore the effects of different ice% on the coupling of $\Delta(O_2/Ar)$ and $\Delta(pCO_2)$. $\Delta(pCO_2)$ is pCO_2 supersaturation, calculated as $\Delta(pCO_2) = (\frac{pCO_{2\,meas}}{pCO_{2\,atm}}) - 1$ (Carrillo et al. 2004; Eveleth et al. 2017). Briefly, in each 220-day simulation, NCP = 20 mmol O_2 m^{-2} d^{-1} between days 60 and 160 (otherwise NCP = 0) and wind speed is held constant at 7.5 m s^{-1}; within a given run, ice% is held constant. The imposed box-car NCP setting shapes the relationship between $\Delta(pCO_2)$ and $\Delta(O_2/Ar)$ into two segments (Figure 8a), with both quantities generally increasing over days 60 to 160 (the bloom period) and both quantities generally decreasing over days 160 to 220 (the post-bloom period). Under the same model conditions, the two segments can also be seen in the relationships between NCP and CO_2 flux (Figure 8b). The largest deviations from initial point appears at day 160. After bloom crashes on day 160, air-sea gas exchange becomes the control process and drives CO_2 and O_2 back toward their equilibrium values.

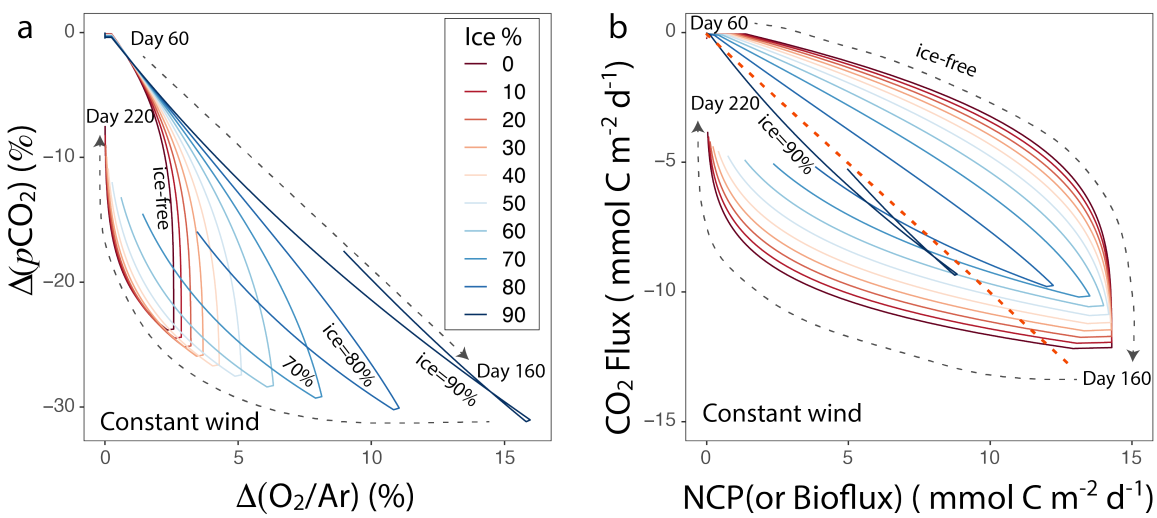

Figure 2.13: Simulated effects of ice concentration (0 to 90%) on correlations of (a) $\Delta(O_2/Ar)$ versus $\Delta(pCO_2)$ and (b) NCP versus CO_2 flux. The model settings were the same as describe in Figure 2.4. The dashed arrows indicate the seasonal evolution of $\Delta(O_2/Ar)$ and $\Delta(pCO_2)$ (days 60 to 220 in Figure 2.4). Negative $\Delta(pCO_2)$ indicates that sea surface pCO_2 is undersaturated with respect to the atmosphere, and negative CO_2 flux indicates CO_2 uptake from the atmosphere. Red dashed line is 1:1 line for NCP and CO_2 flux.

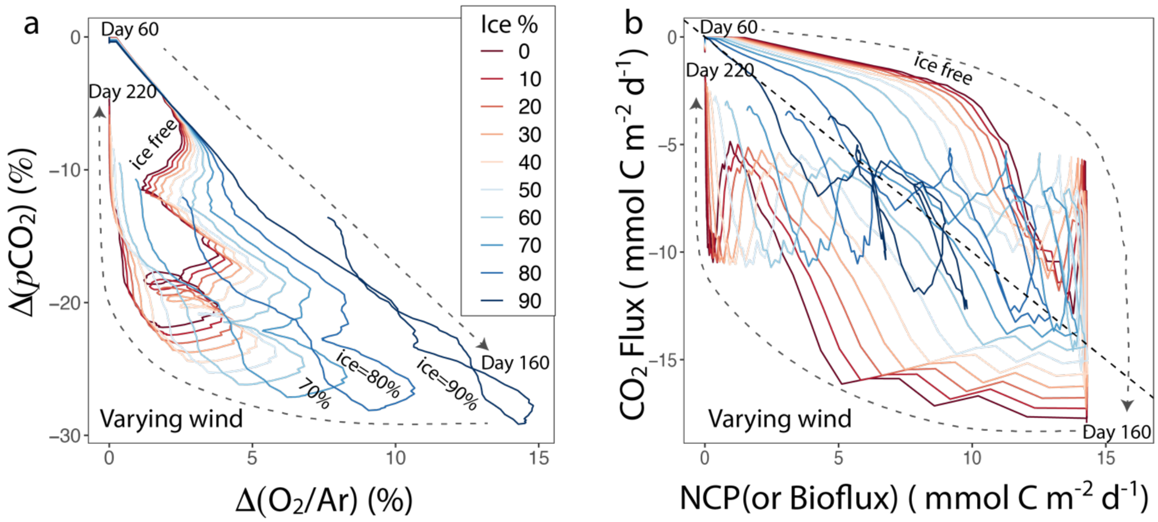

Figure 2.14: Simulated effects of ice concentration (0 to 90%) on correlations of (a) $\Delta(O_2/Ar)$ versus $\Delta(pCO_2)$ and (b) NCP versus CO_2 flux for the case of variable wind speed. The model settings were the same as describe in Figure 2.5. The dashed arrows indicate the seasonal evolution of $\Delta(O_2/Ar)$ and $\Delta(pCO_2)$ (days 60 to 220 in Figure 2.5). Negative $\Delta(pCO_2)$ indicates that sea surface pCO_2 is undersaturated with respect to the atmosphere, and negative CO_2 flux indicates CO_2 uptake from the atmosphere.

On the other hand, different ice% alters these curves by affecting the air-sea gas exchange rates. With a high ice%, gas exchange rates are slow for both CO_2 and O_2 and the residence times are long. Under such a nearly "closed" system isolated from the atmosphere, biological production of O_2 and drawdown of CO_2 are likely to match to each other. Thus, the relationships between $\Delta(pCO_2)$ and $\Delta(O_2/Ar)$ and between NCP and CO_2 flux are near-linear (Figure 2.13). As ice% decreases, the difference between the characteristic timescales of CO_2 gas exchange (~two months in open ocean) and O_2 (~two weeks in open ocean) becomes more apparent, which leads to the more obvious mismatch in time of NCP and CO_2 flux (Figure 2.13 b). With this model, we further examine the effect of a history of varying wind speed (Figure 2.14) rather than constant wind speed. Variable winds may enhance the nonlinearity of the system, but the general couplings between $\Delta(O_2/Ar)$ and $\Delta(pCO_2)$ and between NCP and CO_2 flux do not change much (Figure 2.14).

These simple theoretical cases can help to elucidate the evolving seasonal conditions seen in the more complex field data. Overall, our observations indicate that most of the western Arctic Ocean was net autotrophic during the summers of 2016 and 2018: positive $\Delta(O_2/Ar)$ and negative $\Delta(pCO_2)$ (Figure 2.15). Still, the finer points of the seasonally evolving relationship between $\Delta(O_2/Ar)$ and $\Delta(pCO_2)$ varied regionally (Figures 2.16 a-d). More interestingly, traveling south from the ice-covered region (>78°N) to the ice marginal zone (Mendeleev Ridge–Chukchi Plateau), then to the ice-free Canada Basin, to some extent, is like traveling forward through time to later and later periods in the melt season, which provides us a complete view of the western Arctic summer evolution of NCP and CO_2 uptake, through the stages of pre-melt, ongoing melt, and post-melt.

The heavily ice-covered region of the far north reflected a typical pre-melt stage of primary production in the central Arctic basins. One notable feature was that a weak NCP of 0.5–2 mmol C m^{-2} d^{-1} resulted in relatively large $\Delta(O_2/Ar)$ supersaturation (1%–3%), large negative $\Delta(pCO_2)$ of -10% to -25%, and a small CO_2 flux of -1% to -3% (Figure 2.16 a&e). We attribute this phenomenon to the unique setting of weak primary production within a “closed” system. The ice cover slows O_2 outgassing and CO_2 uptake from the atmosphere, which causes the enhanced $\Delta(O_2/Ar)$ (see higher $\Delta(O_2/Ar)$ with higher ice% in Figure 2.4 b) and maintains a disequilibrium status of $\Delta(pCO_2)$. For the same reason, the magnitude of CO_2 flux was very low and comparable to the NCP (Figure 2.16 e). To have more insights of impacts from sea ice evolution, we mapped ice% on the sampling day onto the Figure 2.16 plots. The less varied high ice% and relatively stable status of $\Delta(O_2/Ar)$ and $\Delta(pCO_2)$ in both years indicate that physical forcings were weak in this region — a setting within which the "closed" system with weak NCP could persist for weeks to months, until the ice starts to deform under the influence of late-summer temperatures.

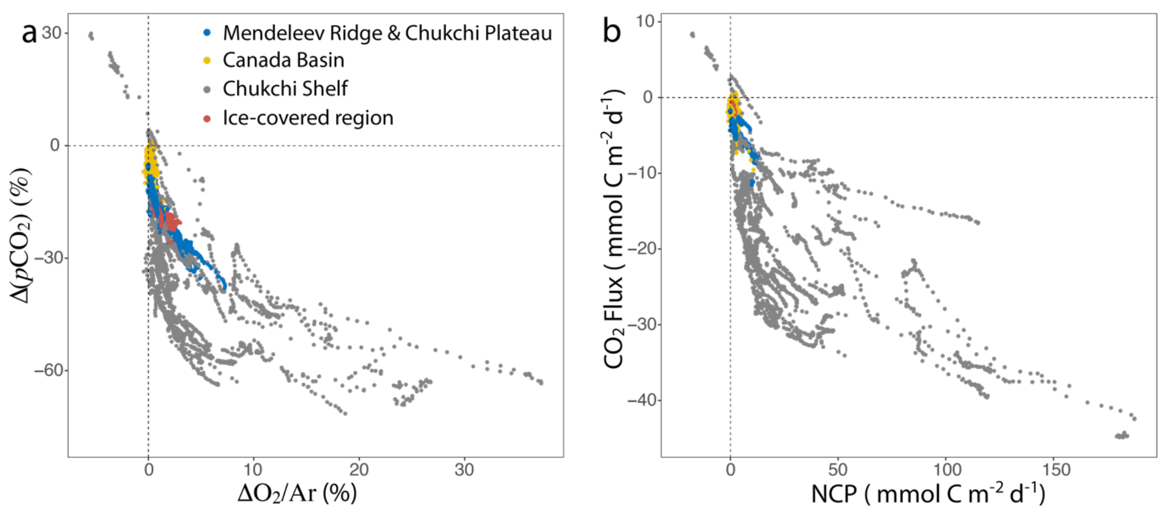

Figure 2.15: Observed relationships between (a) $\Delta(O_2/Ar)$ and $\Delta(pCO_2)$ and (b) NCP and CO_2 flux, color coded by four subregions: Mendeleev Ridge and Chukchi Plateau (blue), Canada Basin (yellow) Chukchi shelf (grey), ice-covered region (red).

The marginal ice zone encountered over the Chukchi Plateau and Mendeleev Ridge provided a good opportunity to examine primary production and CO_2 dynamics during a period of active melting. We found a significant correlation between $\Delta(O_2/Ar)$ and $\Delta(pCO_2)$ in these areas (correlation coefficient $r = -0.94$ for 2016 and -0.92 for 2018; Table 2.2). This strong linear relationship corresponds well with our

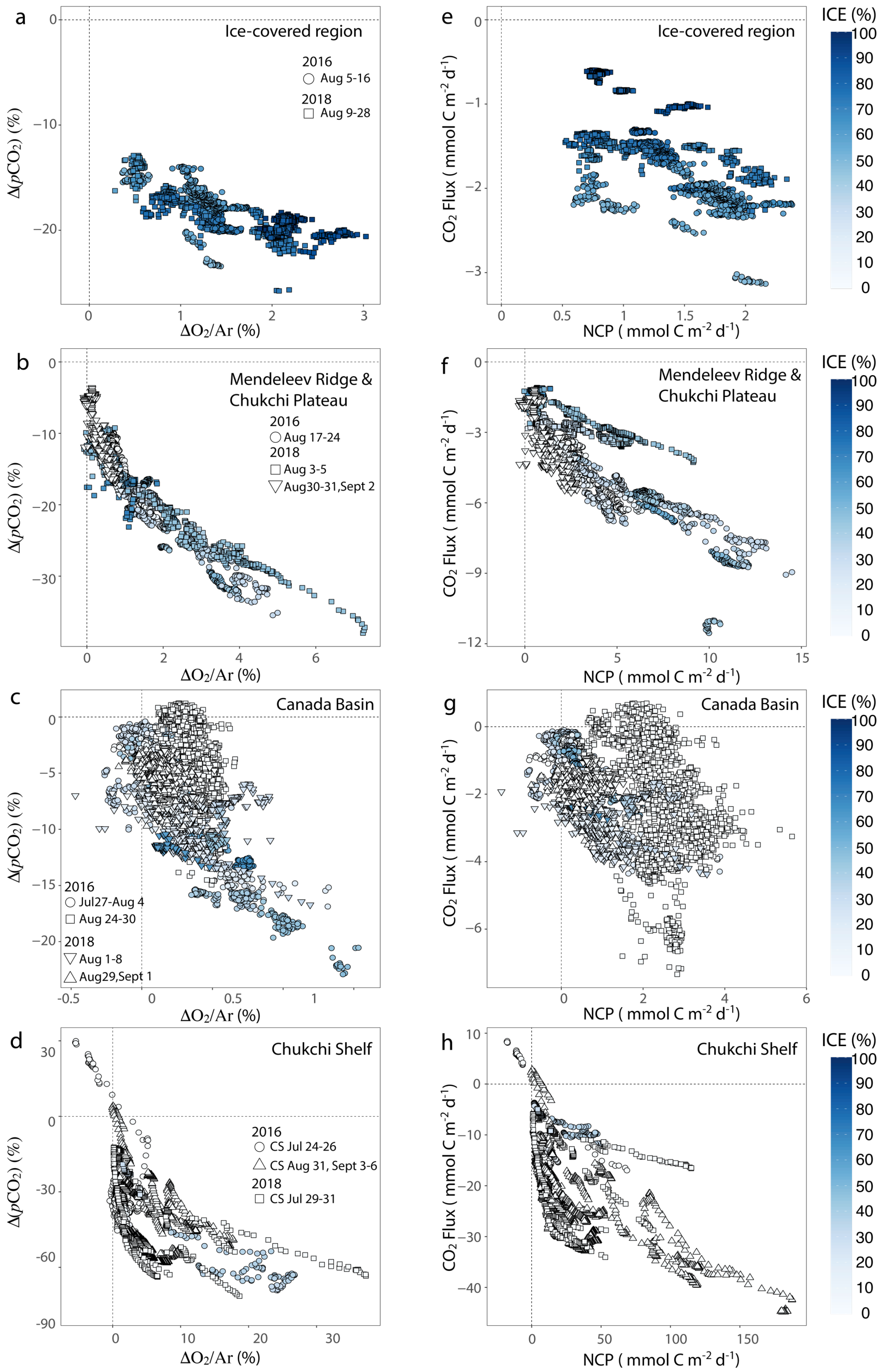

Figure 2.16: Observed relationships between $\Delta(O_2/Ar)$ and $\Delta(pCO_2)$ (a–d) and between NCP and CO_2 flux (e–h). (a and e) Ice-covered region. (b and f) Mendeleev Ridge and Chukchi Plateau. (c and g) Canada Basin. (d and h) Chukchi shelf. Symbol shapes indicate the cruise transects with travel date, and symbol colors indicate ice% values on the visiting day.

simulated results for days 60 to 160 (Figure 2.13 a), implying that thermal effects and water column mixing were negligible and almost all deviations of $\Delta(O_2/Ar)$ and ΔpCO_2 were induced by ongoing primary production. NCP and CO_2 flux (Figure 2.16 f) also mapped curves similar to that seen for our simulation cases of ice% ranged from 30% to 60% (Figure 2.13 b). Also, the seasonal changes in ice% provides clear information about the shift of stage of biological production. For example, the high NCP (5 to 10 mmol C m^{-2} d^{-1}) with a relatively high ice% (30% to 60%) in the early August in 2018 reduced to 0-3 mmol C m^{-2} d^{-1} in the ice-free water (ice%< 15%) at the end of August (Figure 2.16 f).

The observations in the ice-free southern Canada Basin (Figure 2.16 c & g) exhibited the post-melt stage of primary production due to nutrient limitations (McLaughlin & Carmack, 2010; Tremblay et al., 2015; Ji et al., 2019). At this stage, the surface water had become an "open" system, where surface primary production was about to terminate, and air-sea gas exchange took over the dominant role to drive any deviations of $\Delta(O_2/Ar)$ and $\Delta(pCO_2)$ built in previous growing season toward the equilibrium. Warming after ice melt also increased pCO_2, thus hastening the approach to equilibrium for CO_2 (Else et al., 2013). As a result, both $\Delta(O_2/Ar)$ and $\Delta(pCO_2)$ were low during our sampling transits and varied within only narrow ranges (Figure 2.16 c). The seasonal shifts to approach zero in ice% provide one more piece of evidence to indicate that air-sea gas exchange gradually came to dominate $\Delta(O_2/Ar)$ and $\Delta(pCO_2)$ dynamics. We found that the later season $\Delta(O_2/Ar)$ and $\Delta(pCO_2)$ values were closer to equilibrium than the earlier ones (Figure 2.16 c). As a result, the magnitudes of both NCP and CO_2 flux decreased as the season progressed (Figure 2.16 g).

The summertime ice-free Chukchi Shelf, however, represented a different post-melt stage with sustained nutrient supply and strong primary production. The relationship between $\Delta(O_2/Ar)$ and $\Delta(pCO_2)$ in this region was more complex, reflecting high biological and physical heterogeneity there in space and time (Figures 2.16 d). The intensive biological removal of CO_2 far exceeded CO_2 flux from the atmosphere into surface waters, even possibly overriding the possible high pCO_2 signal from the mixing of local bottom water. Thus, air-sea exchange of CO_2 was not efficient enough to drive the large negative $\Delta(pCO_2)$ back to equilibrium within the summer months (Figure 2.16 d), which was an analogue to the pattern seen in our simulation (ice-free case in Figure 2.13 a). This temporal difference between O_2 and CO_2 dynamics is due to the HCO_3^- buffering effect, which determines a much longer time for CO_2 than for O_2 to approaching equilibration with the atmosphere via gas exchange. Although it is challenging to completely explain the seasonal propagation of $\Delta(O_2/Ar)$ and $\Delta(pCO_2)$, it is clear that strong and sustained NCP makes the Chukchi Shelf a large CO_2 sink during summer.

2.6.3 Pacific Water influence

A great deal of recent research has focused on seasonal and interannual NCP changes in the western Arctic Ocean (Juranek et al., 2018; Ji., et al., 2019), but shelf–basin spatial heterogeneity and its controlling mechanisms have yet to be extensively studied. The pronounced loss of summer sea ice in the western Arctic Ocean over recent decades (Wang et al., 2018) provides an ideal experimental field and observational window for examining the impact of sea ice loss on primary production and CO_2 uptake. Here, we aim to clarify and discuss the influence of Pacific Water inflow on summer NCP evolution in the western Arctic Ocean (Figure 2.17).

For the Chukchi shelf, a particularly notable change during recent years has been a dramatic increase of northward annual throughflow of Pacific Water through the Bering Strait. An increase of 50%, from 0.7 Sv to 1.2 Sv, was documented between 2001 and 2014 (Woodgate et al., 2012; Woodgate, 2018). This increased inflow of relatively salty, nutrient-rich water profoundly changed the summer biogeochemical settings on the shelf. Persistent biological hotspots on the Chukchi shelf were attributed to energetic flow (>25 cm s^{-1}) in the mouth of the Bering Strait (Grebmeier et al., 2015) and the flow pathway and confluence of Pacific Water across the shelf (Lowry et al., 2015). As the flow slows down and is confined by topography in the north Chukchi Sea (Stabeno et al., 2018), this more stable sea condition favors higher primary production. Occasional nutrient-rich upwelling across the shelf break may also play an important role in supporting the sustained high NCP of the northern Chukchi Sea (Pickart et al., 2013a & 2013b).

Pacific Water eventually exits the shelf and enters the interior basin via the Barrow and Herald canyons (Corlett and Pickart, 2017; Stabeno et al., 2018; Timmermans et al., 2014). However, Pacific Water does not go directly across the shelf break. Instead, it turns to either east or west direction (Corlett and Pickart, 2017; Li et al., 2019) following topography or subducts into the basin along the isopycnals at ~50 to 150 m due to its high density (Timmermans et al., 2014). This circulation pattern leads to dramatic transitions of SST, SSS (Figure 2.18), $\Delta(O_2/Ar)$, and pCO_2 (Figure 2.1) within a narrow surface front at about 72°N. The nutrient-rich and highly productive Pacific Water thus exerts only limited influence on Canada Basin surface waters.

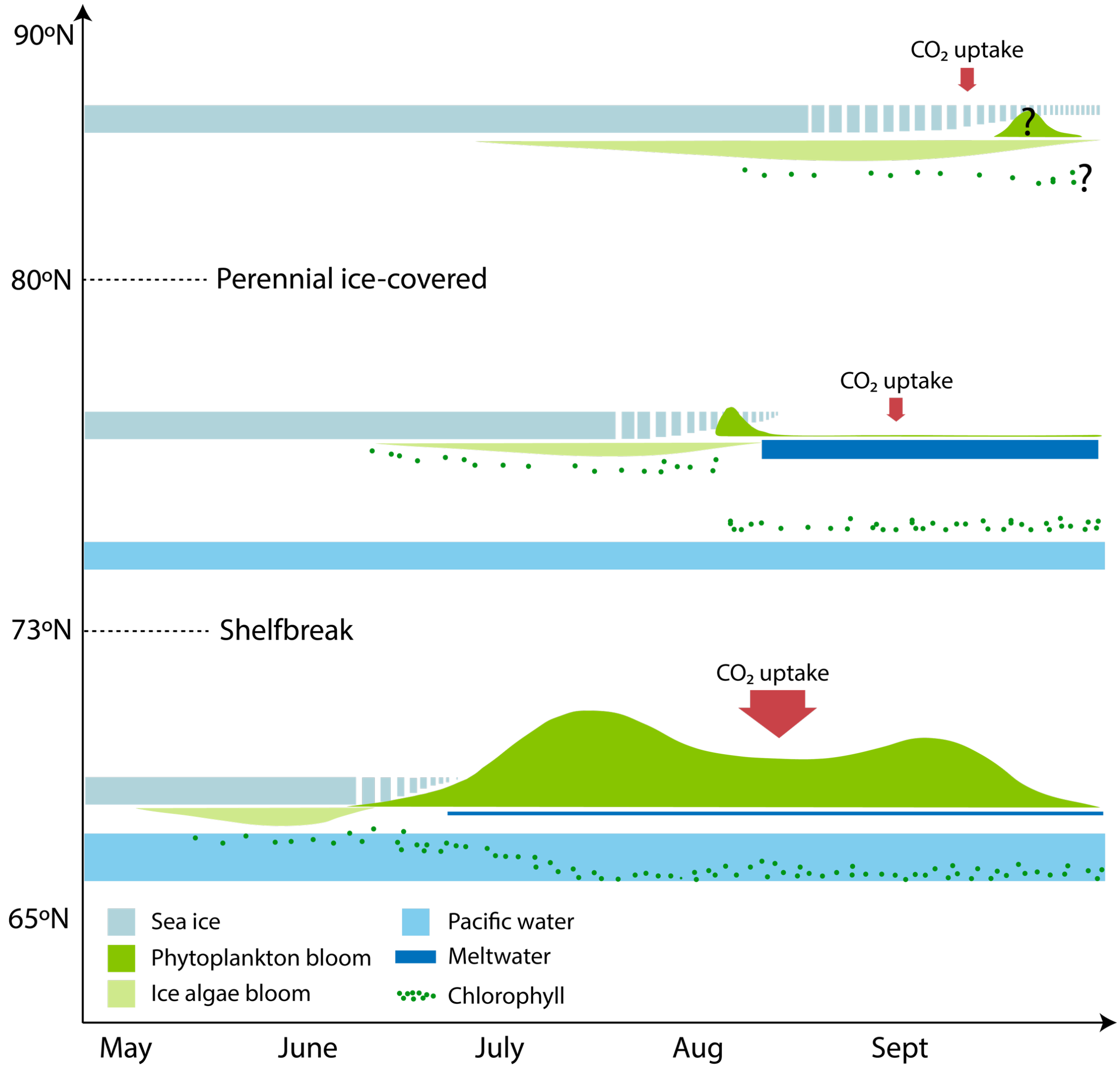

Figure 2.17: Conceptual diagram of the seasonal evolution of NCP at three illustrative locations along a latitudinal gradient in the western Arctic Ocean. Modified after Leu et al. (2011), Falk- Petersen et al. (2007), and Zenkevitch (1963).

On the other hand, most surface waters in the central basin were substantially modified by meltwater. As the sea ice edge retreats northward through the summer, the ice-free area of the basin expands and increases freshwater content occupies the surface. The addition of meltwater strengthens upper layer stratification, thins the surface mixed layer (Peralta-Ferriz and Woodgate 2015), and inhibits the resupply of nutrients from subsurface waters. Beaufort Gyre intensification (in effect from 2004 to 2016) also acts to reduce nutrient supply to the upper waters of the central Canada Basin (Zhang et al., 2020).

As a result of these totally different nutrient supply mechanisms, with the Chukchi Shelf benefiting from sustained nutrient supply from Pacific Water and the central Arctic basin supplied only from ice-trapped brine and nutrients remaining from the previous winter, surface waters in these two regions operate as relatively independent regimes with regard to summer NCP evolution (Figure 2.17). All across the western Arctic Ocean — in the shelf, slope, and southern basin areas — the summer NCP season starts with the under-ice blooms of May–June. In the increasing light of summer, sea ice provides a unique habitat for specialized photosynthetic primary producers (i.e., ice algae, Selz et al .2018; Fernández-Méndez et al., 2018, Lewis el at., 2019). After this shared initial stage, however, the transitions of NCP through the pre-melt, ice-free, and post-melt stages differs among the regions.

On the shelf, after ice break-up, the ice-algae blooms terminate relatively early and then phytoplankton blooms dominate through the remainder of the summer growth season. The sustained supply of nutrients from Pacific Water is essential for supporting the growth of these phytoplankton, which demand relatively high nutrient concentrations. The subsurface chlorophyll maximum (SCM) on the Chukchi Shelf gradually forms over 2 to 3 months, indicating sustained summer NCP (Brown et al., 2015).

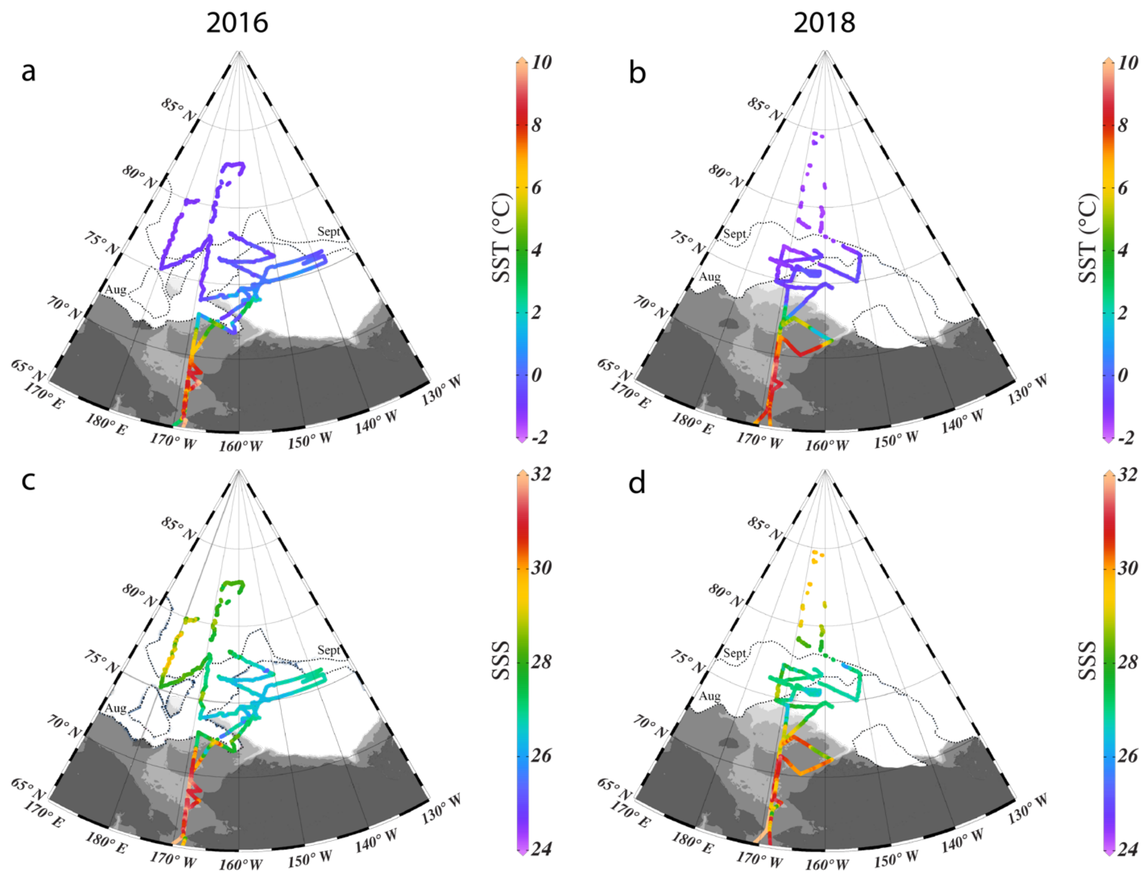

Figure 2.18: Cruise tracks of the 2016 and 2018 cruises, with sea surface temperature (a and b) and sea surface salinity (c and d) shown in color. The white areas indicate monthly sea ice extent (ice concentration >15%) in August and September (National Snow and Ice Data Center, http://nsidc.org/data/seaice_index/).

In contrast, the SCM deepening could complete within a few days in the southern Canada Basin and the adjacent waters (Tremblay et al., 2008; Palmer et al., 2011). The implication is that without external nutrient input, surface phytoplankton blooms in the central Arctic basins or interior seas would be short-lived because the surface nutrient supply would be rapidly depleted. Compared with relatively shallower SCM on the shelf (~15 m; Brown et al., 2015), a much deeper SCM (40-60 m) in the

Arctic basins suggests that the subsurface productivity hardly contributes to NCP in the oligotrophic surface water (Figure 2.17).

In the higher latitudes with thinning ice cover, under-ice blooms likely dominate the NCP. The specialized ice algae (dominantly diatoms) adapted to low light can grow within brine channels, taking advantage of slowly released brine nutrients (Melnikov et al., 2002). Large aggregated long-chained diatoms found on the undersides of ice can sink rapidly to the seafloor after ice deformation, thus serving as an important food source for the benthic food web (Boetius et al., 2013) and a mechanism for rapid carbon export to the seafloor. Using satellite data, Renaut et al. (2018) observed a northward expansion and intensification of phytoplankton growth in the early ice-free season in the Arctic Ocean between 2003 and 2013. During our 2016 and 2018 surveys, we repeatedly observed massive ice-algae attached to the undersides of ice between 76°N and 83°N (Figure 2.19), implying that ice algae blooms are perhaps likewise expanding northward and become ubiquitous.

a b

c

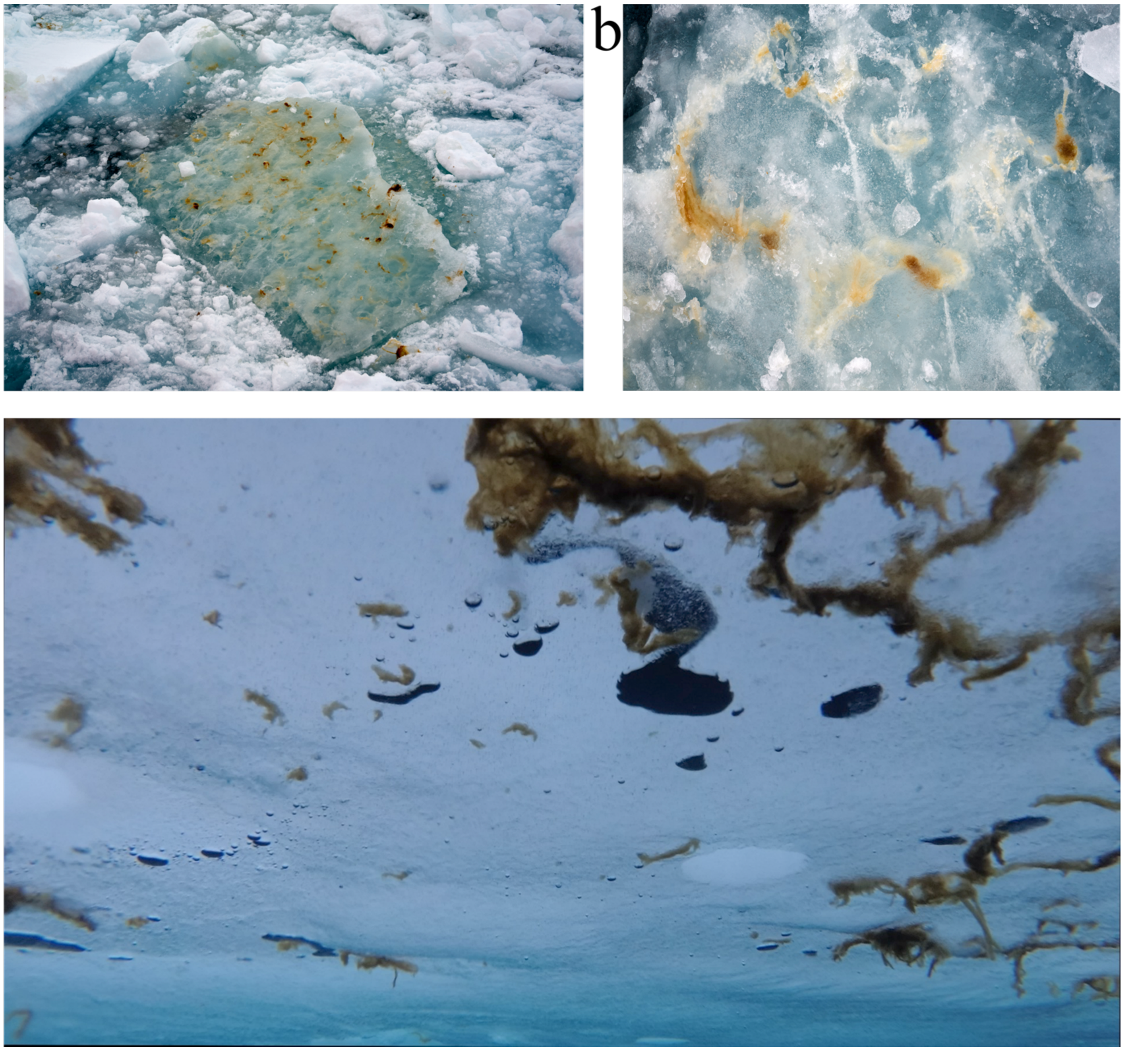

Figure 2.19: (a) Photo of algal bloom attached to underside of sea ice (the chunk of ice had flipped over when the ship broke through the sea ice). (b) Detailed view of algae growing in brine channels. Photos were taken on 19 August 2018, at 84.74°N, 165.67°W. (c) Underwater photo from in situ observation of under-ice bloom on 20 August 2018, at 166.01°W, 84.79°N.

2.7 Summary and implications

This paper reports rates of summertime 2016 and 2018 NCP and CO_2 flux in the western Arctic Ocean and examines their coupling mechanisms. We observed high values of NCP on the Chukchi Shelf and much lower values in the basins, attributable to the heterogeneity of ice conditions, water circulation, and nutrient supply. Our observations present a complete view of the western Arctic summer evolution of NCP and CO_2 uptake, through the stages of pre-melt, ongoing melt, and post-melt. This comprehensive view may help with efforts to understand and model the biogeochemistry of the central Arctic Ocean and also provides an improved understanding of summer NCP evolution.

In order to constrain the uncertainties of NCP and CO_2 fluxes associated with changing sea ice, we suggest taking ice history into account when calculating NCP from $\Delta(O_2/Ar)$ measurement. Not doing so may amplify the sampling bias induced by rapid change in ice condition. Considering the tendency of underestimation of NCP in the heavy ice-covered area, we recommend that productivity incubation experiments should be performed as these experiments integrate over a much shorter timescale, with which we can better interpret the results of NCP measurements along with the $\Delta(O_2/Ar)$ approach.

REFERENCES

Arrigo, K., Perovich, D., Pickart, R., Brown, Z., Van, D., Lowry, K., et al. (2012). Massive phytoplankton blooms under arctic sea ice. *Science, 336*(6087), 1408-1408. doi:10.1126/science.1215065

Bates, N., Moran, S., Hansell, D., & Mathis, J. (2006). An increasing co_2 sink in the arctic ocean due to sea-ice loss. *Geophysical Research Letters, 33*(23). doi:10.1029/2006GL027028

Boetius, A., Albrecht, S., Bakker, K., Bienhold, C., Felden, J., Fernández-Méndez, M., et al. (2013). Export of algal biomass from the melting arctic sea ice. *Science, 339*(6126), 1430-1432. doi:10.1126/science.1231346

Brown, Z., Lowry, K., Palmer, M., Van Dijken, G., Mills, M., Pickart, R., & Arrigo, K. (2015). Characterizing the subsurface chlorophyll a maximum in the Chukchi sea and Canada basin. *Deep-Sea Research Part II: Part A, 118,* 88-104. doi:10.1016/j.dsr2.2015.02.010

Buck, A. L. (1981). New Equations for Computing Vapor Pressure and Enhancement Factor. *Journal of Applied Meteorology, 12,* 1527-1532. doi:10.1175/1520-0450(1981)020<1527:NEFCVP>2.0.CO;2

Butterworth, B. J., & Miller, S. D. (2016). Air-Sea Exchange of Carbon Dioxide in the Southern Ocean and Antarctic Marginal Ice Zone. *Geophysical Research Letters 43*(13), 7223–30. doi:10.1002/2016GL069581.

Cai, W.-J., Chen, L., Chen, B., Gao, Z., Lee, S.H., Chen, J., et al. (2010). Decrease in the CO2 uptake capacity in an ice-free Arctic Ocean basin. *Science, 329,* 556–559. doi:10.1126/science.1189338

Carrillo, C., Smith, R., & Karl, D. (2004). Processes regulating oxygen and carbon dioxide in surface waters west of the antarctic peninsula. *Marine Chemistry, 84*(3), 161-179. doi:10.1016/j.marchem.2003.07.004

Cassar, N., Barnett, B., Bender, M., Kaiser, J., Hamme, R., & Tilbrook, B. (2009). Continuous high-frequency dissolved o2/ar measurements by equilibrator inlet mass spectrometry. *Analytical Chemistry, 81*(5), 1855-64. doi:10.1021/ac802300u

Cassar, N., Nevison, C. D., & Manizza, M. (2014). Correcting Oceanic O_2/Ar-Net Community Production Estimates for Vertical Mixing Using N_2o Observations. *Geophysical Research Letters 41*(24), 8961–70. doi:10.1002/2014GL062040.

Corlett, W., & Pickart, R. (2017). The Chukchi slope current. *Progress in Oceanography, 153,* 50-65. doi:10.1016/j.pocean.2017.04.005

Comiso, J. C. 2000, updated 2015. Bootstrap Sea Ice Concentrations from Nimbus-7 SMMR and DMSP SSM/I-SSMIS, Version 2. [Northern Hemisphere/Daily]. Boulder, Colorado USA. NASA National Snow and Ice Data Center Distributed Active Archive Center. doi: https://doi.org/10.5067/J6JQLS9EJ5HU.

Craig, H., & Hayward, T. (1987). Oxygen supersaturation in the ocean: Biological versus physical contributions, *Science, 235*(4785), 199–202, doi:10.1126/science.235.4785.199.
Else, B., Galley, R., Lansard, B., Barber, D., Brown, K., Miller, L., et al. (2013). Further observations of a decreasing atmospheric co_2 uptake capacity in the Canada basin (arctic ocean) due to sea ice loss. *Geophysical Research Letters, 40*(6), 1132-1137. doi:10.1002/grl.50268
Emerson, S., Quay, P., Stump, C., Wilbur, D., & Knox, M. (1991). O_2, Ar, N_2, and ^{222}Rn in surface waters of the subarctic ocean: Net biological O_2 production. *Global Biogeochemical Cycles, 5*(1), 49-69. doi:10.1029/90GB02656
Evans, W., Mathis, J., Cross, J., Bates, N., Frey, K., Else, B., et al. (2015). Sea-air co_2 exchange in the western Arctic coastal ocean. *Global Biogeochemical Cycles, 29*(8), 1190-1209. doi:10.1002/2015GB005153
Eveleth, R., Timmermans, M., & Cassar, N. (2014). Physical and biological controls on oxygen saturation variability in the upper arctic ocean. *Journal of Geophysical Research: Oceans, 119*(11), 7420-7432. doi:10.1002/2014JC009816
Eveleth, R., Cassar, N., Sherrell, R., Ducklow, H., Meredith, M., Venables, H., et al. (2017). Ice melt influence on summertime net community production along the western Antarctic Peninsula. *Deep-Sea Research Part II, 139,* 89-102. doi:10.1016/j.dsr2.2016.07.016
Falk-Petersen, S., Pavlov, V., Timofeev, S., & Sargent, J. R. (2007). Climate variability and possible effects on arctic food chains: the role of Calanus. In Arctic alpine ecosystems and people in a changing environment (147-166). Springer, Berlin, Heidelberg, doi:10.1007/978-3-540-48514-8
Fernández-Méndez, M., Olsen, L., Kauko, H., Meyer, A., Rösel, A., Merkouriadi, I., et al. (2018). Algal hot spots in a changing arctic ocean: Sea-ice ridges and the snow-ice interface. *Frontiers in Marine Science, 5*. doi:10.3389/fmars.2018.00075
Garcia, H., & Gordon, L. (1992). Oxygen solubility in seawater: Better fitting equations. *Limnology and Oceanography, 37*(6), 1307-1312. doi:10.4319/lo.1992.37.6.1307
Grebmeier, J., Bluhm, B., Cooper, L., Danielson, S., Arrigo, K., Blanchard, A., et al. (2015). Ecosystem characteristics and processes facilitating persistent macrobenthic biomass hotspots and associated benthivory in the Pacific Arctic. *Progress in Oceanography, 136,* 92-114. doi:10.1016/j.pocean.2015.05.006
Hamme, R. C., & Emerson, S. R. (2004). The Solubility of Neon, Nitrogen and Argon in Distilled Water and Seawater. *Deep-Sea Research Part I 51*(11), 1517–28. doi:10.1016/j.dsr.2004.06.009.
Huang, Wei-Jen (2013). Inorganic carbon distribution and dynamics in the Mississippi River plume on the northern Gulf of Mexico. PhD dissertation, UGA.

Islam, F., DeGrandpre, M. D., Beatty, C. M., Timmermans, M. L., Krishfield, R. A., Toole, J. M., & Laney, S. R. (2016). Sea surface pCO_2 and O_2 dynamics in the partially ice-covered Arctic Ocean. *Journal of Geophysical Research: Oceans, 122*(2), 1425-1438. doi:10.1002/ 2016JC012162

Ji, B., Sandwith, Z., Williams, W., Diaconescu, O., Ji, R., Li, Y., et al. (2019). Variations in rates of biological production in the Beaufort Gyre as the Arctic changes: Rates from 2011 to 2016. *Journal of Geophysical Research: Oceans, 124*(6), 3628-3644. doi:10.1029/2018JC014805

Jiang, Z. P., Cai, W-J, Lehrter, J., Chen, B., Ouyang, Z., Le, C., ... & Xu, Y. (2019). Spring net community production and its coupling with the CO_2 dynamics in the surface water of the northern Gulf of Mexico. *Biogeosciences, 16*(18), 3507-3525. doi:10.5194/bg-16-3507-2019

Jönsson, B., Doney, S., Dunne, J., & Bender, M. (2013). Evaluation of the Southern Ocean O_2/Ar-based NCP estimates in a model framework. *Journal of Geophysical Research: Biogeosciences, 118*(2), 385-399. doi:10.1002/jgrg.20032

Juranek, L., Takahashi, T., Mathis, J., & Pickart, R. (2019). Significant biologically mediated CO2 uptake in the Pacific Arctic during the late open water season. *Journal of Geophysical Research: Oceans, 124*(2), 821-843. doi:10.1029/2018JC014568

Laws, E. (1991). Photosynthetic quotients, new production and net community production in the open ocean. Deep Sea Research Part A, *Oceanographic Research Papers, 38*(1), 143-167. doi:10.1016/0198-0149(91)90059-O

Leu, E., Søreide, J., Hessen, D., Falk-Petersen, S., & Berge, J. (2011). Consequences of changing sea-ice cover for primary and secondary producers in the European Arctic shelf seas: Timing, quantity, and quality. *Progress in Oceanography, 90*(1-4), 18-32. doi:10.1016/j.pocean.2011.02.004

Lewis, K. M., Arntsen, A. E., Coupel, P., Joy - Warren, H., Lowry, K. E., Matsuoka, A., et al. (2019). Photoacclimation of Arctic Ocean phytoplankton to shifting light and nutrient limitation. *Limnology and Oceanography, 64*(1), 284-301. doi:10.1002/lno.11039

Li, M., Pickart, R., Spall, M., Weingartner, T., Lin, P., Moore, G., & Qi, Y. (2019). Circulation of the Chukchi Sea shelfbreak and slope from moored timeseries. *Progress in Oceanography, 172,* 14-33. doi:10.1016/j.pocean.2019.01.002

Long, M., Dunbar, R., Tortell, P., Smith, W., Mucciarone, D., & DiTullio, G. (2011). Vertical structure, seasonal drawdown, and net community production in the Ross Sea, Antarctica. *Journal of Geophysical Research: Oceans, 116*(C10). doi:10.1029/2009JC005954

Loose, B., McGillis, W., Schlosser, P., Perovich, D., & Takahashi, T. (2009). Effects of freezing, growth, and ice cover on gas transport processes in laboratory seawater experiments. *Geophysical Research Letters, 36*(5). doi:10.1029/2008GL036318

Loose, B., McGillis, W., Perovich, D., Zappa, C., & Schlosser, P. (2014). A parameter model of gas exchange for the seasonal sea ice zone. *Ocean Science, 10*(1), 17-17. doi:10.5194/os-10-17-2014

Lovely, A., Loose, B., Schlosser, P., McGillis, W., Zappa, C., Perovich, D., et al. (2015), The Gas Transfer through Polar Sea ice experiment: Insights into the rates and pathways that determine geochemical fluxes, *Journal of Geophysical Research: Oceans, 120*, 8177–8194, doi:10.1002/2014JC010607.

Lowry, K., Pickart, R., Mills, M., Brown, Z., Van Dijken, G., Bates, N., & Arrigo, K. (2015). The influence of winter water on phytoplankton blooms in the Chukchi Sea. *Deep-Sea Research Part II: Part A, 118,* 53-72. doi:10.1016/j.dsr2.2015.06.006

Maslanik, J., Stroeve, J., Fowler, C., & Emery, W. (2011). Distribution and trends in Arctic sea ice age through spring 2011. *Geophysical Research Letters, 38*(13). doi:10.1029/2011GL047735

McLaughlin, F., & Carmack, E. (2010). Deepening of the nutricline and chlorophyll maximum in the Canada basin interior, 2003-2009. *Geophysical Research Letters, 37*(24). doi:10.1029/2010GL045459

Melnikov, Igor A., Elena G. Kolosova, Harold E. Welch, and Ludmila S. Zhitina (2002). Sea ice biological communities and nutrient dynamics in the Canada Basin of the Arctic Ocean. Deep Sea Research Part I: Oceanographic Research Papers49, no. 9: 1623-1649. doi:10.1016/S0967-0637(02)00042-0

Mundy, C., Gosselin, M., Ehn, J., Gratton, Y., Rossnagel, A., Barber, D., et al. (2009). Contribution of under-ice primary production to an ice-edge upwelling phytoplankton bloom in the canadian beaufort sea. *Geophysical Research Letters, 36*(17). doi:10.1029/2009GL038837

Onarheim, I., Eldevik, T., Smedsrud, L., & Stroeve, J. (2018). Seasonal and regional manifestation of arctic sea ice loss. *Journal of Climate, 31*(12), 4917-4932. doi:10.1175/JCLI-D-17-0427.1

Palmer, M. A., Arrigo, K. R., Mundy, C. J., Ehn, J. K., Gosselin, M., Barber, D. G., et al. (2011). Spatial and temporal variation of photosynthetic parameters in natural phytoplankton assemblages in the Beaufort Sea, Canadian Arctic. *Polar biology, 34*(12), 1915-1928. doi:10.1007/s00300-011-1050-x

Peralta-Ferriz, C., & Woodgate, R. (2015). Seasonal and interannual variability of pan-arctic surface mixed layer properties from 1979 to 2012 from hydrographic data, and the dominance of stratification for multiyear mixed layer depth shoaling. *Progress in Oceanography, 134,* 19-53. doi:10.1016/j.pocean.2014.12.005

Perrette, M., Yool, A., Quartly, G.D., Popova, E.E. (2011). Near-ubiquity of ice-edge blooms in the Arctic. *Biogeosciences, 8,* 515–524. doi:10.5194/bg-8-515-2011

Pickart, R., Spall, M., & Mathis, J. (2013). Dynamics of upwelling in the alaskan beaufort sea and associated shelf-basin fluxes. *Deep-Sea Research Part I, 76*, 35-51. doi:10.1016/j.dsr.2013.01.007

Pickart, R., Schulze, L., Moore, G., Charette, M., Arrigo, K., Van Dijken, G., & Danielson, S. (2013). Long-term trends of upwelling and impacts on primary productivity in the alaskan beaufort sea. *Deep-Sea Research Part I, 79,* 106-121. doi:10.1016/j.dsr.2013.05.003

Pierrot, D., Neill, C., Sullivan, K., Castle, R., Wanninkhof, R., Lüger, H., et al. (2009). Recommendations for autonomous underway pCO_2 measuring systems and data-reduction routines. *Deep-Sea Research Part II, 56*(8), 512-522. doi:10.1016/j.dsr2.2008.12.005

Peng, G., Meier, W., Scott, D., Savoie, M., A long-term and reproducible passive microwave sea ice concentration data record for climate studies and monitoring. *Earth Syst. Sci. Data 5*, 311e318 (2013).

Prytherch, J., Brooks, I., Crill, P., Thornton, B., Salisbury, D., Tjernström, M., et al. (2017). Direct determination of the air-sea CO_2 gas transfer velocity in Arctic sea ice regions. *Geophysical Research Letters, 44*(8), 3770-3778. doi:10.1002/2017GL073593

Renaut, S., Devred, E., & Babin, M. (2018). Northward expansion and intensification of phytoplankton growth during the early ice-free season in Arctic. *Geophysical Research Letters, 45*(19), 590-10. doi:10.1029/2018GL078995

Reuer, M., Barnett, B., Bender, M., Falkowski, P., & Hendricks, M. (2007). New estimates of Southern Ocean biological production rates from O_2/Ar ratios and the triple isotope composition of o2. *Deep-Sea Research Part I, 54*(6), 951-974. doi:10.1016/j.dsr.2007.02.007

Schlitzer, R. (2018). Ocean Data View, https://odv.awi.de.

Selz, V., Saenz, B., Dijken, G., & Arrigo, K. (2018). Drivers of ice algal bloom variability between 1980 and 2015 in the Chukchi Sea. *Journal of Geophysical Research: Oceans, 123*(10), 7037-7052. doi:10.1029/2018JC014123

Slagstad, D., Ellingsen, I., & Wassmann, P. (2011). Evaluating primary and secondary production in an Arctic Ocean void of summer sea ice: An experimental simulation approach. *Progress in Oceanography, 90*(1-4), 117-131. doi:10.1016/j.pocean.2011.02.009

Stabeno, P., Kachel, N., Ladd, C., & Woodgate, R. (2018). Flow patterns in the eastern Chukchi Sea: 2010-2015. *Journal of Geophysical Research: Oceans, 123*(2), 1177-1195. doi:10.1002/2017JC013135

Stroeve, J., & Notz, D. (2018). Changing state of arctic sea ice across all seasons. *Environmental Research Letters, 13*(10), 103001-103001. doi:10.1088/1748-9326/aade56

Taylor, M., Losch, M., & Bracher, A. (2013). On the drivers of phytoplankton blooms in the Antarctic marginal ice zone: A modeling approach. *Journal of Geophysical Research: Oceans, 118*(1), 63-75. doi:10.1029/2012JC008418

Teeter, L., Hamme, R., Ianson, D., & Bianucci, L. (2018). Accurate estimation of net community production from O_2/Ar measurements. *Global Biogeochemical Cycles, 32*(8), 1163-1181. doi:10.1029/2017GB005874

Timmermans, M., Proshutinsky, A., Golubeva, E., Jackson, J., Krishfield, R., McCall, M., et al. (2014). Mechanisms of pacific summer water variability in the Arctic's central Canada basin. *Journal of Geophysical Research: Oceans, 119*(11), 7523-7548. doi:10.1002/2014JC010273

Tremblay, J., Simpson, K., Martin, J., Miller, L., Gratton, Y., Barber, D., & Price, N. (2008). Vertical stability and the annual dynamics of nutrients and chlorophyll fluorescence in the coastal, southeast Beaufort Sea. *Journal of Geophysical Research: Oceans, 113*(C7). doi:10.1029/2007JC004547

Tremblay, J. E., Anderson, L. G., Matrai, P., Coupel, P., Belanger, S., Michel, C., & Reigstad, M. (2015). Global and regional drivers of nutrient supply, primary production and CO_2 drawdown in the changing Arctic Ocean. Progress in Oceanography, 139,171–196. https:// doi.org/10.1016/j.pocean.2015.08.009

Ulfsbo, A., Cassar, N., Korhonen, M., Heuven, S., Hoppema, M., Kattner, G., & Anderson, L. (2014). Late summer net community production in the central Arctic Ocean using multiple approaches. *Global Biogeochemical Cycles, 28*(10), 1129-1148. doi:10.1002/2014GB004833

Wang, M., Yang, Q., Overland, J., & Stabeno, P. (2018). Sea-ice cover timing in the Pacific Arctic: The present and projections to mid-century by selected CMIP5 models. *Deep-Sea Research Part II, 152*, 22-34. doi:10.1016/j.dsr2.2017.11.017

Wanninkhof, R., Doney, S. C., Takahashi, T., & Mcgillis, W. R. (2002). The Effect of Using Time-Averaged Winds on Regional Air-Sea CO2 Fluxes. *GEOPHYSICAL MONOGRAPH-AMERICAN GEOPHYSICAL UNION*, *127*, 351-356. doi: 10.1029/GM127p0351

Wanninkhof, R., Asher, W. E., Ho, D. T., Sweeney, C., & McGillis, W. R. (2009). Advances in quantifying air-sea gas exchange and environmental forcing. *Annual Review of Marine Science*, 1(1), 213-244. doi:10.1146/annurev.marine.010908.163742

Wanninkhof, R. (2014). Relationship between wind speed and gas exchange over the ocean revisited. *Limnology and Oceanography: Methods, 12*(6), 351-362. doi:10.4319/lom.2014.12.351

Weiss, R. (1974). Carbon dioxide in water and seawater: The solubility of a non-ideal gas. *Marine Chemistry, 2*(3), 203-215. doi:10.1016/0304-4203(74)90015-2

Woodgate, R., Weingartner, T., & Lindsay, R. (2012). Observed increases in Bering Strait oceanic fluxes from the Pacific to the Arctic from 2001 to 2011 and their impacts on the Arctic Ocean water column. *Geophysical Research Letters, 39*(24). doi:10.1029/2012GL054092

Woodgate, R. A. (2018). Increases in the Pacific inflow to the Arctic from 1990 to 2015, and insights into seasonal trends and driving mechanisms from year-round Bering Strait mooring data. *Progress in Oceanography, 160*, 124-154. doi:10.1016/j.pocean.2017.12.007

Yasunaka, S., Siswanto, E., Olsen, A., Hoppema, M., Watanabe, E., Fransson, A., et al. (2018). Arctic ocean CO_2 uptake: An improved multiyear estimate of the air-sea CO_2 flux incorporating chlorophyll a concentrations. *Biogeosciences, 15*(6), 1643-1661. doi:10.5194/bg-15-1643-2018

Zhang, J., Spitz, Y., Steele, M., Ashjian, C., Campbell, R., & Schweiger, A. (2020). Biophysical consequences of a relaxing Beaufort Gyre. *Geophysical Research Letters, 47*(2). doi:10.1029/2019GL085990

Zenkevitch, L. (1963). Biology of the Seas of the USSR. George Allen & Unwin Ltd., London.

Chapter 3

SEA ICE LOSS AMPLIFIES SUMMER-TIME DECADAL CO_2 INCREASE IN THE WESTERN ARCTIC OCEAN

3.1 Abstract

Rapid climate warming and sea-ice loss have induced major changes in the sea surface partial pressure of CO_2 (pCO_2). However, the long-term trends in the western Arctic Ocean are unknown. Here we show that in 1994–2017, summer pCO_2 in the Canada Basin increased at twice the rate of atmospheric increase. Warming and ice loss in the basin have strengthened the pCO_2 seasonal amplitude, resulting in the rapid decadal increase. Consequently, the summer air–sea CO_2 gradient has reduced rapidly, and may become near zero within two decades. In contrast, there was no significant pCO_2 increase on the Chukchi Shelf, where strong and increasing biological uptake has held pCO_2 low, and thus the CO_2 sink has increased and may increase further due to the atmospheric CO_2 increase. Our findings elucidate the contrasting physical and biological drivers controlling sea surface pCO_2 variations and trends in response to climate change in the Arctic Ocean.

Ouyang. Z., Qi, D., Chen, Li., Takahashi, T., Zhong, W., DeGrandpre, M.D., Chen, B., Gao, Z., Nishino, S., Murata, A., Sun, H., Robbins, L. L., Jin, M., Cai, W-J. (2020). Sea-ice loss amplifies summertime decadal CO_2 increase in the western Arctic Ocean. *Nature Climate Change*; 10, 678-684. DOI: 10.1038/s41558-020-0784-2

3.2 Introduction

As a bellwether of climate change, the Arctic Ocean has experienced dramatic physical and ecological changes, including warming and increased sea ice loss (Onarheim et al., 2018; Stroeve et al., 2018), freshened surface water (Giles et al., 2012; Yamamoto-Kawai et al., 2009), altered surface circulation (Timmermans et al., 2014; Corlett and Pickart et al., 2017; Stabeno et al., 2018), and enhanced primary production (Arrigo and van Dijken, 2015). These changes also influence Arctic Ocean carbonate chemistry by decreasing the carbonate mineral saturation state (Yamamoto-Kawai et al., 2009) and expanding the acidified water volume (Qi et al., 2017; Robbins et al., 2013; Anderson et al., 2017). While sea ice melt removes the mechanical barrier for air-sea CO_2 exchange, meltwater increases the surface stratification and suppresses nutrients supplied by upward mixing of subsurface waters (Coupel et al., 2015; Nishino et al., 2011), thus, potentially limiting biological drawdown of CO_2 and ocean CO_2 uptake (Cai et al., 2010).

The direction and magnitude of CO_2 uptake or release across the sea surface are determined by the air-sea difference of $p\mathrm{CO_2}$. On a decadal scale, sea surface $p\mathrm{CO_2}$ has increased almost everywhere in the world's oceans, including the low and mid-latitudes and the Southern Ocean, at rates roughly comparable to that of the atmospheric CO_2 increase (Takahashi et al., 2009; Takahashi et al., 2014; Bates et al., 2006). The trends of $p\mathrm{CO_2}$ in the Arctic Ocean are poorly known, however, due to observational limitations and the added complexity involving sea ice melt. Early observations suggested a strong CO_2 sink with persistently low $p\mathrm{CO_2}$ in the highly productive shelf and slope areas (Bates et al., 2006), while more recent observations from the ice-free basin found high $p\mathrm{CO_2}$ values approaching atmospheric CO_2 levels due to rapid air-sea gas exchange and warming (Cai et al., 2010; Else et al., 2013).

Since these initial assessments, much more sea surface pCO_2 data have been collected, making it possible for the first time to identify the observation-based decadal trends and explore the driving mechanisms. Here, we report new sea surface pCO_2 data together with historical data from multiple international databases (Supplementary Table 3.1) from 1994 to 2017 and examine the seasonal and decadal variations and quantify the contributions of multiple drivers. This study improves the understanding of processes regulating seasonal and interannual variabilities of the Arctic Ocean pCO_2, which is essential for forecasting responses of the ocean carbon cycle to climate change.

3.3 Results and Discussion

3.3.1 Spatial Distribution and Decadal Trends of Sea Surface pCO_2

During the summer (July 1 to October 15) over the past two decades, a distinct spatial distribution of low pCO_2 in the surface waters of shelf areas and high pCO_2 in the central basins gradually formed and persistently appeared in the western Arctic Ocean (Figures 3.1 & 3.2). In the mid-1990s, most of the region was covered by sea ice, and pCO_2 was low on the shelf and near the ice edge (70−74°N) and higher in more northerly, ice-covered regions (Figure 3.2 a). As sea ice retreated poleward in the early 2000s, moderately high pCO_2 appeared in the southern Canada Basin (Figure 3.2 b-d). Since 2008, the central Canada Basin became more frequently ice-free and exhibited conspicuously higher pCO_2 (Figure 3.2 e-i). In more recent years, the near atmospheric (>370 μatm) pCO_2 values have extended farther north into the northern basins (Figure 3.2 j-l). In contrast, pCO_2 on the Chukchi Shelf was equally low or even lower in recent years compared to the 1990s and early 2000s, although some high

pCO$_2$ signals were observed in the shallow nearshore areas (Figure 3.2). This increasingly contrasting spatial distribution of sea surface pCO$_2$ has become the new normal during summertime in the western Arctic Ocean since 2007 (Figures 3.1 & 3.2).

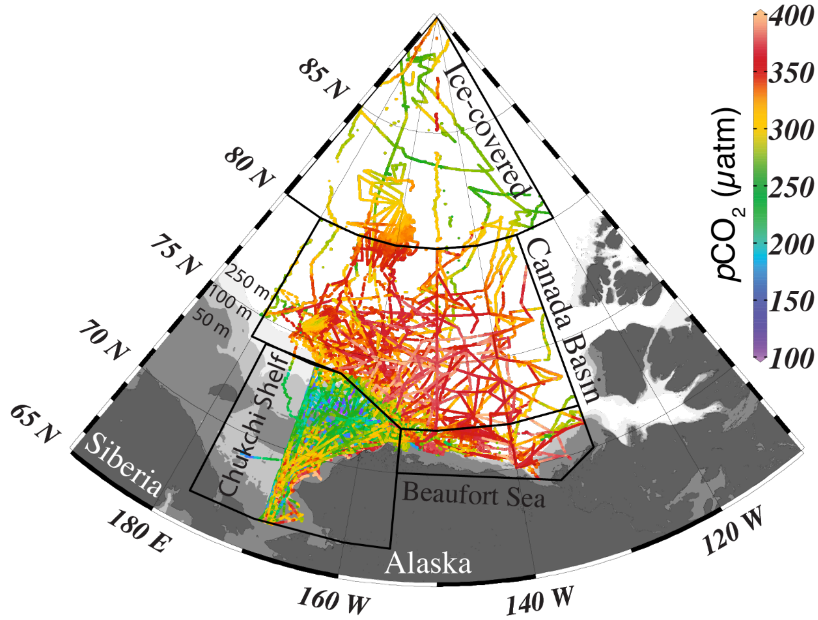

Figure 3.1: The spatial distribution of sea surface pCO$_2$. Map of the western Arctic Ocean is overlaid with pCO$_2$ observations in the summertime (July 1-October 15) from 1994 to 2017. Information about individual cruises is presented in Figure 3.2 and Table 3.2. The western Arctic Ocean (<80ºN) is defined as the combination of three subregions: the Chukchi Shelf, Beaufort Sea and Canada Basin. Based on the spatial heterogeneity of observed pCO$_2$, we separate the Chukchi Shelf and the Canada Basin mainly along 200-250 m isobaths. We set the boundary for the Chukchi Shelf and the coastal Beaufort Sea by 155ºW where the Alaska coastal current loses its major impact and the Mackenzie River runoff occupies the surface water. Data for the Canada Basin and Beaufort Sea are assigned to be north and south of 72°N, respectively. Data observed in the north of 80°N are assigned into the perenially ice-covered region (ice concentration >15%).

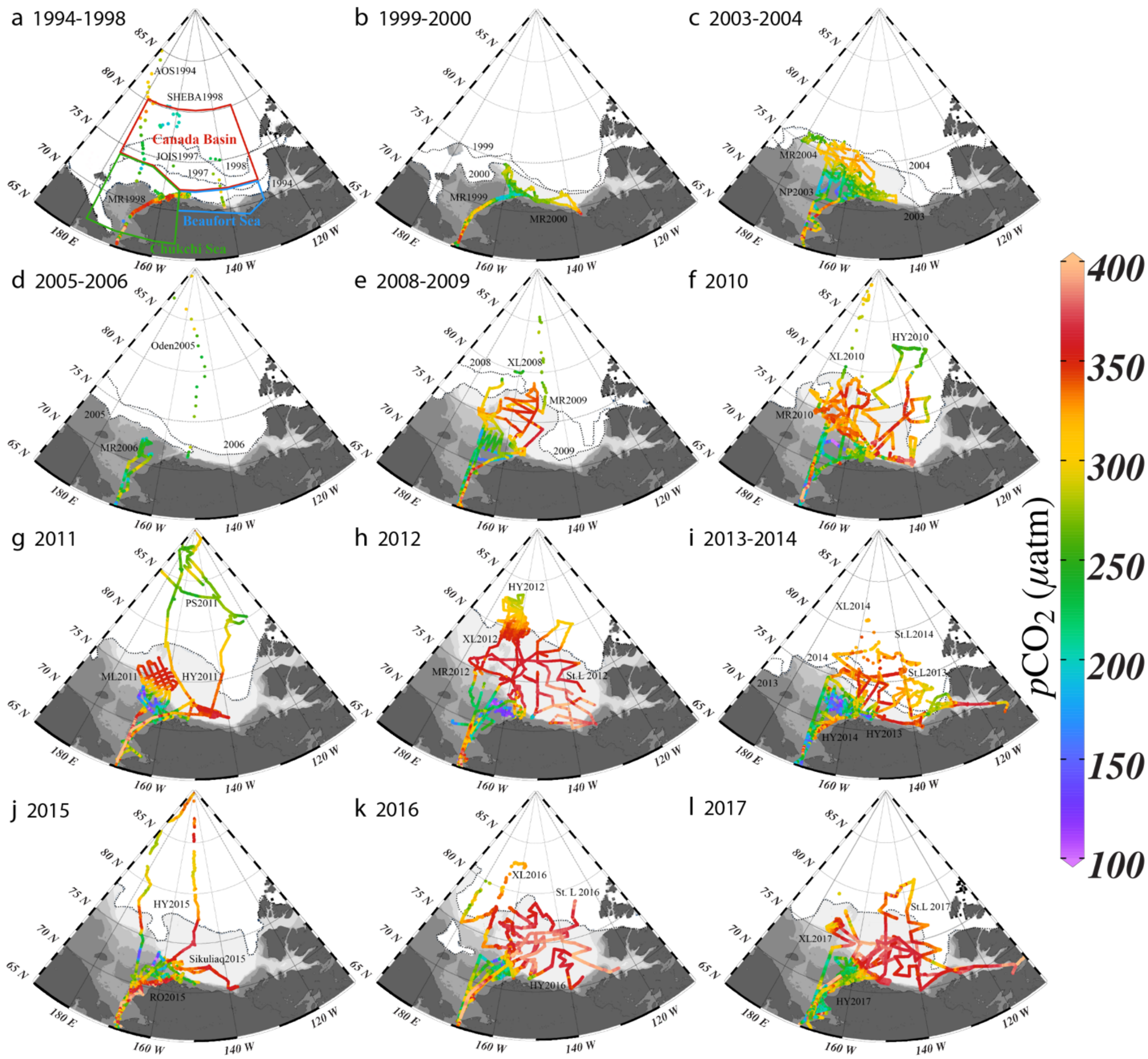

Figure 3.2: The distribution of sea surface pCO_2 at in situ temperature in the western Arctic Ocean. All pCO_2 data was measured by underway pCO_2 systems except datasets in AOS1994, JOIS 1997 and SHEBA 1998 cruises, which were calculated from discrete samples. MR, NP, ODEN, XL, ML, PS, HY, RO, St. L, and Sikuliaq stand for the Research Vessel Mirai, Nathaniel B. Palmer, ODEN, Xuelong, Marcus G. Langseth, Polarstern, Healy, Ronald H. Brown, Louis S. St-Laurent, and Sikuliaq, respectively. A list of cruise information is provided in Supplementary Table 3.1. The white areas indicate monthly sea ice extent (ice concentration >15%) in September which has the minimal sea ice extent (Nation Snow and Ice Data Center, http://nsidc.org/data/seaice_index/).

Because of the observed spatial heterogeneity, we examined the long-term rate of pCO_2 change separately for the Chukchi Shelf, the Beaufort Sea and the mostly ice-free Canada Basin (south of 80º N), as well as the mostly ice-covered high latitudes (north of 80ºN) (Figure 3.1). We first investigated the temporal and spatial coverages of observed pCO_2 data (Figure 3.3) as well as the possible change in pCO_2 seasonality (Figure. 3.4 a-h), and then examined the different timescales (daily, monthly and entire summer) and different grid sizes used for deriving mean values to estimate the long-term trends (Supplementary Table 2). Also, through careful comparisons between deseasonalized and non-deseasonalized analyses (Figure 3.4 i-l) and sensitivity tests, such as randomly removing 15% or 30% of the cruises or measurements (Supplementary Figures S3.1&S3.2), we chose to use non-deseasonalized measurements to derive gridded (0.1° latitude × 0.25° longitude) monthly pCO_2 for each subregion and then conducted linear regressions for the long-term trends (see Methods).

We find that sea surface pCO_2 increased substantially in the nearly ice-free Canada Basin south of 80°N at a rate of 4.6 ± 0.5 μatm yr^{-1} (Figure 3.5a), which is much faster than any other ocean basin (Takahashi et al., 2009; Takahashi et al., 2014; Bates et al., 2014), and more than two times the rate of atmospheric CO_2 increase (1.9 ± 0.1 μatm yr^{-1}). As a result, the summer averaged air-sea CO_2 gradient (ΔpCO_2) reduced from −100 to −50 μatm over the last two decades (Figures 3.5a & 3.6). If this trend continues, the ΔpCO_2 in the ice-free basin will shrink to near 0 μatm in the 2030s, suggesting that the surface water in the basin will not be as large of a CO_2 sink as previously predicted (Bates et al., 2006). In contrast, on the Chukchi Shelf, sea surface pCO_2 does not exhibit a statistically significant long-term trend (Figure 3.5b).

In the adjacent Beaufort Sea, the pCO_2 increased at a slightly lower rate than that in the Canada Basin (Figure 3.5 c). For most of the perenially ice-covered areas in the western Arctic Ocean north of 80°N, pCO_2 increased at a rate of only 1.8 ± 1.1 μatm yr^{-1}, which is statistically comparable to the rate of atmospheric CO_2 increase (Figure 3.5 d).

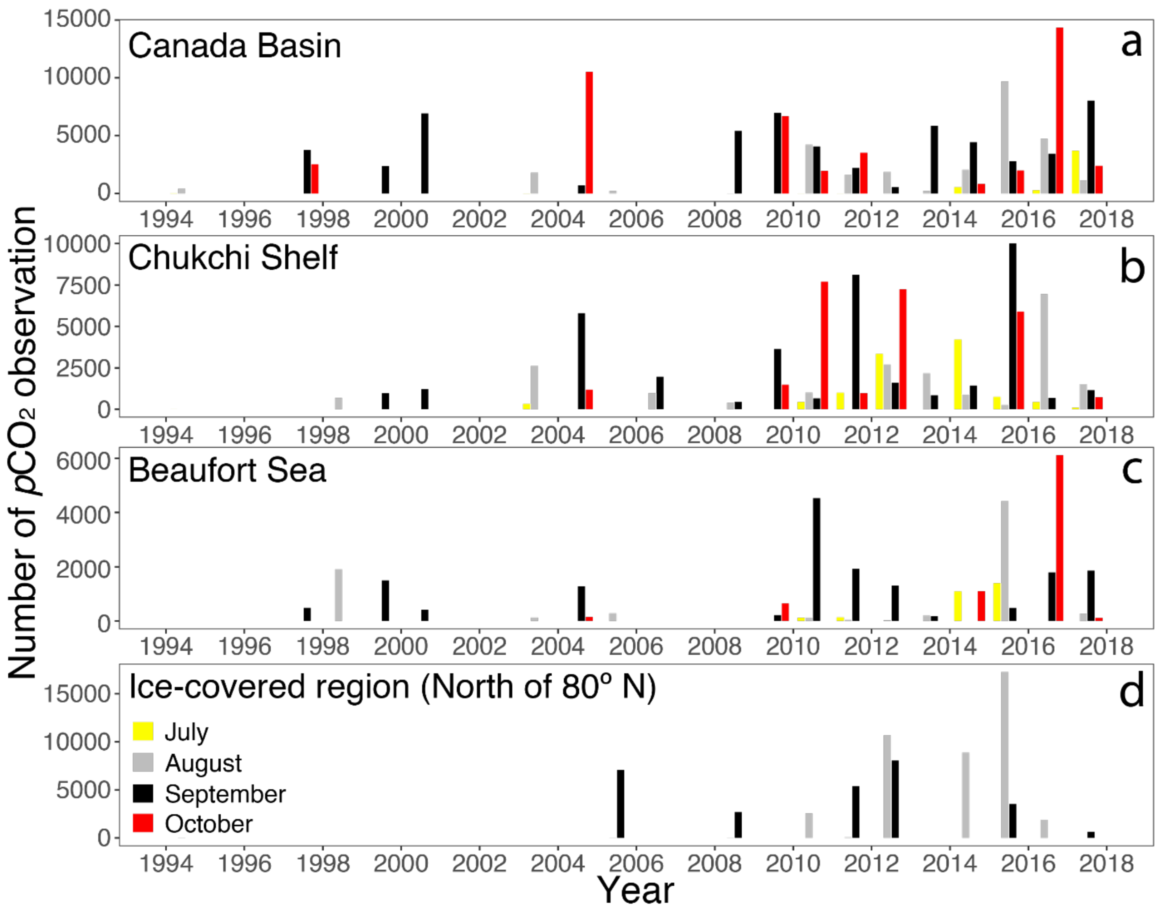

Figure 3.3: Monthly time series of the number of sea surface pCO_2 measurements in the western Arctic Ocean. (a) Canada Basin, (b) Chukchi Shelf, (c) Beaufort Sea, (d) Ice-covered region (north of 80ºN).

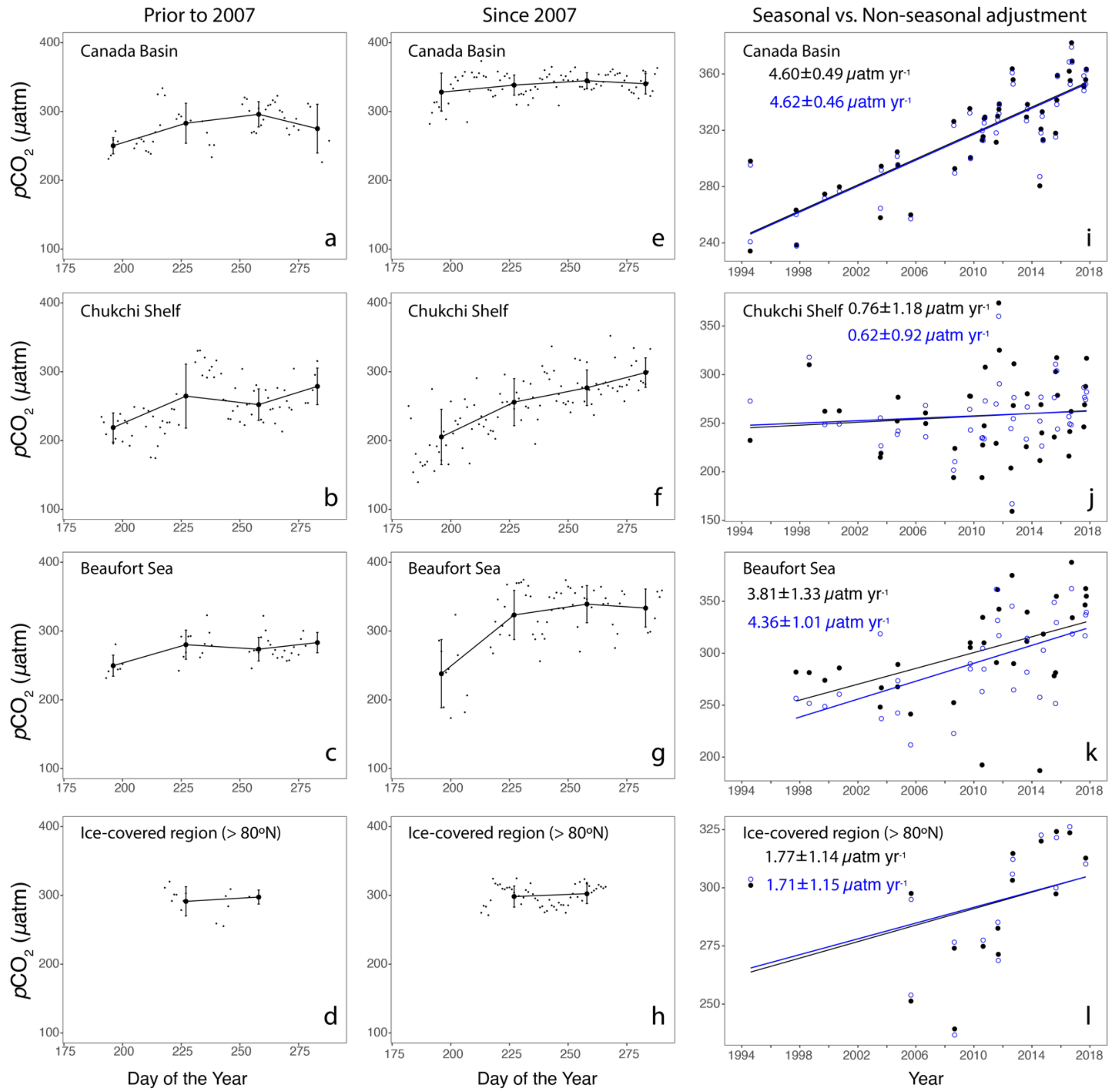

Figure 3.4: The change in the seasonality of pCO_2 and deseasonalized long-term trends. We examined the seasonal variation of pCO_2 by binning gridded (0.1° latitude × 0.25° longitude) values into Julian-Day for two periods: years prior to 2007 (a-d) and 2007 to 2017 (e-h). We deseasonalized data to calculate monthly means of pCO_2 following the method described in ref[16]. Briefly, we detrended pCO_2 data first and then adjusted the monthly means by adding or subducting the anomaly with respect to the long-term summer mean (averaged over 1994-2017), assuming that the seasonal variations remained unchanged over years. The black and blue dots represent non- and seasonal adjusted monthly means of pCO_2, respectively (i-l). The rates of change with standard error are noted.

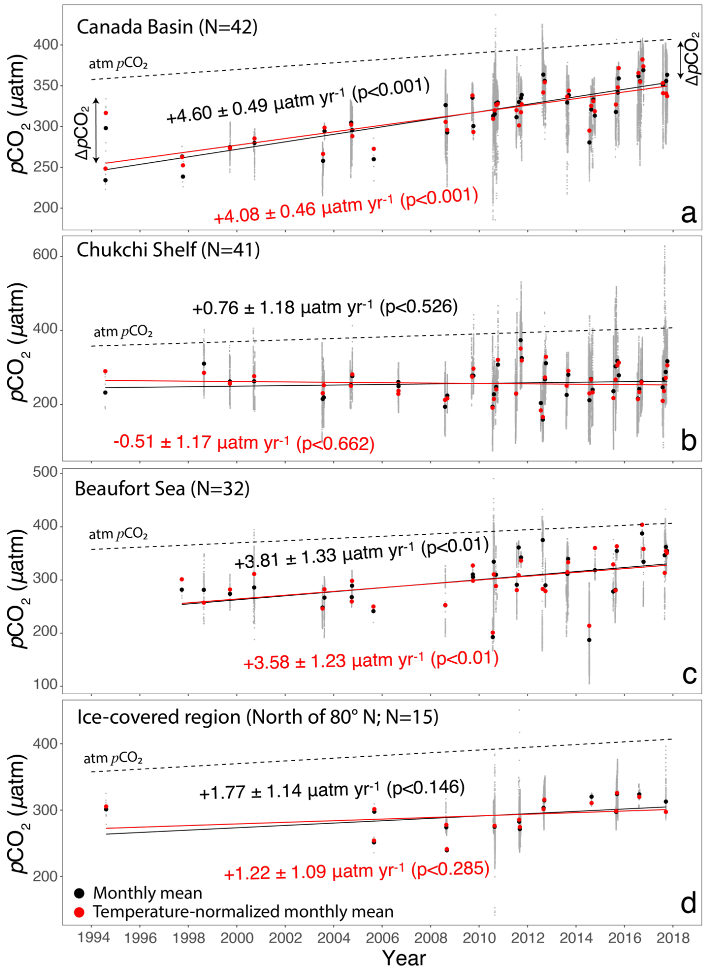

Figure 3.5: Decadal change trends of sea surface pCO_2 in the western Arctic Ocean. The grey dots represent the raw observations of pCO_2 in the Canada Bain (**a**), the Chukchi Shelf (**b**), the Beaufort Sea (**c**), and the high latitudes (north of 80°N) (**d**). The black and red dots indicate the monthly mean based on the gridded-average pCO_2 (0.1° latitude × 0.25° longitude) at in situ SST and the long-term means of SST, respectively. The rates of change with standard error are computed from monthly means. N is the number of monthly mean values used. The red lines represent the non-thermal component of the total pCO_2 trends (see Methods). The dashed lines represent the atmospheric CO_2 increasing at a mean rate of 1.9 μatm yr^{-1}. We tested whether the trends were significantly different from 0 using ANOVA and whether the trends were significantly different from the trend of atmospheric CO_2 using ANCOVA. Only the trend of sea surface pCO_2 observed in the Canada Basin is significantly different from the trend of atmospheric pCO_2 (~1.9 µatm yr^{-1}). The arrows in (a) indicate the statistically significant change in ΔpCO_2 (also see Figure 3.6)

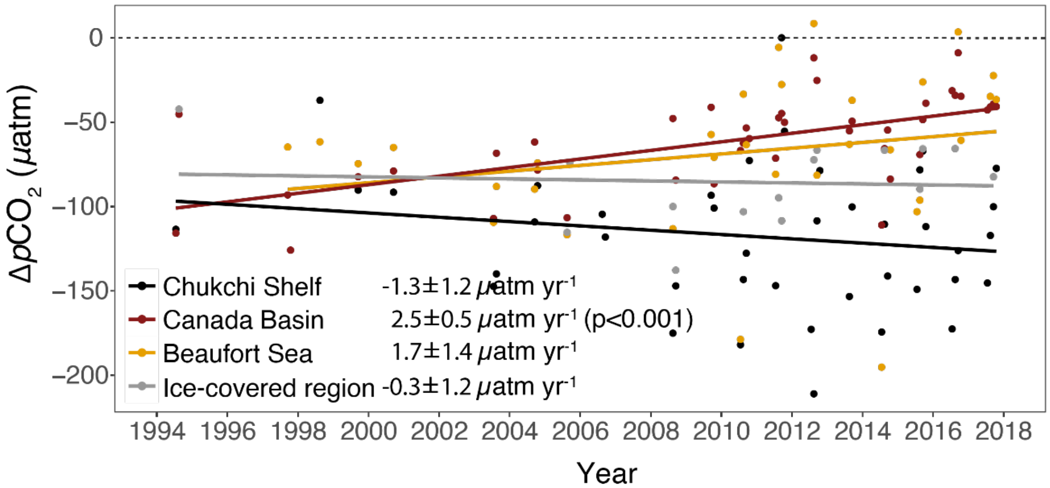

Figure 3.6 The trends of CO_2 air-sea gradient (ΔpCO_2). The summer ΔpCO_2 vary in the Chukchi Shelf, the Canada Basin, the Beaufort Sea and ice-covered region over the period of 1994 to 2017. The rates of change of ΔpCO_2 were computed with monthly mean values (positive rates indicate decrease in ΔpCO_2, while negative rates indicate increase in ΔpCO_2). The dashed line indicates a complete air-sea gas equilibrium. ANOVA was performed for all regressions. Only ΔpCO_2 in the Canada Basin shows a significant trend.

3.3.2 Pacific Water Influence and Control Mechanism

The contrasting long-term trends between the Chukchi Shelf and Canada Basin indicate different mechanisms controlling the spatial and temporal variations in the surface pCO_2 and air-sea CO_2 flux. For the western Arctic Ocean, one notable change over the past few decades has been that the annual Bering Strait throughflow has increased (Woodgate et al., 2012; Woodgate, 2018), bringing more nutrients onto the Chukchi Shelf which enhances primary production (Arrigo et al., 2015; Hill et al., 2018). The inflow of this nutrient-rich Pacific Summer Water, which is slowed down in the areas south of the Chukchi shelfbreak with a residence time of ~90 days

(Stabeno et al., 2018), facilitates high biological productivity and the persistence of low pCO_2 and a large ocean CO_2 sink on the central and northern Chukchi Shelf (Grebmeier et al., 2015).

As the Pacific water flows poleward over the shelfbreak into the Canada Basin, most of it subducts into the subsurface regime (Timmermans et al., 2014; Spall et al., 2018) because its density is greater than the surface waters in the southern Canada Basin and the Beaufort Sea slope (Figure 3.7). This mechanism accounts for the observed dramatic transition from low pCO_2 on the shelf to high pCO_2 in the surface waters of the basin and slope within a very narrow front along the shelfbreak (over 200-250 m isobath, 72-74°N, Figures 3.1 & 3.2). This transition could be intensified by the strengthened summer easterly winds and currents which favor east-west flows rather than across shelfbreak transport (Brugler et al., 2014; Figure 3.7). On the other hand, accelerated sea ice loss leads to a larger ice-free area in the Canada Basin. As the barrier to air-sea CO_2 exchange has been removed, the atmospheric CO_2 could invade surface water rapidly and, because of lack of vertical mixing, push sea surface pCO_2 towards atmospheric level within ~two months (Cai et al., 2010; Else et al., 2013; Figure 3.7 b). This process substantially reduces the air-sea CO_2 gradient and acts as a new sea-surface barrier inhibiting further CO_2 uptake later in the season. In addition, the spin-up of anti-cyclonic flow in the Beaufort Gyre in the last two decades has resulted in a fresher and shallower surface mixed layer in the Canada Basin (Giles et al., 2012; Peralta-Ferriz and Woodgate, 2015). In turn, the accumulation of freshwater strengthens the stratification at the base of the surface mixed layer and minimizes vertical mixing. As a consequence, the nutrient-enriched subsurface water from the Chukchi Shelf cannot play a direct role in reducing the basin surface pCO_2

(Coupel et al., 2015; Nishino et al., 2011; Figure 3.7). Note that since the Beaufort Sea does not receive abundant nutrients from the Pacific Water, rather its nutrients mostly come from the Mackenzie River and upwelled waters from the basin subsurface (Mathis et al., 2012), its long-term variation of sea surface pCO_2 is different than that in the Chukchi Shelf and is more like that found in the Canada Basin except with larger seasonal and interannual variability (Figures 3.4 & 3.5).

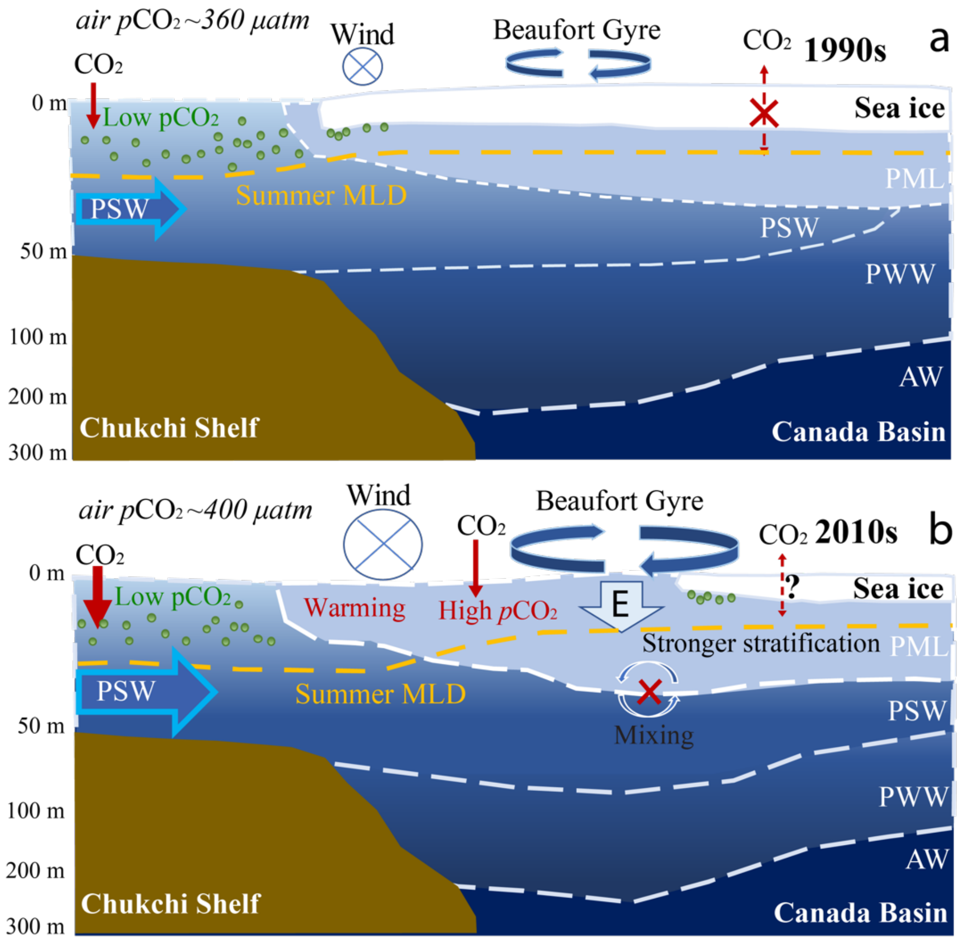

Figure 3.7: Schematic representation of recent environmental changes in the western Arctic during the ice-melt season. The changes in physical setting in the upper ocean along the Chukchi shelf to the Canada Basin in the 1990s (**a**) and 2010s (**b**). Over the past few decades, amplified warming in the polar region caused rapid sea ice retreat and changes in the circulation in the upper ocean. Increased Pacific Summer Water (PSW, blue arrows) flows through the Chukchi Shelf and subducts into the basin along the corresponding isopycnals. Stronger summer westward wind strengthens the Beaufort Gyre (oval arrows) in the Canada Basin, which results in a stronger Ekman pumping and convergence (indicated by the arrow, E). The upper water column was depressed and built up a stronger stratification due to the combination of the accumulation of surface ice melt water and the stronger Ekman pumping. The yellow dashed line indicates the summer mixed layer depth (MLD), which is shallowing from spring to summer and becomes shallower in the basin than that on the shelf. PML, PWW, and AW indicate Polar Mixed Layer, Pacific Winter Water and Atlantic Water, respectively.

3.3.3 Drivers and Contributions to *p*CO_2 Increase

To quantitatively evaluate how sea surface *p*CO_2 on the shelf and basin respond differently to environmental changes, we focused on the analysis of sea surface *p*CO_2 in the two most contrasting subregions: the Chukchi Shelf and Canada Basin. We started with a separation of the observed sea surface *p*CO_2 change into its thermal and non-thermal components, with the former driven by the long-term change in sea surface temperature (SST), and the latter driven by the long-term variations in all other factors including dissolved inorganic carbon (DIC), alkalinity (Alk) and a freshwater term measured by salinity change, following a well-established method (Takahashi et al., 1993; Takahashi et al., 2002; Lovenduski et al., 2007; Landschützer et al., 2018; see Methods). This separation showed that the thermal component induces a substantial higher increase in sea surface *p*CO_2 in the Chukchi Shelf (1.3±0.6 μatm yr^{-1}) and a moderate increase in the Canada Basin (0.6±0.3 μatm yr^{-1}; Table 3.1). However, the non-thermal component of *p*CO_2 leads to a substantial increase in the Canada Basin but not in the Chukchi Shelf (red lines in Figure 3.7; Table 3.1). Thus, the dominant mechanisms controlling *p*CO_2 in these two regions are different.

Given the fact that both warming and atmospheric CO_2 uptake are driving *p*CO_2 to rise, we suggest that biological CO_2 drawdown is responsible for counteracting any discernible long-term increase on the Chukchi Shelf. To examine this postulation further, we used a 1-D box model to investigate how net community production (NCP) affects the long-term *p*CO_2 trend (see Methods). We found that a high NCP (>10 mmol C m^{-2} d^{-1}) is essential for maintaining the low *p*CO_2 values on the shelf (Figure 3.14). The patchy and widely variable primary production (Grebmeier et al., 2015) is likely responsible for the observed high seasonal and interannual variabilities (Figure 3.7 b). Further, by moderately increasing NCP by

30% after 2006 in our simulation (see Methods) as suggested by satellite observations (Arrigo et al., 2015), the impacts of warming and CO_2 invasion from the atmosphere on increasing $p$$CO_2$ are nearly balanced, resulting in a relatively low $p$$CO_2$ value through the entire summer and no discernible long-term trend (Figure 3.8). If this summer pattern persists in the future and earlier ice-melt and longer growth periods for autotrophs occur as anticipated (Wang et al., 2018), we predict that the Chukchi Shelf will be a greater CO_2 sink as atmospheric CO_2 continues to increase.

Table **3.1:** **Estimated contributions to the long-term $p$$CO_2$ trend in the Chukchi Shelf and Canada Basin.**

	Chukchi Shelf	Canada Basin				
	Rates (μatm yr^{-1})	Rates (μatm yr^{-1})	Drivers	Driver rate of change	Change in Drivers (1994-2017)	Contribution to the long-term trends (μatm yr^{-1})
Thermal component	1.25±0.57*	0.57±0.26*	ΔSST[34]	0.05±0.03* °C yr^{-1}	1.15±0.69°C	0.68
Non-thermal component	-0.51±1.17	4.08±0.46***	ΔsDIC	2.56±1.24†* 2.28±1.17‡ µmol kg^{-1} yr^{-1}	58.9±28.52† 54.44±26.91‡ µmol kg^{-1}	6.13-6.89
			ΔSSS	- 0.10±0.02*** (-0.17±0.04)* ppt yr^{-1}	-2.30±0.46 (-3.91±0.92) ppt	-1.99 (-3.39)
Sum	0.74	4.65				4.82-5.58 (3.42-4.18)

The thermal component and non-thermal component were separated by normalizing observed $p$$CO_2$ to the long-term summer mean SST. The rates (± standard error) were estimated by linear regression using monthly means. The symbol "*" indicates the level of significance of the trends (***$p<0.001$, **$p<0.01$, *$p<0.05$). † and ‡ indicate the change rate in sDIC normalized by using a zero concentration and a non-zero concentration freshwater endmembers, respectively. The numbers in the brackets indicate the results derived from a larger decrease in salinity (see Methods). ppt stands for parts per thousand, which measures salt content in seawater.

By considering the changes in the thermodynamics of the CO_2 system in the surface seawater, we can also quantify the drivers for the pCO_2 trend in the Canada Basin (see Methods). The sea surface warming rate of 0.05 ℃ yr^{-1} over 1982-2015 (Timmermans et al., 2015) directly results in an increase in sea surface pCO_2 by 0.7 μatm yr^{-1} in the Canada Basin, which corroborates the contribution of the thermal component of 0.6 μatm yr^{-1} derived from the observations (Table 3.1). Then, the non-thermal component can be decomposed into two drivers. The first driver is associated with the long-term increase in surface DIC. The second driver is associated with the long-term increase in freshwater input due to sea ice melt, which not only dilutes the surface salinity, but also affects the carbonate chemistry (see Methods).

Our decomposition reveals that the net increase in DIC in the surface Canada Basin could lead to an increase of pCO_2 of 6.1-6.9 μatm yr^{-1}, while freshwater input lowers the increase rate by -2.0 to -3.4 μatm yr^{-1} (last column in Table 3.1). As a net result, the non-thermal component increases pCO_2 by 2.7-4.9 μatm yr^{-1}, which contributes about 80% to 88% of the total pCO_2 long-term trend in the Canada Basin (Table 3.1).

While the non-thermal component explains most of the trend, it is still unclear which mechanism mainly drives the long-term DIC increase. The most likely one is sea ice loss induced natural and anthropogenic CO_2 uptake. We used a 1-D box model to simulate seasonal pCO_2 evolution associated with the changing ice concentration (ice%) and estimate the change in salinity normalized DIC (see Methods). Our simulation suggests that loss of summer sea ice in the Canada Basin has accelerated atmospheric CO_2 uptake (Figure 3.8 c), leading to a net increase in DIC in the surface ocean by 2.5 ± 0.2 μmol kg^{-1} yr^{-1} (Figure 3.8 d), which corroborates with the observed rates of 2.3-2.6 μmol kg^{-1} yr^{-1} (Figure 3.9 b&e). This agreement supports our proposed mechanism that increased air-sea CO_2 uptake due to sea ice loss is primarily responsible for net DIC increase, and hence most of the observed long-term sea surface pCO_2 rise. Although more accurate estimates may be obtained with improved models and increased observations, it would not significantly change our mechanistic understanding.

The simulated pCO_2 implies that the decline in ice% in the Canada Basin not only promotes CO_2 uptake but also results in an amplification of pCO_2 seasonal variability (Figure 3.8 c), particularly when combined with seasonal SST forcing. This synergistic effect resulting from warming, ice melt dilution, and atmospheric CO_2 uptake on seawater pCO_2 is illustrated in Figure 3.10. As summer ice% rapidly decreased over the 1990s-2010s, the seasonal SST amplitude increased due to the positive albedo-warming feedback (Steele et al., 2016; Perovich et al., 2012). Expanded open water area promoted CO_2 uptake and diluted seawater, with a lower initial pCO_2, allowed a larger DIC increase (Figure 3.10). We suggest that this rapid DIC increase in diluted water would lead to a rapid increase of the dissolved CO_2 fraction in DIC, an increase in DIC/TA ratio and a decrease in acid-base buffer capacity (Figure 3.11). In turn, the lower buffer capacity water has a larger and disproportionate pCO_2 increase responding to any further DIC perturbation. Together, these processes lead to a larger summer pCO_2 variation and a faster long-term summertime pCO_2 trend (Figure 3.10).

Arctic Ocean sea ice loss, a critical consequence of climate change associated with a fresher and isolated surface mixed layer, serves as an amplifier for seasonal variation and decadal increase of pCO_2 in the Canada Basin. In contrast to thermal and biophysical effects that dominate the pCO_2 seasonal cycles in the low and mid-latitudes, subarctic seas, and most of the Southern Ocean (Takahashi et al., 2009; Takahashi et al., 2014; Takahashi et al., 1993; Landschützer et al., 2018), the sea ice melt cycle in the Arctic Ocean operates as a unique mechanism, and magnifies changes in pCO_2 over seasonal to decadal scales. The accelerated sea ice loss anticipated in the near future (Wang et al., 2018) will increase seasonal variations of sea surface pCO_2, decrease the CO_2 sink in the Canada Basin and increase it on the Chukchi Shelf, and increase the long-term ocean acidification rates in the Arctic Ocean, which may profoundly affect carbon cycle, biogeochemical dynamics and ecosystem functions.

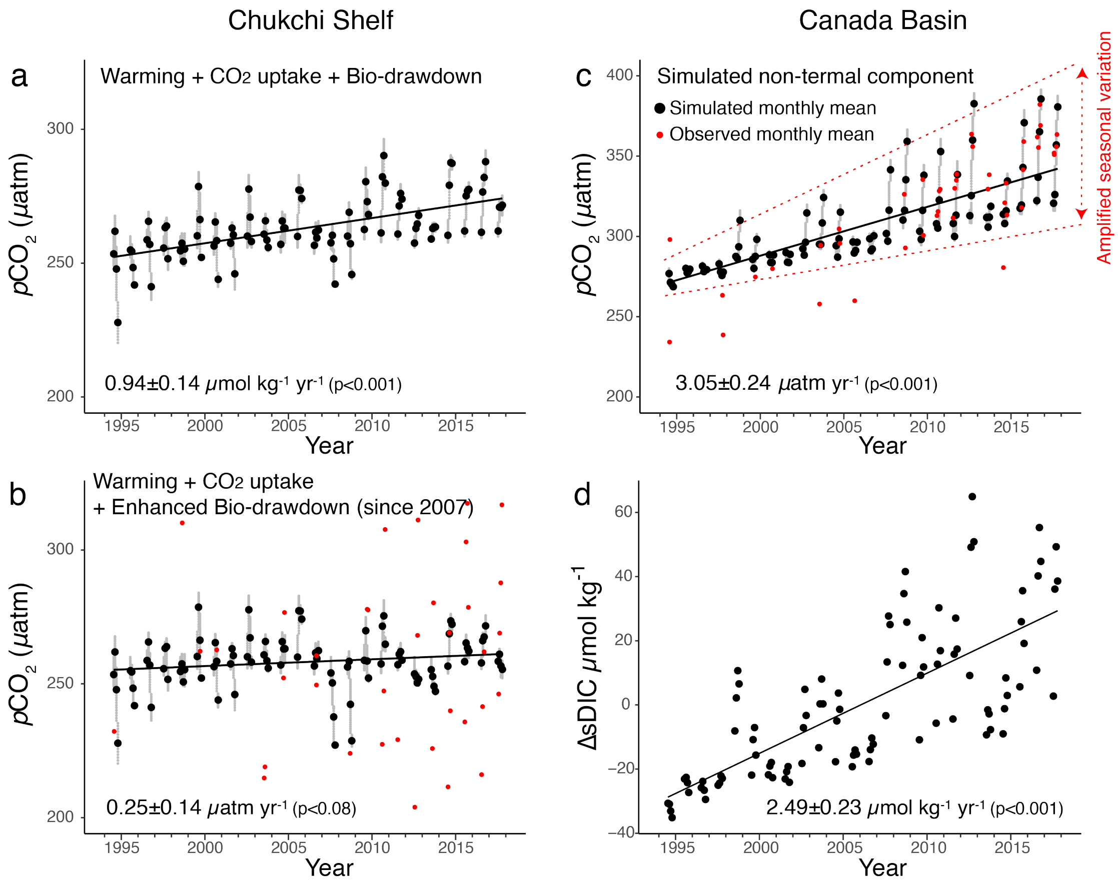

Figure 3.8: Simulation of sea surface pCO_2 in the Chukchi Shelf and Canada Basin. Simulated summer (July 1st-October 15th) pCO_2 on the Chukchi Shelf is driven by warming, CO_2 uptake, and biological CO_2 drawdown (**a**), and driven by warming, CO_2 uptake, and increased biological CO_2 drawdown (**b**). We applied an increased net community production (NCP) of 30%[ref 8] since 2007 (see Methods for simulation conditions). (**c**) The simulated pCO_2 in the Canada Basin is mainly driven by CO_2 uptake from atmosphere CO_2 associated with sea ice melting processes. To only examine the non-thermal component effect, we used a long-term mean of SST and kept the weak biological CO_2 drawdown rate constant (see Methods for simulation conditions). Grey dots represent the simulated daily pCO_2. The rates of change (with ± standard error) were computed using monthly means (black dots). (**d**) The change in salinity normalized DIC anomaly (ΔsDIC) with respect to the long-term mean of sDIC. ANOVA was performed to test whether the slopes are significantly different from 0.

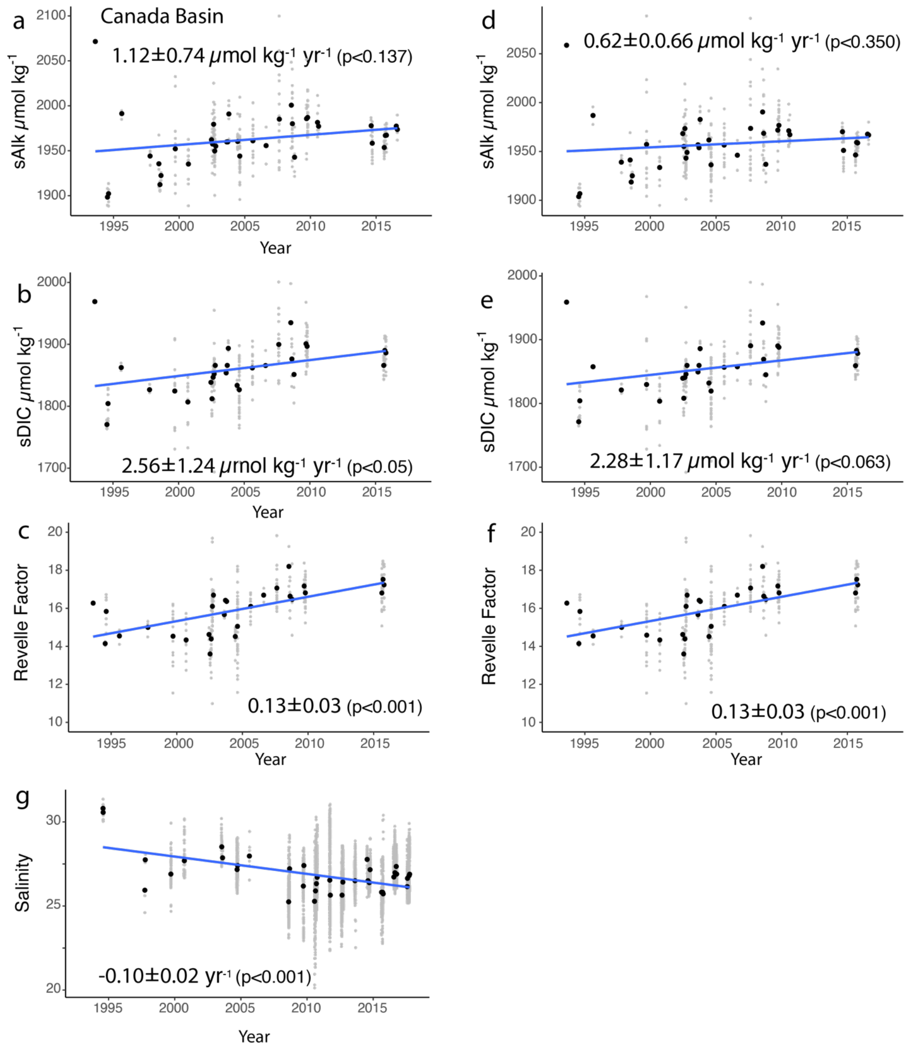

Figure 3.9: The long-term trends of sea surface sAlk, sDIC, Salinity, and Revelle Factor in the Canada Basin. The discrete samples of sea surface (depth <20 m) Alk and DIC were obtained from the Global Data Analysis Project version 2 database (grey dots). We calculated salinity normalized DIC (sDIC=DIC×S_0/SSS) and Alk (sAlk=Alk×S_0/SSS) and then averaged the data to calculate monthly means (black dots) for the linear regressions (a and b). The S_0 is the reference salinity, i.e. the long-term mean of SSS. We also conducted a non-zero endmember salinity normalization for DIC and Alk (d and e; see Methods). The corresponding Revelle Factor were calculated in CO2SYS program (c and f). The underway measurement of salinity was used for examining the long-term trend (g). We tested whether the slope significantly different from 0 by ANOVA. The rates of change with standard error are shown.

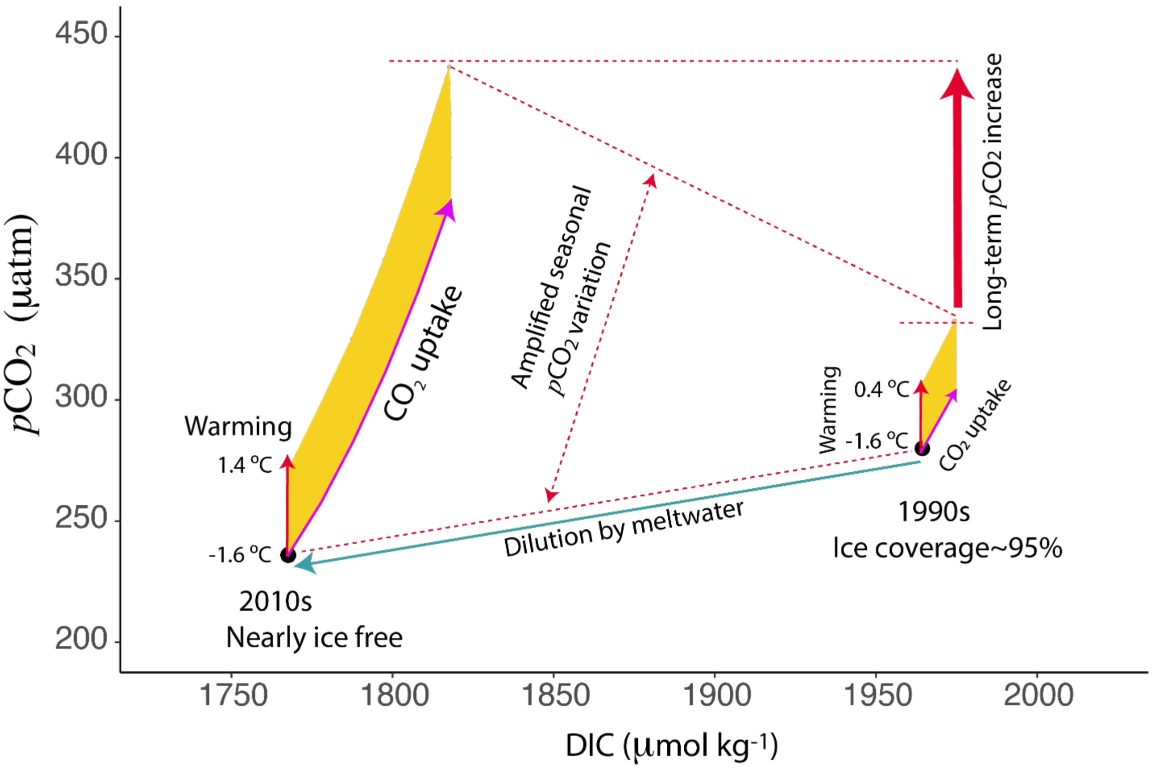

Figure 3.10: Sea ice-loss amplifying surface water pCO_2 in the Canada Basin. Black dots represent the initial condition for pCO_2 and DIC at -1.6 °C. The arrows indicate the processes of warming (red), CO_2 uptake from the atmosphere (purple), dilution by ice meltwater (cyan). Sea ice reduction from 95% to ice-free is accompanied by a salinity decrease of 3.5 (Table 3.5). The yellow shaded areas indicate the possible seasonal variations of pCO_2, which are amplified by the synergistic effect of ice melt, warming and CO_2 uptake. To examine the change of pCO_2, we allowed 2 °C and 3 °C warming, and 10 and 50 μmol kg^{-1} DIC perturbations due to air-sea CO_2 exchange in the 1990s and 2010s, respectively, which are consistent with the long-term warming rate of 0.5 °C per decade and the estimated increase in sDIC by 2.3-2.6 µmol kg^{-1} per year (Table 3.1 and Figure 3.8 d).

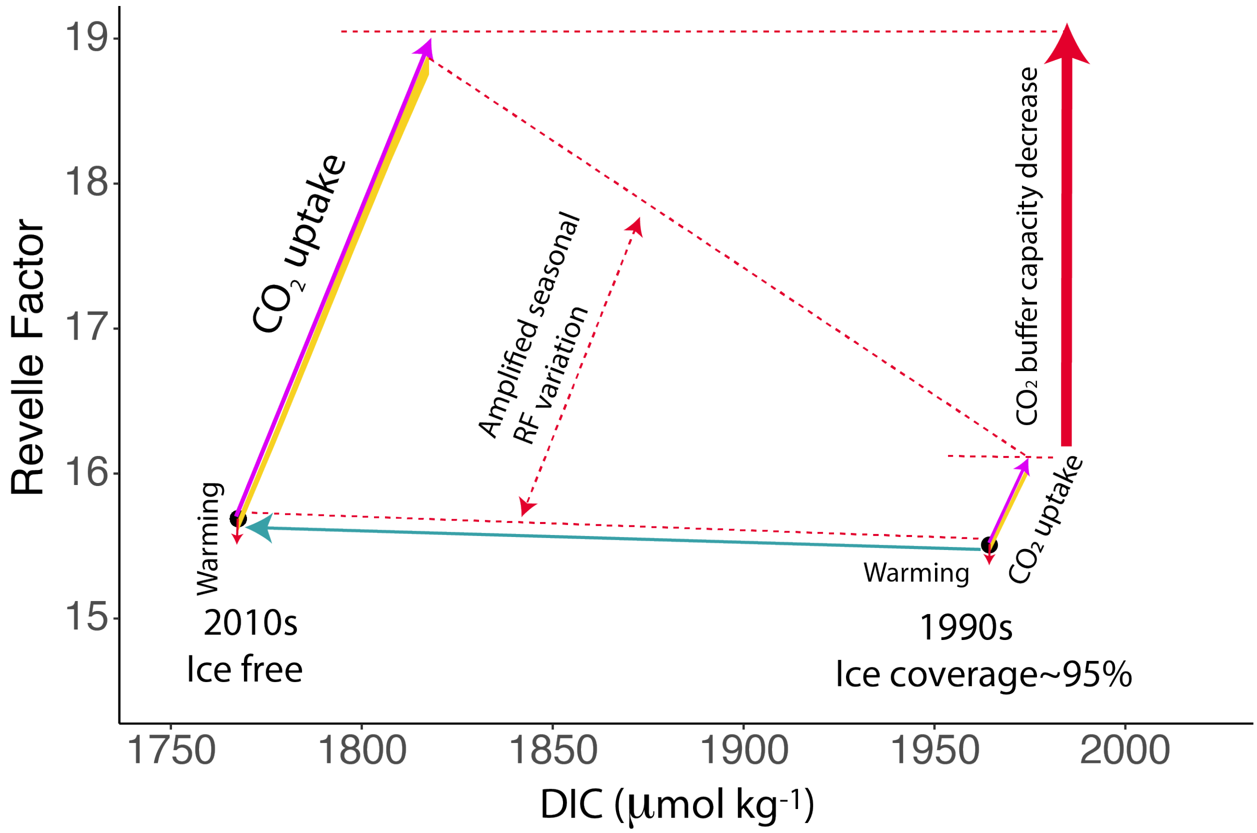

Figure 3.11: Sea ice-loss amplifying the decrease in surface water Revelle Factor (RF) in the Canada Basin. Black dots represent the initial condition for RF and DIC at -1.6 °C. The arrows indicate the processes of warming (red), CO_2 uptake from the atmosphere (purple), dilution by ice meltwater (cyan). Sea ice reduction from 95% to ice-free is accompanied by a salinity decrease of 3.5 (Table 3.5). The yellow shaded areas indicate the possible seasonal variations of RF, which are amplified by the synergistic effect of ice melt, warming and CO_2 uptake. To estimate the change of RF, we allowed 2 °C and 3 °C warming, and 10 and 50 μmol kg^{-1} DIC perturbations due to air-sea CO_2 exchange in 1990s and 2010s, respectively, which are consistent with the long-term warming rate of 0.5 °C per decade and the estimated increase in sDIC by 2.3-2.6 µmol kg^{-1} per year (Table 3.1 and Figure 3.8 d). Note that higher RF indicates lower acid-base buffer capacity.

3.4 Methods

3.4.1 The synthesis of pCO_2 dataset

To examine decadal changes in surface pCO_2 and estimate the summer carbon uptake in the western Arctic Ocean, we compiled a dataset of pCO_2 measurements via multiple international databases (Supplementary Table 1), including Surface Ocean CO_2 Atlas (SOCAT v5, http://www.socat.info; Bakker et al., 2016), Japan Agency for Marine-Earth Science and Technology (JAMSTEC, https://www.jamstec.go.jp/e/), Carbon Dioxide Information Analysis Center (CDIAC, https://cdiac.ess-dive.lbl.gov), USGS database (https://pubs.er.usgs.gov), LDEO Database Version 2017 (https://www.nodc.noaa.gov/ocads/data/0160492.xml; Takahashi et al., 2018), NSF Arctic Data Center (https://arcticdata.io), and Chinese National Arctic and Antarctic Data Center (http://www.chinare.org.cn). This extensive dataset contains more than 358,000 sea surface pCO_2 data points and associated sea surface temperature (SST) and sea surface salinity (SSS) data. All data are archived in publicly accessible databases (Table 3.2), and the entire dataset is provided in the Supplementary information.

3.4.2 Underway sea surface pCO_2 data.

During 2008, 2010, 2012, 2014, 2016 and 2017 CHINARE (Chinese Arctic Research Expedition) cruises, the sea surface underway pCO_2 was measured with a nondispersive infrared analyzer of CO_2 in the equilibrated headspace gas by an underway CO_2 system (General Oceanic, USA). The system was monitored and calibrated with four certified gas standards every 3 hours, which could provide an overall precision of ± 2 μatm in pCO_2 measurement. The underway CO_2 system and data reduction procedure is described in Pierrot et al., (2009). Combined with the historical and recent measurements from multiple international programs, we only retained sea ice melting season data (July 1st – October 15th) for data synthesis. To keep the data consistency, we chose to report and analyze all the data as pCO_2, thus, the reported CO_2 fugacity (fCO_2) from some programs (Table 3.2) were converted to pCO_2 at SST using the equation (1) (Pierrot et al., 2009):

$$pCO_2 = fCO_2 \times (1.00436 - 4.669 \times 10^{-5} \times SST) \quad (3.1)$$

where SST is the sea surface temperature in degrees Celsius. Note that the difference between pCO_2 and fCO_2 conversion is less than measurement precision of ± 2 μatm, thus, the error induced by conversion is negligible.

3.4.3 Discrete sea surface pCO_2 data.

The pCO_2 datasets of AOS (1994), JOIS (1997), SHEBA (1998) and ODEN (2005) were calculated from the discrete dissolved inorganic carbon (DIC) and total alkalinity (Alk) samples taken in the surface mixed layer (<20 m). The DIC and Alk values were calibrated with deep water before the calculation (Qi et al., 2017). The pCO_2 was calculated by CO2SYS program (Pierrot et al., 2006) with recommended constants of Lueker et al. 2000 (Chen et al., 2015). The uncertainty of pCO_2 values computed from Alk and DIC is about ± 13 μatm with a mean systematic difference from the measured pCO_2 of -0.7 μatm (Woosley et al., 2017).

3.4.4 Sea surface pCO_2 trends assessment

Although the assembled dataset has extensive measurements, the temporal and spatial coverage of pCO_2 varies greatly with months and years. Before identifying the long-term trends of pCO_2, we first examined the temporal distribution of pCO_2 measurements for each subregion (Figure 3.3). We noticed that the amount of pCO_2 observation for each month could vary greatly among years depending on the number and timing of cruises, and sea ice conditions in a particular year. For example, the number of pCO_2 values substantially increased after 2007 (Figure 3.3). Thus, simple linear regressions with raw data could amplify the sampling bias due to an uneven spread of seasonal pCO_2 measurements. Despite the statistically significant p-value, raw data is not a good candidate for the assessment of long-term trends (Table 3.3). One way to reduce this bias is to average pCO_2 measurements into a specific temporal interval (i.e. daily, monthly, summer means), and then examine the long-term trends with these temporal-averaged values. We found that the rates derived from the summer means (includes all data measured in July 1st – October 15th) are much lower than that from daily and monthly means, which indicates that simply averaging pCO_2 measurements into a summer mean may not be a good approach due to losing too much seasonal information. Instead, the rates derived from daily and monthly means tend to be close to each other (Table 3.3).

Another issue for pCO_2 observation is spatially unevenly distributed sampling, which may induce bias from the over-weighted impact of highly dense data points concentrated within a small area. To deal with this issue, we averaged all data points into given grids. We examined different grid sizes (0.1° latitude × 0.25° longitude or 0.25° latitude × 0.5° longitude) for averaging into a daily mean, a monthly mean and a summer mean (Table 3.3). The two grid sizes we applied led to consistent pCO_2 trends in all subregions. Here, we choose to report long-term pCO_2 trend with gridded-averaged (0.1° latitude × 0.25° longitude) monthly means. By doing this, we not only reduce sampling bias in spatial coverage but also retain more temporal information, considering the scarcity of pCO_2 measurement in the Arctic Ocean. We test whether the trends are significantly different from 0 using ANOVA.

We further examined the seasonality of the pCO_2 by plotting pCO_2 on Julian days for each subregion (Figure 3.4 a-h). We noticed that, unlike relatively static year-by-year seasonality in low and temperate latitude oceans (Takahashi et al., 2009; Landschützer et al., 2018), the seasonality of pCO_2 in the Arctic Ocean is susceptible to perturbations of sea ice melting cycle which may vary greatly among years. This unique seasonal driver could result in the shift in pCO_2 seasonality as the ice-free area has extended into the Canada Basin since 2007. We demonstrated the possible change in the pCO_2 seasonality in different subregions by examining the seasonal evolution of pCO_2 in two periods (i.e., before and after 2007; Figure 3.4). Clearly, except for the ice-covered area (north of 80ºN), the seasonality of pCO_2 in most of our study area has changed in both magnitude and amplitude. Bearing this in mind, we carefully compared the deseasonalized trends with the non-deseasonalized results (Figure 3.4 i-l) assuming the climatological mean seasonality remained unchanged over this period using the method described in Takahashi et al., (2009). Although we found the long-term trend of pCO_2 increased after seasonal adjustment in the Beaufort Sea, the deseasonalized trends in other subregions were within uncertainties of the presented trends. In addition, we were concerned that deseasonalization of pCO_2 in the Arctic Ocean may induce extra bias as the current synthesized pCO_2 data with limited seasonal coverage cannot reflect a completed and solid seasonal cycle. Therefore, we reported pCO_2 trends without deseasonalization here.

To examine whether the observed pCO_2 trends are significantly different from the atmospheric CO_2 trend, we conducted an analysis of covariance (ANCOVA) for each subregion. Only the trend of sea surface pCO_2 observed in the Canada Basin was found significantly different from the trend of atmospheric CO_2, which supports our finding that summer sea surface pCO_2 trend in the Canada Basin is significantly higher than that of the atmospheric CO_2.

3.4.5 Uncertainty analysis of the long-term trends

As we mentioned above, the current synthesized pCO_2 dataset is inhomogeneously distributed over time and space, which mainly contributes to the uncertainty of the reported trends in sea surface pCO_2. The uncertainty is also closely associated with the account of measurements used for deriving the long-term trend in each subregion.

To quantify the uncertainty for the pCO_2 trends, we conducted a sensitivity test by randomly removing 15% cruises or 15% measurements from the raw dataset and gridded the data by grid size of 0.1° latitude × 0.25° longitude for averaging monthly means for every year, and then re-examined the slope of regression. By repeating this process 100 times, we found that both approaches gave similar results (Figure 3.12), but the derived pCO_2 trends were more sensitive to the removal of cruises than the removal of part of data points. We also noticed that the regional-varying sensitivities depend on the total number of cruises or data points. For example, the ice-covered region with the least number of cruises and measurements was the most sensitive area to respond to any change in this unevenly sampled dataset than the other three subregions (Figure 3.12). We further ran a second test by randomly removing 30% cruises or measurements (Figure 3.13). It gave the similar trends as in the case of 15%

removal but with larger standard deviations. This indicated that adding or removing parts of measurements only slightly increased the uncertainty but did not significantly change the trends. Here, we reported the uncertainty of the long-term pCO_2 trends with the standard deviation of the mean of 100 slopes (Supplementary Figures S3.1 & S3.2). For the Canada Basin and the Beaufort Sea, the relative uncertainty (standard deviation/mean) of pCO_2 is less than 8% and 15%, respectively, whereas the uncertainty could reach as high as 65%-75% in the Chukchi Shelf and ice-covered region.

3.4.6 Separation of the thermal and non-thermal components

We separate the observation-based pCO_2 into the thermal component, which is driven by the seasonal and long-term variation in SST, and non-thermal components, which is driven by the seasonal and long-term variation in all other factors, including DIC, TA, and salinity. To calculate the thermal component, we first calculated the summer mean of pCO_2, $< pCO_2>_{summer}$, with gridded data for each year, and then perturbed $< pCO_2>_{summer}$ with the SST differences between the observed SST and the 23-year long-term mean SST, <SST>, and the temperature sensitivity of CO_2 (γ_T) of 4.23%/℃ (Takahashi et al., 1993), as follows:

$$pCO_{2\ thermal} = <pCO_2>_{summer} \times \exp(\gamma_T \times (SST - <SST>)) \tag{3.2}$$

The non-thermal component was calculated by normalizing observed pCO_2 to the long-term summer mean SST, <SST>, to remove the temperature effect (Takahashi et al., 2002), as follows:

$$pCO_{2\,\text{non-thermal}} = pCO_2 \times \exp(\gamma_T \times (\langle SST \rangle - SST)) \tag{3.3}$$

The two components of observed pCO_2 are listed in Table 3.1.

3.4.7 Drivers of the long-term pCO_2 trends

To determine the potential drivers for long-term trends in observed pCO_2 in the Arctic Ocean, we decomposed the variation of pCO_2 into multiple components, i.e. SST, SSS, dissolved inorganic carbon (DIC) and total alkalinity (Alk). Therefore, the change in pCO_2, $\mathrm{d}pCO_2$, could be expressed as,

$$\mathrm{d}pCO_2 = \frac{\partial pCO_2}{\partial SST} \times \mathrm{dSST} + \frac{\partial pCO_2}{\partial DIC} \times \mathrm{dDIC} + \frac{\partial pCO_2}{\partial Alk} \times \mathrm{dAlk} + \frac{\partial pCO_2}{\partial SSS} \times \mathrm{dSSS} \tag{3.4}$$

where the ‘d’ indicates the deviation of the property from the respective norm. As freshwater fluxes (d*fw*) can also induce changes in DIC and Alk, it is often useful and convenient to separate the influence of freshwater flux from other biogeochemical processes by calculating salinity normalized DIC and Alk. We used salinity normalized DIC ($\mathrm{sDIC}=\mathrm{DIC}\times S_0/\mathrm{SSS}$) and Alk ($\mathrm{sAlk}=\mathrm{Alk}\times S_0/\mathrm{SSS}$) to substitute the terms in Eq. (3.4) and combined all terms affected by freshwater fluxes into one (Takahashi et al., 1993; Lovenduski et al., 2007; Landschützer et al., 2018). The SSS and S_0 represent the observed and reference salinity. Here, S_0 is taken as summer mean salinity. This gives,

$$dpCO_2 = \frac{\partial pCO_2}{\partial SST} \times dSST + \frac{\partial pCO_2}{\partial DIC} \times SSS/S_0 \times dsDIC + \frac{\partial pCO_2}{\partial Alk} \times SSS/S_0 \times dsAlk + \frac{\partial pCO_2}{\partial fw} \times dfw \quad (3.5)$$

$$\frac{\partial pCO_2}{\partial fw} \times dfw = \left(\frac{sDIC}{S_0}\frac{\partial pCO_2}{\partial DIC} + \frac{sAlk}{S_0}\frac{\partial pCO_2}{\partial Alk} + \frac{SSS}{S_0}\frac{\partial pCO_2}{\partial SSS}\right) \times dSSS \quad (3.6)$$

We estimated the regional mean values of the partial derivatives of pCO_2 with the following approximating equations, expressed as the pCO_2 sensitivities, γ, with regard to respective drivers[44] (i.e., γ_{DIC} and γ_{Alk} are the Revelle factor for DIC and TA, respectively, and γ_{SSS} is the salinity sensitivity of pCO_2.),

$$\frac{\partial pCO_2}{\partial DIC} = \frac{pCO_2}{DIC} \times \gamma_{DIC} \quad (3.7)$$

$$\frac{\partial pCO_2}{\partial Alk} = \frac{pCO_2}{Alk} \times \gamma_{Alk} \quad (3.8)$$

$$\frac{\partial pCO_2}{\partial SSS} = \frac{pCO_2}{SSS} \times \gamma_{SSS} \quad (3.9)$$

By substituting Eq. (3.7)- Eq. (3.9) into Eq (3.6), it gives

$$\frac{\partial pCO_2}{\partial fw} \times dfw = \frac{pCO_2}{S_0} (\gamma_{DIC} + \gamma_{Alk} + \gamma_{SSS}) \times dSSS \quad (3.10)$$

As we are considering deviations from the summer mean, SSS/S_0 in (5) and (6) approximates to 1 and can be dropped. With this simplification, we replaced 'd' with the long-term change of summer pCO_2, $\Delta^{LT}pCO_2$,

$$\Delta^{LT} pCO_2 = \Delta^{LT} pCO_{2\ \text{thermal}} + \Delta^{LT} pCO_{2\ \text{non-thermal}}$$

$$=(\gamma_T \times \Delta^{LT} SST \times pCO_2) + (\gamma_{DIC} \times \frac{pCO_2}{DIC} \times \Delta^{LT} sDIC) + (\gamma_{Alk} \times \frac{pCO_2}{Alk} \times \Delta^{LT} sAlk) + ((\gamma_{DIC} + \gamma_{Alk} + \gamma_{SSS}) \times \frac{pCO_2}{S_0} \times \Delta^{LT} SSS) \quad (3.11)$$

Equation (3.11) represents the long-term change in pCO_2 and is driven by two components: the thermal component (the first term of the right-hand side) and non-component (the remaining three terms). The above-outlined approach has been used extensively in analyzing key processes controlling surface pCO_2 variations in the global ocean and various ocean regions (Takahashi et al., 1993; Lovenduski et al.,2007; Landschützer et al., 2018; Sarmiento and Gruber, 2006).

For further analysis, we focused on quantifying the contribution of each component to the long-term pCO_2 trend in the Canada Basin. We started by examining the long-term changes in sDIC, sAlk and SSS in our study regions with the discrete DIC, Alk samples and underway measurement of SSS during multiple cruises over 1994-2016. The discrete DIC and Alk data were obtained from the Global Data Analysis Project version 2 database 2019 (GLODAP v2.2019; Olsen et al., 2019).

Considering that DIC and Alk in the sea ice also affect surface DIC and Alk when ice melts, the salinity normalization widely used in the open ocean (described above) may not reflect the reality in the meltwater-influenced Arctic surface water. Therefore, we conducted a non-zero endmembers salinity normalization (Friis et al., 2003) for DIC and alkalinity as well to justify the potential drivers and their contributions to long-term pCO_2 change. Simply, DIC and Alk were normalized to a reference salinity (S_0) using a non-zero freshwater endmember as follows (Friis et al., 2003),

$$\mathrm{sDIC} = \frac{DIC - DIC_{salinity=0}}{SSS} \times \mathrm{S_0} + DIC_{salinity=0} \tag{3.12}$$

$$\mathrm{sAlk} = \frac{Alk - Alk_{salinity=0}}{SSS} \times \mathrm{S_0} + Alk_{salinity=0} \tag{3.13}$$

Ice meltwater salinity, Alk and DIC values were set as 5 ppt, 450 µmol/kg, and 400 µmol/kg respectively (Rysgaard et al., 2007), which are equivalent to $DIC_{salinity=0}$= 60 µmol kg^{-1} and $Alk_{salinity=0}$ =104 µmol kg^{-1}.

Both salinity normalization approaches suggest that no trend was found in sAlk in the Canada Basin (Figure 3.9 a&d). Therefore, we dropped the sAlk term subsequently (which is the practice in literature (Landschützer et al., 2018)). Thus, the non-thermal part of the equation (3.11) reduces to drivers of sDIC and freshwater fluxes.

$$\Delta^{LT}\mathrm{pCO_2} = (\gamma_T \times \Delta^{LT}SST \times pCO_2) + (\gamma_{DIC} \times \frac{pCO_2}{DIC} \times \Delta^{LT}sDIC) + ((\gamma_{DIC} + \gamma_{Alk} + \gamma_{SSS}) \times \frac{pCO_2}{S_0} \times \Delta^{LT}SSS) \tag{3.14}$$

We next determined the temporal trends for each driver by deriving the temporal derivative of the long-term difference of $p\mathrm{CO_2}$. As we are examining the long-term trend of pCO$_2$, the terms of $\frac{pCO_2}{DIC}$ and $\frac{pCO_2}{S_0}$ are not changing with time (though they vary within a season), considered as constants, thus, it gives,

$$\frac{d\Delta^{LT}pCO_2}{dt} = (\ \gamma_T \times pCO_2 \times \frac{d\Delta^{LT}SST}{dt}) +$$

$$(\gamma_{DIC} \times \frac{pCO_2}{DIC} \times \frac{d\Delta^{LT}sDIC}{dt}) +$$

$$(\gamma_{DIC} + \gamma_{Alk} + \gamma_{SSS}) \times \frac{pCO_2}{S_0} \times \frac{d\Delta^{LT}SSS}{dt} \tag{3.15}$$

where γ_{DIC} is the long-term mean, calculated from discrete DIC and Alk using CO2SYS program (Pierrot et al., 2006), and $(\gamma_{DIC} + \gamma_{Alk} + \gamma_{SSS})$ is the total pCO$_2$ sensitivity for salinity variation, which was adopted as constant 1.7 here following the estimation for the high latitudes (Takahashi et al., 1993; Sarmiento and Gruber, 2006).

According to equation (3.15), the long-term trend of pCO$_2$ is attributable to three drivers. The first one is the long-term change in SST, which is primarily the result of increased absorption of solar radiation associated with sea ice loss[36]. The second one is the change in salinity normalized DIC, as a result of ocean circulation/mixing, biological activity, natural and anthropogenic CO_2 invasion. The third driver is the long-term changes in SSS, mainly due to ice-melt water dilution and river discharge input.

Here, we quantified the contribution of each component to the long-term pCO$_2$ trend. The warming trend in the summer mixed layer in the Arctic Ocean is about 0.5±0.3°C per decade from 1982 to 2015 (Timmermans et al., 2015). Thus, for the thermal component, we used the warming trend of SST ($\frac{d\Delta^{LT}SST}{dt}$ = 0.05±0.03°C yr^{-1}) to estimate the thermal effect on the long-term pCO_2 trend (Table 3.1). For the non-thermal component, we estimated the long-term trends in sDIC and SSS. Based on the discrete DIC data obtained from GLODAP v2.2019 (Olsen et al., 2019), we found that the salinity normalized DIC (sDIC) in the Canada Basin increased at a rate of 2.3±1.2-2.6±1.2 μmol kg^{-1} yr^{-1} (Figure 3.9 b&e). Thus, we adopted a $\frac{d\Delta^{LT}sDIC}{dt}$ = 2.3-2.6 μmol kg^{-1} yr^{-1} for the assessment. While the underway observation of SSS indicates a decrease of -1.0 ppt per decade (1994-2017; Figure 3.9 g), another synthesis study (1979-2012) reported an even larger salinity decrease (-1.7 ppt per decade) during summer months (Peralta-Ferriz and Woodgate, 2015). Therefore, the range of $\frac{d\Delta^{LT}SSS}{dt}$ of -0.10 to -0.17 ppt per year was taken into consideration.

The results of equation (15) and its components are listed in Table 1.

3.4.8 Box model simulation of summer sea surface *p*CO₂

To investigate the different behaviors of sea surface pCO_2 on the shelf and in the basin and their responses to the Arctic environmental changes, we performed a 1-D modeling exercise of seasonal change of pCO_2 (July 1st to October 15th) from 1994 - 2017. Due to the model limitation that there is no physical circulation and mixing components, we do not expect such simple model can precisely reconstruct the summer pCO_2 variation in the past, but we believe this simple model effectively and sufficiently illustrates the most important processes controlling the surface water pCO_2, such as warming, reduced ice concentration, enhanced biological activity, and increased freshwater input. Below we first introduce the choice of parameters and then describe the simulation process.

SSS vs. Ice concentration. The Pacific Summer Water flowing through the Bering Strait was modified by mixing with the Pacific Winter Water, river runoff and ice meltwater, which dominates the water masses on the Chukchi Shelf. For most of the period of July to October, the Chukchi has already become ice-free (sea ice concentration (ice%) < 15%). To simplify the analysis, we assumed that water mass circulation and mixing on the Chukchi Shelf have not changed markedly in the recent past, thus, we use constant salinity (29.8 ppt) on the Chukchi Shelf for simulaiton, which is the long-term summer mean and determined from the underway salinity measurements. In contrast, the summer ice melting water mixed with the upper polar water determines the water characters in the central basins. Therefore, there is a possible relationship between ice concentration and water salinity (Peralta-Ferriz and Woodgate, 2015), which becomes more apparent in recent years as multi-year ice has been replaced by one-year ice in most of the Canada Basin (Stroeve and Notz, 2018). We established an empirical relationship between ice concentration and salinity in the Canada Basin based on the underway measurement of salinity accompanied by satellite ice concentration data. We found that there is a significant relationship between surface salinity and ice concentration averaged back to 5 days prior to the sampling day during CHINARE 2016 cruise (Figure 3.15). A similar correlation was observed in a more comprehensive analysis in the Canada Basin (see Figure 8c in Peralta-Ferriz and Woodgate, (2015)). Thus, with ice% satellite data from 1994 to 2017, we estimated the corresponding salinity using this empirical equation for the Canada Basin surface water (Figure 3.15). It is encouraging that our salinity calculated from ice% decreases at a rate of -0.7 ppt per decade, which agrees well with the rate based on underway observations of -1.0 ppt per decade (Figure 3.9).

SSS vs. TA. The relationship between surface salinity and TA is derived from the mixing curve of discrete samples obtained from Global Data Analysis Project version 2 database (Olsen et al., 2019), which were sampled during multiple cruises from 1994 to 2016. We examined the relationships separately for the Chukchi Shelf and Canada Basin due to the spatial heterogeneity of surface water (Figure 3.16). We found two significant relationships between SSS and TA for respective subregions, but we did not notice any apparent shift of relationships from the early period (prior 2007) and later period (since 2007) as ice extent greatly retreated northward (Figure 3.16).

Initial pCO_2, DIC and TA. According to the observed pCO_2 in the 1990s in the Chukchi Shelf and Canada Basin (Figure 3.5 a & d), we set the initial pCO_2 = 260 μatm and 280 μatm, respectively, representing the pCO_2 condition in the early July or before ice melt. As we noticed that pCO_2 in the ice-covered high latitudes increases at a rate of 1.8 μatm yr^{-1}, indicating a background increase in pCO_2 following the atmospheric CO_2 increase, we added 1.8 μatm on 280 μatm for the Canada basin for each subsequent year. The initial TA was calculated from SSS using the relationship described above, and the initial DIC was determined by the initial TA and pCO_2 in CO2SYS program.

Net Community Production (NCP) setting. The NCPs in the Chukchi Shelf and Canada Basin reported in previous studies are summarized in Table 3.4. As the primary production is patchy and widely variable on the shelf on the interannual time scale, it is difficult to set values for each month or find the best value works well for the entire shelf. We conducted sensitivity tests by using different NCP rates for the simulation and found that a slight change (e.g. within the range of 5-30 mmol C m^{-2} d^{-1}) in value of NCP for Chukchi Shelf would only affect the lowest values of pCO_2 during the summer, but not significantly change the long-term trends (Figure 3.14). Thus, to keep the model simple, we choose a value of 10 mmol C m^{-2} d^{-1} for simulation, which generally reflected the observed pCO_2 trend on the Chukchi Shelf. In order to investigate the impact of recent enhanced NCP on the Chukchi Shelf (Arrigo et al., 2015), we applied an increase of NCP by 30% since 2007 to compare with the constant NCP scenarios (Figure 3.8 a&b).

On the other hand, the NCP in the Canada Basin was much lower than that in the Chukchi Shelf (Supplementary Table 3) and no significant change trend was observed (Ji et al., 2019). Thus, we set a constantly low NCP of 1 mmol C m^{-2} d^{-1} for the basin surface water for simulation.

Simulation step. The time interval of the simulation step is 1 day. For each simulation step, sea surface pCO_2 was calculated using the CO2SYS program with TA and DIC. The daily change in DIC inventory in the surface mixed layer was calculated as follows:

$$\Delta DIC_t = (FCO_2 + NCP + \Delta DIC_{(diluted)}) \ / \ MLD \tag{3.16}$$

$$DIC_{t+1} = DIC_t + \Delta DIC_t \tag{3.17}$$

where FCO_2, NCP, and $\Delta DIC_{(diluted)}$ indicate the changes in DIC inventory induced by CO_2 air-sea flux, net community production, and meltwater dilution, respectively.

The air-sea CO_2 flux (FCO_2) was calculated following:

$$FCO_2 = K_s \times k_{CO2} \times \Delta pCO_2 \tag{3.18}$$

where K_s and k_{CO2} are the solubility of CO_2 and the CO_2 gas transfer velocity, respectively. The solubility of CO_2 was calculated from daily average SST (Weiss, 1974) and estimated salinity. The k_{CO2} is calculated with the monthly second moment of wind speed at 10 m height $<U_{10}^2>$ following the equation described in Wanninkhof, (2014):

$$k_{CO2} = -0.251 \times <U_{10}^2> \times (Sc/660)^{-0.5} \times (1 - ice\%/100) \qquad (3.19)$$

where Sc indicates the Schmidt number. The 4-times daily surface (10 m) wind speed was obtained from the NCEP-DOE Reanalysis 2 data (https://www.esrl.noaa.gov/psd/data/gridded/data.ncep.reanalysis2.html). For each day, the 6-hourly wind speed squared was calculated and then averaged into a daily mean and subsequently into monthly mean value. k_{CO2} was adjusted according to the sea ice concentration (ice%). Daily sea ice concentration (ice%) was obtained from the Scanning Multichannel Microwave Radiometer (SMMR) on the Nimbus-7 satellite and from the Special Sensor Microwave/Imager (SSM/I) sensors on the Defense Meteorological Satellite Program's (DMSP)-F8, -F11, and -F13 satellites with a resolution of 25 km×25 km (Comiso, 2015).

The monthly averaged atmospheric CO_2 concentrations in dry air (xCO_2) were downloaded from NOAA Earth System Research Laboratory at Point Barrow, Alaska (https://www.esrl.noaa.gov/gmd/dv/data/index.php?parameter_name=Carbon%2BDioxide&frequency=Monthly%2BAverages&site=BRW), and corrected to pCO_2 for water vapor pressure using the following equation:

$$pCO_2^{air}{}_{(monthly)} = xCO_{2(Monthly)} \times (Psl_{(Monthly)} - Pw_{(Monthly)}) \qquad (3.20)$$

where Psl and Pw are the sea level and water vapor pressures, respectively. The monthly Psl was obtained from the satellite reanalysis product (NCEP-DOE Reanalysis 2, https://www.esrl.noaa.gov/psd/data/gridded/data.ncep.reanalysis2.html) with a resolution of 2.5° × 2.5°. The monthly Pw was calculated from Psl and SST (Buck, 1981).

With monthly pCO_2^{air}, the difference between atmospheric and sea surface pCO_2 (ΔpCO_2) was calculated. The long-term change trends of ΔpCO_2 in four subregions were examined with monthly ΔpCO_2 (Figure 3.6).

We simplified the ice melt dilution process in the simulation by assuming that ratio of TA/DIC in the ice nearly equals to that in the surface seawater, thus, the change in DIC by dilution could be estimated as follows,

$$\Delta DIC_{t(diluted)} = (TA_{t+1} - TA_t) \ / \ TA_t \times DIC_t \qquad (3.21)$$

With the new DIC and TA for the next simulation step, a new pCO_2 was calculated, and this simulation process repeats until the last day.

The model simulation settings and the sources of data used in the model are summarized in Table 3.5.

3.5 Supplementary information

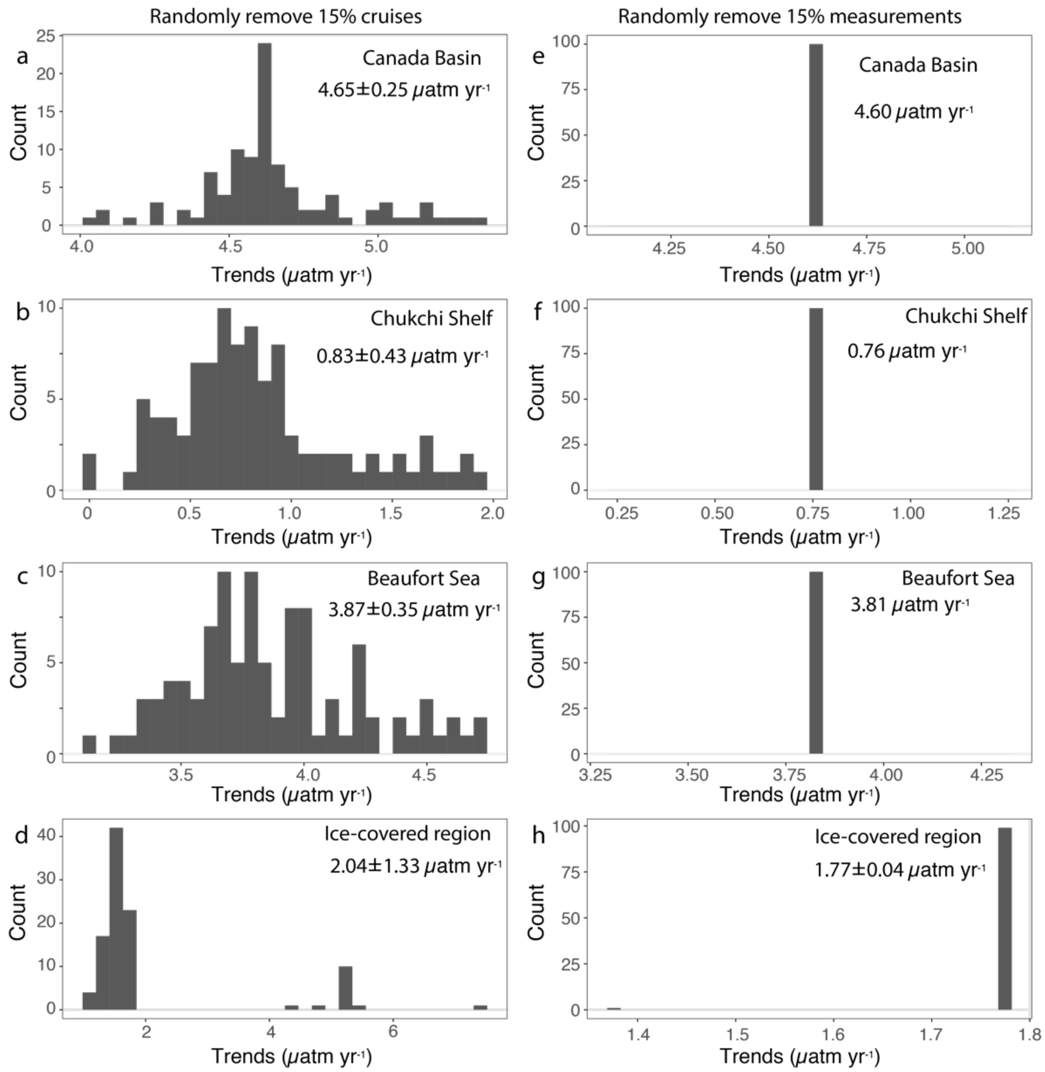

Figure 3.12: The sensitivity test for the long-term trends of pCO_2. We examined the uncertainty of pCO_2 trends by randomly removing 15% of cruises data (a-d) or 15% of total measurements (e-h) and then re-tested the trend for 100 times. The mean and one standard deviation of the 100 trends are shown for each subregion.

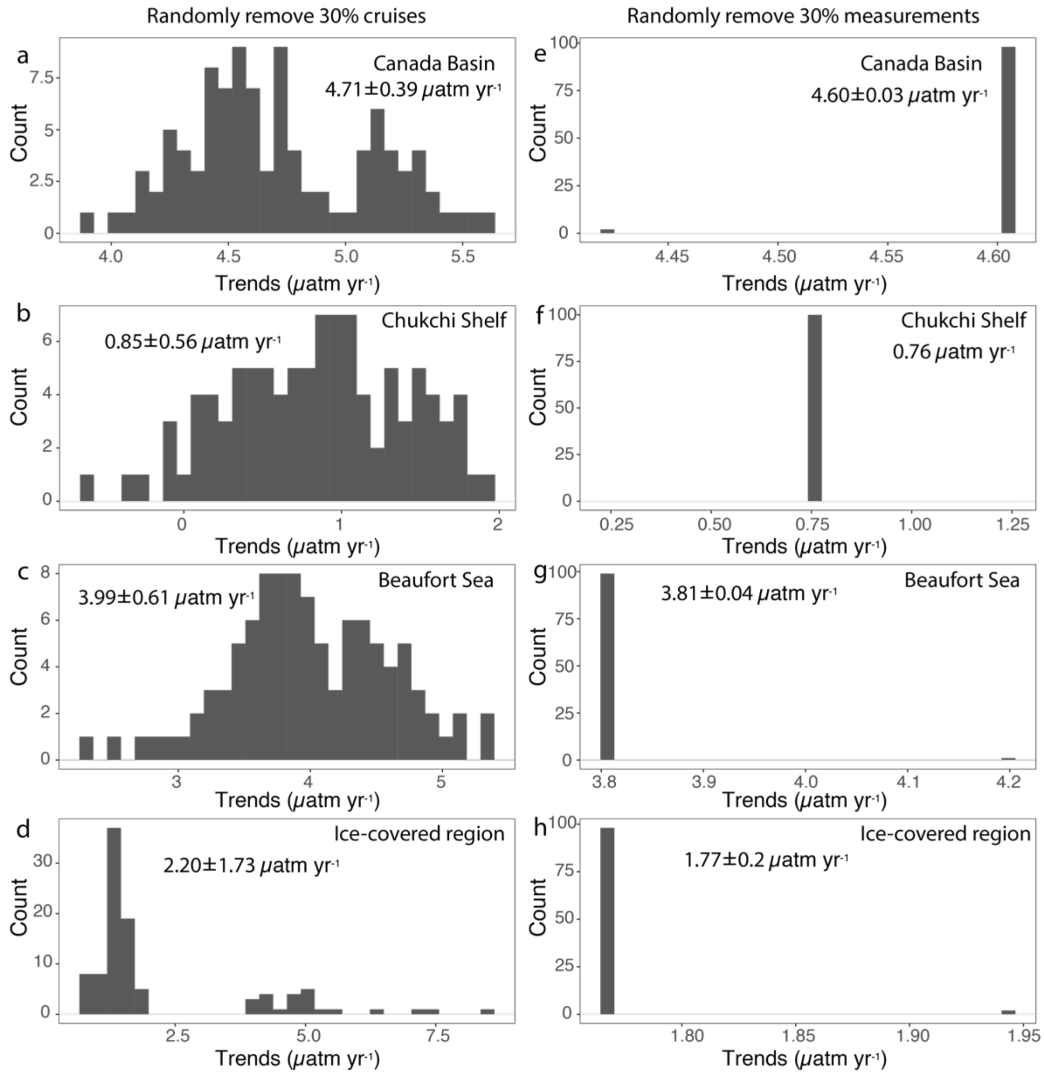

Figure 3.13: The sensitivity test for the long-term trends of pCO_2. We examined the uncertainty of pCO_2 trends by randomly removing 30% of cruises data (a-d) or 30% of total measurements (e-h) and then re-tested the trend for 100 times. The mean and one standard deviation of the 100 trends are shown for each subregion.

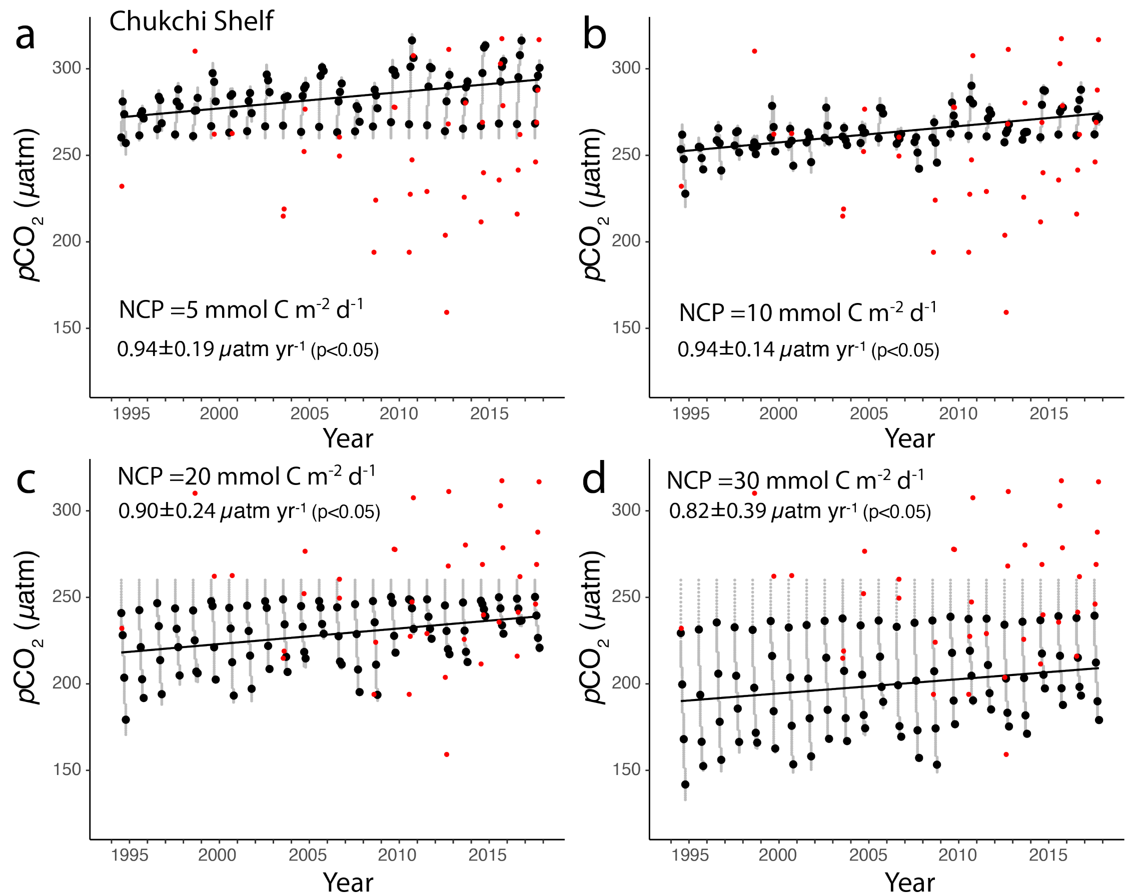

Figure 3.14: Simulation of sea surface pCO_2 on the Chukchi Shelf. To examine how the values and changes in net community production (NCP) affect the long-term pCO_2 trend on the Chukchi Shelf, we simulated the summer (July 1st-October 15th) pCO_2 variations with different NCP values, (a) NCP= 5 mmol C m^{-2} d^{-1}, (b) NCP= 10 mmol C m^{-2} d^{-1}, (c) NCP= 20 mmol C m^{-2} d^{-1}, and (d) NCP= 30 mmol C m^{-2} d^{-1} (see Method for simulation condition). Grey dots represent the simulated daily pCO_2 and black dots represent simulated monthly means. The red dots represent observed monthly means of sea surface pCO_2. The change rates (with ± standard error) were computed with monthly means. ANOVA was performed to test whether the slopes were significantly different from 0.

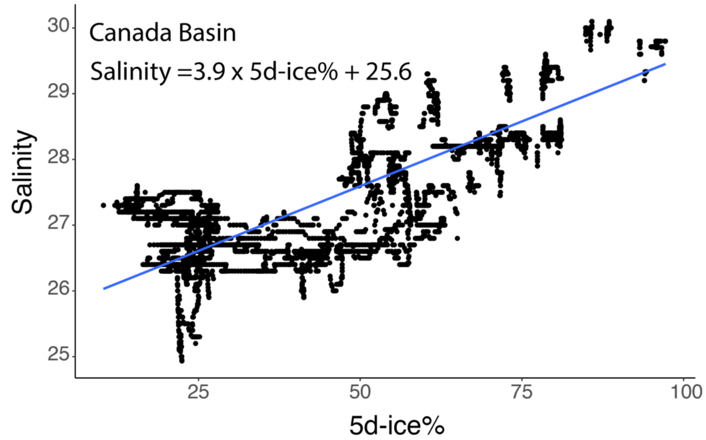

Figure 3.15: The relationship between sea surface salinity and ice concentration in the Canada Basin. 5d-ice% is the average of ice concentration over the past 5 days prior to the sampling day. Sea surface salinity was measured underway during the CHINARE 2016 Cruise. Sea ice concentration data along the cruise track were obtained from the Scanning Multichannel Microwave Radiometer (SMMR) on the Nimbus-7 satellite and from the Special Sensor Microwave/Imager (SSM/I) sensors on the Defense Meteorological Satellite Program's (DMSP)-F8, -F11, and -F13 satellites with a resolution of 25 km ×25 km.

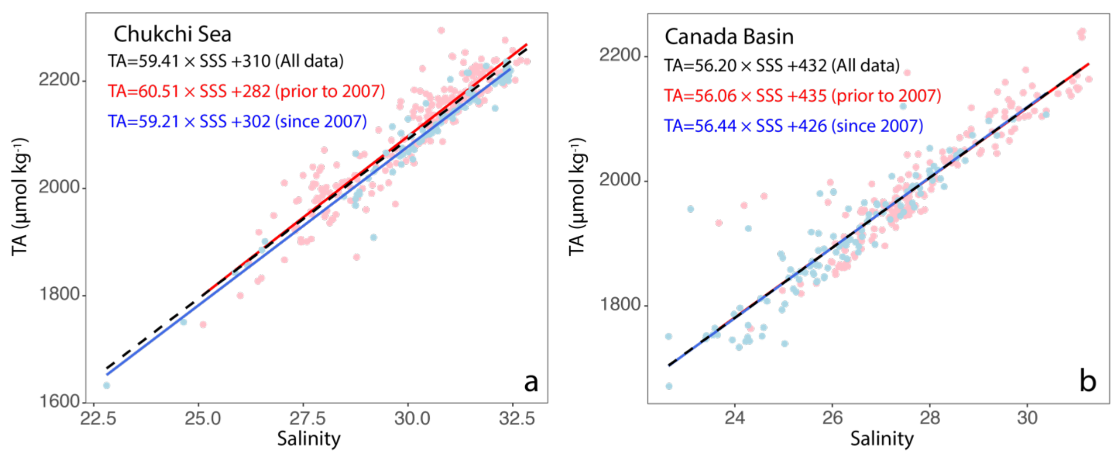

Figure 3.16: The relationship between sea surface salinity and total alkalinity in the Chukchi Shelf (a) and Canada Basin (b). The discrete TA and SSS samples are obtained from Global Data Analysis Project version 2 database. We examined the possible shift in the relationship by separating data into two time periods: before and after 2007, and then ran the linear regressions.

Table **3.2: A summary of the pCO_2 measurements in the western Arctic Ocean during 1994-2017.**

Year	Research period	Contributor	Country of Origin & Research Vessel	# of measurement	Data type and source
1994	July 26- Aug 15	AOS	AOS	32	Discrete (CDIAC)
1997	Sept 24 - Oct 15	JOIS	JOIS	16	Discrete (CDIAC)
1998	July 5- Sept 28	SHEBA	USA (SHEBA)	23	Discrete (CDIAC)
	Aug 19-Aug-29	Murata, A	Japan (Mirai)	467	Underway fCO_2 (SOCAT v5)
1999	Sept 13-Sept 24	Murata, A	Japan (Mirai)	1171	Underway fCO_2 (SOCAT v5)
2000	Sept 6-Sept 29	Murata, A	Japan (Mirai)	2606	Underway fCO_2 (SOCAT v5)
2003	July 9 -Aug 17	Takahashi, T; Newberger, T.; Sutherland, S.C.	USA (Palmer)	15609	Underway fCO_2 (SOCAT v5)
2004	Sept 3- Oct 9	Murata, A	Japan (Mirai)	3868	Underway fCO_2 (SOCAT v5)
2005	Aug 21-Sept 20	Anderson, L	ODEN	36	Discrete (CDIAC)
2006	Aug 30- Sept 7	Murata, A	Japan (Mirai)	854	Underway fCO_2 (SOCAT v5)
2008	Aug 1-Sept 9	Wanninkhof, R	China (Xuelong)	12478	Underway fCO_2 (SOCAT v5)
2009	Sept 10-Oct 12	Nishino, S	Japan (Mirai)	3596	Underway pCO_2 (JAMSTEC)
2010	Sept 4-Oct14	Nishino, S	Japan (Mirai)	4458	Underway pCO_2 (JAMSTEC)
	July 19-Aug 31	Chen, L; Cai, W-J	China (Xuelong)	5155	Underway fCO_2 (SOCAT v5)
	Aug5-Sept 5	Robbins, L	USA (Healy)	25345	Underway pCO_2 (USGS Data Series 741)
2011	Sept 11- Oct 6	Takahashi, T; Newberger, T.; Sutherland, S.C.	USA (Marcus G. Langseth)	7633	Underway fCO_2 (SOCAT v5)
	June 28 -July 26; Aug 17- Sept 26	Robbins, L	USA (Healy)	32299	Underway fCO_2 (SOCAT v5) (USGS Data Series 748)
	Aug 22- Sept 8	Van Heuven, S.	Germany (Polarstern)	17787	Underway fCO_2 (SOCAT v5)
2012	Aug12-Sept25	Robbins, L	USA (Healy)	16934	Underway fCO_2 (SOCAT v5) (USGS Data Series 862)
	Aug 6-Sept 6	DeGrandpre, M	Canada (Louis S. St-Laurent)	8620	Underway fCO_2 (SOCAT v5)
	Sept 13-Oct 5	Nishino, S	Japan (Mirai)	2713	Underway pCO_2 (JAMSTEC)
	July17-Sept 8	Chen, L; Cai, W-J.	China (Xuelong)	11287	Underway fCO_2 (SOCAT v5)
2013	Aug 3- Sept 1	DeGrandpre, M	Canada (Louis S. St-Laurent)	7221	Underway fCO_2 (SOCAT v5)
	Aug 5- Sept 13	Takahashi, T; Newberger, T.; Sutherland, S.C.	USA (Healy)	17144	Underway fCO_2 (SOCAT v5)
2014	July 27-Sept 9	Chen, L; Qi, D; Cai, W-J;	China (Xuelong)	14467	Underway pCO_2 (SOCAT v5)
	July 9--Aug 2; Aug10-Aug 29	Takahashi, T; Newberger, T.; Sutherland, S.C.	USA (Healy)	12444	Underway fCO_2 (SOCAT v5)
	Sept 15-Oct14	DeGrandpre, M	Canada (Louis S. St-Laurent)	5736	Underway pCO_2 (NSF Arctic Data Center)

2015	July 14-July 24; Aug 11-Oct 21	Takahashi, T; Newberger, T.; Sutherland, S.C.	USA (Healy)	26204	Underway fCO_2 (SOCAT v5)
	Aug 6- Aug 21; Aug 22- Sept 4	Wanninkhof,R; Pierrot, D	USA (Ronald H. Brown)	9527	Underway fCO_2 (SOCAT v5)
	Aug 13-Sept 25	Sutherland, S.C.; Newberger, T.;Takahashi, T.	USA (Sikuliaq)	12880	Underway fCO_2 (SOCAT v5)
2016	July 24-Sept4	Chen, L; Qi, D; Cai, W-J	China (Xuelong)	15277	Underway pCO_2 (Chinese NAADC)
	July 8- Aug 5	Takahashi, T; Newberger, T.; Sutherland, S.C.	USA (Healy)	11133	Underway pCO_2 (LDEO v2017)
	Sept 4-Sept 27	Takahashi, T; Newberger, T.; Sutherland, S.C.	USA (Sikuliaq)	7001	Underway pCO_2 (LDEO v2017)
	Sept 24-Oct 16	DeGrandpre, M	Canada (Louis S. St-Laurent)	6361	Underway pCO_2 NSF Arctic Data Center
2017	July 30-Sept 23	Chen, L; Qi, D; Cai, W-J	China (Xuelong)	6171	Underway pCO_2 (Chinese NAADC)
	July 28-Aug 5	Takahashi, T; Newberger, T.; Sutherland, S.C.	USA (Healy)	2941	Underway pCO_2 (LDEO v2017)
	Aug 29- Sept 12	Takahashi, T; Newberger, T.; Sutherland, S.C.	USA (Healy)	5246	Underway pCO_2 (LDEO v2017)
	Sept 22-Oct 9	Takahashi, T; Newberger, T.; Sutherland, S.C.	USA (Healy)	5998	Underway pCO_2 (LDEO v2017)
	Aug 7 –Aug 22	Takahashi, T; Newberger, T.; Sutherland, S.C.	USA (Sikuliaq)	4924	Underway pCO_2 (LDEO v2017)
	Aug 26- Sept 17	Takahashi, T; Newberger, T.; Sutherland, S.C.	USA (Sikuliaq)	7840	Underway pCO_2 (LDEO v2017)
	Sept 7-Oct 2	DeGrandpre, M	Canada (Louis S. St-Laurent)	7132	Underway pCO_2 (NSF Arctic Data Center)
Total				358618	

Table **3.3:** **The long-term trends of pCO$_2$ in the western Arctic Ocean via different approaches.**

		Canada Basin			Chukchi Shelf			Beaufort Sea			Ice-covered region		
		Un-gridded	0.1° lat × 0.25° lon gridded	0.25° lat × 0.5° lon gridded	Un-gridded	0.1° lat × 0.25° lon gridded	0.25° lat × 0.5° lon gridded	Un-gridded	0.1° lat × 0.25° lon gridded	0.25° lat × 0.5° lon gridded	Un-gridded	0.1° lat × 0.25° lon gridded	0.25° lat × 0.5° lon gridded
Raw	N	135984	10920	5123	94437	7815	3422	34235	2038	867	68683	3567	1642
	In situ	5.16±0.02 ***	4.40±0.07 ***	4.48±0.09 ***	2.96±0.05 ***	1.15±0.14 ***	0.85±0.20 ***	4.95±0.05 ***	4.12±0.19 ***	4.23±0.27 ***	6.87±0.04 ***	6.26±0.19 ***	4.83±0.25 ***
Summer-averaged	N	17	17	17	17	17	17	17	17	17	10	10	10
	In situ	4.44±0.63 ***	4.67±0.61 ***	4.69±0.62 ***	-0.71±1.22	-0.06±1.07	-0.19±1.08	3.02±1.33 *	3.43±1.31 *	3.56±1.22 *	1.27±0.93	1.32±1.00	1.30±0.99
Daily-averaged	N	482	494	478	354	422	408	163	163	151	158	156	151
	In situ	4.49±0.23 ***	4.40±0.22 ***	4.44±0.23 ***	0.27±0.54	0.35±0.50	0.44±0.48	4.18±0.57 ***	4.18±0.57 ***	4.04±0.61 ***	1.86±0.40 ***	1.77±0.40 ***	1.70±0.40 ***
Monthly-averaged	N	42	42	42	41	41	41	32	32	32	15	15	15
	In situ	4.46±0.50 ***	4.60±0.49 ***	4.62±0.49 ***	0.40±1.23	0.76±1.18	0.67±1.18	3.76±1.17 **	3.81±1.33 **	3.82±1.28 **	1.73±1.13	1.77±1.14	1.76±1.13
	Deseasonalized		4.62±0.46 ***			0.62±0.92			4.36±1.01 ***			1.71±1.15	
	Temperature-normalized at the long-term mean of SST		4.08±0.46 ***			-0.51±1.17			3.58±1.23 **			1.22±1.09	
			-0.15 ºC			3.67 ºC			2.57ºC			-1.31ºC	

The rates (with ± standard error) were estimated by linear regression. N is the number of data points used for the regression. ANOVA was used for all regressions to test whether the slope is significantly different from 0. The symbol "*" indicates the level of significance (***p<0.001, **p<0.01, *p<0.05).

Table **3.4: NCP in the Chukchi and Canada Basin.**

Regions	Year	Periods	Location	Original values in refs	NCP (mmol C m^{-2} day^{-1})	Reference
Chukchi Shelf	2002	summer	Northern Chukchi	0.78 g C m^{-2} d^{-1}	65	Hill and Cota (2005)
	2002	Jul-Aug	Northeast Chukchi	10.5 ± 9. 3 mmol C m^{-2} d^{-1}	11	Moran et al., (2005)
	2002-2004	Summer	Northeast Chukchi	20.0 ±14.5 mmol C m^{-2} d^{-1}	20	Lepore et al., (2007)
	Long-term mean	Annual	Northern Chukchi	10 (5-20) g C m^{-2} yr^{-1}	2.3	Codispoti et al., (2013)
	2011-2012	Oct	Northern Chukchi	1-10 mmol O_2 m^{-2} yr^{-1}	4	Juranek et al., (2019)
	Long-term mean (1950-2012)	Jul	Northern Chukchi	2016 (±465) mg C m^{-2} d^{-1}	168	Hill et al., (2018)
	Long-term mean (1950-2012)	Aug	Northern Chukchi	696 (±110) mg C m^{-2} d^{-1}	58	Hill et al., (2018)
	Long-term mean (1950-2012)	Sept	Northern Chukchi	126 (±22) mg C m^{-2} d^{-1}	11	Hill et al., (2018)
	Long-term mean (1950-2012)	Annual	Chukchi Sea	97 (±7) g C m^{-2} y^{-1}	22	Arrigo and van Dijken (2011)
	Long-term mean	Annual	Southern Chukchi	70 (40-120) g C m^{-2} yr^{-1}	16	Lepore et al., (2007)
	Long-term mean (1950-2012)	Jul	Southern Chukchi	3015 (±840) mg C m^{-2} d^{-1}	251	Hill et al., (2018)
	Long-term mean (1950-2012)	Aug	Southern Chukchi	247 (±56) mg C m^{-2} d^{-1}	20	Hill et al., (2018)
	Long-term mean (1950-2012)	Sept	Southern Chukchi	437 (±100) mg C m^{-2} d^{-1}	36	Hill et al., (2018)
	2011-2012	Oct	Southern Chukchi	10-20 mmol C m^{-2} day^{-1}	15	Juranek et al., (2019)
Canada Basin	2002	Summer	Edge of the Canada Basin	0.32 g C m^{-2} d^{-1}	27	Hill and Cota (2005)
	1998-2009	Annual	Beaufort Sea (including Canada Basin)	71 g C m^{-2} y^{-1}	16	Arrigo and van Dijken (2011)
	Long-term mean	Annual	Beaufort Northern (Canada Basin)	1 (0.5-5) g C m^{-2} yr^{-1}	0.2	Moran et al., (2005)
	2011	Aug-Sept	Canada Basin	0- 1 mol C m^{-2} (90 days)	0-11	Ulfsbo et al., (2014)
	2011-2016	Summer	Canada Basin	1.3-2.9 mmol O_2 m^{-2} d^{-1}	1-2.2	Ji et al., (2019)

Table **3.5: The conditions and data sources for summer *p*CO2 simulation.**

<table>
<tr><th>Simulation area</th><th>Chukchi shelf</th><th>Canada Basin</th></tr>
<tr><td>Simulation period</td><td colspan="2">107 days for each year; July 1st to October 15th from 1994 to 2017</td></tr>
<tr><td>Air pCO$_2$ (μatm)</td><td colspan="2">The monthly averaged atmospheric CO$_2$ concentrations in dry air (xCO$_2$) were downloaded from NOAA Earth System Research Laboratory at Point Barrow, Alaska (https://www.esrl.noaa.gov/gmd/dv/data/index.php?parameter_name=Carbon%2BDioxide&frequency=Monthly%2BAverages&site=BRW), and corrected to pCO$_2$ for water vapor pressure.</td></tr>
<tr><td>Monthly second moment of wind speed at 10 m height <U$_{10}^2$></td><td colspan="2"><U$_{10}^2$> was used for pCO$_2$ simulation, which was averaged from the daily wind (NCEP-DOE Reanalysis 2 data, https://www.esrl.noaa.gov/psd/data/gridded/data.ncep.reanalysis2.html). For each day, the 6-hourly wind speed squared was calculated and then averaged into a daily mean and then into monthly mean values.</td></tr>
<tr><td>Ice concentration (%)</td><td colspan="2">Daily sea ice concentration data were obtained from the Scanning Multichannel Microwave Radiometer (SMMR) on the Nimbus-7 satellite and from the Special Sensor Microwave/Imager (SSM/I) sensors on the Defense Meteorological Satellite Program's (DMSP)-F8, -F11, and -F13 satellites with a resolution of 25 km × 25 km.</td></tr>
<tr><td>SST</td><td colspan="2">The monthly SST was obtained from a Group for High Resolution Sea Surface Temperature (GHRSST) Level 4 sea surface temperature (SST) analysis. https://podaac-opendap.jpl.nasa.gov/opendap/allData/ghrsst/data/GDS2/L4/GLOB/CMC/CMC0.2deg/v2/</td></tr>
<tr><td>SSS</td><td>For most years between July to October, the Chukchi was ice-free (ice%< 15%). Thus, we set SSS as a constant (29.8), the long-term summer mean, which was determined using the underway salinity measurement.</td><td>Considering melting water dilution dominates the salinity change in the basin, SSS was calculated following an empirical equation:
SSS = 3.94 × ice% + 25.6,
which was derived from underway SSS and ice% averaged back to 5 days prior during CHINARE 2016 cruise (Figure 3.15).</td></tr>
<tr><td>Estimated TA (µmol kg^{-1})</td><td>Daily TA was calculated from the relationships between TA and salinity, which were derived from the surface discrete samples (<20m), obtained from GLODAPv2 (Figure 3.16a).
TA=59.41× SSS + 310</td><td>Daily TA was calculated from the relationships between TA and salinity, which were derived from the surface discrete samples (<20m), obtained from GLODAPv2 (Figure 3.16b).
TA=56.20 × SSS + 432</td></tr>
<tr><td>Initial pCO$_2$ (μatm)</td><td>260</td><td>280+1.8 * add-on years (start from 1994)</td></tr>
<tr><td rowspan="2">NCP (mmol C m^{-2} day^{-1})</td><td>NCP=10</td><td rowspan="2">NCP=1</td></tr>
<tr><td>Enhanced NCP scenario:
NCP=10
NCP=13 for 2007-2017</td></tr>
<tr><td>Mixed layer depth (m)</td><td>We adopt the monthly MLD as described in ref[27]
20 m</td><td>We adoptedt the monthly MLD as described in ref[27]
MLD=10 for July,
MLD=10 for August,
MLD=15 for September,
MLD=15 for October,</td></tr>
</table>

REFERENCES

Anderson, L. G., Ek, J., Ericson, Y., Humborg, C., Semiletov, I., Sundbom, M., & Ulfsbo, A. Export of calcium carbonate corrosive waters from the East Siberian Sea. Biogeosciences, 14,1811-1823 (2017).

Arrigo, K. R., & van Dijken, G. L. Continued increases in Arctic Ocean primary production. Progress in Oceanography, 136, 60-70 (2015).

Arrigo, K. R. & van Dijken, G. L. Secular trends in Arctic Ocean net primary production. *J. Geophys. Res. Ocean* **116,** (2011).

Bakker et al. A multi-decade record of high quality fCO_2 data in version 3 of the Surface Ocean CO_2 Atlas (SOCAT). *Earth System Science Data* 8, 383-413 (2016).

Bates, N.R et al., A Time-Series View of Changing Surface Ocean Chemistry Due to Ocean Uptake of Anthropogenic CO_2 and Ocean Acidification. Oceanography, 27(1), pp.126-141 (2014).

Bates, N. R., S. B. Moran, D. A. Hansell, J. T. Mathis. An increasing CO_2 sink in the Arctic Ocean due to sea-ice loss. *Geophys. Res. Lett.* 33, 1–7 (2006).

Brugler, E. T. et al., Seasonal to interannual variability of the Pacific water boundary current in the Beaufort Sea. *Prog. Oceanogr.* 127, 1–20 (2014).

Buck, A. L., New Equations for Computing Vapor Pressure and Enhancement Factor. *Journal of Applied Meteorology* 12, 1527-1532 (1981).

Cai, W.-J. et al., Decrease in the CO_2 uptake capacity in an ice-free Arctic Ocean basin. *Science* 329, 556–559 (2010).

Chen, B., W.J. Cai, L. Chen, The marine carbonate system of the Arctic Ocean: Assessment of internal consistency and sampling considerations, summer 2010. *Mar. Chem.* 176, 174–188 (2015).

Codispoti, L. A. et al. Synthesis of primary production in the Arctic Ocean: III. Nitrate and phosphate-based estimates of net community production. *Prog. Oceanogr.* **110,** 126-150 (2013).

Comiso. J. C., Updated 2015: Bootstrap sea ice concentrations from Nimbus-7 SMMR and DMSP SSM/I-SSMIS, version 2. [Northern Hemisphere/Daily]. Boulder, CO: NASA National Snow and Ice Data Center Distributed Active Archive Center. (2000).

Codispoti, L. A. et al. Synthesis of primary production in the Arctic Ocean: III. Nitrate and phosphate-based estimates of net community production. *Prog. Oceanogr.* **110,** 126-150 (2013).

Corlett, W. B., R. S. Pickart, The Chukchi slope current. *Prog. Oceanogr.* 153, 50–65 (2017).

Coupel, P. et al., The impact of freshening on phytoplankton production in the Pacific Arctic Ocean. *Prog. Oceanogr.* 131, 113–125 (2015).

Else, B. G. T. et al., Further observations of a decreasing atmospheric CO_2 uptake capacity in the Canada Basin (Arctic Ocean) due to sea ice loss. *Geophys. Res. Lett.* 40, 1132–1137 (2013).

Friis, K., Körtzinger, A., & Wallace, D. W. The salinity normalization of marine inorganic carbon chemistry data. Geophysical Research Letters, 30(2) (2003).

Giles, K. A., S. W. Laxon, A. L. Ridout, D. J. Wingham, S. Bacon, Western Arctic Ocean freshwater storage increased by wind-driven spin-up of the Beaufort Gyre. *Nat. Geosci.* 5, 194–197 (2012).

Grebmeier, J. M. et al., Ecosystem characteristics and processes facilitating persistent macrobenthic biomass hotspots and associated benthivory in the Pacific Arctic. Progress in Oceanography, 136, 92-114 (2015).

Hill, V., Ardyna, M., Lee, S. H., & Varela, D. E. Decadal trends in phytoplankton production in the Pacific Arctic Region from 1950 to 2012. Deep Sea Research Part II: Topical Studies in Oceanography, 152, 82-94 (2018).

Hill, V. & Cota, G. Spatial patterns of primary production on the shelf, slope and basin of the Western Arctic in 2002. *Deep-Sea Res. II* **52,** 3344-3354 (2005).

Ji, B. Y., Sandwith, Z. O., Williams, W. J., Diaconescu, O., Ji, R., Li, Y., ... & Stanley, R. H. Variations in Rates of Biological Production in the Beaufort Gyre as the Arctic Changes: Rates from 2011 to 2016. Journal of Geophysical Research: Oceans (2019).

Juranek, L., Takahashi, T., Mathis, J. & Pickart, R. Significant Biologically Mediated CO_2 Uptake in the Pacific Arctic During the Late Open Water Season. *J. Geophys. Res. Ocean* **124,** 821-843 (2019).

Landschützer, P., Nicolas Gruber, Dorothee CE Bakker, Irene Stemmler, and Katharina D. Six. Strengthening seasonal marine CO_2 variations due to increasing atmospheric CO_2. Nature Climate Change 8, no. 2: 146 (2018).

Lepore, K. et al. Seasonal and interannual changes in particulate organic carbon export and deposition in the Chukchi Sea. *J. Geophys. Res. Ocean* **112,** (2007).

Lovenduski, N. S., Gruber, N., Doney, S. C., & Lima, I. D. Enhanced CO2 outgassing in the Southern Ocean from a positive phase of the Southern Annular Mode. Global Biogeochemical Cycles, 21(2) (2007).

Mathis, Jeremy T. et al. Storm-induced upwelling of high pCO_2 waters onto the continental shelf of the western Arctic Ocean and implications for carbonate mineral saturation states. Geophysical Research Letters 39, no. 7 (2012).

Moran, S. B. et al. Seasonal changes in POC export flux in the Chukchi Sea and implications for water column-benthic coupling in Arctic shelves. *Deep-Sea Res. II* **52,** 3427-3451 (2005).

Nishino, S., T. Kikuchi, M. Yamamoto-Kawai, Y. Kawaguchi, T. Hirawake, M. Itoh, Enhancement/reduction of biological pump depends on ocean circulation in the sea ice reduction regions of the Arctic Ocean. *Journal of oceanography* 67(3), 305-314 (2011).

Olsen, A., Lange, N., Key, R. M., Tanhua, T., Álvarez, M., Becker, S., ... & van Heuven, S. GLODAPv2. 2019–an update of GLODAPv2, Earth Syst. Sci. Data Discuss (2019).

Onarheim, I. H., Eldevik, T., Smedsrud, L. H., & Stroeve, J. C. Seasonal and regional manifestation of Arctic sea ice loss. Journal of Climate, 31(12), 4917-4932 (2018).

Peralta-Ferriz, C., & Woodgate, R. A. Seasonal and interannual variability of pan-Arctic surface mixed layer properties from 1979 to 2012 from hydrographic data, and the dominance of stratification for multiyear mixed layer depth shoaling. Progress in Oceanography, 134, 19-53 (2015).

Perovich, D. K., & Polashenski, C. Albedo evolution of seasonal Arctic sea ice. Geophysical Research Letters, 39(8) (2012).

Pierrot, D. et al.,Recommendations for autonomous underway pCO2 measuring systems and data-reduction routines. *Deep. Res. Part II Top. Stud. Oceanogr.* 56, 512–522 (2009).

Pierrot, D., E. Lewis, D. W. R. Wallace, MS Excel program developed for CO2 system calculations, ORNL/CDIAC-105a, Carbon Diox- ide Inf. Anal. Cent., Oak Ridge Natl. Lab., Oak Ridge, Tenn. (2006).

Qi, D. et al., Increase in acidifying water in the western Arctic Ocean. *Nature Climate Change* 7, 195-201 (2017).

Robbins, L. L. et al., Baseline monitoring of the Western Arctic Ocean estimates 20% of Canadian Basin surface waters are undersaturated with respect to aragonite. *PloS one* 8(9), e73796 (2013).

Rysgaard, S., Glud, R. N., Sejr, M. K., Bendtsen, J., & Christensen, P. B. Inorganic carbon transport during sea ice growth and decay: A carbon pump in polar seas. Journal of Geophysical Research: Oceans, 112(C3) (2007).

Sarmiento, J. L., & Gruber, N. Ocean biogeochemical dynamics. Princeton University Press (2006).

Spall, M. A. et al., Transport of Pacific Water into the Canada Basin and the formation of the Chukchi Slope Current. *J. Geophys. Res. Ocean* 123, 7453-7471 (2018).

Steele, M., & Dickinson, S. The phenology of A rctic O cean surface warming. Journal of Geophysical Research: Oceans, 121(9), 6847-6861 (2016).

Stabeno, P., N. Kachel, C. Ladd, R. Woodgate, Flow patterns in the Eastern Chukchi Sea:2010–2015. *J. Geophys. Res. Ocean.* 123, 1177-1195 (2018).

Stroeve, J., & Notz, D. Changing state of Arctic sea ice across all seasons. Environmental Research Letters, 13(10), 103001 (2018).

Takahashi, T. et al., Climatological mean and decadal change in surface ocean pCO_2, and net sea–air CO_2 flux over the global oceans. Deep Sea Research Part II: Topical Studies in Oceanography 56 (8-10), 554-577 (2009).

Takahashi, T. et al. Climatological distributions of pH, pCO_2, total CO_2, alkalinity, and $CaCO_3$ saturation in the global surface ocean, and temporal changes at selected locations. Marine Chemistry, 164, 95-125 (2014).

Takahashi, T., Olafsson, J., Goddard, J. G., Chipman, D. W., & Sutherland, S. C. Seasonal variation of CO_2 and nutrients in the high-latitude surface oceans: A comparative study. Global Biogeochemical Cycles, 7(4), 843-878 (1993).

Takahashi, T. et al. Global sea-air CO_2 flux based on climatological surface ocean pCO_2, and seasonal biological and temperature effects. Deep.-Sea Res. II 49, 1601–1622 (2002).

Takahashi, T., S. Sutherland, A. Kozyr, Global Ocean Surface Water Partial Pressure of CO2 Database: Measurements Performed During 1957-2017 (LDEO Database Version 2017). NOAA/NCEI/OCADS, NDP-088 (V2017), NCEI Accession Number 0160492. https://www.nodc.noaa.gov/ocads/data/0160492.xml) (2018).

Timmermans, M.-L., C. Ladd and K. Wood, 2015: Sea surface temperature [NOAA (ed.)]. Arctic Report Card, NOAA, https://arctic.noaa.gov/Report-Card/Report-Card-2015/ArtMID/5037/ArticleID/220/Sea-Surface-Temperature).

Timmermans, M.-L. et al., Mechanisms of Pacific Summer Water variability in the Arctic's Central Canada Basin. *J. Geophys. Res. Ocean.* 119, 7523-7548 (2014).

Ulfsbo, A. et al. Late summer net community production in the central Arctic Ocean using multiple approaches. *Global Biogeochem. Cycles* **28,** 1129-1148 (2014).

Wang, M., Yang, Q., Overland, J.E. and Stabeno, P. Sea-ice cover timing in the Pacific Arctic: The present and projections to mid-century by selected CMIP5 models. Deep Sea Research Part II: Topical Studies in Oceanography, 152, 22-34 (2018).

Wanninkhof, R. Relationship between wind speed and gas exchange over the ocean revisited. *Limnology and Oceanography: Methods* 12, 351–362 (2014).

Weiss, R., Carbon dioxide in water and seawater. The solubility of a non-ideal gas. *Mar. Chem.* 2, 203-215 (1974).

Woodgate, R. A., Weingartner, T. J., & Lindsay, R. Observed increases in Bering Strait oceanic fluxes from the Pacific to the Arctic from 2001 to 2011 and their impacts on the Arctic Ocean water column. Geophysical Research Letters, 39(24) (2012)..

Woodgate, R. A. Increases in the Pacific inflow to the Arctic from 1990 to 2015, and insights into seasonal trends and driving mechanisms from year-round Bering Strait mooring data. Progress in Oceanography, 160, 124-154 (2018).

Woosley, R. J., F. J. Millero, T. Takahashi, Internal consistency of the inorganic carbon system in the Arctic Ocean. *Limnol. Oceanogr. Methods*, 15(10), 887-896 (2017).

Yamamoto-Kawai, M. , F. A. McLaughlin, E. C. Carmack, S. Nishino, K. Shimada, N. Kurita, Surface freshening of the Canada Basin, 2003-2007: River runoff versus sea ice meltwater. *J. Geophys. Res. Ocean.* 114, (2009).

Yamamoto-Kawai, M., F. A. McLaughlin, E. C. Carmack, S. Nishino, K. Shimada, Aragonite undersaturation in the Arctic Ocean: Effects of ocean acidification and sea ice melt. *Science* 326, 1098-1100 (2009).

Chapter 4

MULTI-FACTOR IMPACTS ON CHANGES IN THE OCEANIC CO_2 SINK IN THE WESTERN ARCTIC OCEAN FROM 1994 TO 2019

4.1 Abstract

In the past few decades, rapid sea ice loss has turned the Arctic Ocean from a perennial ice-covered ocean to a seasonal ice-free ocean. Such a shift at the air-ice-sea interface has resulted in substantial changes in the Arctic carbon cycle and related biogeochemical processes. Our recent study of long-term partial pressure of carbon dioxide (pCO_2) trends in the western Arctic Ocean has suggested that summer carbon flux dynamics greatly differ between regions; the inflow Chukchi Sea continues to absorb CO_2 as atmospheric CO_2 increases, whereas the oligotrophic Canada Basin becomes a weakened carbon sink. To confirm our proposed implications and better evaluate how the ocean uptake of atmospheric CO_2 responds to rapid sea ice changes, we examined the changes in air-sea CO_2 flux and carbon uptake in the western Arctic Ocean from 1994 to 2019 by two complementary approaches: pCO_2 observation-based estimation and a data-driven box model evaluation. The compilation of observations showed that CO_2 uptake in the summer Chukchi Sea significantly increased at a rate of 1.4 $\pm$0.6 Tg C decade^{-1}, which was primarily due to an enlarged open area with a

---

Ouyang, Z., Li, Y., Qi, D., Zhong, W., Murata, A., Nishino, S., Wu, Y., Jin, M., Cai, W-J. Multi-factor impacts on changes in oceanic CO_2 sink in the western Arctic Ocean over 1994 to 2019. Submitted to *Global Biogeochemical Cycles.*

longer ice-free period and increased primary production and partially due to enhanced wind. However, no significant increase in CO_2 uptake was found in the Canada Basin and Beaufort Sea based on these compiled data. By employing a box-model practice, we confirmed that the annual CO_2 sink significantly increased in the Chukchi Sea by 1.6 ± 0.3 Tg C decade^{-1} and CO_2 sink in the Beaufort Sea was relatively constant over the years. Our model results further revealed that the greatly decreased sea ice extent in summer indeed promoted CO_2 uptake and resulted in a CO_2 sink of 0.6 ± 0.3 Tg C decade^{-1} in the Canada Basin, but this sink was counteracted by a rapidly decreasing air-sea pCO$_2$ gradient. Our results indicate that the change in air-sea pCO$_2$ gradient alone is not good enough to describe the change in the Arctic Ocean CO_2 sink, which is determined by the complicated interplay between the air-sea gradient of pCO$_2$ and other environmental drivers.

4.2 Introduction

The Arctic Ocean was predicted to be an important sink for CO_2 as the sea surface pCO$_2$ under the sea-ice cover was found to be very low (Bates et al., 2006; Bates and Mathis, 2009), but its CO_2 uptake potential has been questioned (Cai et al., 2010). Accelerated sea ice loss has turned the Arctic Ocean from a perennial ice-covered ocean to a seasonal ice-free ocean, resulting in substantial changes in the Arctic carbon cycle and related biogeochemical processes. On one hand, increasing freshwater from ice meltwater and river runoff strengthens the upper ocean stratification, which suppresses the nutrient supply from deep water and hence surface primary production and the resultant CO_2 uptake (Lewis et al., 2020; Randelhoff et al., 2020). On the other hand, earlier onset of ice melt and larger open area can stimulate a longer growth season with increased primary production, which substantially influences CO_2 sinks and sources (Arrigo et al., 2010). Additional complexity is added when sea ice, the mechanical barrier to air-sea gas exchange, is considered. Thus, it is challenging to quantitatively assess CO_2 sink with changes in sea ice.

The western Arctic Ocean has undergone dramatic climate-driven ice loss and substantial alterations in the seasonal biogeochemical dynamics in recent decades. The western Arctic Ocean consists of the inflow shelf, Chukchi Sea, which is impacted by the nutrient-rich Pacific Ocean Water (Woodgate et al., 2012; Woodgate 2018), the interior shelf, Beaufort Sea, which is narrow and influenced by the Mackenzie River, and the oligotrophic Canada Basin, which is greatly influenced by the nutrient-poor Beaufort gyre and sea ice meltwater (Ardyna and Arrigo, 2020). The two most contrasting regions, the Chukchi Sea shelf and Canada Basin, have showed quite different responses to climate-related drivers. Specifically, primary production has increased by ~96% over 1998-2018 on the Chukchi Sea shelf (Lewis et al., 2020), while primary production was consistently low over the same time span in the Canada Basin (Ji et al., 2019; Lewis et al., 2020). Additionally, summer sea surface pCO_2 increased at twice the rate of atmospheric CO_2 in the oligotrophic Canada Basin from 1994 to 2017, whereas no significant pCO_2 increase was found on the nutrient-rich Chukchi Sea shelf (Ouyang et al., 2020). Ouyang et al. (2020) further suggested that if these trends of pCO_2 continues, the Canada Basin will not be as large a CO_2 sink as previously estimated (Bates et al., 2006; Bates and Mathis, 2009), and the CO_2 sink on the Chukchi Sea shelf will increase due to the atmospheric CO_2 increase. However, the interannual change in the CO_2 sink of the western Arctic is poorly known. Only a few studies have examined the interannual variation in CO_2 flux and carbon sink and the uncertainties remain large (Arrigo et al., 2010; Yasunaka et al., 2016&2018; Manizza et al., 2019).

Early attempts to quantify the CO_2 flux and sink in the western Arctic Ocean were based on snapshots of a single cruise (Murata and Takizawa, 2003; Bates et al., 2006), which likely overestimated or underestimated the carbon sink when instantaneous CO_2 fluxes were scaled to the entire region (Evans et al., 2015, Manizza et al., 2019). With a more extensive pCO_2 dataset collected over 2003-2014, Evans et al., (2015) examined the monthly climatology of air-sea pCO_2 gradient (ΔpCO_2) and CO_2 fluxes for the Chukchi and Beaufort coastal seas. However, this approach still suffered from a sparsity of pCO_2 data, especially for winter months and high latitudes which were covered by sea ice for most of the time. To increase data coverage in both time and space, different approaches have been explored and applied to better estimate the Arctic Ocean CO_2 budget. Arrigo et al., (2010) reconstructed the pCO_2 field in the Arctic Ocean by combining in situ data and remote sensing techniques. Although this technique can provide a pCO_2 map with a very high resolution in time (daily-based), the limitation is that reconstructed pCO_2 only covers spring to fall when satellite data are available. Recently, a two-step neural network-method (self-organizing map feed-forward neural-network, SOM-FFN) was developed and widely used for estimating the global ocean carbon budget (Landschützer et al., 2013, 2014, 2016; Laruelle et al., 2017). Although this neural-network interpolation technique can skillfully reconstruct monthly air-sea CO_2 fluxes (Roobaert et al., 2019), compared to open oceans, the performance of SOM-FFN deteriorates in the Arctic coastal seas and the higher latitudes where the ocean is regularly covered by sea ice (Laruelle et al., 2017) because of insufficient observations for training the model (Gloege et al., 2020). Also, due to the unevenly observed sea surface pCO_2 in seasons (many more observations in summer and fall than in winter and spring), the performance of SOM-FFN and data coverage becomes inadequate in winter and spring. Only a few attempts were made with a biogeochemistry model to fill the gaps in the data and to examine temporal variability of the CO_2 sink (Manizza et al., 2013 & 2019).

To resolve the spatial and temporal variability in air-sea CO_2 flux and determine how the carbon sink and source changes in response to multiple sea ice-related changes, we quantified the air-sea CO_2 fluxes and carbon sink for the western Arctic Ocean from 1994 to 2019. We compiled and synthesized a more extensive dataset of sea surface pCO_2 from several international databases, which extends the assessment to 2019. However, increasing the number of pCO_2 observation still does not fully resolved the data inadequacy in seasonal and regional coverage, which makes it difficult to assess whether there are any trends in CO_2 fluxes among different regions. To fill these data and knowledge gaps, we used a box model to reconstruct the daily pCO_2 maps for the western Arctic Ocean from 1994 to 2019. With the modeled data, we are able to further disentangle and identify the respective effects of sea ice, wind speed and sea-air gradient of pCO_2 on the seasonal and interannual variabilities of CO_2 flux and carbon sink.

4.3 Methods

4.3.1 Study Area

The western Arctic Ocean covers the areas between 65°N to 85°N and 125°W to 180°W. According to characteristics of hydrography, topography, ocean circulation, and sea ice condition, we divided the study area into three biogeochemical provinces:

(1) the nutrient-rich Chukchi Shelf (CS), which sometimes is further divided into the southern Chukchi Shelf (sCS, 65°N–69°N) and the northern Chukchi Shelf (nCS, >69°N); (2) the oligotrophic Canada Basin (CB, <85°N), separated from the Chukchi Shelf mainly along shelf breaks (~250 m isobaths); (3) the coastal Beaufort Sea (BS), separated from the Chukchi Sea and Canada Basin along 152°W and 72°N, respectively. The highest-latitude area of Makarov Basin with perennial ice cover (>85°N) is not included in present study (Figure 4.1).

4.3.2 Observation-based CO_2 flux calculation

4.3.2.1 Data Sets and processing

Underway sea surface *p*CO_2 data. To examine decadal changes in CO_2 flux in the western Arctic Ocean, we first synthesized a dataset of *p*CO_2 measurements via multiple international databases (Table 4.5), including Surface Ocean CO_2 Atlas (SOCAT v2020, http://www.socat.info; Bakker et al., 2016), Japan Agency for Marine-Earth Science and Technology (JAMSTEC, https://www.jamstec.go.jp/e/), Carbon Dioxide Information Analysis Center (CDIAC, https://cdiac.ess-dive.lbl.gov), USGS database (https://pubs.er.usgs.gov), LDEO Database Version 2018(Takahashi et al., 2019; https://www.nodc.noaa.gov/ocads/data/0160492.xml), NSF Arctic Data Center (https://arcticdata.io), and Chinese National Arctic and Antarctic Data Center (http://www.chinare.org.cn). This extensive dataset contains more than 513,000 sea surface *p*CO_2 (pCO_2^{sea}) data points and associated sea surface temperature (SST) and sea surface salinity (SSS) data. All data are archived in publicly accessible databases (Table 4.5).

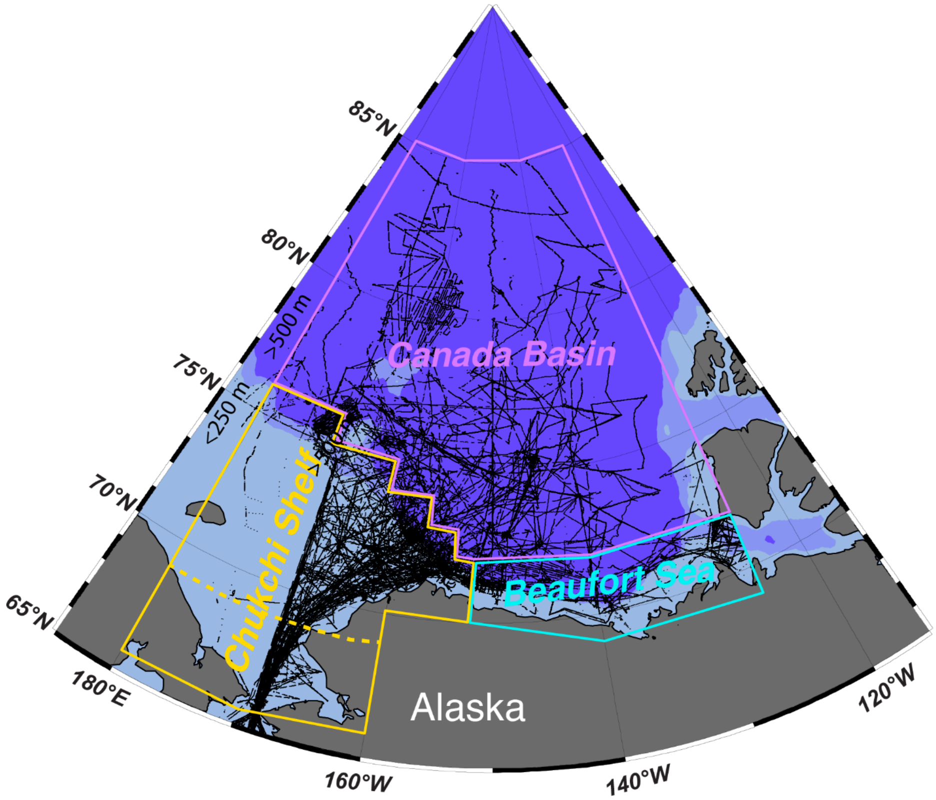

Figure 4.1: The western Arctic Ocean map with bathymetry information (<250 m, 250-500 m, and >500 m). Black lines indicate the cruise tracks of the sea surface pCO2 measurements through 1994 to 2019. We divided the western Arctic Ocean into three subregions (a): (1) Chukchi Sea shelf (CS), which sometimes further divided into the southern Chukchi Shelf (sCS, 65°N–69°N) and the northern Chukchi Shelf (nCS, >69°N), as shown by the yellow dash line; (2) Canada Basin (CB), separated from the Chukchi Shelf mainly along the 250-500 m isobaths; (3) the coastal Beaufort Sea (BS), separated from the Chukchi Sea and Canada Basin along 152°W and 72°N, respectively. Figure is produced by Ocean Data View (Schlitzer, 2018).

For consistency, we chose to report and analyze all the data as pCO_2. Thus, the reported CO_2 fugacity (fCO_2) data from some programs (Table 4.5) were converted back to pCO_2 at SST (℃) using equation 4.1 (Takahashi et al., 2019):

$$pCO_2 = fCO_2 \times (1.00436\text{-}4.669 \times 10^{-5} \times SST) \tag{4.1}$$

Note that the difference between pCO_2 and fCO_2 conversion is less than the measurement precision of ± 2 μatm, thus, the error induced by conversion is negligible. In particular, the air-sea gradient ΔpCO_2 and ΔfCO_2 are essentially the same.

Discrete sea surface pCO_2 data. To expand the data coverage in both time and space, we added pCO_2 data into the analysis, which were calculated from the discrete dissolved inorganic carbon (DIC) and total alkalinity (TAlk) samples taken in the surface mixed layer (<20 m). The discrete DIC and TAlk data were obtained from the Global Data Analysis Project version 2 database 2019 (GLODAP v2.2019). The pCO_2 was calculated by the 'seacarb' package in R language (Gattuso et al., 2018) with carbonate dissociation constants of Millero et al., (2006) recommended by Evans et al, (2015). The uncertainty of pCO_2 values computed from TAlk and DIC is about ± 13 μatm with a mean systematic difference from the measured pCO_2 of -0.7 μatm (Woosley et al., 2017).

Air pCO₂. The pCO_2^{air} was calculated from monthly average atmospheric CO_2 concentrations in dry air (xCO_2) measured at Point Barrow, Alaska (https://www.esrl.noaa.gov/gmd/dv/data/index.php?parameter_name=Carbon%2BDioxide&frequency=Monthly%2BAverages&site=BRW). Then xCO_2 was corrected to pCO_2 for water vapor pressure:

$$pCO_2^{air}{}_{(daily)} = xCO_{2(monthly)} \cdot (Psl_{(daily)} - Pw_{(daily)}) \tag{4.2}$$

where Psl is sea level pressure and Pw is water vapor pressure. Daily Psl data were obtained from a satellite reanalysis product (NCEP-DOE Reanalysis 2, https://www.esrl.noaa.gov/psd/data/gridded/data.ncep.reanalysis2.html) with a resolution of 2.5° × 2.5°. Daily Pw data were calculated from Psl and SST (Buck, 1981).

Wind speed second moments. The second moment of wind speed at 10 m height $<U_{10}^2>$ was obtained from the NCEP-DOE Reanalysis 2 data (https://www.esrl.noaa.gov/psd/data/gridded/data.ncep.reanalysis2.html). For each day, the 6-hourly wind speed squared was calculated and then averaged into a daily mean and subsequently into a monthly mean value.

Sea ice concentration. Daily sea ice concentration (ice%) was obtained from the Scanning Multichannel Microwave Radiometer (SMMR) on the Nimbus-7 satellite and from the Special Sensor Microwave/Imager (SSM/I) sensors on the Defense Meteorological Satellite Program's (DMSP)-F8, -F11, and -F13 satellites with a resolution of 25 km × 25 km (Comiso, 2017).

4.3.2.2 Monthly CO_2 flux calculation

In general, our method follows Laruelle et al., (2014) and Evans et al., (2015) with a few modifications. Figure 4.2 shows the scheme of observation-based CO_2 flux calculation. Firstly, the synthesized pCO_2 datasets associated with SST and SSS were averaged into 1° latitude × 1° longitude grids for each day, then into each month in a particular year. Accordingly, all other parameters of pCO_2^{air}, $<U_{10}^2>$, and ice% were re-gridded into 1° latitude × 1° longitude grid and averaged into a monthly mean to match gridded pCO_2^{sea}. The monthly sea-air CO_2 flux (F_{CO2}, unit: mmol C m^{-2} d^{-1}) for each 1° latitude × 1° longitude grid was calculated following,

$$F_{CO2} = K_s \cdot k_{CO2} \cdot (pCO_2^{sea} - pCO_2^{air}) \quad (4.3)$$

where K_s is the solubility of CO_2 (mol m^{-3} atm^{-1}), and k_{CO2} is the CO_2 gas transfer velocity (m d^{-1}). The K_s was calculated using underway SST and SSS (Weiss, 1974). The value of k_{CO2} is estimated from the parameterization of Wanninkhof (2014), depending on second moment of wind speed at 10 m height above the sea surface, $<U_{10}^2>$ (m^2/s^2):

$$k_{CO2} = 0.251 \cdot <U_{10}^2> \cdot (Sc/660)^{-0.5} \quad (4.4)$$

Laruelle et al., (2014) and Evans et al., (2015) first corrected CO_2 flux for ice cover by applying a linear ice correction (Butterworth and Miller, 2016; Prytherch et al., 2017) in each individual grid, which had sea surface pCO_2 data (Equation 4.5), and then averaged all CO_2 fluxes into a monthly regional mean by considering weighting of area in each grid (Equation 4.6; dashed arrows in Figure 4.2).

$$F_{CO2\ (ice\text{-}corrected)(i)} = F_{CO2(i)} \times (1\text{-}ice\%_{(i)}) \quad (4.5)$$

$$F_{CO2(area\text{-}weighted)} = \sum_{i=1}^{n}(FCO_{2(i)} \times (1 - ice\%_{(i)}) \times A_i) \,/\, \sum_{i=1}^{n} A_i \quad (4.6)$$

where i represents the ith grid with pCO_2 observations present and A is the area of the corresponding grid. This upscaling method was designed for the western Arctic coastal ocean and works well for these regions where sea ice concentration is relatively lower or uniform and data coverage of sea surface pCO_2 observation is relatively higher. However, only correcting ice% in the grids with pCO$_2$ observation limits this method's skill for estimating CO_2 flux to regions with large sea ice gradients (i.e., Canada Basin). As most sea surface pCO$_2$ observations were concentrated in the southern Canada Basin, it tends to overweight the observed fluxes in the grids of low or no ice when we calculated a regional mean (see more discussion in supplementary information). Therefore, we modified calculation of regional CO_2 flux by changing the sequence of the CO_2 flux calculation and correction of sea ice concentration (solid arrows in Figure 4.2). Briefly, we first calculated an area-weighted monthly CO_2 flux (without ice correction) from all the grids with pCO$_2$ observation for a given subregion (equation 4.7), and assumed that this regional monthly CO_2 flux can largely represent the potential magnitude in CO_2 flux for the entire biogeochemical province in the respective month.

$$F_{CO2(\text{area-weighted})} = \sum_{i=1}^{n}(F_{CO2(\text{without ice correction})\,(i)} \times A_i) \,/\, \sum_{i=1}^{n} A_i \qquad (4.7)$$

Then, we corrected CO_2 flux for sea ice concentration (ice%) presented in that month for each grid as follows,

$$F_{CO2(\text{corrected})i} = F_{CO2(\text{area-weighted})} \times (1\text{-ice\%}_{(i)}) \qquad (4.8)$$

In this way, we used a regional mean CO_2 flux to generate a CO_2 flux map, which was corrected not only for ice% in the grids with pCO$_2$ observation, but also for ice% in the grids without pCO$_2$ value. Note that because the satellite data are unable to resolve fine-scale ice structure (i.e. cracks and leads) that allows air-sea gas exchange, we adopted the technique used by Takahashi et al. (2009) that assuming ice% always equals to 90% for all grids where satellite ice% is larger than 90%. Finally, we computed monthly area-weighted CO_2 flux using CO_2 flux values in all grids in a particular subregion following equation (4.6).

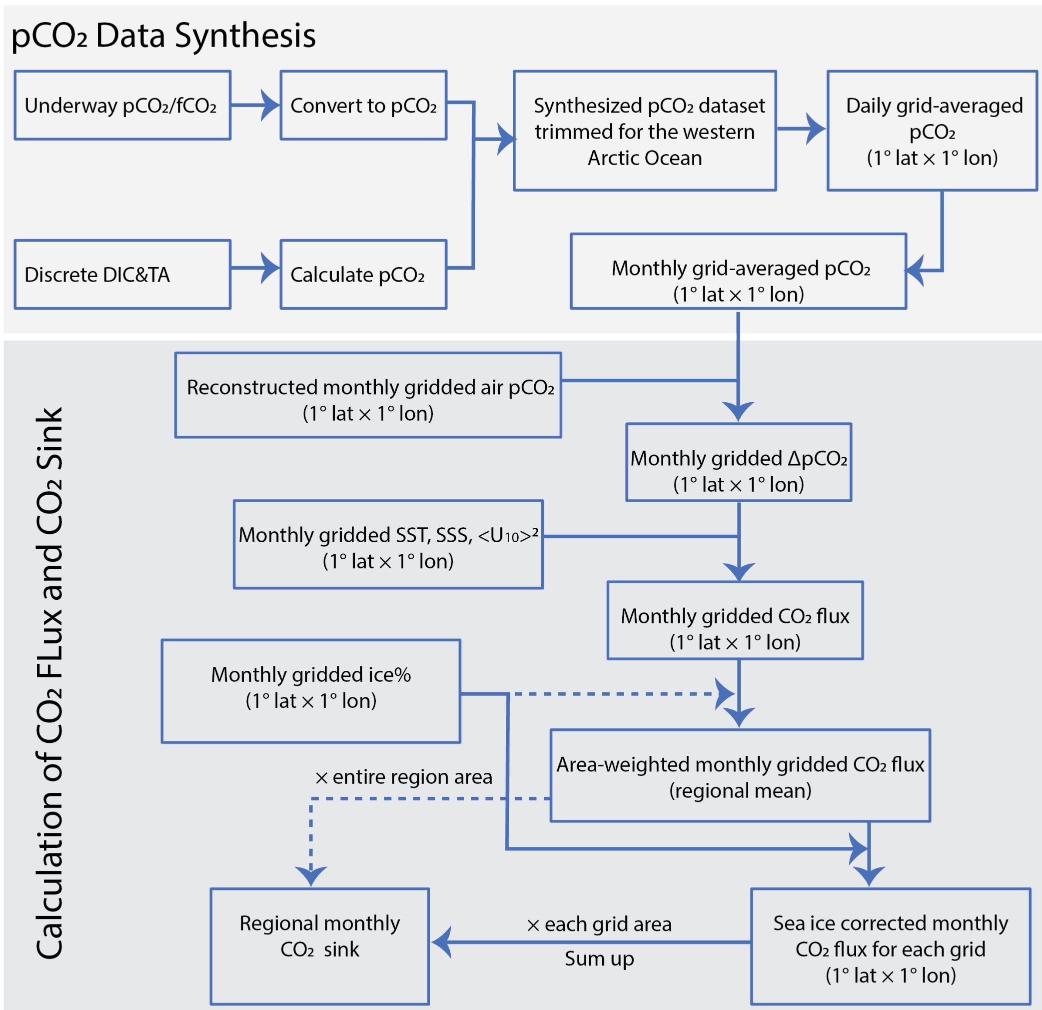

Figure 4.2: Synthesis of pCO_2 datasets and calculation of monthly CO_2 flux and CO_2 sink. The dashed arrows indicate the approaches used in Laruelle et al., (2014) and Evans et al., (2015). We made some modifications as indicated by solid arrows.

4.3.3 Model-based CO_2 flux calculation

Although we attempted to extend monthly mean CO_2 fluxes derived from limited data points to entire subregions, this upscaling method alone was deemed to be insufficient. For instance, few observations were made in winter and spring. Although the CO_2 flux is expected to be near zero in the ice-covered wintertime, it could be substantial during the early ice-free season in spring and during ice formation time in the later fall (Juranek et al., 2019). It is thus hard to assess the year-around CO_2 flux or interannual variations. Here, we employed a data-driven box model to reproduce pCO$_2$ time series and spatial distribution from 1994 to 2019 and to examine the complex seasonal and interannual dynamics of CO_2 flux and CO_2 uptake. The model simulation allows us to increase temporal resolution from monthly to daily, which greatly facilitates understanding short-term CO_2 flux fluctuations associated with rapid changes in sea ice. Finally, we used this modeled pCO$_2$ dataset to assess the possible trends of CO_2 flux and carbon sink in the western Arctic Ocean.

4.3.3.1 Data sources.

The daily sea surface temperature (SST) data were obtained from a Group for High Resolution Sea Surface Temperature (GHRSST) Level 4 sea surface temperature (SST) analysis (https://podaac-opendap.jpl.nasa.gov/opendap/allData/ghrsst/data/GDS2/L4/GLOB/CMC/CMC0.2deg/v2/). The daily sea surface salinity (SSS) and mixed layer depth (MLD) data were obtained from global ocean ensemble physics reanalysis product (https://resources.marine.copernicus.eu/?option=com_csw&view=details&product_id=GLOBAL_REANALYSIS_PHY_001_031). Prior to directly using SSS product in our model, we compared the modeled and observed SSS within a given grid on the same day. We noticed that although the product assimilated observed salinity profiles, they are limited in space and time, especially lack of automated observations (such as ITP) before 2000. This SSS product also tended to have a much lower decline rate in SSS during 1994-2019 and a higher surface salinity (by 0.5~2 psu) for summer months (July to October) after 2000. Therefore, we adjusted SSS based on the mean of residual in a given month for each subregion to reduce apparent systematic bias. After adjustment, the root mean square error (RMSE) of residuals were 2.5, 1.0, and 1.2 psu in the Chukchi Sea, Beaufort Sea and Canada Basin, respectively (Figure 4.3). The data sources of the daily second moment of wind speed ($<U_{10}^2>$), sea ice concentration (ice%) and reconstructed air $p$$CO_2$ were described in section 4.3.2.1. All datasets used in model simulation were re-gridded from their original spatial resolution to a 1° × 1° grid.

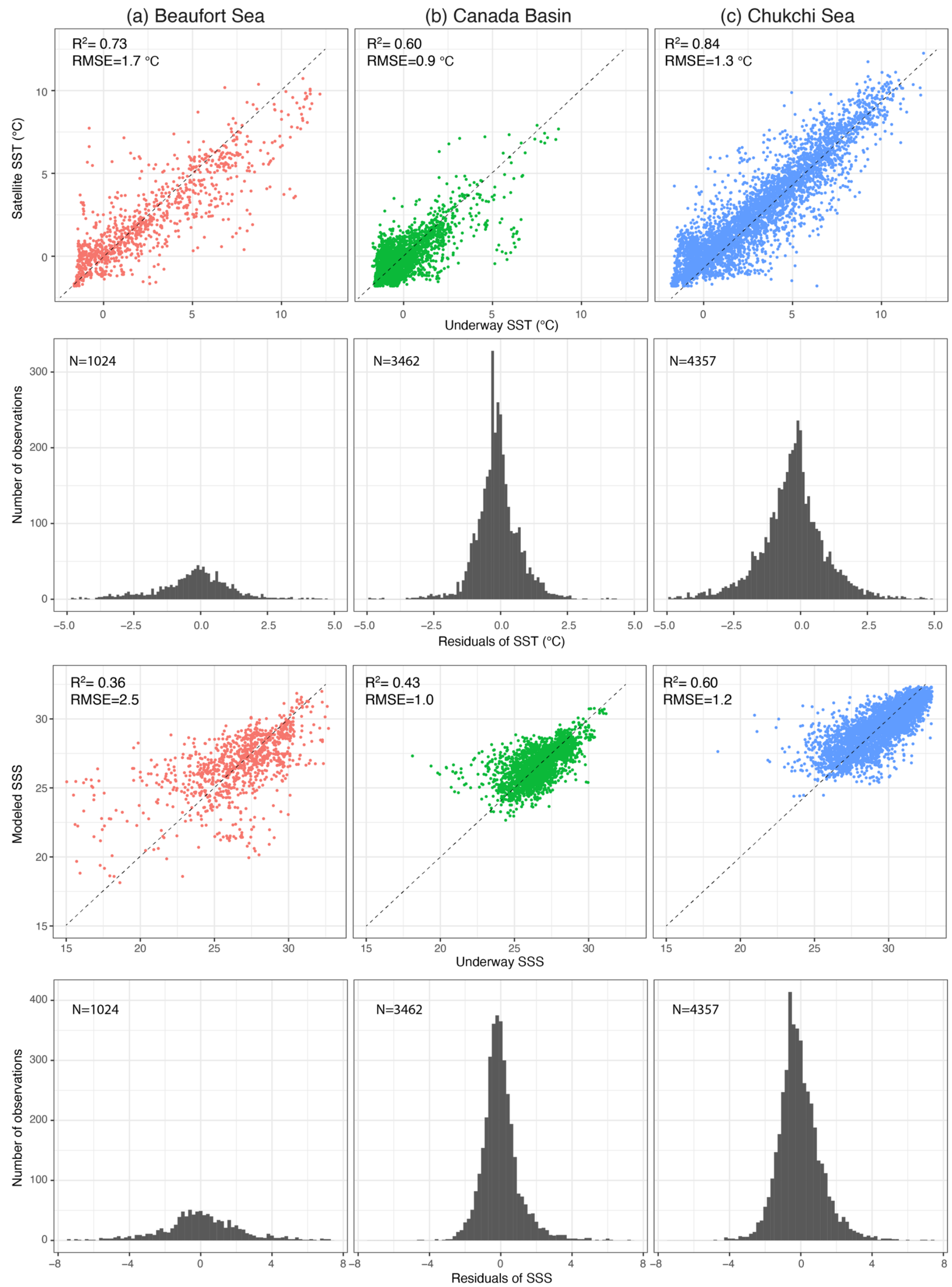

Figure 4.3: Observations versus satellite SST and modeled SSS in (a) the Beaufort Sea, (b) the Canada Basin, and (c) the Chukchi Sea. Comparisons are conducted using daily gridded averages. The R^2 and root mean squared error (RMSE) are noted in the figures. N is the number of data pairs used for statistical analysis. The dashed 1:1 line is provided for reference.

4.3.3.2 Model setting and simulation step.

Estimate of total alkalinity (TAlk). Total alkalinity in surface water was calculated from SSS. The relationship between TAlk and SSS was determined by using the discrete samples obtained from the Global Data Analysis Project version 2 database (Olsen et al., 2020). We noticed that the relationships varied with months and regions due to seasonal river runoff input and the sea ice melt and formation cycle. Therefore, we established the relationships between SSS and TAlk for each month and separately for the Chukchi Shelf, Beaufort Sea and Canada Basin (Table 4.6). For the months without any observation (almost always the winter months), we linearly interpolated the slope and intercept of the relationship using the adjacent months values assuming that seasonal evolution of SSS and TAlk is relatively slow and smooth.

Net Community Production (NCP). The NCP in the Chukchi Shelf and Canada Basin reported in previous studies are summarized in Table 4.7. As primary production is patchy and widely variable on the shelf and in coastal regions on the interannual time scale, it is very difficult to set values for each month or find the best value suitable for the entire region. However, we noticed some general patterns for seasonal variation in NCPs in all three subregions. All across the western Arctic Ocean — in the shelf, slope, and southern basin areas — the growth season starts in May–June. The NCP peaks appear in June-July, with possible shift towards earlier time in the southern Chukchi Shelf and towards later in the northern Canada Basin. However, due to totally different nutrient supply mechanisms (Ouyang et al. 2020; Mathieu and Arrigo, 2020), the evolution of NCPs deviates from each other in the three subregions as the seasons proceed. The Chukchi Shelf benefits from sustained nutrient supply from Pacific Water, which supports a high NCP lasting through summer to fall. The coastal Beaufort Sea nutrient supply is from river discharge, which can create some potential biological hotspots. However, it is likely to be only locally important because the nutrients are contained and consumed within near-coastal regions (Tremblay et al., 2014; Ardyna et al., 2017). In contrast, nutrient sources and supplies are limited in the Canada Basin, only being from ice-trapped brine and the remaining in the mixed layer from the previous winter. Furthermore, summer stratification strengthens its oligotrophic characteristics (Ji et al., 2019; Mathieu and Arrigo, 2020). More interestingly, a recent study of NCP evolution in the western Arctic Ocean found that NCP in the Canada Basin is closely associated with ice melting stages (Ouyang et al., 2020). Therefore, instead of using monthly averaged NCP, we incorporated NCP estimation based on the relationship between ice concentration and NCP into our model. Briefly, NCP (6 mmol C m^{-2} d^{-1}) was relatively high during the actively melting period (ice% 30% to 50%), whereas NCP (1-2 mmol C m^{-2} d^{-1}) was lower in the pre-melt (ice%>80%) and post-melt period (ice%< 15%) (Figure 4.4). This relationship was established by examining the histories of wind and ice in a given location combined with underway measurement of $\Delta(O_2/Ar)$ (Ouyang et al., 2021).

On the other hand, a recent study reported that Chl a concentration and integrated production increased by 26% and 96%, respectively, on the Chukchi Shelf from 1998 to 2018 (Lewis et al. 2020). According to this result, we applied an increase of NCP by 30% from 1994 to 2019 on the Chukchi Shelf in our model exercise. In contrast, the NCP in the Canada Basin and Beaufort Sea was much lower than that on the Chukchi Shelf and no significant trend was found. Thus, we set a

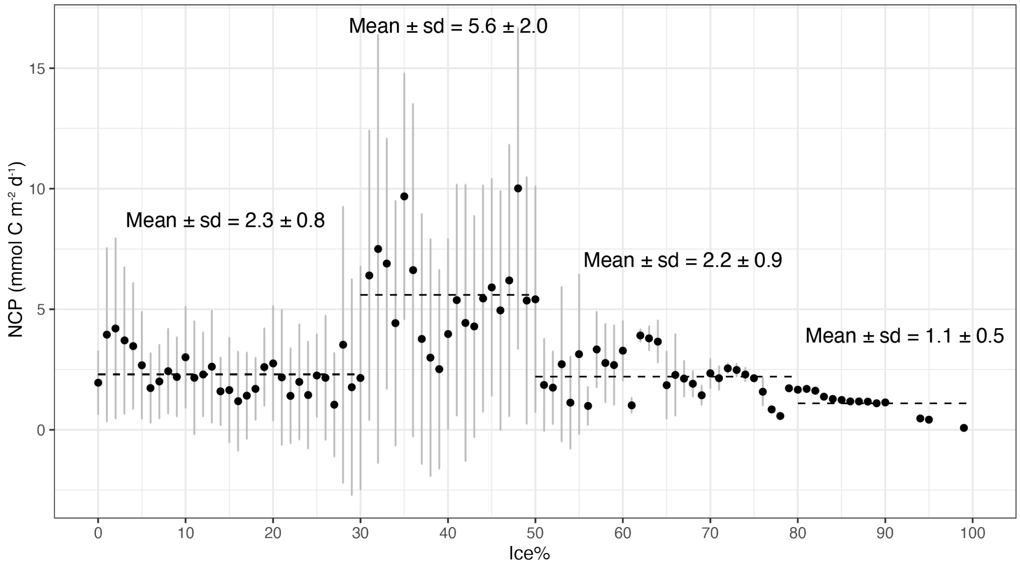

Figure 4.4: NCP variation with sea ice concentration in the Canada Basin. We measured NCP underway using the O_2/Ar approach during CHINARE cruises in 2016 and 2018 (see Ouyang et al. 2021). Here, we examined the correlation between NCP and sea ice concentration by averaging NCP for every 1% ice concentration interval. Black dots and grey bars are the means and standard deviations of NCP at the corresponding ice%. We also examined the means and standard deviations of NCP for four larger ice% ranges (<30%, 30%-50%, 50%-80%, and >80%), which are noted in the figure.

Table **4.1:** **Preset monthly NCP for simulation**

<table>
<tr><th rowspan="2">NCP
(mmol C m^{-2} d^{-1})</th><th colspan="2">Chukchi Sea</th><th rowspan="2">Beaufort Sea</th><th rowspan="2">Canada Basin</th></tr>
<tr><th>Southern</th><th>Northern</th></tr>
<tr><td>Jan</td><td>0</td><td>0</td><td>0</td><td>0</td></tr>
<tr><td>Feb</td><td>0</td><td>0</td><td>0</td><td>0</td></tr>
<tr><td>Mar</td><td>0</td><td>0</td><td>0</td><td>0</td></tr>
<tr><td>Apr</td><td>10</td><td>0</td><td>0</td><td>0</td></tr>
<tr><td>May</td><td>30</td><td>10</td><td>2</td><td>0</td></tr>
<tr><td>Jun</td><td>20</td><td>30</td><td>20</td><td rowspan="5">Across July to October, 1 mmol C m^{-2} d^{-1} for ice% > 80%;
3 mmol C m^{-2} d^{-1} for 50% < ice% < 80%;
6 mmol C m^{-2} d^{-1} for 30% < ice% < 50%;
2 mmol C m^{-2} d^{-1} for ice%< 15%.</td></tr>
<tr><td>Jul</td><td>35</td><td>20</td><td>10</td></tr>
<tr><td>Aug</td><td>20</td><td>20</td><td>5</td></tr>
<tr><td>Sept</td><td>25</td><td>10</td><td>3</td></tr>
<tr><td>Oct</td><td>15</td><td>4</td><td>3</td></tr>
<tr><td>Nov</td><td>0</td><td>0</td><td>0</td><td>0</td></tr>
<tr><td>Dec</td><td>0</td><td>0</td><td>0</td><td>0</td></tr>
</table>

constant seasonal cycle of NCP in these two regions over the simulation period. The preset NCPs used in our model are presented in Table 4.1.

Simulation step. The goals of this model exercise are to fill the data coverage gaps in both temporal and spatial and to evaluate the CO_2 flux trends in western Arctic Ocean. The model resolutions are 1 day in time and 1° × 1° grid in space. The initial sea surface pCO_2 is set as 340 μatm assuming that pCO_2 is equilibrated with atmospheric pCO_2 on the day of Jan 1, 1994. For each simulation step in each grid, sea surface pCO_2 was calculated from TA and DIC at the corresponding step using the 'seacarb' package in R language (Gattuso et al., 2018). The daily change in DIC inventory in the surface mixed layer was calculated as follows:

$$\Delta \mathrm{DIC}_t = (\mathrm{FCO}_{2t} + \mathrm{NCP}_t + \mathrm{E}_t) \times \Delta t / (\mathrm{MLD}_t \times \rho) + \Delta \mathrm{DIC}_{(\mathrm{diluted})t} \quad (4.9)$$

where FCO_{2t}, NCP_t, and $\Delta DIC_{(diluted)t}$ indicate the changes in DIC inventory in the mixed layer induced by CO_2 air-sea flux, net community production, and meltwater dilution at simulation time step t, respectively. The surface seawater density, ρ, is calculated using SST and SSS. The calculation of FCO_2 term was similar to equation (4.3) with daily ice% correction (equation 4.8). We computed the change in DIC by dilution ($\Delta DIC_{(diluted)t}$) by simplifying the ice melt dilution or ice formation processes in the simulation and assuming that ratio of TA/DIC in the ice nearly equals to that in the surface seawater. Thus,

$$\Delta \mathrm{DIC}_{(\mathrm{diluted})t} = (\mathrm{TA}_{t+1} - \mathrm{TA}_t) / \mathrm{TA}_t \times \mathrm{DIC}_t \quad (4.10)$$

Due to limitations of the box model, the physical mixing processes are dependent on the variations of SSS and MLD, thus, we are not able to resolve the dynamic vertical or lateral mixing. Therefore, we introduced an adjustable error term (E) to equation (4.9). This error term accounts for any other perturbation in DIC inventory, such as respiratory DIC addition, deep water upwelling, local water mixing and brine rejection. We adjusted the E term for each month and for each subregion to minimize the systematic bias (see section 4.3.3.2). DIC at time step *t+1* was iteratively calculated as follows,

$$\mathrm{DIC}_{t+1} = \mathrm{DIC}_t + \Delta\mathrm{DIC}_t \tag{4.11}$$

With the new DIC and TA for the next simulation step, a new $p\mathrm{CO_2}$ was calculated, and this simulation process repeats until the last day. In short, this data-driven model exercise can provide us a daily $p\mathrm{CO_2}$ map with 1° × 1° spatial resolution over the entire western Arctic Ocean from 1994 to 2019 and can, to some degree, reflect the mechanistic based and data-driven nature.

4.3.4 Model validation

To evaluate the performance of our box model, we compared simulated $p\mathrm{CO_2}$ with the synthesized $p\mathrm{CO_2}$ on the same day at the given grid. Over the entire western Arctic Ocean, the mean of differences between simulated and observed $p\mathrm{CO_2}$ is 1.4 μatm and the root mean square error (RMSE) is 50.9 μatm. The model performance varies among three subregions. To be specific, simulated $p\mathrm{CO_2}$ better fits the observed $p\mathrm{CO_2}$ in the Canada Basin than in the Beaufort Sea and Chukchi Sea. Based on daily

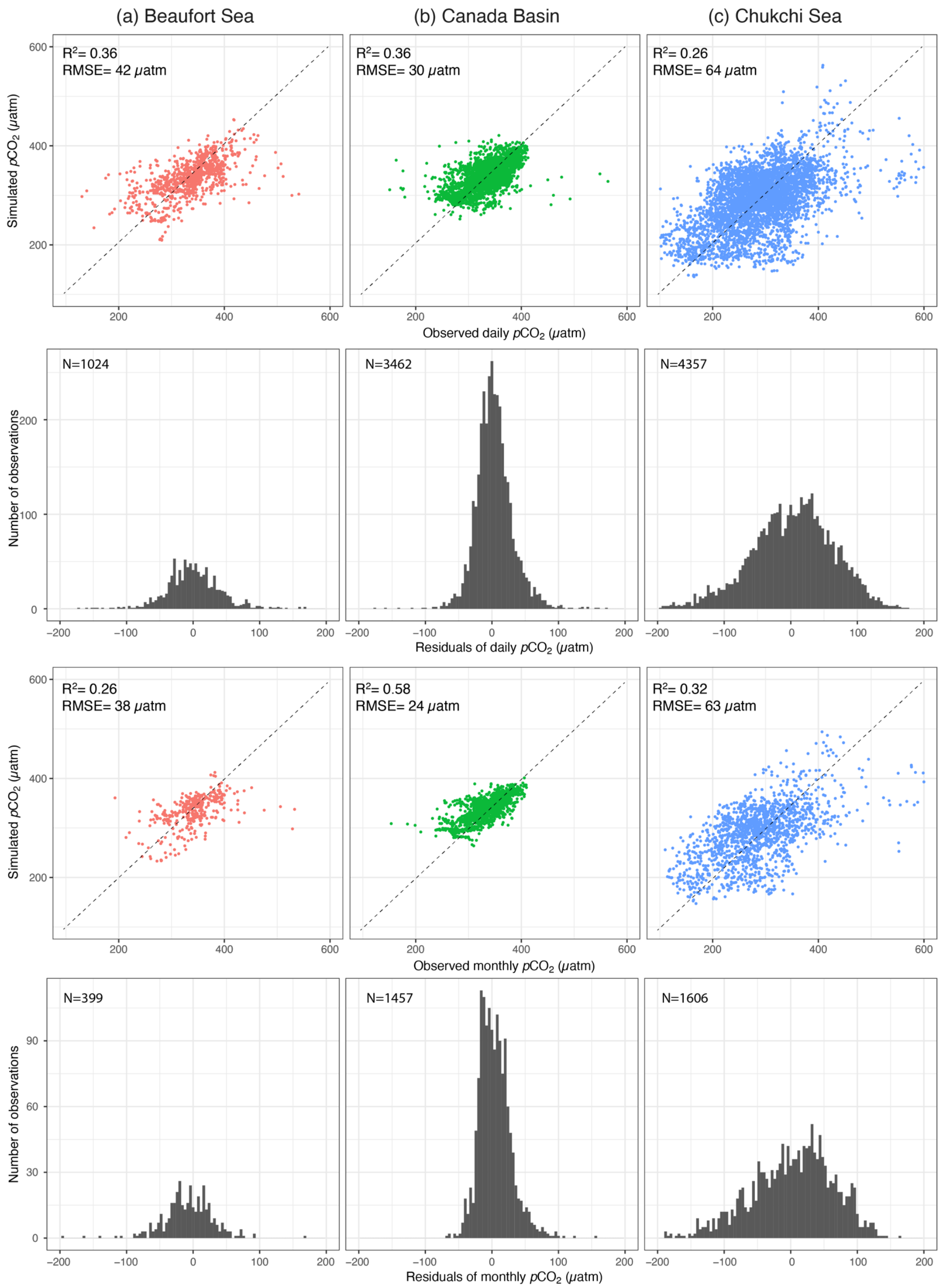

Figure 4.5: Sea surface $p\mathrm{CO_2}$ Observations versus modeled $p\mathrm{CO_2}$ in (a) the Beaufort Sea, (b) the Canada Basin, and (c) the Chukchi Sea. The comparisons were conducted using both daily (upper panels) and monthly (lower panels) gridded averages. The R^2 and root mean squared error (RMSE) are noted in the figures. N is the number of data pairs used for statistical analysis. The dashed 1:1 line is provided for reference.

resolution result, the RMSEs are 30.4 μatm, 42.2 μatm, and 64.4 μatm in the Canada Basin, Beaufort Sea and Chukchi Sea, respectively (Figure 4.5). This is likely because the model could not capture some high-frequency variabilities in the shelf regions including coastal upwelling in the Beaufort Sea and patchy biological production and vertical mixing in the Chukchi Sea. The residuals in all three subregions have a normal or nearly normal distribution and the average biases are less than ±3 μatm (Figure 4.5). When we average daily pCO_2 into a monthly mean to do further comparisons, the RMSEs become smaller (23.7 μatm, 38.1 μatm and 63.4 μatm in the Canada Basin, Beaufort Sea and Chukchi Sea, respectively), which are comparable to the results of neural network interpolation approaches which are also based on monthly time resolution (Laruelle et al. 2017; Yasunaka et al. 2018) over the entire western Arctic Ocean.

While the comparison of residuals and RMSEs allow us to quantitatively assess the performance of our model, it does not provide sufficient information about validity of the reconstruction of complex seasonality of pCO_2. To check this capability of our box model, we further examined the average residual and RMSE for each month in a particular subregion. We found that, in the absence of vertical and lateral mixing terms in the model, the preset regional NCPs tend to cause an extremely low summer pCO_2 in the Chukchi Sea and Beaufort Sea in some summer months. To reduce this systematic error, we constrain the average residual in each month within ±10 μatm by adjusting the error term, E (Table 4.8), in equation (4.9). Through trial-and-error processes, we found that a negative E is needed for some summer months in the Chukchi Sea and Beaufort Sea to achieve the criteria of average bias of within ±10 μatm. A negative E indicates an addition of DIC in the mixed layer, which is likely induced by horizontal advection of DIC or local mixing with deep water on the shelf and coastal region. In contrast, there is no apparent seasonal discrepancy between modeled and observed pCO_2 in the Canada Basin, indicating that DIC perturbation due to mixing in this region is minimum. Thus, we set E term to 0 in the Canada Basin. For winter and early spring, a small negative E (up to -2 μmol kg^{-1} day^{-1}) is set to account for possible net respiration and winter ventilation (Shadwick et al., 2011). Adding an E-term not only leads to a smaller RMSE, but also better captures pCO_2 seasonality. We checked simulated climatological monthly mean of pCO_2 with the observed monthly means extracted from SOCAT dataset (Figure 4.6). We give the comparisons in 15 grids that represent the typical locations with relatively more abundant observed data. Generally, our simulation can capture the seasonality of pCO_2 through spring to fall on the Chukchi Sea shelf and in the Beaufort Sea. The maximum pCO_2 appears in the late spring before the growth season start whereas minimum pCO_2 appears in the early summer. In contrast, the modeled climatological monthly pCO_2 deviated more from the observed seasonality of pCO_2 in the Canada Basin because the climatological monthly means can lump the interannual variations in pCO_2, which primarily depends on the interannual variation in ice condition (Degrandpre et al., 2020). From the simulated results, we noticed that the seasonality of pCO_2 changes in both phase and magnitude in the periods before and after year 2007, in which the western Arctic Ocean experienced a massive sea ice retreat. Since then, multi-year ice was gradually replaced by first-year ice. However, it is very challenging to validate this shift with limited observations.

4.3.5 Uncertainty analysis

There are two main uncertainties in estimating the CO_2 flux. The gas exchange velocity parameterization contributes the largest uncertainty, which is about 20% (Wanninkhof, 2014). Applying ice correction for gas exchange velocity could further enlarge the uncertainty up to ~40% (Loose et al., 2014; Lovely et al. 2015). The second uncertainty for CO_2 flux comes from analytical errors. The uncertainty for the measurements is about ± 0.5 μatm for air pCO_2 and ± 2 μatm for sea surface pCO_2. Accounting for a few pCO_2 calculated from DIC and TA with an uncertainty of ±5-7 μatm (Chen et al., 2015; Woosley et al., 2017), the total uncertainties for pCO_2 measurements are less than 1% of the long-term mean. Combined with an uncertainty of 5% for sea-ice concentration (Peng et al., 2013) and uncertainties of 20% to 40% for gas exchange velocity parametrization, we estimated the overall uncertainty of the observation-based CO_2 fluxes calculation to be 21% to 42% following the error propagation equation (i.e. $[0.2^2(\text{or } 0.4^2) + 0.05^2 + 0.01^2]^{0.5}$).

For the estimates using model-simulated pCO_2, additional uncertainty comes from the deviation between simulated pCO_2 and observed pCO_2. As the pCO_2 observations are unevenly distributed in season, we seperately assessed the uncertainties of simulated pCO_2 for winter-spring (November-June) and summer-fall (July-October) for each subregion. For winter-spring, the uncerntainties of simulated pCO_2 (RMSE) are 23 μatm, 26 μatm, and 58 μatm in the Canada Basin, Beaufort Sea and Chukchi Sea, respectively, which are about 43%, 58%, 116% of the long-term average ΔpCO_2 in winter-spring in the respective subregion. Accordingly, the uncertainties of model-based CO_2 fluxes in winter-spring are 52%, 65% and 120% in the Canada Basin, Beaufort Sea and Chukchi Sea, respectively, assuming the uncertainties of for gas exchange velocity parametrization is 30% (i.e. $[0.3^2 + 0.05^2 +$

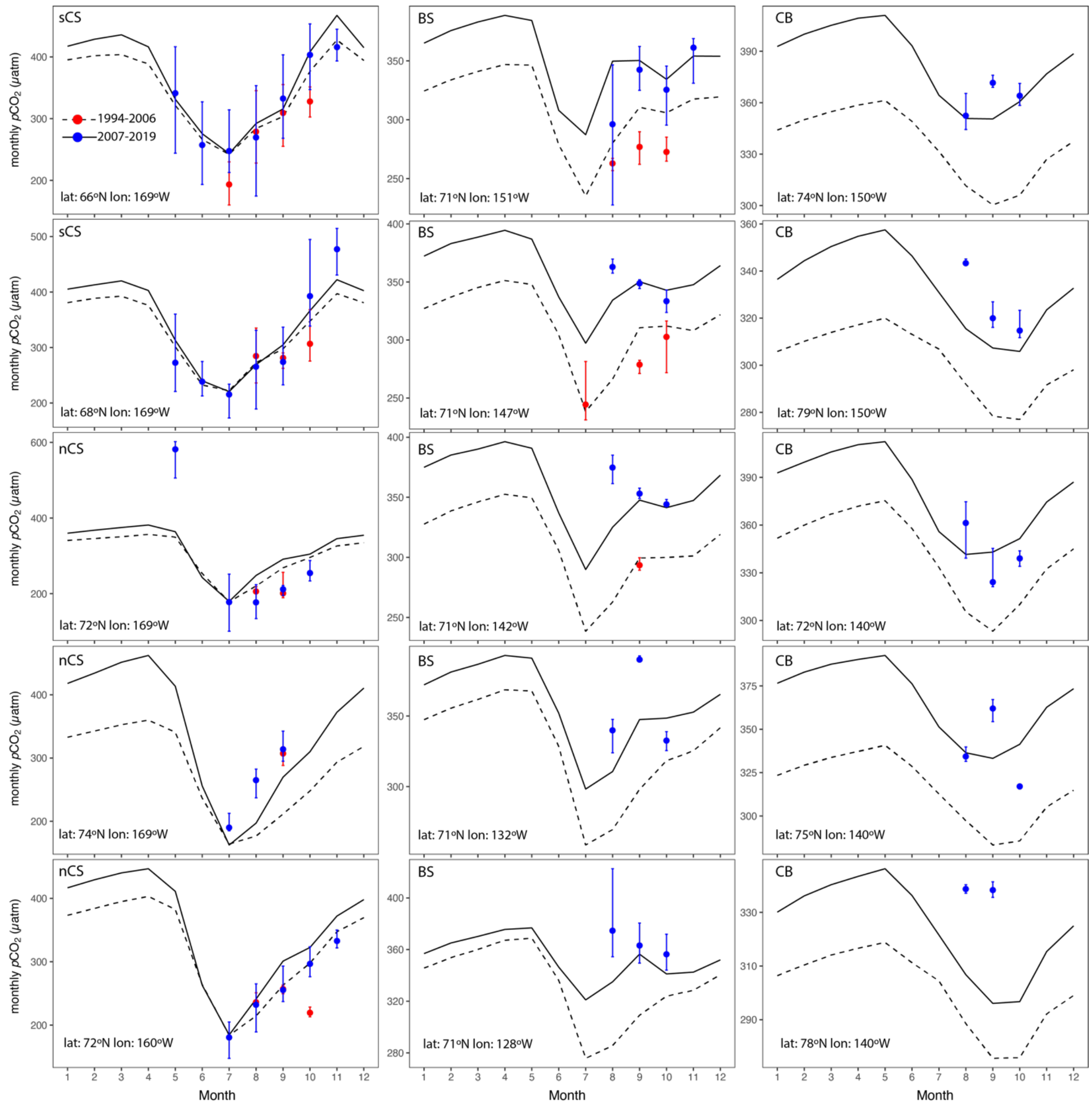

Figure 4.6: Simulated climatological monthly mean pCO_2 (lines) versus the monthly mean extracted from SOCAT dataset (dots) at 15 selected grid locations in the southern Chukchi Sea (sCS), northern Chukchi Sea (nCS), Beaufort Sea (BS) and Canada Basin (CB). The dashed and solid lines indicate the climatology of pCO_2 for the periods of 1994-2006 and 2007-2019, respectively. The red and blue dots are climatological monthly mean of observed pCO_2 in the periods of 1994-2006 and 2007-2019, respectively. The error bars represent the interannual variability, reported as the maximum and minimum recorded pCO_2 value in the given month and grid.

$0.01^2]^{0.5}$+(uncertainty of simulated $pCO_2)^2$). For summer-fall, the uncertainties of simulated pCO_2 (RMSE) are 31 µatm, 42 µatm, and 62 µatm in the Canada Basin, Beaufort Sea and Chukchi Sea, respectively, which are about 61%, 81%, and 58% of the long-term average ΔpCO_2 in summer-fall, resulting in uncertainties of 68%, 86% and 65% in CO_2 fluxes in respective subregions.

4.4 Results

4.4.1 Monthly climatology of ΔpCO_2

With the synthesized pCO_2 dataset, we examined the monthly climatology of sea-air gradient of pCO_2 over years from 1994 to 2019. Although the pCO_2 observations were unevenly distributed in space and time, we can still clearly see the different patterns in ΔpCO_2 between winter-spring (November to June) and summer (July to October). A weak positive ΔpCO_2 (<45 μatm) was sustained from December through April, demonstrated by limited number of observations in the Beaufort Sea (Figure 4.7). These results suggest a weak carbon source over the western Arctic Ocean during winter-spring. The highest positive ΔpCO_2 appeared in May and early June in the northern Chukchi Sea and the mouth of Mackenzie River, ranging from 100 to 200 μatm, which reflected a potential strong carbon source in those areas (Figure 4.7). These high positive ΔpCO_2 values likely reflect the accumulation of pCO_2 produced as a result of water column and benthic respiration in nearshore waters over the winter and early spring under the ice cover.

The transition of carbon source-sink status occurred in late May through early June. The areas of positive ΔpCO_2 reduced with sea ice retreat and more areas with

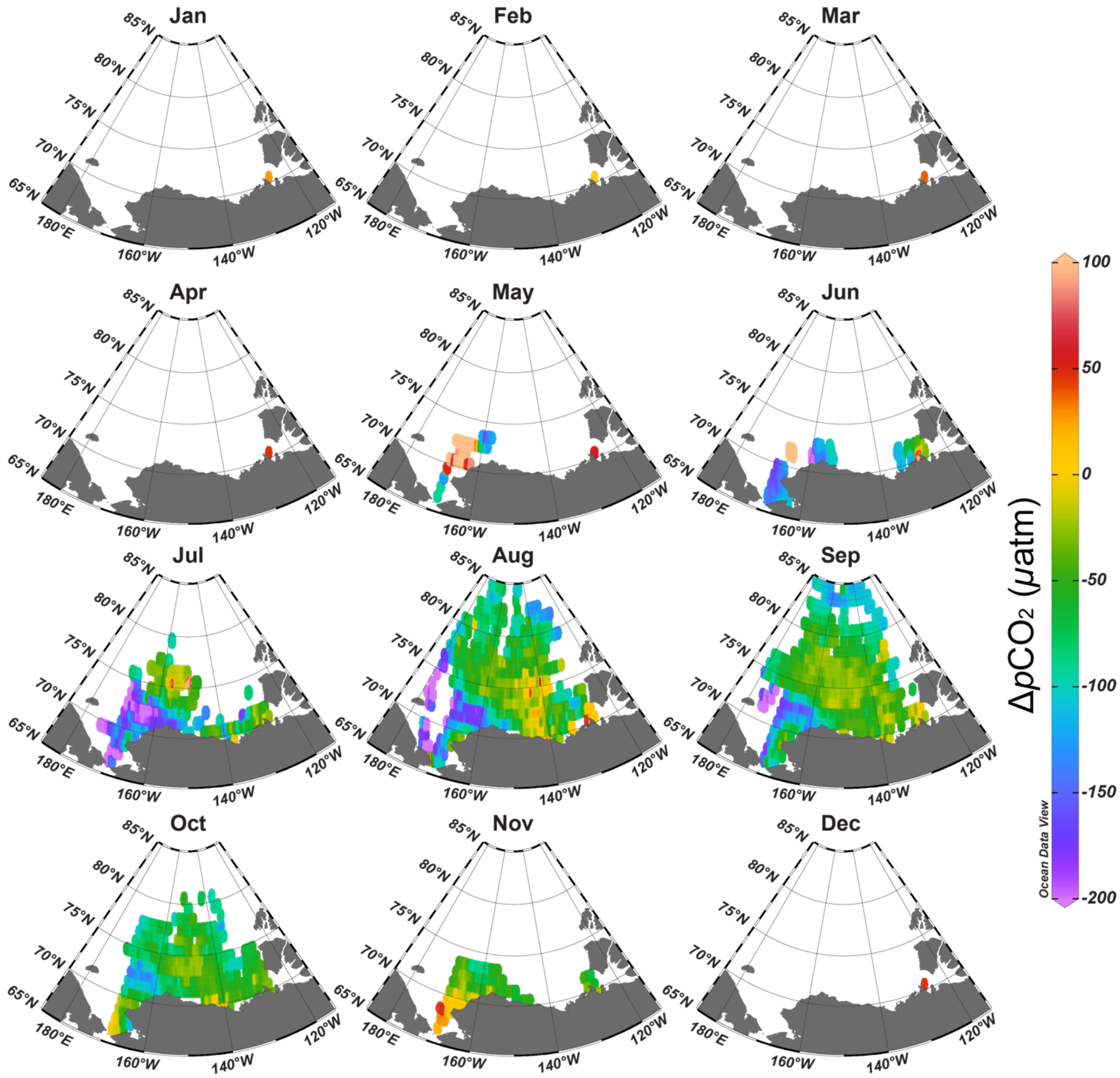

Figure 4.7: Observation-based monthly climatology of $\Delta p CO_2$ in 1°×1° grids in the western Arctic Ocean. $\Delta p CO_2$ is defined as $pCO_2^{sea} - pCO_2^{air}$ and negative values of $\Delta p CO_2$ indicate that sea surface pCO_2 is lower than the atmospheric pCO_2.

negative ΔpCO_2 extended from the southern Chukchi Sea to the northern part and from Beaufort coastal sea into Canada Basin in the following summer months. Starting in July, the Chukchi Sea turned into one of the largest CO_2 sinks in the Arctic Ocean as a result of seasonal primary production, indicated by the greatest negative ΔpCO_2 (-150 to -200 μatm). These negative ΔpCO_2 values can persist through the entire summer to September in the Chukchi Sea. In contrast, the initial large negative ΔpCO_2 in both the Beaufort Sea and central Canada Basin cannot be maintained through the end of summer. Instead, ΔpCO_2 gradually reduced in absolute size toward the atmospheric equilibrium, indicating a weakening carbon sink as the seasons progressed (Figure 4.7). At a few locations in the southern Canada Basin and Beaufort Sea, ΔpCO_2 can even become positive during extreme warming and ice melting events and change the region from a CO_2 sink to a CO_2 source (data not shown). However, this transition lasted only for a few days or weeks, which cannot change the dominant carbon sink status over the entire western Arctic Ocean in summer-fall. Note that the variation in ΔpCO_2 at the higher latitudes in summer was relatively small due to a much less extensive ice melt and less warming and much weaker biological activity. Starting in November as sea ice started to form, ΔpCO_2 might shift from weak negative to positive in the Beaufort Sea and Canada Basin, which is likely a result of brine rejection and vertical mixing during ice formation (Shadwick et al., 2011; Else et al., 2012). In addition, a large area of positive ΔpCO_2 appeared in the southern Chukchi Sea, which is likely due to benthic respiration and upwelling events.

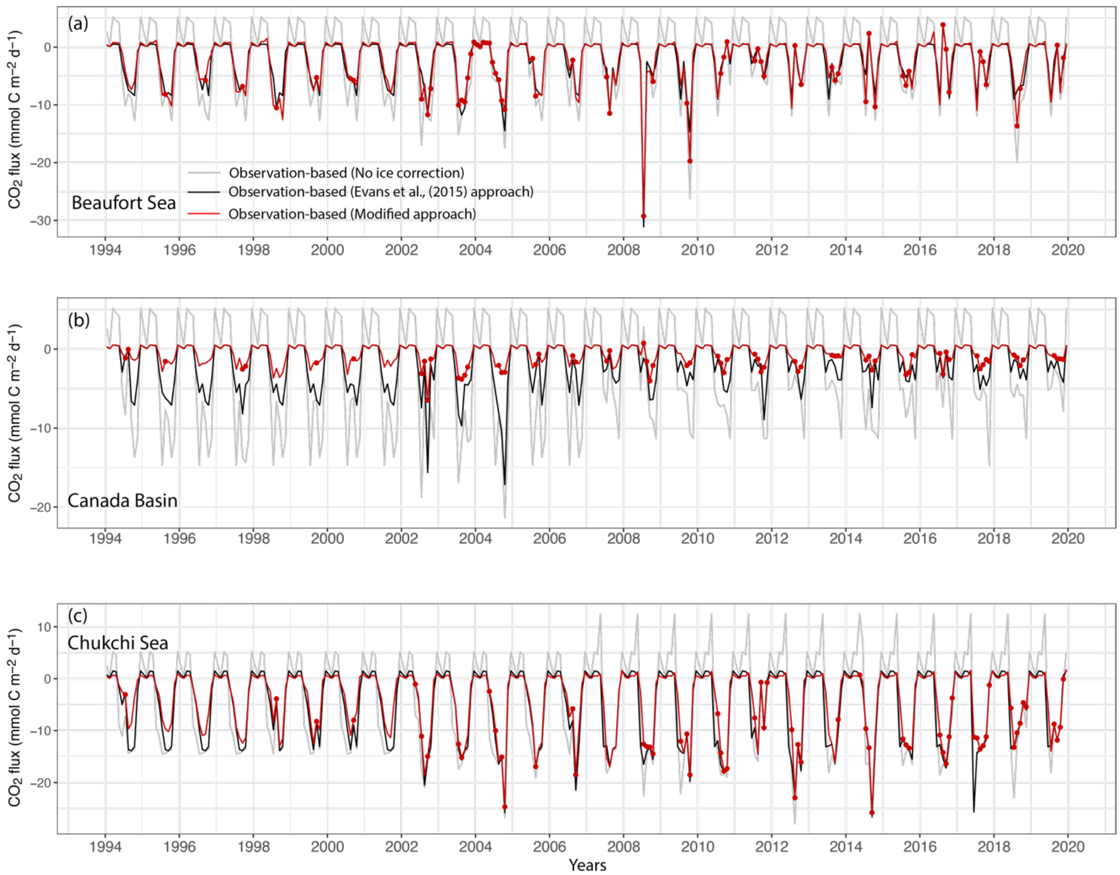

Figure 4.8: Temporal variations of CO_2 flux in the (a) Beaufort Sea, (b) Canada Basin, and (c) Chukchi Sea. Grey, black and red lines represent monthly CO_2 fluxes based on observations, estimated by using the approach of no ice correction, ice correction described in Evans et al., (2015) and modified ice correction in this study, respectively. Red dots show the months, in which observations are available. For those months without any observations, we reconstructed monthly CO_2 flux with climatological monthly means separately for the periods of 1994-2006 and 2007-2019 (See Tables 4.9-4.12). Note that negative values of CO_2 flux indicate CO_2 uptake from the atmosphere.

4.4.2 Seasonal and interannual variabilities of regional CO_2 flux

Due to the unique environmental settings in the Arctic Ocean, the direction and magnitude of the CO_2 flux is not only determined by ΔpCO_2, but also greatly regulated by sea ice cover. Thus, we reported the area-weighted monthly CO_2 flux for each subregion with three values: (1) CO_2 flux without ice% correction, (2) CO_2 flux adjusted for sea ice concentration (ice%) following the process in Evans et al., (2015), and (3) CO_2 flux adjusted for ice% following the modified
approach in this study (Figure 4.8 and Tables 4.9-4.12). In fact, the values of sea-air CO_2 flux without ice% correction provide an upper bound of CO_2 flux for a future Arctic Ocean, in which sea ice disappears in the summer and is much less in the winter. Furthermore, the difference between CO_2 fluxes with and without the ice% correction clearly reflects the suppression of CO_2 gas exchange by ice. Although not all months have pCO_2 observations, we assumed that the CO_2 flux in a given month without an observation is similar to the climatological monthly mean in that month. Therefore, we first filled the data gap with climatological monthly means within each subregion for the periods of 1994-2006 and 2007-2019, and then filled the remaining gaps across all the subregions (Tables 4.9-4.12).

After filling in data gaps, a more complete seasonal cycle of CO_2 flux appeared. For the winter-spring months (November to June), the potential CO_2 efflux was suppressed by ice cover (grey vs red and black lines in Figure 4.8), resulted in a very weak sea-to-air CO_2 flux (~ 0.4-1.0 mmol m^{-2} d^{-1}) in all subregions. Because of this reason, the potential large uncertainty in estimating winter-spring pCO_2 due to lack of sufficient observational data likely will not dominate the uncertainties in the annual flux estimation. As larger areas became open water in the subsequent season and the growth season started, the rate of CO_2 uptake from the atmosphere gradually strengthened. The largest influx of CO_2 repeatedly occurred in September and October due to relatively large ΔpCO_2 and the strongest wind during the year (Evans et al., 2015). The long-term means of monthly CO_2 fluxes among summer months can reach up to -7.5, -5.0 and -19.4 mmol m^{-2} d^{-1} in the Beaufort Sea, Canada Basin, and Chukchi Sea, respectively (Figure 4.8 and Tables 4.9-4.12). Starting in November, the CO_2 influx may shift to an equilibrium or an outgassing state. Such patterns of seasonal CO_2 flux evolution were generally similar to each other in all subregions, but some new features in a finer scale in the Beaufort Sea have appeared in recent years. For example, an initial strong CO_2 uptake in the late spring (June) was rapidly weakened in summer months (July to September), and then strengthened again in October (Figure 4.9 a).

By comparing CO_2 fluxes derived from Evans et al., (2015) and our modified approaches, we found that the difference was relatively small in both the Beaufort Sea and Chukchi Sea (red and black lines in Figure 4.8 a&c), in which data coverage is higher and seasonal cycles of ice retreat and advance were relatively stable from year to year. The difference, however, becomes much larger in the Canada Basin (Figure 4.8 b). For instance, the monthly CO_2 flux estimated by Evans et al. (2015) approach can be up to 5 times higher than the results of our modified approach (Figure 4.8 b). Methodologically, the relatively higher values by Evans et al. (2015) approach came from overweighting the observed fluxes in the southern Canada Basin, where higher CO_2 fluxes coincide with larger open-water area. The nonlinear effects between those two factors in the method led to a potential bias in the assessment of regional average. In comparison, our modified approach applied the sea ice correction on a pre-weighted FCO_2, largely reducing the artifacts (see more discussion in Supplementary

Information). As such, we chose the modified method for the subsequent analysis of seasonal and interannual variability. As the CO_2 uptake in summer months (July-October) dominates the annual flux, we used the summer maximum-to-minimum difference and annual summer mean to characterize the seasonal range and interannual variability of air-sea CO_2 flux (Figure 4.10). We noticed that the CO_2 flux in low-ice year tended to be large (e.g., massive melting events in 1998, 2007, 2008, and 2012 were likely to induce larger CO_2 fluxes), while the CO_2 flux in high-ice year (1994,1996, and 2013) were weak (Figure 4.10, Figure 4.14). However, the CO_2 fluxes did not always follow sea ice changes and other climate drivers may play roles (see discussion in section 4.5.2). By comparing the ranges of seasonal and interannual variations in CO_2 fluxes, we also found that, for most years, the Canada basin is the region where interannual variations exceed the seasonal variations, whereas the Beaufort and Chukchi Seas are the opposite.

4.4.3 Seasonal and interannual variabilities of regional CO_2 sink

In order to examine the long-term change in total CO_2 sinks, we conducted and compared three calculations of CO_2 sink (Figure 4.11). For the first approach, we used the regional monthly means of CO_2 flux, which was corrected for sea ice, to multiply the days of the month and the ocean surface area to compute the total CO_2 sink in a given subregion (followed the methods in Evans et al., 2015). The second one is our modified approach (see Method; Figure 2). Using monthly CO_2 flux map corrected for every 1°×1° grid, we calculated the amount of CO_2 uptake or outgassing in each grid and integrate all grids to get the monthly carbon sink for the given subregion. For the third approach, we used modeled pCO_2 to calculate daily CO_2 uptake for each 1°×1° grid, and then summed up the results of all grids into a regional monthly value.

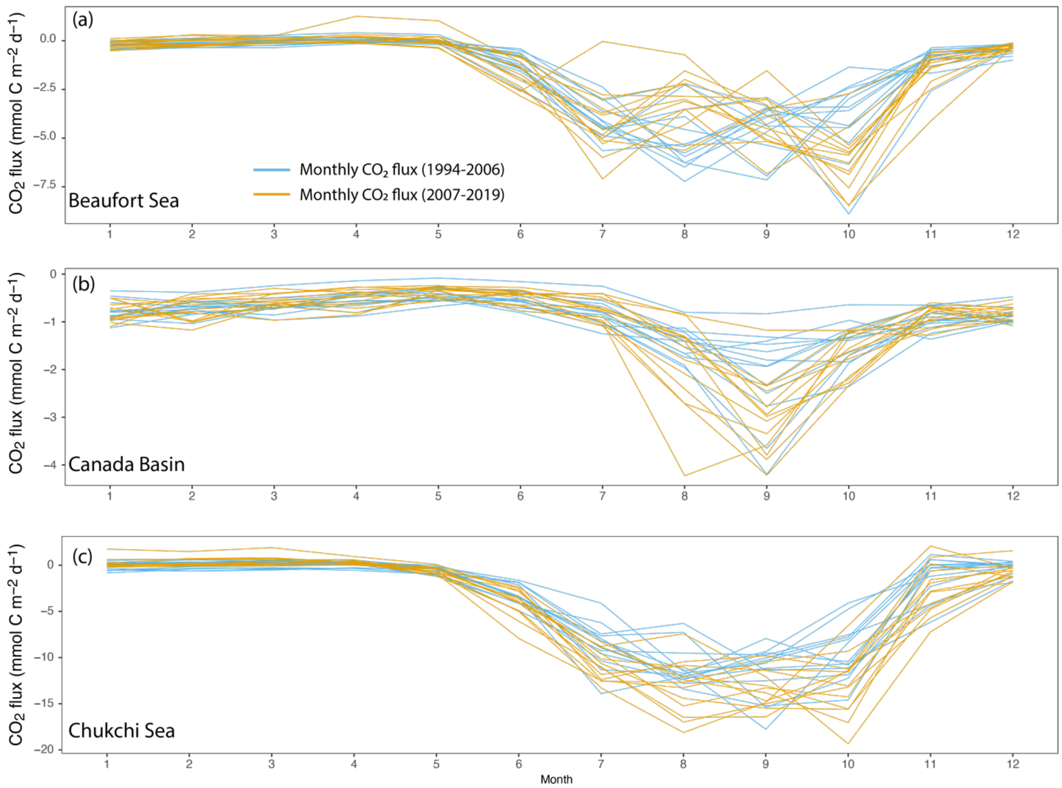

Figure 4.9: Monthly variations of CO_2 flux in the (a) Beaufort Sea, (b) Canada Basin, and (c) Chukchi Sea. The results of CO_2 fluxes derived from the modified approach are shown here. To examine the possible changes in CO_2 flux seasonality, we separately exhibit the monthly CO_2 flux variation for two periods: 1994-2006 (blue lines) and 2007-2019 (orange lines). Note that negative values of CO_2 flux indicate CO_2 uptake from the atmosphere.

All three subregions showed a similar seasonality in CO_2 sinks, characterized by a near-neutral or a very weak CO_2 source in winter and spring and a much larger CO_2 sink in summer and fall (Figure 4.11). CO_2 uptake in July through October contributed 86-99% and 60-87% of the total year-round sink based on observations and modeled results, respectively (Table 4.2). Similar to the CO_2 flux estimate, the difference in the CO_2 sink between Evans et al., (2015) and our modified approaches was smaller in both the Beaufort Sea and Chukchi Sea (red and black lines in Figure 4.11 a&c), while it becomes much larger in the Canada Basin (Figure 4.11 b). We found that our box model largely captured the seasonal and interannual variations in all three subregions. It is encouraging that the modeled results matched very well with the results of our modified observation-based approach, except for some summer months with extreme values in the Beaufort Sea and Chukchi Sea (Figure 4.11 a&c). Therefore, we will focus on the result of our modified approach and modeled results in the following section.

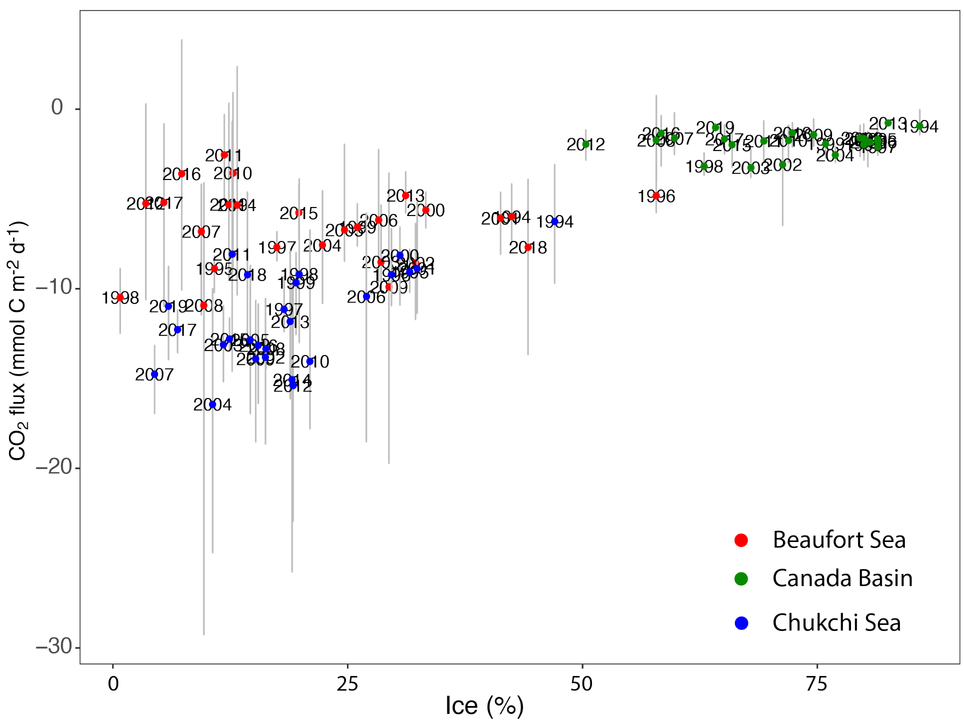

Figure 4.10: Regional CO_2 flux versus ice concentration in summer (July to October). The colored dots represent the summer means of CO_2 flux in the Beaufort Sea (red), Canada Basin (green) and Chukchi Sea (blue) in particular year (noted in figures). The error bars (grey) associated with the data represent the seasonal variability, reported as the highest and lowest monthly values through July to October for a given subregion.

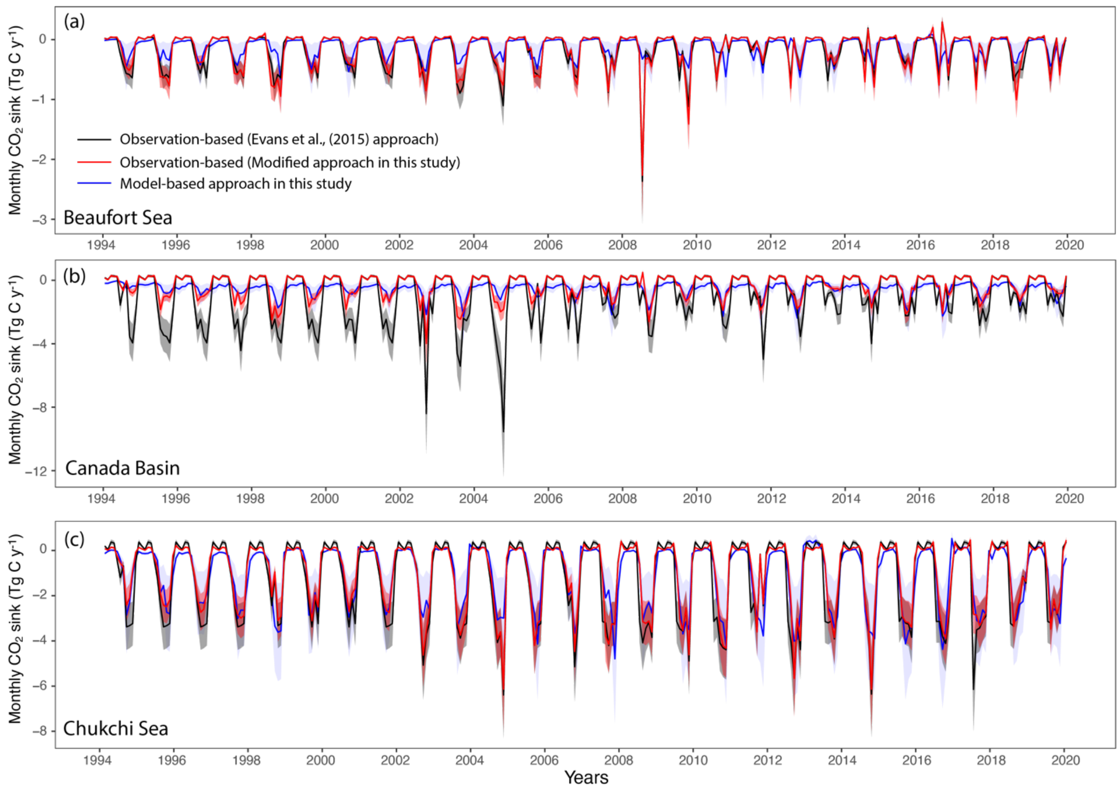

Figure 4.11: Temporal variations in the carbon sink in the (a) Beaufort Sea, (b) Canada Basin, and (c) Chukchi Sea. Black and red lines indicate the observation-based carbon sink changes, estimating using the approach in Evans et al., (2015) and modified approach in this study, respectively. Blue lines indicate the modeled-based estimation of carbon sink changes. The shaded areas correspond to the uncertainties of carbon sink estimation (see Section 4.3.5).

Table **4.2:** **Regional annual and summer (July-October) carbon sink (Tg C yr^{-1}). Negative sign denotes a CO_2 flux from the atmosphere into the ocean. The surface areas of each subregion are 0.20 × 10^6 km^2 for the Beaufort Sea, 1.48 × 10^6 km^2 for the Canada Basin, and 0.66 ×10^6 km^2 for the Chukchi Sea. ANOVA was performed to test whether the yearly change calculated for 1994-2019 was significantly different from 0. The asterisks indicate the levels of significance (***P < 0.001, **P < 0.01, *P < 0.05).**

year	Beaufort Sea				Canada Basin				Chukchi Sea			
	Annual		Summer		Annual		Summer		Annual		Summer	
	Obs-based[a]	Modeled	Obs-based[a]	Modeled	Obs-based[a]	Modeled	Obs-based[a]	Modeled	Obs-based[a]	Modeled	Obs-based[a]	Modeled
1994	-1.6	-1.3	-1.7	-1.1	-1.8	-2.8	-2.2	-1.5	-7.9	-8.2	-6.2	-7.3
1995	-2.6	-1.5	-2.7	-1.2	-4.7	-5.1	-5.0	-2.7	-12.2	-11.4	-9.0	-9.0
1996	-1.2	-1.5	-1.3	-1.1	-3.9	-5.9	-4.2	-2.7	-12.6	-12.1	-9.2	-8.9
1997	-2.3	-1.7	-2.3	-1.3	-4.8	-5.8	-5.1	-2.9	-15.6	-13.6	-11.0	-9.9
1998	-3.4	-1.5	-3.2	-1.3	-8.5	-8.0	-8.5	-4.7	-12.5	-13.7	-9.0	-12.5
1999	-1.9	-1.6	-1.9	-1.4	-4.6	-5.8	-4.9	-3.5	-12.6	-10.7	-9.6	-10.3
2000	-1.5	-1.5	-1.6	-1.3	-4.0	-5.7	-4.3	-3.0	-10.3	-10.4	-8.0	-9.7
2001	-1.6	-1.2	-1.7	-1.1	-4.1	-6.3	-4.4	-3.3	-11.3	-10.0	-8.8	-9.0
2002	-2.4	-1.7	-2.4	-1.5	-7.3	-8.0	-7.6	-4.8	-17.1	-11.6	-13.6	-10.3
2003	-2.4	-1.4	-2.4	-1.3	-7.8	-7.6	-8.1	-5.0	-17.2	-11.0	-12.9	-10.6
2004	-2.2	-1.3	-2.2	-1.2	-6.3	-5.5	-6.6	-3.2	-17.6	-12.1	-16.1	-11.0
2005	-2.0	-1.5	-2.0	-1.3	-3.8	-5.8	-4.1	-3.2	-16.8	-11.7	-12.7	-11.0
2006	-1.8	-1.6	-1.8	-1.4	-3.8	-6.7	-4.2	-3.6	-13.6	-10.9	-10.3	-10.4
2007	-2.1	-1.4	-2.1	-1.2	-3.9	-8.2	-4.0	-5.3	-15.2	-14.7	-14.4	-11.5
2008	-3.4	-1.5	-3.3	-1.3	-4.3	-7.1	-4.5	-5.0	-13.1	-12.8	-13.1	-10.8
2009	-2.8	-1.6	-2.8	-1.3	-3.3	-5.0	-3.6	-3.1	-14.0	-13.9	-13.7	-12.8
2010	-1.2	-1.5	-1.1	-1.2	-4.2	-6.7	-4.5	-4.2	-13.6	-13.7	-13.8	-12.6
2011	-0.8	-1.6	-0.8	-1.3	-4.4	-7.0	-4.7	-4.4	-8.1	-14.5	-8.1	-12.0
2012	-1.8	-1.6	-1.6	-1.0	-5.0	-8.2	-5.1	-6.0	-15.0	-14.1	-15.1	-13.5
2013	-1.3	-1.7	-1.4	-1.4	-1.6	-4.0	-1.9	-2.0	-11.6	-11.5	-11.7	-11.7
2014	-1.7	-1.5	-1.6	-1.3	-3.8	-6.0	-4.1	-3.2	-14.4	-16.0	-14.7	-13.8
2015	-1.7	-1.5	-1.7	-1.4	-4.8	-8.1	-5.2	-5.2	-13.1	-17.4	-12.7	-13.8
2016	-1.1	-1.4	-1.1	-1.4	-3.4	-7.6	-3.6	-5.6	-13.8	-13.7	-12.9	-12.7
2017	-1.7	-1.7	-1.6	-1.2	-4.4	-5.9	-4.4	-4.0	-14.0	-13.9	-12.0	-11.7
2018	-2.2	-1.3	-2.2	-1.2	-3.1	-5.5	-3.4	-3.6	-10.9	-13.4	-9.2	-10.9
2019	-1.8	-1.5	-1.6	-1.3	-2.7	-6.2	-2.7	-3.7	-10.8	-13.2	-10.7	-11.4
Mean ± uncertainty	-1.9±0.6	-1.5±1.2	-1.9±0.6	-1.3±1.0	-4.4±1.3	-6.3±4.0	-4.6±1.4	-3.8±2.1	-12.1±3.6	-12.7±7.6	-11.5±3.5	-11.1±6.7
Yearly change ± standard error	0.02±0.02	-0.003±0.003	0.03±0.02	-0.003±0.003	0.07±0.04	-0.04±0.03	0.07±0.04	-0.06±0.03*	-0.13±0.06	-0.16±0.04***	-0.14±0.06*	-0.15±0.03***

[a] Carbon sink was estimated using the modified approach described in this study.

4.5 Discussion

4.5.1 Long-term trend of CO_2 sink

The long-term means of the CO_2 sink based on observations were -1.9 ± 0.6, -4.4 ± 1.3 and -12.1 ± 3.6 Tg C yr^{-1} in the Beaufort Sea, Canada Basin, and Chukchi Sea, respectively (Table 4.2). The modeled results showed similar mean values but with a larger uncertainty: -1.5 ± 1.2, -6.3 ± 4.0 and -12.7 ± 7.6 Tg C yr^{-1} in the Beaufort Sea, Canada Basin, and Chukchi Sea, respectively. Our estimated long-term means of carbon sinks agree well with each other and are comparable to recent studies (Arrigo et al., 2010; Manizza et al., 2019; Table 4.3), but at the lower end of earlier estimates (Bates et al., 2006; Bates and Mathis, 2009; Table 4.3). Compared with estimates in Evans et al. (2015), our estimated CO_2 sink in the Beaufort Sea agrees with theirs, but our estimated CO_2 sink in the Chukchi Sea was much higher than their estimate of -4.4 Tg C yr^{-1}. The most likely reason is due to their underestimation of the area of Chukchi Sea by ~50% (2.9×10^{11} m^2 in Evans et al., (2015) and 6.6×10^{11} m^2 in this study). After adjusting this area, their carbon sink becomes ~-10.0 Tg C yr^{-1}, which is comparable to our result and the results of -9.0 ± 1.1 Tg C yr^{-1} in Arrigo et al. (2010) and -13.3 ± 2.5 Tg C yr^{-1} in Manizza et al. (2019). Combining all three subregions together, the mean carbon sink for the entire western Arctic Ocean was -18.4 ± 5.5 Tg C yr^{-1} based on observation and -20.5 ± 15.6 Tg C yr^{-1} from our model (Table 4.3). These estimated CO_2 sinks agreed well with the numerical model result of -17.6 ± 5.0 Tg C yr^{-1} (Manizza et al., 2019) and the remotely sensed data study (-18.6 ± 3.3 Tg C yr^{-1}, Arrigo et al., 2010) within a similar areal definition of the western Arctic Ocean (Table 4.3).

We examined the long-term trend of carbon sink for each subregion, respectively. We found that none of the trends computed from observations were significant (Table 4.2). Only the modeled result in the Chukchi Sea showed a significantly increased carbon sink at a rate of -0.16±0.04 Tg C yr^{-1} over 1994 to 2019 (Figure 4.12 a & Table 4.2). As CO_2 uptake in the summer accounted for most of the annual sink, we further examined the long-term trends of carbon sink for summer (Table 4.2). Although the CO_2 sink in the Beaufort Sea remained unchanged over years, the summer carbon sink in the Chukchi Sea significantly increased by -0.14 to -0.16 Tg C yr^{-1}, according to both observation-based and modeled results (Table 4.2). Such an increase is consistent with the projection that Chukchi would be an enlarged CO_2 sink based on a recent compilation of $p$$CO_2$ observation (Ouyang et al., 2020). However, observation-based estimates did not confirm the prediction that the carbon sink in the Canada Basin would decrease as $\Delta p$$CO_2$ has reduced by 50% over the past two decades (Ouyang et al., 2020). Instead, our model results showed a slightly larger carbon sink in the Canada Basin (Table 4.2). These contrasting results suggest that the change trend of sea-air gradient of $p$$CO_2$ alone may be not enough to resolve the trend of carbon sink in the Arctic Ocean as other important factors may also play important roles in controlling the changes in carbon sink.

Table **4.3: Estimates of the air-sea CO_2 flux and carbon sink in the western Arctic Ocean.**

Region	Period	Air-sea CO_2 flux (mmol C m^{-2} d^{-1})	Annual CO_2 sink (Tg C yr^{-1})	Method	Reference
Beaufort Sea	1994-2019	-2.2±0.7	-1.9±0.6	Observation	This study
	1994-2019	-1.7±1.4	-1.5±1.2	Box-model	This study
	2006-2013	-1.0±0.6	-4.3±2.5	Biogeochemical Model	Manizza et al. (2019)
	2003-2014	-1.0	-4.0	Observation	Evans et al. (2015)
	1996-2007		-0.9±0.5	Biogeochemical Model	Manizza et al. (2013)
	1998-2003		-9.1±2.4*	Multiple linear regression with remote sensing data	Arrigo et al. (2010)
	1998-2000	-12	-2	Observation	Murata and Takizawa (2003)
Canada Basin	1994-2019	-0.6±0.2	-4.4±1.3	Observation	This study
	1994-2019	-1.0±0.7	-6.3±4.0	Box-model	This study
	2006-2013	0.0	+0.6 ± 1.1	Biogeochemical Model	Manizza et al. (2019)
	1996-2007		−0.5 ± 0.2	Biogeochemical Model	Manizza et al. (2013)
Chukchi Sea	1994-2019	-4.1±1.2	-12.1±3.6	Observation	This study
	1994-2019	-4.3±2.6	-12.7±7.6	Box-model	This study
	2006-2013	-3.0±0.6	-13.3±2.5	Biogeochemical Model	Manizza et al. (2019)
	1997-2014	-5.0±3.0		SOM technique	Yasunaka et al. (2018)
	1997-2013	-4.0±4.0		SOM technique	Yasunaka et al. (2016)
	2003-2014	-3.5 ± 2.0	-4.4	Observation	Evans et al. (2015)
	1996-2007		-2.3±0.6	Biogeochemical Model	Manizza et al. (2013)
	1998-2003		-9.0±1.1	Multiple linear regression with remote sensing data	Arrigo et al. (2010)
	2002-2004	−14.0 ± 2.0	-46.0 ± 6.0	Observation	Bates et al. (2006)
	1998-2000	-12	-11	Observation	Murata and Takizawa (2003)
Western Arctic Ocean	1994-2019		-18.4±5.5	Observation	This study
	1994-2019		-20.5±15.6	Box-model	This study
	2006-2013		-17.6±5.0	Biogeochemical Model	Manizza et al. (2019)
	2003-2014		-10.9 ± 5.7	Observation	Evans et al. (2015)
	1998-2003		-18.6±3.3	Multiple linear regression with remote sensing data	Arrigo et al. (2010)
	1998-2004		-19.0 to -74.9	Integration of many studies	Bates and Mathis (2009)

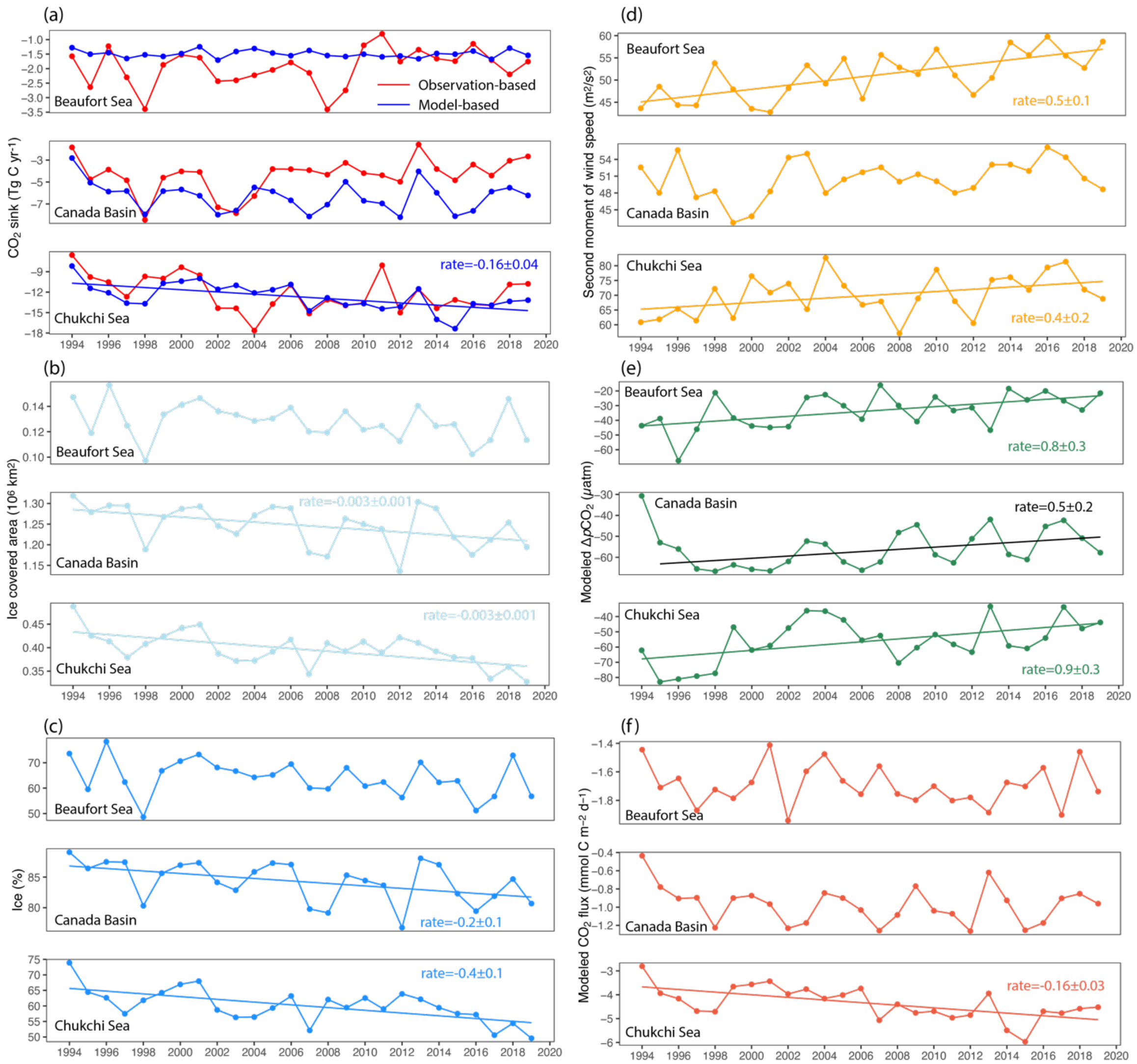

Figure 4.12: Interannual variation in carbon sinks (a) and other associated variables (b-f). We tested whether the trends were significantly different from 0 by conducting an analysis of variance (ANOVA); only the significant rates (changes per year) are shown. The trend of modeled ΔpCO_2 in the Canada Basin is significant when we excluded the point in 1994.

4.5.2 Climate variability and CO_2 sink response

In order to better understand how the CO_2 sink responds to changes in sea ice cover, wind speed and ΔpCO_2 in different regions, we need to first identify the main controlling factors for CO_2 sink in each subregion. Thus, we computed the correlation coefficients between the estimated carbon sink and possible factors as indicators (Table 4.4). Then, we examined the temporal variability of these factors to confirm the most likely controlling mechanism (Figure 4.12 b-f). Taking advantage of the gapless modeled data, we could check the temporal variability of ΔpCO_2 and CO_2 flux without interpolation or extrapolation.

Among the three factors, sea ice, wind and ΔpCO_2, the primary and secondary controlling factors for the monthly carbon sink are ice-covered area (equivalent to ice%) and ΔpCO_2 in all three subregions. The wind speed only plays a minor role in the Beaufort Sea and Canada Basin and is not significantly correlated to carbon sink in the Chukchi Sea (Table 4.4). Based on this evaluation, we can explain the temporal variation in the estimated carbon sink for each subregion. In the Beaufort Sea, a stronger wind (Figure 4.12d) tended to increase gas exchange velocity and hence CO_2 flux. However, the stronger wind appears to be cancelled by a reduced ΔpCO_2 (Figure 4.12 e). More importantly, the relatively stable ice condition (Figure 4.12 b&c) dominates the interannual variation in regional CO_2 flux (Figure 4.12 f), which leads the Beaufort Sea to be a relatively stable CO_2 sink over years. In the Canada Basin, the carbon sink would be expected to increase with a decline in ice-covered area and ice% (Figure 4.12 b&c) but that is offset by a significantly lower ΔpCO_2 (Figure 4.12e). Thus, no significant change was found in the carbon sink in the Canada Basin. If we only focus on the changes in summer (Figure 4.13), the modeled CO_2 flux and carbon sink slightly increases in the Canada Basin, which suggests that the loss of summer sea ice effectively promotes CO_2 uptake and a larger carbon sink, likely compensating for the reduction of ΔpCO_2. In the Chukchi Sea, our model results suggested that annual mean of ΔpCO_2 significantly decreased over the years (Figure 4.12 e). A similar trend was also reported by Yasunaka et al., (2018). However, this decreased trend of annual ΔpCO_2 was not necessarily translated into a lower CO_2 flux and carbon sink because the annual rate of ΔpCO_2 reflected not only unchanged ΔpCO_2 in the summer (Figure 4.13 e), in which CO_2 uptake was extremely high (Figure 4.13 f), but also a smaller ΔpCO_2 in fall to spring, in which the CO_2 exchange is suppressed by sea ice. Thus, the annual increase in CO_2 flux (Figure 4.13 f) and CO_2 sink (Figure 4.12 a) in the Chukchi Sea were dominated by its summer trends. We attributed that primarily to an earlier sea ice loss and later ice formation with a larger open area (Figure 4.12 b&c) and increased primary production (Lewis et al., 2020), and partially to enhanced wind (Figure 4.12 d).

Table **4.4:** **Correlation coefficients (*r*) between monthly CO_2 sinks and the associated variables. All correlation coefficients given here are statistically significant ($p<0.05$); a hyphen (-) indicates non-significant correlation.**

	Beaufort Sea		Canada Basin		Chukchi Sea	
	Obs-based[a]	Modeled	Obs-based[a]	Modeled	Obs-based[a]	Modeled
Ice%	0.74	0.82	0.72	0.89	0.88	0.90
Second moment of wind speed	-0.11	-0.19	-	-0.34	-	-
Modeled ΔpCO_2	0.46	0.62	0.47	0.57	0.68	0.73
Modeled CO_2 flux	0.77	1.00	0.73	1.00	0.92	1.00

[a] CO_2 sink was estimated using the modified approach described in this study.

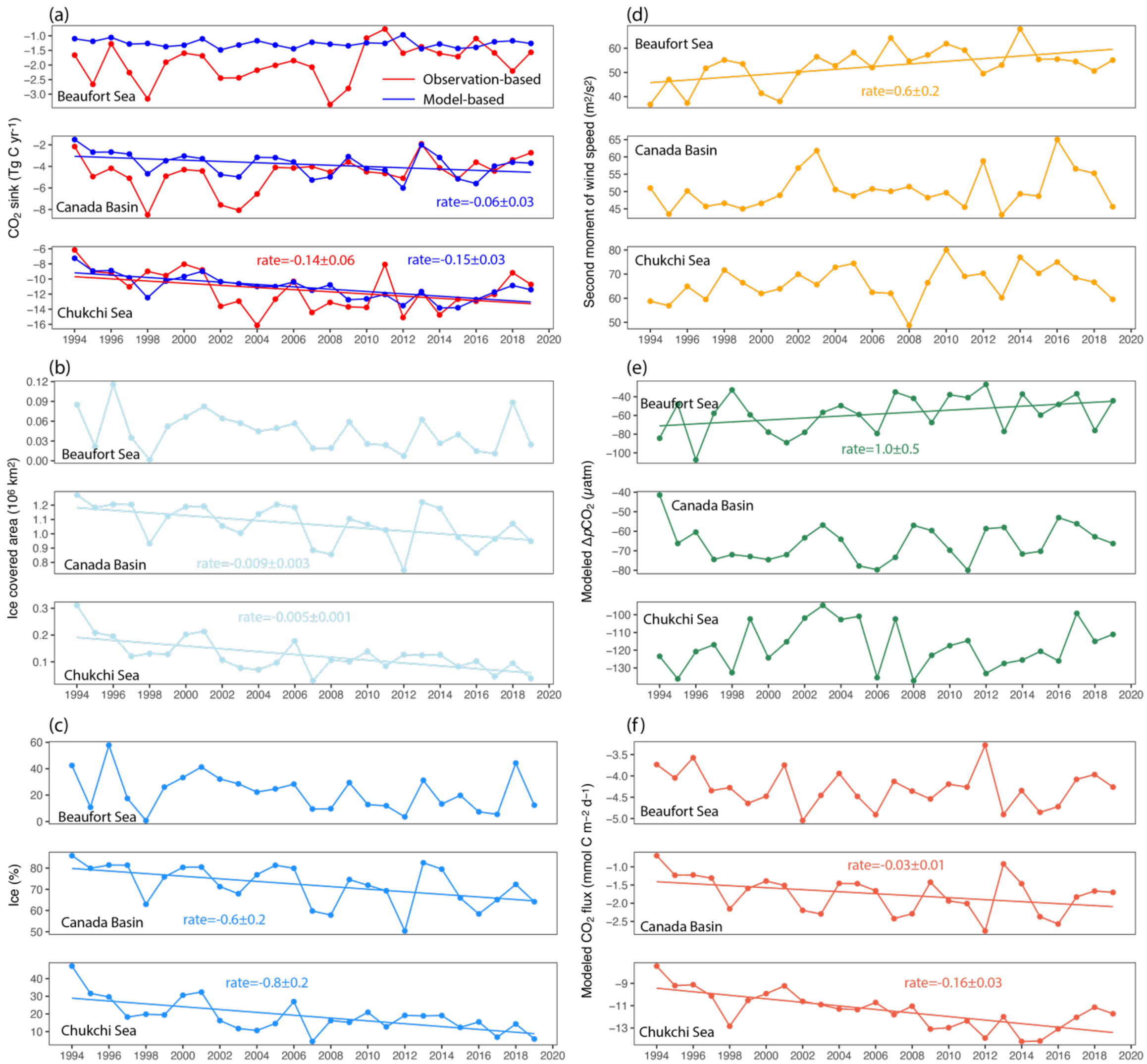

Figure 4.13: Interannual variation (summer only; July-October) in carbon sinks (a) and other associated variables (b-f). We tested whether the trends were significantly different from 0 by conducting an analysis of variance (ANOVA). Only the significant rates (changes per year) are shown.

4.5.3 Model limitation and further uncertainty reduction

In our box model, we focused on the main physical and biogeochemical processes determining the carbonate dynamics in the surface mixed layer, such as warming, sea ice loss and enhanced primary production. A box model enabled us to reconstruct a seamless time-series map of sea surface pCO_2 and establish the possible links between climate variability and carbon sink response. The model we used for this study appears to be highly suitable for identifying the main controlling factors and resolving the complicated relationships among them. However, simplified model settings and multiple presumptions inevitably add uncertainties to both spatial and temporal variations of the various quantities, in particular the final regional CO_2 sinks. Here, we would like to discuss some limitations in our current model and possible ways to further reduce the uncertainty.

Using remote sensing products of SST and sea ice concentration with daily resolution permits us to monitor the rapid changes in SST and sea ice, but we have to rely on an ensemble reanalysis SSS product to reflect the possible lateral and vertical mixing in the water column, seasonal cycle of river discharge, and surface water freshening due to sea ice loss. The current SSS product tended to have a higher surface salinity (by 0.5~2 psu) for summer (July to October). Adjustment of SSS should be done to reduce apparent systematic bias (see Section 4.3.3.1). Coupling with a more skilled physical-driven oceanic model may resolve more dynamic mixing processes, such as eddy transport and shelf-basin interactions, and reduce the large deviation between observed and modeled pCO_2 along the boundaries between the subregions.

Another potential source of the uncertainty of modeled pCO_2 arises from insufficient quantification of net community production. For the Chukchi Sea and Beaufort Sea, we set monthly NCP depending on several previous studies (Table 4.7) and applied a long-term trend in NCP (Lewis et al., 2020). We also introduced an E-term (equation 4.9) to account for possible over- or underestimation of primary production. However, a regional monthly mean NCP does not resolve the highly varied and patchy NCP in the inflow shelf and river influenced coastal sea. Although we adjusted the NCP magnitude based on the assumption that it has a proportional relationship with NPP increase (Lewis et al., 2020), the caveat is that we used a fixed monthly NCP seasonal cycle which may neglect the observed changes in primary production timing in the Arctic (Song et al., 2021). One possible way to improve our NCP setting is to incorporate the satellite Chl a data and its derived primary production into our model (Arrigo et al, 2010; Yasunaka et al., 2018). However, the availability of satellite data still suffers from the presence of sea ice cover in the higher latitude area. Future improvement of the remote sensing technique is needed to greatly improve the quantification of change in primary production in those areas. This is very challenging as multi-streams of satellite data are current masked in very high latitudes (e.g., Yasunaka et al., 2018). To deal with this issue, for the first time, we incorporated NCP estimation based on the relationship between ice concentration and NCP into our model practice for the high latitudes (i.e., Canada Basin). Although this NCP setting worked well for simulating seasonal pCO_2 evolution in the recent years (2007-2019), we do not have enough pCO_2 and NCP observations in the earlier period (1994-2006) to check whether this relationship is still valid. For future model, multiple practices for better quantifying NCP in the Arctic Ocean are recommended, including productivity incubation experiments, underway NCP measurements via the $\Delta(O_2/Ar)$ approach, and remote sensing techniques.

4.6 Summary

In this study, we used a synthesized dataset of sea surface pCO_2 to estimate the CO_2 flux and examine the long-term change in carbon sink for the western Arctic Ocean for the 1994-2019 period. In order to improve spatial and temporal coverage of pCO_2 data, we also performed a data-driven model exercise and produced daily pCO_2 maps with 1°×1° spatial resolution. Our results show a long-term carbon sink of -18.4±5.5 Tg C yr^{-1} and -20.5±15.6 Tg C yr^{-1} based on observation and model results, respectively, for the entire western Arctic Ocean. We did not find any significant trend in carbon sink for any of three subregions (Beaufort Sea, Canada Basin and Chukchi Sea) based on observed data, but our modeled results suggested that carbon sink in the Chukchi Sea significantly increased by -0.16±0.03 Tg C yr^{-1}. Further examination of summer trend suggested that long-term trend in annual CO_2 sink was dominated by CO_2 uptake in the summer. Using model results allows us to further examine the dominant factors driving the interannual variability of CO_2 flux and carbon sink. For the Chukchi Sea, we attributed the increased carbon sink primarily to a longer ice-free period and higher primary production, and partially to stronger winds. For the Canada Basin, summer active sea ice loss effectively promotes CO_2 uptake but the increased carbon sink likely to be offset by reduction of ΔpCO_2. As a net result, the Canada Basin showed a weakly increased carbon sink of -0.06±0.03 Tg C yr^{-1} in the summer.

4.7 Supplementary Information

Notes on Sea Ice Correction Methods for CO_2 Flux

The mathematical expressions of air-sea CO2 flux between two different methods at individual pixels,

Evans et al. 2015

$$F_{\mathrm{CO2(correct,}\ i)} = F_{\mathrm{CO2}(i)} \times \left(1 - ice\%_{(i)}\right) \tag{4.12}$$

This study

$$F_{\mathrm{CO2(correct,}\ i)} = \frac{\sum_{i=1}^{n}(F_{\mathrm{CO2}(i)} \times A_i)}{\sum_{i=1}^{n} A_i}(1 - ice\%_{(i)}) \tag{4.13}$$

and for regional averages,

Evans et al. 2015 (i.e. sea ice correction is only applied to F_{CO_2})

$$F_{\mathrm{CO2(correct,}\ avg)} = \frac{\sum_{i=1}^{n}[F_{\mathrm{CO2}(i)} \times (1 - ice\%_{(i)}) \times A_i]}{\sum_{i=1}^{n} A_i} \tag{4.14}$$

This study (i.e., sea ice correction provides spatial variability on a pre-weighted F_{CO_2}),

$$F_{\mathrm{CO2(correct,}\ avg)} = \frac{\sum_{i=1}^{n}(F_{\mathrm{CO2}(i)} \times A_i)}{\sum_{i=1}^{n} A_i} \frac{\sum_{i=1}^{n}[(1 - ice\%_{(i)}) \times A_i]}{\sum_{i=1}^{n} A_i} \tag{4.15}$$

The ratio between the methods of Evans et al (2015) and this study can be computed as follows, at individual pixels as well as for regional averages,

Individual pixel (from Eqs. 4.12 and 4.13),

$$r_{\mathrm{indiv}} = \frac{\text{Evan et al.}}{\text{this study}} = \frac{F_{\mathrm{CO2}(i)}}{\frac{\sum_{i=1}^{n}(F_{\mathrm{CO2}(i)} \times A_i)}{\sum_{i=1}^{n} A_i}} \tag{4.16}$$

Regional averages (from Eqs. 4.14 and 4.15),

$$r_{\text{region}} = \frac{\text{Evan et al.}}{\text{this study}} = \frac{\frac{\sum_{i=1}^{n}\left[F_{\text{CO2}(i)} \times \left(1-ice\%_{(i)}\right) \times A_i\right]}{\sum_{i=1}^{n} A_i}}{\frac{\sum_{i=1}^{n}\left(F_{\text{CO2}(i)} \times A_i\right)}{\sum_{i=1}^{n} A_i} \frac{\sum_{i=1}^{n}\left[\left(1-ice\%_{(i)}\right) \times A_i\right]}{\sum_{i=1}^{n} A_i}} = \frac{\frac{\sum_{i=1}^{n}\left[F_{\text{CO2}(i)} \times \left(1-ice\%_{(i)}\right) \times A_i\right]}{\sum_{i=1}^{n}\left[\left(1-ice\%_{(i)}\right) \times A_i\right]}}{\frac{\sum_{i=1}^{n}\left(F_{\text{CO2}(i)} \times A_i\right)}{\sum_{i=1}^{n} A_i}} \tag{4.17}$$

Due to the covariance of $F_{\text{CO2}(i)}$, $\left(1 - ice\%_{(i)}\right)$, and A_i in the western Arctic Ocean, that is, high $F_{\text{CO2}(i)}$ are generally found in the regions of higher open-water area and/or larger grid size (lower latitude). This effect results in the "weights" in the numerator emphasizing the contribution of open-water area more than the "weights" of grid size in the denominator. As such, we expect $r_{\text{region}} > 1$, meaning Evan et al. (2015) method shall always provide higher regional averages of F_{CO2} than this study.

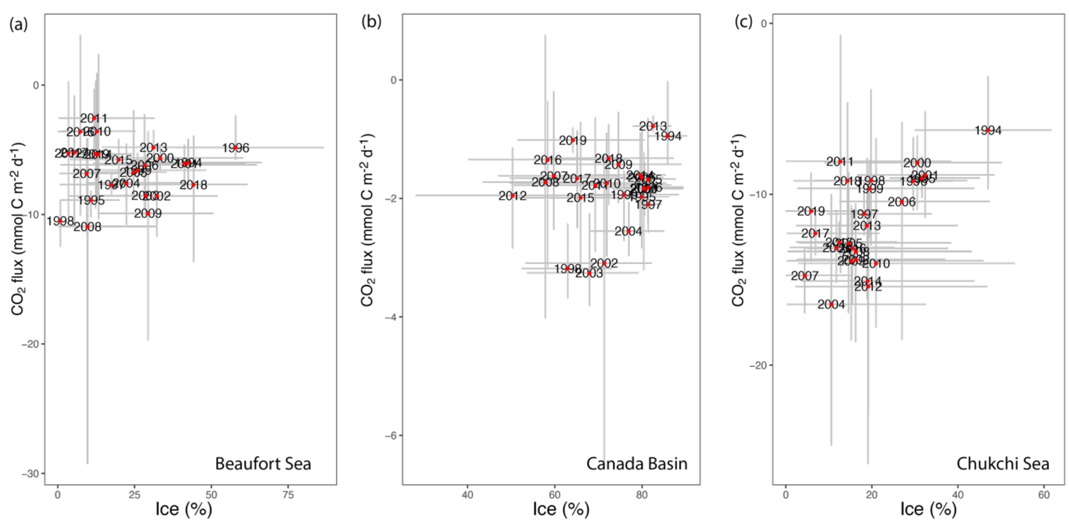

Figure 4.14: Regional CO_2 flux versus ice concentration in summer months (July to October). The red dots represent the summer mean of ice concentration and CO_2 flux in particular year (noted in figures). The error bars (grey) associated with the data represent the seasonal variability, reported as the highest and lowest monthly values through July to October for a given subregion.

Table **4.5: A summary of pCO_2 measurements in the western Arctic Ocean during 1994-2019.**

Year	Research period	Contributor	Country of Origin	# of measurement	Data type and source
1998	Aug 19-Aug-29	Murata, A	Japan (Mirai)	467	Underway fCO_2 (SOCAT)
1999	Sept 13-Sept 24	Murata, A	Japan (Mirai)	1171	Underway fCO_2 (SOCAT)
2000	Sept 6-Sept 29	Murata, A	Japan (Mirai)	2440	Underway fCO_2 (SOCAT)
2002	Sept 4	Murata, A	Japan (Mirai)	15	Underway fCO_2 (SOCAT)
2003	July 9 -Aug 17	Takahashi, T; Newberger, T.; Sutherland, S.C.	USA (N. B. Palmer)	15841	Underway fCO_2 (SOCAT)
	Aug 21-Aug 24	Takahashi, T; Newberger, T.; Sutherland, S.C.	USA (N. B. Palmer)	879	Underway pCO_2 (LDEO)
2004	Sept 3- Oct 9	Murata, A	Japan (Mirai)	3852	Underway fCO_2 (SOCAT)
2005	July 27-Aug 17	Fransson, A.	Oden	8005	Underway fCO_2 (SOCAT)
2006	Aug 30- Sept 7	Murata, A	Japan (Mirai)	853	Underway fCO_2 (SOCAT)
2008	Aug 1-Sept 9	Wanninkhof, R	China (Xuelong)	12477	Underway fCO_2 (SOCAT)
2009	Sept 10-Oct 12	Nishino, S	Japan (Mirai)	3596	Underway pCO_2 (JAMSTEC)
2010	Sept 4-Oct14	Nishino, S	Japan (Mirai)	4444	Underway pCO_2 (JAMSTEC)
	Aug 26-Oct 8	Papakyriakou, T.	Canada (CCGS Amundsen)	8080	Underway fCO_2 (SOCAT)
	July 19-Aug 31	Chen, L; Cai, W-J	China (Xuelong)	9633	Underway fCO_2 (SOCAT)
	Aug5-Sept 5	Robbins, L	USA (Healy)	22914	Underway pCO_2 (USGS Data Series 741)
2011	Aug 13-Oct 10	Papakyriakou, T.	Canada (CCGS Amundsen)	5117	Underway fCO_2 (SOCAT)
	Aug 22-Sept 8	van Heuven, S.	Germany (Polarstern)	12729	Underway fCO_2 (SOCAT)
	Sept 11- Oct 6	Takahashi, T; Newberger, T.; Sutherland, S.C.	USA (Marcus G. Langseth)	7831	Underway fCO_2 (SOCAT)
	June 28 -July 26; Aug 17- Sept 26; Oct 4-Oct 25; Nov 13-Nov 30	Takahashi, T; Newberger, T.; Sutherland, S.C.	USA (Healy)	43977	Underway fCO_2 (SOCAT)
2012	Aug 12-Sept 25; Oct 8-Oct 23	Takahashi, T; Newberger, T.; Sutherland, S.C.	USA (Healy)	26144	Underway fCO_2 (SOCAT)
	Aug 6-Sept 6	DeGrandpre, M	Canada (Louis S. St-Laurent)	7902	Underway fCO_2 (SOCAT)
	Sept 13-Oct 5	Murata, A.	Japan (Mirai)	2712	Underway pCO_2 (JAMSTEC)
	July17-Sept 8	Chen, L; Cai, W-J.	China (Xuelong)	3186	Underway fCO_2 (SOCAT)
2013	Aug 3- Sept 1	DeGrandpre, M	Canada (Louis S. St-Laurent)	7221	Underway fCO_2 (SOCAT)
	Aug 5- Sept 13; Oct 8-Oct 28	Takahashi, T; Newberger, T.; Sutherland, S.C.	USA (Healy)	23813	Underway fCO_2 (SOCAT)
2014	July 27-Sept 9	Chen, L; Qi, D; Cai, W-J;	China (Xuelong)	14467	Underway pCO_2 (SOCAT)
	Aug 17- Aug 29	Papakyriakou, T.	Canada (CCGS Amundsen)	2142	Underway fCO_2 (SOCAT)
	May 16-June 21; July 9-July 27; Aug10-Aug 29	Takahashi, T; Newberger, T.; Sutherland, S.C.	USA (Healy)	20496	Underway fCO_2 (SOCAT)
	Aug 27	van Heuven, S.	Germany (Polarstern)	624	Underway fCO_2 (SOCAT)
	Sept 15-Oct14	DeGrandpre, M	Canada (Louis S. St-Laurent)	5736	Underway pCO_2 (NSF Arctic Data Center)
2015	July 14-July 24; Aug 11-Oct 21	Takahashi, T; Newberger, T.; Sutherland, S.C.	USA (Healy)	26204	Underway fCO_2 (SOCAT)
	Aug 11- Aug 21; Aug 22- Sept 4	Wanninkhof,R; Pierrot, D	USA (Ronald H. Brown)	9527	Underway fCO_2 (SOCAT)
	Aug 13-Sept 25	Sutherland, S.C.; Newberger, T.;Takahashi, T.	USA (Sikuliaq)	12880	Underway fCO_2 (SOCAT)
	Sept 7- Sept 15	van Heuven, S.	Germany (Polarstern)	4871	Underway fCO_2 (SOCAT)
	Aug 23- Aug 25	Papakyriakou, T.	Canada (CCGS Amundsen)	2037	Underway fCO_2 (SOCAT)

2016	July 24-Sept4	Chen, L; Qi, D; Cai, W-J	China (Xuelong)	15277	Underway pCO_2 (Chinese NAADC)
	July 8- Aug 5	Takahashi, T; Newberger, T.; Sutherland, S.C.	USA (Healy)	11133	Underway pCO_2 (LDEO)
	Sept 4-Sept 27; Oct 16-Nov 7	Takahashi, T; Newberger, T.; Sutherland, S.C.	USA (Sikuliaq)	15308	Underway fCO_2 (SOCAT)
	Sept 25-Oct 17	DeGrandpre, M	Canada (Louis S. St-Laurent)	5598	Underway fCO_2 (SOCAT)
	Aug 27- Sept 14	Papakyriakou, T.	Canada (CCGS Amundsen)	1278	Underway fCO_2 (SOCAT)
	Aug 30-Sept 22	Nishino, S	Japan (Mirai)	2953	Underway pCO_2 (JAMSTEC)
2017	July 30-Sept 23	Chen, L; Qi, D; Cai, W-J	China (Xuelong)	9254	Underway pCO_2 (Chinese NAADC)
	July 28-Aug 5; Aug 29- Sept 12; Sept 22-Oct 9; Oct 21-Nov 3	Takahashi, T; Newberger, T.; Sutherland, S.C.	USA (Healy)	20325	Underway fCO_2 (SOCAT)
	June 12-June 24 Aug 7 –Aug 22; Aug 26- Sept 17	Takahashi, T; Newberger, T.; Sutherland, S.C.	USA (Sikuliaq)	17586	Underway fCO_2 (SOCAT)
		Takahashi, T; Newberger, T.; Sutherland, S.C.	USA (Sikuliaq)	7840	Underway pCO_2 (LDEO v2017)
	Sept 7-Oct 2	DeGrandpre, M	Canada (Louis S. St-Laurent)	7132	Underway pCO_2 (NSF Arctic Data Center)
	Aug 27-Sept 21	Murata, A.	Japan (Mirai)	4354	Underway pCO_2 (JAMSTEC)
2018	June 9- June 21; Aug 4-Aug 27; Sept 2- Sept 30	Takahashi T.; Sweeney C.; Newberger T.; Sutherland S.C.; Munro D.R.	USA (Sikuliaq)	21089	Underway fCO_2 (SOCAT)
	Aug 9-Aug 24; Sept 17-Oct 16	Takahashi T.; Sweeney C.; Newberger T.; Sutherland S.C.; Munro D.R.	USA (Healy)	16396	Underway fCO_2 (SOCAT)
	July 29-Sept 3	Chen, L; Qi, D; Cai, W-J	China (Xuelong)	7958	Underway pCO_2 (Chinese NAADC)
	Nov 3 -Nov 25	Murata, A.	Japan (Mirai)	3222	Underway pCO_2 (JAMSTEC)
2019	Nov 8-Nov 26	Takahashi T.; Sweeney C.; Newberger T.; Sutherland S.C.; Munro D.R.	USA (Sikuliaq)	5554	Underway fCO_2 (SOCAT)
	Aug 9- Aug 21; Sept 7- Oct 13	Takahashi T.; Sweeney C.; Newberger T.; Sutherland S.C.; Munro D.R.	USA (Healy)	20474	Underway fCO_2 (SOCAT)
				1662	Discrete sample (GLODAP 2019)
Total				513589	

Table **4.6: Intercepts and slopes for the relationships between SSS and TA in different subregions.**

	Chukchi Sea				Beaufort Sea		Canada Basin	
	Southern		Northern					
	Intercept	Slope	Intercept	Slope	Intercept	Slope	Intercept	Slope
Jan	1640.1*	17.85*	690.3*	47.69*	1501.2	23.05	496.5*	55.09*
Feb	1684.1*	16.64*	742.2*	46.33*	2052.6	5.38	581.4*	52.30*
Mar	1728.1*	15.44*	794.0*	44.98*	1895.1*	10.32*	666.4*	49.51*
Apr	1772.0*	14.23*	845.9	43.62	1737.6*	15.26*	751.3*	46.72*
May	1816.0	13.03	897.7	42.27	1580.1*	20.20*	836.3*	43.93*
Jun	1836.7*	12.04*	509.6	54.76	1422.6*	25.14*	921.3	41.14
Jul	1857.4	11.05	225.2	62.88	1265.1	30.08	605.5	50.29
Aug	1799.0	12.35	306.8	59.91	1297.2	27.97	400.4	57.09
Sept	1740.6	13.67	614.0	49.25	923.7	40.03	459.4	55.08
Oct	1508.2	21.46	534.7	51.77	1068.6	34.87	241.6	63.46
Nov	1552.2*	20.26*	586.6*	50.41*	756.7	47.30	326.6*	60.67*
Dec	1596.2*	19.05*	638.5*	49.05*	1339.6	27.96	411.5*	57.88*

*indicates the values in the month without observation. We linearly interpolated the slope and intercept using the values in the adjacent months assuming that seasonal evolution of SSS and TA is relatively slow and smooth.

Table **4.7: NCP in the western Arctic Ocean. For the values reported as NPP, we covert them into NCP by multiplying f-ratios (NCP=NPP×f). f-ratios are adopted from Codispoti et al., (2013), which are 0.3, 0.2, 0.25 and 0.1 for the southern Chukchi Sea, northern Chukchi Sea, Beaufort Sea, and Canada Basin, respectively.**

Regions	Periods	Year	Original values in refs (NPP or NCP)	NCP (mmol C m^{-2} day^{-1})	Reference
Chukchi Shelf	Annual	Long-term mean	70 (40-120) g C m^{-2} yr^{-1} (NCP)	16.0	Codispoti et al. 2013
Southern Chukchi	May	Long-term mean (1950-2012)	[a] 0.47×2166 mg C m^{-2} d^{-1} (NPP)	25.5	Hill et al. 2018
	Jun	Long-term mean (1950-2012)	[a] 0.47×882 mg C m^{-2} d^{-1} (NPP)	10.4	Hill et al. 2018
	Jul	Long-term mean (1950-2012)	[a] 0.47×3015 mg C m^{-2} d^{-1} (NPP)	35.4	Hill et al. 2018
	Jul	2016	7 mmol C m^{-2} d^{-1} (NCP)	7.0	Ouyang et al. 2021
	Jul	2018	40 mmol C m^{-2} d^{-1} (NCP)	40.0	Ouyang et al. 2021
	Aug	Long-term mean (1950-2012)	247 (±56) mg C m^{-2} d^{-1} (NPP)	6.2	Hill et al. 2018
	Sept-Oct	Long-term mean (1950-2012)	437 (±100) mg C m^{-2} d^{-1} (NPP)	10.9	Hill et al. 2018
	Sept	2016	46 mmol C m^{-2} d^{-1} (NCP)	46.0	Ouyang et al. 2021
	Sept	2018	22 mmol C m^{-2} d^{-1} (NCP)	22.0	Ouyang et al. 2021
	Oct	2011-2012	10-20 mmol C m^{-2} d^{-1} (NCP)	15.0	Juranek et al. 2019
Northern Chukchi	Annual	Long-term mean	10 (5-20) g C m^{-2} yr^{-1} (NCP)	0.5	Codispoti et al. 2013
	May	Long-term mean (1950-2012)	[a] 0.46×407 mg C m^{-2} d^{-1} (NPP)	3.1	Hill et al. 2018
	Jun	Long-term mean (1950-2012)	[a] 0.46×2401 mg C m^{-2} d^{-1} (NPP)	18.4	Hill et al. 2018
	Jul	Long-term mean (1950-2012)	[a] 0.27×2016 mg C m^{-2} d^{-1} (NPP)	9.0	Hill et al. 2018
	Jul-Aug	2016	13 mmol C m^{-2} d^{-1} (NCP)	13.0	Ouyang et al. 2021
	Jul-Aug	2018	23 mmol C m^{-2} d^{-1} (NCP)	23.0	Ouyang et al. 2021
	Aug	Long-term mean (1950-2012)	[a] 0.51×696 mg C m^{-2} d^{-1} (NPP)	5.9	Hill et al. 2018
	Sept-Oct	Long-term mean (1950-2012)	[a] 0.64×126 mg C m^{-2} d^{-1} (NPP)	1.3	Hill et al. 2018
	Sept	2016	21 mmol C m^{-2} d^{-1} (NCP)	21.0	Ouyang et al. 2021
	Sept	2018	4 mmol C m^{-2} d^{-1} (NCP)	4.0	Ouyang et al. 2021
	Oct	2011-2012	1-10 mmol O_2 m^{-2} yr^{-1} (NCP)	4.0	Juranek et al. 2019
Beaufort Sea	Annual	Long-term mean	15 (10-30) g C m^{-2} yr^{-1}(NCP)	0.9	Codispoti et al. 2013
	May	1987	20-100 mg C m^{-2} d^{-1}(NCP)	0.4-2.1	Carmack et al., 2004
	Jun	1987	100-150 mg C m^{-2} d^{-1}(NCP)	2.1-3.1	Carmack et al., 2004
	Jun	2008	1.4 g C m^{-2} d^{-1}(NPP)	29.2	Mundy et al 2009
	Jun	Long-term mean (1950-2012)	[a] 0.39×1427 mg C m^{-2} d^{-1}(NPP)	11.6	Hill et al. 2018
	Jul	Long-term mean (1950-2012)	[a] 0.49×1004 mg C m^{-2} d^{-1}(NPP)	10.2	Hill et al. 2018
	Aug	Long-term mean (1950-2012)	[a] 0.51×314 mg C m^{-2} d^{-1}(NPP)	3.3	Hill et al. 2018
	Jul-Aug	1987	200 mg C m^{-2} d^{-1}(NCP)	4.2	Carmack et al., 2004
	Jul-Sept	2011-2016	0.5-4 mmol O_2 m^{-2} d^{-1}(NCP)	0.4-2.9	Ji et al. 2019

	Sept-Oct	Long-term mean (1950-2012)	[a] 0.65×64 mg C m^{-2} d^{-1}(NPP)	0.9	Hill et al. 2018
Canada Basin	Annual	Long-term mean	1 (0.5-5) g C m^{-2} yr^{-1}(NCP)	0.2	Codispoti et al. 2013
	May	Long-term mean (1950-2012)	[a] 0.51×90 mg C m^{-2} d^{-1}(NPP)	0.4	Hill et al. 2018
	Jun	Long-term mean (1950-2012)	[a] 0.51×412 mg C m^{-2} d^{-1}(NPP)	1.8	Hill et al. 2018
	Jul	Long-term mean (1950-2012)	[a] 0.51×401 mg C m^{-2} d^{-1}(NPP)	1.7	Hill et al. 2018
	Aug	Long-term mean (1950-2012)	[a] 0.51×240 mg C m^{-2} d^{-1}(NPP)	1.0	Hill et al. 2018
	Aug	2016&2018	0.3-2.4 mmol C m^{-2} d^{-1} (NCP)	1.0	Ouyang et al. 2021
	Jul-Sept	2011-2016	1.3-2.9 mmol O_2 m^{-2} d^{-1}(NCP)	1-2.2	Ji et al. 2019
	Jul-Sept	2007-2008	48.1 mg C m^{-2} d^{-1} (NPP)	0.4	Varela et al., 2013
	Aug-Sept	2011	0-1 mol C m^{-2} (90 days) (NCP)	0-11	Ulfsbo et al. 2014
	Sept-Oct	Long-term mean (1950-2012)	[a] 0.61×72 mg C m^{-2} d^{-1}(NPP)	0.4	Hill et al. 2018

[a] Assume that the surface layer is equivalent to the layer between light levels of between 100% and 50% in the study of Hill et al. 2018.

Table **4.8: Error term in simulation. The negative values indicate DIC addition in the mixed layer, which is likely induced by horizontal advection of DIC and/or local mixing with deep carbon-rich water on the shelf and coastal region. For winter and early spring, a small negative E is set accounting for possible respiration and winter ventilation.**

Error term	Chukchi Sea		Beaufort Sea	Canada Basin
(mmol C m^{-2} d^{-1})	Southern	Northern		
Jan	-2	-2	-1	0
Feb	-2	-2	-1	0
Mar	-2	-2	-1	0
Apr	0	-2	-1	0
May	0	0	0	0
Jun	0	0	0	0
Jul	0	-20	-5	0
Aug	-45	-16	-10	0
Sept	0	-6	0	0
Oct	-75	0	0	0
Nov	-10	-15	-1	0
Dec	-2	-2	-1	0

Table **4.9:** **Monthly area-weighted sea-air CO_2 flux (mmol m^{-2} d^{-1}) in the Beaufort Sea. Note that negative values of CO_2 flux indicate CO_2 uptake from the atmosphere.**

Beaufort Sea	Jan		Feb		Mar		Apr		May		Jun		Jul		Aug		Sept		Oct		Nov		Dec	
	flux[a]	flux[b]	flux[a]	flux[b]	flux[a]	flux[b]	flux[a]	flux[b]	flux[a]	flux[b]	flux[a]	flux[b]	flux[a]	flux[b]	flux[a]	flux[b]	flux[a]	flux[b]	flux[a]	flux[b]	flux[a]	flux[b]	flux[a]	flux[b]
1994																								
1995															-8.4	-8.2								
1996																	-4.9	-5.8						
1997																	-6.8	-6.8						
1998															-10.6	-10.5								
1999																	-5.5	-5.3						
2000															-5.5	-5.4	-5.8	-5.8						
2001																								
2002													-4.4	-9.0			-11.4	-11.7	-5.4	-7.2				
2003													-9.7	-10.0	-11.8	-9.2	-10.6	-9.5	-5.2	-5.3	-0.7	-1.2	0.5	0.9
2004	0.3	0.4	0.1	0.1	0.5	0.8	0.5	0.7	0.4	0.7	-2.9	-2.6	-4.8	-4.5	-6.0	-5.6	-10.2	-9.3	-14.5	-10.8				
2005													-2.2	-2.0	-7.1	-8.5								
2006															-2.2	-2.2								
2007													-3.6	-5.1	-11.6	-11.5								
2008													-31.1	-29.3					-5.0	-6.0				
2009																	-9.1	-9.7	-14.6	-19.7				
2010															-3.6	-4.6	-1.8	-1.7	1.1	0.9				
2011													-1.3	-2.4	-0.2	-0.3	-2.5	-2.5	-5.6	-5.0				
2012															0.4	0.3			-6.7	-6.5				
2013															-2.9	-3.5	-6.0	-5.8	-4.6	-4.6				
2014													-4.8	-9.4	2.5	2.4			-8.2	-10.3				
2015													-4.0	-5.0	-5.3	-6.6	-4.2	-4.2						
2016															3.9	3.9	-0.4	-0.4	-8.8	-7.8				
2017															-0.8	-0.8	-2.5	-2.5	-6.8	-6.5				
2018															-7.5	-13.7	-6.7	-7.2						
2019																	0.3	0.3			-2.9	-1.9		
Climatological flux (1994-2006)	0.3	0.4	0.1	0.1	0.5	0.8	0.5	0.7	0.4	0.7	-2.9	-2.6	-5.3	-6.4	-7.4	-7.1	-7.9	-7.7	-8.4	-7.8	-0.7	-1.2	0.5	0.9
Climatological flux (2007-2019)													-9.0	-10.2	-2.5	-3.4	-3.7	-3.7	-6.6	-7.3	-2.9	-1.9		
Climatological flux (1994-2019)	0.3	0.4	0.1	0.1	0.5	0.8	0.5	0.7	0.4	0.7	-2.9	-2.6	-7.3	-8.5	-4.5	-4.9	-5.5	-5.5	-7.0	-7.4	-1.8	-1.6	0.5	0.9

[a] CO_2 flux was estimated using Evans et al., (2015) approach.

[b] CO_2 flux was estimated using the modified approach described in this study.

Table **4.10: Monthly area-weighted sea-air CO_2 flux (mmol m^{-2} d^{-1}) in the Canada Basin. Note that negative values of CO_2 flux indicate CO_2 uptake from the atmosphere.**

Canada Basin	Jan	Feb	Mar	Apr	May	Jun	Jul		Aug		Sept		Oct		Nov		Dec
							flux[a]	flux[b]	flux[a]	flux[b]	flux[a]	flux[b]	flux[a]	flux[b]	flux[a]	flux[b]	
1994							-0.9	-1.1	-0.1	0.0							
1995									-6.2	-1.5							
1996																	
1997											-8.2	-2.5	-4.5	-2.2			
1998																	
1999											-6.4	-1.7					
2000											-4.6	-1.2					
2001																	
2002							-7.4	-3.1	-2.2	-1.5	-15.6	-6.5	-2.0	-1.2			
2003							-8.3	-3.7	-9.7	-3.8	-4.4	-3.3	-4.6	-2.3			
2004									-8.0	-2.1	-10.4	-3.0	-17.2	-2.9			
2005									-2.9	-1.9	-0.4	-0.6					
2006									-1.4	-0.8	-2.6	-1.6					
2007									-2.5	-1.5	-0.7	-0.2					
2008							-1.1	0.8	-2.2	-1.5	-6.4	-4.0	-6.4	-2.1			
2009											-4.7	-2.1	-2.9	-1.7			
2010							-1.3	-0.9	-2.2	-1.8	-5.2	-3.0	-5.5	-1.3			
2011							-1.3	-0.6	-2.2	-1.3	-1.8	-2.9	-9.0	-2.3			
2012									-1.6	-1.6	-3.5	-2.8	-6.4	-2.2			
2013									-1.3	-0.8	-2.2	-0.9	-3.9	-0.8			
2014							-2.7	-1.4	-1.8	-0.9	-7.4	-2.6	-1.6	-1.5			
2015									-4.0	-3.2	-4.1	-2.9	-1.9	-0.7			
2016							-1.0	-0.5	-3.7	-3.2	-0.4	-0.4	-3.6	-1.3			
2017							-1.9	-0.9	-5.1	-2.5	-3.3	-2.0	-4.6	-1.3	-3.6	-1.6	
2018							-1.4	-0.8	-1.6	-1.1	-3.7	-2.1	-2.5	-1.4			
2019									-2.5	-0.8	-1.3	-1.2	-3.3	-1.2	-4.2	-1.3	
Climatological flux (1994-2006)							-5.5	-2.6	-4.4	-1.7	-6.6	-2.6	-7.1	-2.2			
Climatological flux (2007-2019)							-1.5	-0.6	-2.6	-1.7	-3.4	-2.1	-4.3	-1.5	-3.9	-1.5	
Climatological flux (1994-2019)							-2.7	-1.2	-3.2	-1.7	-4.6	-2.3	-5.0	-1.7	-3.9	-1.5	

[a] CO_2 flux was estimated using Evans et al., (2015) approach.

[b] CO_2 flux was estimated using the modified approach described in this study.

Table **4.11: Monthly area-weighted sea-air CO_2 flux (mmol m^{-2} d^{-1}) in the northern Chukchi Sea. Note that negative values of CO_2 flux indicate CO_2 uptake from the atmosphere.**

Northern Chukchi Sea	Jan	Feb	Mar	Apr	May		Jun		Jul		Aug		Sept		Oct		Nov		Dec
					flux[a]	flux[b]	flux[a]	flux[b]	flux[a]	flux[b]	flux[a]	flux[b]	flux[a]	flux[b]	flux[a]	flux[b]	flux[a]	flux[b]	
1994									-1.0	-1.8									
1995																			
1996																			
1997																			
1998											-4.0	-3.3							
1999													-9.0	-8.7					
2000													-9.7	-8.6					
2001																			
2002					-1.0	-1.1	-0.7	-1.5	-9.0	-8.9	-23.0	-20.7	-15.3	-14.8					
2003									-13.6	-12.3	-17.4	-16.7							
2004					-1.0	-1.4	-4.5	-3.4	-11.7	-9.4	-17.8	-17.2	-16.0	-16.0					
2005									-8.1	-7.3	-16.4	-16.4							
2006											-7.5	-4.7	-22.2	-18.7					
2007											-16.9	-16.8							
2008									-14.7	-10.1	-12.6	-11.5	-11.8	-11.8	-15.1	-13.9			
2009									-10.4	-8.4			-11.1	-11.1	-24.2	-22.6			
2010									-10.8	-4.5	-16.0	-13.2	-17.2	-17.0	-22.9	-22.3			
2011									-10.8	-8.5			-2.5	-2.5	-13.6	-13.0	-3.1	-3.1	
2012									-15.5	-7.4	-20.2	-20.7	-13.6	-13.4	-19.8	-17.9			
2013											-11.3	-11.4	-17.2	-17.0	-15.4	-12.6			
2014					2.0	2.0	1.3	2.0	-5.9	-6.3	-12.1	-11.5	-25.7	-24.8					
2015									-12.3	-12.2	-13.8	-13.5	-15.6	-15.3	-19.6	-17.0			
2016									-11.8	-9.7	-13.9	-12.4	-16.9	-15.8	-15.6	-14.6	-6.5	-5.6	
2017							-27.7	-10.2	-12.6	-9.2	-13.2	-12.8	-13.3	-13.3	-14.0	-13.3	-4.7	-4.6	
2018							-12.4	-3.2	-11.4	-11.1	-11.1	-10.6	-9.2	-9.1	-9.9	-9.9	-9.6	-8.6	
2019											-8.4	-8.2	-10.1	-10.1	-11.7	-11.7	-3.6	-3.9	
Climatological flux (1994-2006)					-1.0	-1.3	-2.6	-2.5	-8.7	-7.9	-14.4	-13.2	-14.4	-13.4					
Climatological flux (2007-2019)					2.0	2.0	-12.9	-3.8	-11.6	-8.7	-13.6	-13.0	-13.7	-13.4	-16.5	-15.3	-5.5	-5.2	
Climatological flux (1994-2019)					0.0	-0.2	-8.8	-3.3	-10.6	-8.5	-13.9	-13.0	-13.9	-13.4	-16.5	-15.3	-5.5	-5.2	

[a] CO_2 flux was estimated using Evans et al., (2015) approach.

[b] CO_2 flux was estimated using the modified approach described in this study.

Table **4.12: Monthly area-weighted sea-air CO_2 flux (mmol m^{-2} d^{-1}) in the southern Chukchi Sea. Note that negative values of CO_2 flux indicate CO_2 uptake from the atmosphere.**

Southern Chukchi Sea	Jan	Feb	Mar	Apr	May		Jun		Jul		Aug		Sept		Oct		Nov		Dec
					flux[a]	flux[b]	flux[a]	flux[b]	flux[a]	flux[b]	flux[a]	flux[b]	flux[a]	flux[b]	flux[a]	flux[b]	flux[a]	flux[b]	
1994									-9.2	-7.8									
1995																			
1996																			
1997																			
1998											-6.5	-5.8							
1999													-6.8	-6.6					
2000													-6.1	-5.9					
2001																			
2002					-1.4	-1.1			-20.3	-19.3			-16.2	-15.7					
2003									-13.9	-13.6	-9.5	-9.5							
2004					-8.4	-6.2			-12.5	-12.1			-12.1	-11.8					
2005											-18.9	-18.9							
2006											-10.1	-9.9	-18.7	-18.0					
2007																			
2008									-22.9	-22.0	-19.0	-19.0	-18.4	-18.4	-17.3	-16.7			
2009									-27.2	-25.7			-8.9	-8.9	-3.4	-3.3			
2010									-16.2	-15.1	-18.7	-18.5	-20.7	-20.7	1.3	1.3			
2011							-6.0	-5.0	-4.4	-4.3			5.8	5.8	3.8	3.7	9.9	7.8	
2012									-19.9	-18.7	-31.5	-31.3	-10.2	-9.9	-10.1	-9.4			
2013															10.0	9.5			
2014					-3.8	-4.2			-22.1	-22.0	-19.8	-19.8	-29.4	-29.4					
2015									-9.6	-9.5	-9.8	-9.8	-6.4	-6.4					
2016									-15.8	-15.0	-20.9	-20.9	-18.4	-18.4	1.3	1.3	3.7	3.1	
2017							-18.2	-15.0	-20.0	-19.8	-16.5	-16.5	-11.3	-11.3	-3.5	-3.5	13.1	11.1	
2018							-17.5	-14.7	-21.1	-20.8	-9.8	-9.8	-6.9	-6.9	14.8	14.7	7.2	6.5	
2019											-10.6	-10.6	-18.4	-18.4	-0.8	-0.8	16.3	14.0	
Climatological flux (1994-2006)					-4.9	-3.7			-14.0	-13.2	-11.3	-11.0	-12.0	-11.6					
Climatological flux (2007-2019)					-3.8	-4.2	-13.9	-11.6	-17.9	-17.3	-17.4	-17.4	-13.0	-13.0	-0.4	-0.3	10.0	8.5	
Climatological flux (1994-2019)					-4.5	-3.8	-13.9	-11.6	-16.8	-16.1	-15.5	-15.4	-12.7	-12.6	-0.4	-0.3	10.0	8.5	

[a] CO_2 flux was estimated using Evans et al., (2015) approach.

[b] CO_2 flux was estimated using the modified approach described in this study.

REFERENCES

Ardyna, M., & Arrigo, K. R. (2020). Phytoplankton dynamics in a changing Arctic Ocean. Nature Climate Change, 1-12.

Ardyna, M. et al. Shelf-basin gradients shape ecological phytoplankton niches and community composition in the coastal Arctic Ocean (Beaufort Sea). Limnol. Oceanogr. 62, 2113–2132 (2017).

Arrigo, K., Pabi, S., van Dijken, G., & Maslowski, W. (2010). Air-sea flux of CO2 in the Arctic Ocean, 1998–2003. Journal ofGeophysical Reseach, 115, G04024. https://doi.org/10.1029/2009JG001,224

Bakker et al. A multi-decade record of high quality data in version 3 of the Surface Ocean CO2 Atlas (SOCAT). Earth Syst. Sci. Data 8, 383–413 (2016).

Bates, N.R., Moran, S.B., Hansell, D.A., Mathis, J.T., 2006. An increasing CO2 sink in the Arctic Ocean due to sea-ice loss. Geophys. Res. Lett. 33, L23609. http://dx.doi.org/10.1029/2006GL027028.

Bates, N. R., &Mathis, J. T. (2009). The Arctic Oceanmarine carbon cycle: Evaluation ofair-sea CO2 exchanges, ocean acidification impacts and potential feedbacks. Biogeosciences, 6(11), 2433–2459. https://doi.org/10.5194/bg-6-2433-2009

Bélanger, S., Babin, M., & Tremblay, J. É. (2013). Increasing cloudiness in Arctic damps the increase in phytoplankton primary production due to sea ice receding. *Biogeosciences*, *10*(6), 4087.

Buck, A. L. New equations for computing vapor pressure and enhancement factor. J. Appl. Meteorol. 20, 1527–1532 (1981).

Butterworth, B. J., & Miller, S. D. (2016). Air-Sea Exchange of Carbon Dioxide in the Southern Ocean and Antarctic Marginal Ice Zone. Geophysical Research Letters 43(13), 7223–30. doi:10.1002/2016GL069581.

Cai, W. J., Chen, L., Chen, B., Gao, Z., Lee, S. H., Chen, J., ... & Zhang, H. (2010). Decrease in the CO2 uptake capacity in an ice-free Arctic Ocean basin. Science, 329(5991), 556-559.

Carmack, E. C., Macdonald, R. W., & Jasper, S. (2004). Phytoplankton productivity on the Canadian Shelf of the Beaufort Sea. *Marine Ecology Progress Series*, *277*, 37-50.

Chen, B., Cai, W. J., & Chen, L. (2015). The marine carbonate system of the Arctic Ocean: assessment of internal consistency and sampling considerations, summer 2010. Marine Chemistry, 176, 174-188.

Codispoti, L. A., Kelly, V., Thessen, A., Matrai, P., Suttles, S., Hill, V., ... & Light, B. (2013). Synthesis of primary production in the Arctic Ocean: III. Nitrate and phosphate based estimates of net community production. *Progress in Oceanography*, *110*, 126-150.

Comiso, J. C. 2017. Bootstrap Sea Ice Concentrations from Nimbus-7 SMMR and DMSP SSM/I-SSMIS, Version 3. Boulder, Colorado USA. NASA National Snow and Ice Data Center Distributed Active Archive Center. doi: https://doi.org/10.5067/7Q8HCCWS4I0R.

Else, B. G. T., Papakyriakou, T. N., Galley, R. J., Mucci, A., Gosselin, M., Miller, L. A., ... & Thomas, H. (2012). Annual cycles of pCO2sw in the southeastern Beaufort Sea: New understandings of air-sea CO2 exchange in arctic polynya regions. Journal of Geophysical Research: Oceans, 117(C9).

Evans, W., Mathis, J., Cross, J., Bates, N., Frey, K., Else, B., et al. (2015). Sea-air co_2 exchange in the western Arctic coastal ocean. Global Biogeochemical Cycles, 29(8), 1190-1209. doi:10.1002/2015GB005153

Gattuso J.-P., Epitalon J.-M., Lavigne H. & Orr J., 2018. seacarb: seawater carbonate chemistry. R package version 3.2.10. http://CRAN.R-project.org/package=seacarb

Gloege, L., McKinley, G., Landschützer, P., Fay, A., Frölicher, T., Fyfe, J., ... & Rodger, K. (2020). Quantifying errors in observationally-based estimates of ocean carbon sink variability.

Hill, V., Ardyna, M., Lee, S. H., & Varela, D. E. (2018). Decadal trends in phytoplankton production in the Pacific Arctic Region from 1950 to 2012. *Deep Sea Research Part II: Topical Studies in Oceanography*, *152*, 82-94.

Ji, B., Sandwith, Z., Williams, W., Diaconescu, O., Ji, R., Li, Y., et al. (2019). Variations in rates of biological production in the Beaufort Gyre as the Arctic changes: Rates from 2011 to 2016. Journal of Geophysical Research: Oceans, 124(6), 3628-3644. doi:10.1029/2018JC014805

Juranek, L., Takahashi, T., Mathis, J., & Pickart, R. (2019). Significant biologically mediated CO2 uptake in the Pacific Arctic during the late open water season. *Journal of Geophysical Research: Oceans*, *124*(2), 821-843.

Landschützer, P., Gruber, N., Bakker, D. C. E., Schuster, U., Nakaoka, S., Payne, M. R., et al. (2013). A neural network - based estimate ofthe seasonal to inter - annual variability of the Atlantic Ocean carbon sink. Biogeosciences, 10(11), 7793 – 7815. https://doi.org/10.5194/bg - 10 - 7793 - 2013

Landschützer, P., Gruber, N., Bakker, D. C. E., & Schuster, U. (2014). Recent variability of the global ocean carbon sink. Global Biogeochemical Cycles, 28, 927–949. https://doi.org/10.1002/2014GB004853

Landschützer, P., Gruber, N., & Bakker, D. C. E. (2016). Decadal variations and trends of the global ocean carbon sink. Global Biogeochemical Cycles, 30, 1396–1417. https://doi.org/10.1002/2015GB005359

Laruelle, G. G., Lauerwald, R., Pfeil, B., & Regnier, P. (2014). Regionalized global budget of the CO2 exchange at the air - water interface in continental shelf seas. Global Biogeochemical Cycles, 28, 1199 – 1214. https://doi.org/10.1002/2014GB004832

Laruelle, G. G., Landschützer, P., Gruber, N., Tison, J. L., Delille, B., & Regnier, P. (2017). Global high - resolution monthly pCO2 clima- tology for the coastal ocean derived from neural network interpolation. Biogeosciences, 14(19), 4545 – 4561. https://doi.org/10.5194/bg - 14 - 4545 - 2017

Lewis, K. M., van Dijken, G. L., & Arrigo, K. R. (2020). Changes in phytoplankton concentration now drive increased Arctic Ocean primary production. Science, 369(6500), 198-202.

Loose, B., McGillis, W., Perovich, D., Zappa, C., & Schlosser, P. (2014). A parameter model of gas exchange for the seasonal sea ice zone. Ocean Science, 10(1), 17-17. doi:10.5194/os-10-17-2014

Lovely, A., Loose, B., Schlosser, P., McGillis, W., Zappa, C., Perovich, D., et al. (2015), The Gas Transfer through Polar Sea ice experiment: Insights into the rates and pathways that determine geochemical fluxes, Journal of Geophysical Research: Oceans, 120, 8177–8194, doi:10.1002/2014JC010607.

Manizza, M., Follows, M. J., Dutkiewicz, S., Menemenlis, D., Hill, C. N., & Key, R. M. (2013). Changes in the Arctic Ocean CO2 sink (1996–2007): A regional model analysis. Global Biogeochemical Cycles, 27, 1108–1118. https://doi.org/10.1002/2012GB004491

Manizza, M., Menemenlis, D., Zhang, H., & Miller, C. E. (2019). Modeling the recent changes in the Arctic Ocean CO2 sink (2006–2013). Global Biogeochemical Cycles, 33(3), 420-438.

Millero, F. J., T. B. Graham, F. Huang, H. Bustos-Serrano, and D. Pierrot (2006), Dissociation constants of carbonic acid in seawater as a function of salinity and temperature, Mar. Chem., 100, 80–94.

Mundy, C. J., Gosselin, M., Ehn, J., Gratton, Y., Rossnagel, A., Barber, D. G., ... & Papakyriakou, T. (2009). Contribution of under-ice primary production to an ice-edge upwelling phytoplankton bloom in the Canadian Beaufort Sea. *Geophysical Research Letters*, *36*(17).

Murata, A., &Takizawa, T. (2003). SummertimeCO2 sink in shelf and slope waters of the western Arctic Ocean. Continental Shelf Research, 23, 753–776.

Olsen, A., R. M. Key, S. van Heuven, S. K. Lauvset, A. Velo, X. Lin, C. Schirnick, A. Kozyr, T. Tanhua, M. Hoppema, S. Jutterström, R. Steinfeldt, E. Jeansson, M. Ishii, F. F. Pérez and T. Suzuki. The Global Ocean Data Analysis Project version 2 (GLODAPv2) – an internally consistent data product for the world ocean, Earth Syst. Sci. Data, 8, 297–323, 2016, doi:10.5194/essd-8-297-2016.

Olsen, A., Lange, N., Key, R. M., Tanhua, T., Bittig, H. C., Kozyr, A., Àlvarez, M., Azetsu-Scott, K., Becker, S., Brown, P. J., Carter, B. R., Cotrim da Cunha, L., Feely, R. A., van Heuven, S., Hoppema, M., Ishii, M., Jeansson, E., Jutterström, S., Landa, C. S., Lauvset, S. K., Michaelis, P., Murata, A., Pérez, F. F., Pfeil, B., Schirnick, C., Steinfeldt, R., Suzuki, T., Tilbrook, B., Velo, A., Wanninkhof, R. and Woosley, R. J.(2020). GLODAPv2.2020 – the second update of GLODAPv2. doi:10.5194/essd-2020-165.

Ouyang, Z., Qi, D., Chen, L., Takahashi, T., Zhong, W., DeGrandpre, M. D., ... & Sun, H. (2020). Sea-ice loss amplifies summertime decadal CO 2 increase in the western Arctic Ocean. Nature Climate Change, 10(7), 678-684.

Ouyang, Zhangxian, Di Qi, Wenli Zhong, Liqi Chen, Zhongyong Gao, Hongmei Lin, Heng Sun, Tao Li, and Wei-Jun Cai. (2021) Summertime evolution of net community production and CO2 flux in the western Arctic Ocean. Global Biogeochemical Cycles: e2020GB006651.

Peng, G., Meier, W., Scott, D., Savoie, M., A long-term and reproducible passive microwave sea ice concentration data record for climate studies and monitoring. Earth Syst. Sci. Data 5, 311e318 (2013).

Prytherch, J., Brooks, I., Crill, P., Thornton, B., Salisbury, D., Tjernström, M., et al. (2017). Direct determination of the air-sea CO2 gas transfer velocity in Arctic sea ice regions. Geophysical Research Letters, 44(8), 3770-3778. doi:10.1002/2017GL073593

Randelhoff A, Holding J, Janout M, Sejr MK, Babin M, Tremblay J-É and Alkire MB (2020) Pan-Arctic Ocean Primary Production Constrained by Turbulent Nitrate Fluxes. Front. Mar. Sci. 7:150. doi: 10.3389/fmars.2020.00150

Roobaert, A., Laruelle, G. G., Landschützer, P., Gruber, N., Chou, L., & Regnier, P. (2019). The spatiotemporal dynamics of the sources and sinks of CO2 in the global coastal ocean. Global Biogeochemical Cycles, 33(12), 1693-1714.

Shadwick, E. H., Thomas, H., Chierici, M., Else, B., Fransson, A., Michel, C., ... & Tremblay, J. É. (2011). Seasonal variability of the inorganic carbon system in the Amundsen Gulf region of the southeastern Beaufort Sea. Limnology and Oceanography, 56(1), 303-322.

Song, H, R. Ji, M. Jin, Y. Li, Z. Feng, O., Varpe, and C. Davis (in final revision), Strong and regionally distinct links between sea-ice phenology and primary production in the Arctic, Limnology and Oceanography. In press.

Takahashi, T., Sutherland, S. C., Wanninkhof, R., Sweeney, C., Feely, R. A., Chipman, D. W., ... & Watson, A. (2009). Climatological mean and decadal change in surface ocean pCO2, and net sea–air CO2 flux over the global oceans. Deep Sea Research Part II: Topical Studies in Oceanography, 56(8-10), 554-577.

Takahashi, Taro; Sutherland, Stewart C.; Kozyr, Alex (2019). Global Ocean Surface Water Partial Pressure of CO2 Database: Measurements Performed During 1957-2018 (LDEO Database Version 2018) (NCEI Accession 0160492). Version 7.7. NOAA National Centers for Environmental Information. Dataset. https://doi.org/10.3334/CDIAC/OTG.NDP088(V2015).

Tremblay, J.-É. et al. Impact of river discharge, upwelling and vertical mixing on the nutrient loading and productivity of the Canadian Beaufort Shelf. Biogeosciences 11, 4853–4868 (2014).

Ulfsbo, A., Cassar, N., Korhonen, M., van Heuven, S., Hoppema, M., Kattner, G., & Anderson, L. G. (2014). Late summer net community production in the central Arctic Ocean using multiple approaches. *Global Biogeochemical Cycles*, *28*(10), 1129-1148.

Varela, D. E., Crawford, D. W., Wrohan, I. A., Wyatt, S. N., & Carmack, E. C. (2013). Pelagic primary productivity and upper ocean nutrient dynamics across Subarctic and Arctic Seas. *Journal of Geophysical Research: Oceans*, *118*(12), 7132-7152.

Wanninkhof, R. (2014). Relationship between wind speed and gas exchange over the ocean revisited. Limnology and Oceanography: Methods, 12(6), 351-362. doi:10.4319/lom.2014.12.351

Weiss, R. (1974). Carbon dioxide in water and seawater: The solubility of a non-ideal gas. Marine Chemistry, 2(3), 203-215. doi:10.1016/0304-4203(74)90015-2

Woodgate, R., Weingartner, T., & Lindsay, R. (2012). Observed increases in Bering Strait oceanic fluxes from the Pacific to the Arctic from 2001 to 2011 and their impacts on the Arctic Ocean water column. Geophysical Research Letters, 39(24). doi:10.1029/2012GL054092

Woodgate, R. A. (2018). Increases in the Pacific inflow to the Arctic from 1990 to 2015, and insights into seasonal trends and driving mechanisms from year-round Bering Strait mooring data. Progress in Oceanography, 160, 124-154. doi:10.1016/j.pocean.2017.12.007

Woosley, R. J., Millero, F. J. & Takahashi, T. Internal consistency of the inorganic carbon system in the Arctic Ocean. Limnol. Oceanogr. Methods 15, 887–896 (2017).

Yasunaka, S., Murata, A., Watanabe, E., Chierici, M., Fransson, A., van Heuven, S., et al. (2016). Mapping of the air-sea CO2 flux in the arctic ocean and its adjacent seas: Basin-wide distribution and seasonal to interannual variability. Polar Science, 10(3), 323–334. https://doi.org/10.1016/j.polar.2016.03.006

Yasunaka, S., Siswanto, E., Olsen, A., Hoppema, M., Watanabe, E., Fransson, A., ... & Takahashi, T. (2018). Arctic Ocean CO2 uptake: An improved multiyear estimate of the air-sea CO2 flux incorporating chlorophyll a concentrations.

Chapter 5

CONCLUSIONS

The changes related to the Arctic carbon cycle associated with global warming and climate change have attracted increased attention. How the increasing anthropogenic CO_2 affects the Earth ecosystem and climate is of great interest to the scientific communities and society. The Arctic Ocean, as an ocean with the least human activity, has experienced the most rapid environmental changes, which has prominent implications for the well-being of society. Thus, it is important to convey the new information to the policy-makers and the general public.

Our research in the western Arctic Ocean has improved our understanding of how the inorganic carbon cycle is likely being impacted by climate warming through sea-ice loss and it fills a substantial knowledge gap on how the sensitive and vulnerable carbonate system responds to anticipated environmental changes in the Arctic Ocean. Since data coverage in the Arctic Ocean is sparse, this dissertation will also benefit our evaluation of vulnerable carbonate chemistry in the high-latitudes, assessment of ocean acidification, and decision-support activities.

This dissertation includes an in-situ survey (Chapter 2), in which we conducted underway measurements of sea surface $\Delta(O_2/Ar)$ (from which net community production (NCP) can be derived) and pCO_2 (from which CO_2 flux can be derived) in summers of 2016 and 2018. The seasonal and regional variabilities in metabolic status and the coupling of NCP and air–sea CO_2 fluxes in the western Arctic Ocean have been examined and demonstrated. Our observations present a complete view of the western Arctic summer evolution of NCP and CO_2 uptake, through the stages of pre-melt, ongoing melt, and post-melt. In the heavily ice-covered areas (>79ºN), where air-sea gas exchange was suppressed, even a weak NCP could result in relatively high O_2 saturation and low pCO_2. Within the marginal ice zone (15%<ice%<60%), NCP and CO_2 flux become large and were strongly inversely correlated, suggesting an air to sea CO_2 flux induced primarily by ongoing biological CO_2 removal from surface waters. In ice-free waters, the coupling of NCP and CO_2 flux varied according to nutrient supply. In the oligotrophic Canada Basin, NCP and CO_2 flux were both small, controlled mainly by the air-sea gas exchange. On the nutrient-rich Chukchi Shelf, NCP was strong, resulting in high O_2 release and CO_2 uptake. This regional overview of NCP and CO_2 flux in the western Arctic Ocean, in its various stages of ice-melt and nutrient status, provides useful insight into the possible mechanism that controls long-term changes in primary production and CO_2 sink in the Arctic Ocean.

In addition, we employed a box model to explore the effect of sea ice history (in addition to wind history) on estimating NCP and CO_2 fluxes. Our model results demonstrate that accounting for local sea ice history is important in estimating NCP from $\Delta(O_2/Ar)$ in polar regions. This methodology improvement will benefit the scientific community for constraining the uncertainties of NCP associated with changing sea ice, when the $\Delta(O_2/Ar)$ approach is used.

With regard to rapid changes in Arctic biogeochemical processes, another interesting scientific question is how fast is sea surface pCO_2 changing driven by ice loss? Variability in the ocean sink of anthropogenic CO_2 in the Arctic Ocean has important implications for future climate change and ocean acidification. By compiling all available sea surface pCO_2 data from multiple international databases between 1994 and 2017, for the first time, we examined and identified the observation-based decadal trends and quantified the contributions of several drivers (Chapter 3). We showed that summer pCO_2 in the Canada Basin increased by 4.6±0.5 μatm yr^{-1}, more than twice faster than the rate of atmospheric CO_2 increase. If this trend continues, the summer air–sea CO_2 gradient may become near zero and the summer CO_2 sink may vanish in the Canada Basin within two decades. We further quantitatively evaluated how sea surface pCO_2 responds to different environmental drivers by decomposing the variation in pCO_2 into thermal and non-thermal components. Our analysis revealed that the thermal component (warming) contributed ~15% of the total pCO_2 increase whereas the non-thermal component (ice-loss induced DIC increase and SSS decrease) contributed ~85% of the total pCO_2 long-term trend. We suggested that increased air–sea CO_2 uptake due to sea-ice loss is primarily responsible for the net DIC increase, which has strengthened the pCO_2 seasonal amplitude and resulted in the rapid increase over recent decades. In contrast, our results showed that pCO_2 on the Chukchi Shelf did not change significantly because strong and increasing biological uptake has kept pCO_2 low. Based on this unchanged trend, we predicted that the summer CO_2 sink on the Chukchi Shelf may increase further due to the higher atmospheric CO_2.

However, the examination of long-term trends in sea surface pCO_2 and air-sea pCO_2 gradient did not resolve the debate for future CO_2 uptake in the Arctic Ocean, and the interannual change in the CO_2 sink is still poorly known. To resolve the spatial and temporal variability in air-sea CO_2 flux and determine how the CO_2 sink and source changes in response to multiple sea ice-related environmental changes, we quantified the air-sea CO_2 fluxes and oceanic CO_2 sink for the entire western Arctic

Ocean over the period of 1994 to 2019 (Chapter 4). Our assessment included two complementary approaches: one is an observation-based approach and another is a model-based approach. For the observation-based approach, we compiled and synthesized a more extensive dataset of sea surface pCO_2 covering from 1994 to 2019. However, increasing the number of pCO_2 observations does not sufficiently improve the data seasonal and regional coverage, which suffers from sparsity of pCO_2 data and makes it difficult to assess whether there are any trends in CO_2 fluxes among different regions. To increase data coverage in both time and space and to fill in gaps for an integrated assessment, we employed a box model approach to reconstruct daily time series maps of pCO_2 for the western Arctic Ocean. With seamless modeled data, we were able to further disentangle and identify the effects of sea ice, wind speed and sea-air gradient of pCO_2 on the seasonal and interannual variabilities of CO_2 flux and carbon sink. The observation-based results showed that CO_2 uptake in the summer Chukchi Sea significantly increased at a rate of 1.4 $\pm$0.6 Tg C decade^{-1}, which was primarily due to a longer ice-free period and higher primary production and partially due to enhanced wind. However, no significant increase in CO_2 uptake was noticed in both the Canada Basin and Beaufort Sea based on this synthesized dataset. With modeled results, we confirmed that annual CO_2 sink significantly increased in the Chukchi Sea by 1.6$\pm$0.3 Tg C decade^{-1} and CO_2 sink in the Beaufort Sea was invariable over the years. More interestingly, our model results further revealed that the greatly decreased sea ice extent in summer indeed promoted CO_2 uptake and resulted in a weak increased CO_2 sink by 0.6$\pm$0.3 Tg C decade^{-1} in the Canada Basin, but this increasing sink was counteracted by a smaller air-sea pCO_2 gradient.

In summary, this dissertation improves the understanding of processes regulating seasonal, interannual and decadal variabilities of $p$$CO_2$, CO_2 flux and oceanic CO_2 sink in the western Arctic Ocean, which is essential for forecasting responses of the ocean carbon cycle to future climate change. However, there are still several scientific knowledge gaps that remain to be addressed in the future. Even with the insights provided from our newly synthesized dataset, the uncertainties of the response of the carbon cycle in the Arctic Ocean remain large. Thus, continued observations are strongly needed to monitor future changes. As the western Arctic Ocean, only constitutes ~20% of total area of Arctic Ocean, it will be of great interest and importance to apply the methodology described in this dissertation to an integrated analysis of the entire Arctic Ocean to better assess the CO_2 sink and constrain accompanying uncertainties. In the growing interests for high-resolution, gapless sea surface $p$$CO_2$ distribution, our simplified box-model with $1^{o}\times1^{o}$ spatial resolution is insufficient to resolve the $p$$CO_2$ distribution in the highly dynamic areas (e.g., shelfbreak), leaving room for future enhancement of resolution, incorporation of multi-stream satellite data (e.g., Chl a and SSS), and improvement of modeling skills.

Appendix A

PERMISSION

Title: Sea-ice loss amplifies summertime decadal CO2 increase in the western Arctic Ocean

Author: Zhangxian Ouyang, Di Qi, Liqi Chen, Taro Takahashi, Wenli Zhong, Michael D. DeGrandpre, Baoshan Chen, Zhongyong Gao, Shigeto Nishino, Akihiko Murata, Heng Sun, Lisa L. Robbins, Meibing Jin & Wei-Jun Cai

Publication: Nature Climate Change

Publisher: Springer Nature

Date: Jun 15, 2020

Citation: Ouyang, Z., Qi, D., Chen, L., Takahashi, T., Zhong, W., DeGrandpre, M.D., Chen, B., Gao, Z., Nishino, S., Murata, A. and Sun, H., 2020. Sea-ice loss amplifies summertime decadal CO_2 increase in the western Arctic Ocean. *Nature Climate Change*, *10*(7), pp.678-684.

Please note that, as the author of this Springer Nature article, I retain the right to more information on this, please visit: https://s100.copyright.com/AppDispatchServlet

Appendix B

PERMISSION

Title: Summertime evolution of net community production and CO_2 flux in the western Arctic Ocean

Author: Zhangxian Ouyang, Di Qi, Wenli Zhong, Liqi Chen, Zhongyong Gao, Hongmei Lin, Heng Sun, Tao Li, Wei-Jun Cai

Publication: Global Biogeochemical Cycles

Publisher: AGU

Date: Jan 17, 2021

Citation: Ouyang, Z., Qi, D., Zhong, W., Chen, L., Gao, Z., Lin, H., Sun, H., Li, T. and Cai, W.J., Summertime evolution of net community production and CO2 flux in the western Arctic Ocean. Global Biogeochemical Cycles, p.e2020GB006651.

Please note that, as the author of this Springer Nature article, I retain the right to more information on this, please visit: https://www.agu.org/Publish-with-AGU/Publish/Author-Resources/Policies/Permission-policy#repository